Process conditions of Magnesium alloys for unconventional sheet metal forming applications

Politecnico di Bari

Department of Mechanics, Mathematics and Management
MECHANICAL AND MANAGEMENT ENGINEERING
Ph.D. Program
SSD: ING-IND/16–Manufacturing technology and systems

Final Dissertation

Process conditions of Magnesium alloys for unconventional sheet metal forming applications

by
Guglielmi Pasquale

Supervisors

Prof. Palumbo Gianfranco

Prof. Sorgente Donato

Prof. Kaya Ali Arslan

Coordinator of Ph.D. Program:
Prof. Giuseppe Pompeo Demelio

Course n°32, 01/11/2016 – 31/10/2019

Politecnico di Bari

Department of Mechanics, Mathematics and Management
MECHANICAL AND MANAGEMENT ENGINEERING
Ph.D. Program
SSD: ING-IND/16–Manufacturing technology and systems

Final Dissertation

Process conditions of Magnesium alloys for unconventional sheet metal forming applications

by
Guglielmi Pasquale

Referees

Prof. Garcia Romeu Maria Luisa

Prof. Renna Paolo

Supervisors

Prof. Palumbo Gianfranco

Prof. Sorgente Donato

Prof. Kaya Ali Arslan

Coordinator of Ph.D. Program:
Prof. Giuseppe Pompeo Demelio

Course n°32, 01/11/2016 – 31/10/2019

"Every great dream begins with a dreamer.
Always remember,
you have within you the strength,
the patience, and the passion
to reach for the stars to change the world."

Harriet Tubman

Dedication

To my wife Lucrezia
and our child Luca
for the patience and the continuous support:
reason of life and safe haven always!

To my family:
a genuine example and an immense source of encouragement!
I owe my parents everything!

To all my friends!

Acknowledgements

I would like to thank my tutor, Prof. Gianfranco Palumbo, a real mentor and a friend, for his guidance and support during my graduate studies and research activities:
I owe you so much, starting from the capability to analyze and solve the problems, even when these seem insurmountable.
I hope you can be proud of me!

I would also like to thank my friend Prof. Donato Sorgente for all:
for having always been close to me, for having given me the capability to tackle the problems in reference to my research topics with a critical spirit and rigorous method. For comforting words, even when everything seemed to go wrong.

Thanks to Prof. Ali Arslan Kaya for the considerable cooperation in the present research activity, for the enormous transfer of knowledge in terms of metallographic analysis and for his great hospitality.

Thanks also to Prof. Maria Luisa Romeu Garcia and Prof. Ines Ferrer for
their hospitality and for the possibility to conclude the experimental activities for the present research topic in their splendid Girona.

Finally, I thank my co-workers Mech. Eng. Antonio Piccininni and Mech. Eng. Liliana Cusanno.
Antonio is the true complement to my research figure: We have been sharing joys and sorrows for ten years now. I hope that we can work together successfully for a long time!
Liliana was a pleasant discovery both from a human and a professional point of view.

Simply thanks for all!

Contents

List of Figures

List of Tables

Introduction

Over the last years, the requirements in terms of exhaust gas emissions and fuel consumption have become stricter. It is imperative that beside the standards about limiting the pollutants released out from industry and power plants, emissions coming from engine–powered vehicles must be monitored.

There are several standards, in different countries (such as Tier 3 in the US, LEV III in California, and Euro 6 rules in the EU), and all of these aims to lower vehicle emissions and further improvements in air quality [1].

Since road transport constitutes about 20 percent of the total CO_2 emission, the European Union (EU) built up a legal structure with the precise aim of reducing emission and consequently the fuel consumptions. The transport sector is the only one in the EU where Greenhouse Gas (GHG) emissions are still rising [2]. Starting from the value of the fuel consumption (5 litres per 100 km) registered in the 2009, the EU has imposed mandatory targets for the average CO_2 emissions of each vehicle manufacturer at 95 CO_2/km within the 2021 [3].

This purpose can be reached following different strategies: (i) Reduction of vehicles weight, (ii) Downsizing of the engine parts and (iii) Improvement of fuel efficiency can be considered relevant and valid solutions. Regarding the first strategy, metal alloys with low densities, called "*Light Alloys*" such as Aluminium (Al), Magnesium (Mg) and Titanium (Ti) alloys, are required [3].

In fact, a weight reduction of 10% allows to obtain an improvement in terms of fuel consumption equal to about 5.5% [4,5]. In addition, it was estimated that, using 1 kg of light alloys to replace heavier materials, leads to a CO_2 emission reduction of 20 kg within the life of the vehicle [4].

With reference to the third of the abovementioned approaches, also the optimization of the aerodynamic aspects represents a promising strategy: since in most cases complex geometry and small thickness of components are required, very complex shapes, which cannot always be manufactured with the conventional manufacturing techniques, are necessary.

Main objectives of automotive products development include (i) increase in quality, (ii) safety and (iii) reduction of environmental impact. These objectives should be achieved in an efficient, cost effective way to optimize consumer value. Many different types of constructions, operational and processing materials are used in the automotive manufacturing chain, and their selection and proper use can have a significant impact on these objectives [6]. Supported by these technological aspects, unconventional sheet-metal forming processes (i.e. SuperPlastic Forming, SPF, and Single Point Incremental Forming, SPIF) are recurrently adopted instead of the conventional methodologies (i.e. Stamping).

Furthermore, Mg alloys appear to be very attractive for several structural and biomedical applications due to their lightness and good mechanical properties associated to the properties very close to those of human bone.

Moreover, Mg-based metals, including pure Mg and its alloys, are becoming increasingly popular in the medical industry due to their biodegradability [7]. For this reason, some Mg alloys could become an alternative to the other metals to manufacture prostheses, used to both fuse fractured bones and help eliminate cardiovascular problems associated with the use of stents. In fact, in addition to the excellent biodegradability, they are characterized by high biocompatibility as well as by the suitable mechanical compatibility with the human bones.

As anticipated, Biometals have been used for a long time in medicine, mainly in prostheses, but also as joining elements in case of bone fractures bones or in vascular stents that are used to solve cardiovascular problems, among others. Traditionally used metals - Stainless steel and Ti alloys - have advantages (their resistance to corrosion in the physiological environment), but also disadvantages (the decrease in bone density in the proximity of the prosthesis, which decrease the bone resistance). In addition, in many cases, it is necessary to carry out a second surgery step to eliminate the material once it has fulfilled its function. In the last years, medicine, which is known to be highly conservative, is pushing the research efforts towards the direction of implant surgery requiring only one step approach: this goal was obtained after the introduction of implants and fixation supports which are biodegradable. These needs have led to considering Mg and its alloys as very promising candidates for the development of temporary, degradable implants [8].

Usually the temporary prostheses and/or medical devices are highly customized as a result of the complex geometries needed for individual patients. This aspect motivated once again investigation about unconventional techniques such as SPF and SPIF.

Based on the above given accounts, Mg alloys have become very interesting for the automotive, aeronautics and biomedical fields. At this point, the actual limitation of the use of Mg and its alloys is mainly due to its mechanical and deformation properties. Fortunately, despite the low formability at room temperature resulting from its Hexagonal Close-Packed (HCP) crystal structure which has a low number of atomic slip planes, as temperature increases, additional slip systems and deformation mechanisms become active [9]. This allows a drastic increase of the material deformation properties. Furthermore, magnesium and its alloys show superplastic properties that are likely to be employed industrially.

In close correlation with the abovementioned aspects, the present research activity was aimed to design both material and manufacturing process via unconventional techniques. In particular, based on an up-to-date literature review, the motivation of this research was to obtain new Mg alloys capable of competing with the commercially available Mg alloys. With respect to an innovative Mg alloy system, the attention was focused on the identification of different alloying elements able to increase the deformation capacity. Several different Mg alloys were fabricated by casting and evaluated. The screening phase was based on the comparison of the results coming from hardness (at room temperature) and tensile (at worm and high temperature) tests, aiming to the identify the best one from a formability point of view. Finally, the best performing Mg alloy (Mg-2Zn-2Ce) that we have obtained via casting was extensively investigated in superplastic conditions. At the end of the experimental campaign conducted, comparison of the results deriving from the Mg-2Zn-2Ce alloy were compared with those of the commercial AZ31B Mg alloy (deriving from

the literature and, in any case, tested during the present research activity). experimental evidences showed that the new Mg-2Zn-2Ce alloy allow to obtain SuperPlastic behavior very close to the one of the AZ31B Mg alloy [10].
As anticipated, the other principal aspect investigated was represented by the sheet metal forming process design, applying a numerical/experimental approach, finalized to obtain very complex shape with high accuracy.
Since the new Mg alloy developed, as documented in the chapter 3, was characterized by mechanical properties and deformation behavior very close to that of the commercial AZ31B Mg alloy, the numerical/experimental SPF process design was related to the latter Mg alloy.
To obtain a sound complex component, an optimized manufacturing process involves a Finite Element (FE) modelling [11]. To correctly calibrate such a model, the adoption of a robust constitutive material models is imperative. Various constitutive models able to catch the deformation behavior of the AZ31B Mg alloys at high temperature are available in literature. The same cannot apply to the novel Mg alloy studied. In addition, the new experimental Mg alloy was obtained via casting and this aspect coupled with that of Electro Discharge Machining (EDM) for samples extraction involved prolonged time periods both in terms of casting production and extraction of the samples.
For this reason, two different cases (with reference to both biomedical field and automotive application), involving SPF process, were designed considering the AZ31B Mg alloy.
Numerical/experimental approach was adopted to only SPF procedure in order to design the forming process correctly and then to evaluate the capability of the material model implemented to predict the real deformation behavior of the alloy. In particular, an innovative approach was used to determine the constants of such a model: they were determined exclusively by means of bulge tests. This choice was aimed at evaluating the deformation behavior of the alloy under conditions more similar to the ones characterizing the industrial metal forming process.
In the first case, our study focussed on a spherical vessel obtained via SPF. As a well-known fact, one of the most critical aspects of the components obtained by SPF is the inherent non-uniform thickness distribution after forming. The present research activity allowed to overcome this problem by exploiting a hybrid approach to the manufacture of the vessel. In fact, SPF tests were carried out starting from SPIFed samples with an optimized thickness distribution able to guarantee, at the end of SPF step, a high uniformity of thickness in the most critical apical zone. Numerical analyses of SPF forming step were performed in accordance with the material model suggested by Enikeev and Kruglov [12].
In this case, comparisons in terms of dome height with respect to the forming time and thickness distribution on the spherical vessel according to the gas pressure were carried out.
Furthermore, in order to optimize the thickness distribution of the final component, another important way considered was the selective Laser Heat Treatment (LHT) of the undeformed sheet before the forming step. With this aim, the effects of a selective LHT on the AZ31B Mg alloy sheet were evaluated using a numerical/experimental approach. Tests using different laser power levels of a CO_2 laser and keeping the spot stationary were aimed in order to determine experimentally the microstructural evolution of the investigated alloy. In addition, the same tests were adopted to both set and to validate the numerical model for

the simulation of the LHT of the samples by implementing the Miao's constitutive material model [13]. Finally, the obtained LHTed samples were numerically and experimentally tested by means of bulge tests to produce a shape very similar to the previous one obtained coupling SPIF and SPF. Numerical analyses of SPF process were performed exploiting the Carpenter material model [14] preventively calibrated experimentally.
The second case studied was a customized bioabsorbable cheekbone prostheses obtained by means of both SPF and SPIF processes.
As an additional aspect to the numerical/experimental approach used for SPF manufacturing process, for the SPIF process, process parameters optimization was performed using an experimental approach based on Design of Experiments (DoE) changing the value of the main process parameters, such as Step down, Feed rate and Spindle speed.
Finally, results in terms of thickness distribution, roughness and shape accuracy, coming from both SPF and SPIF processes, were compared.

1. Magnesium (Mg) and its alloys: a challenge for process and product innovation

Magnesium is the lightest common structural metal with a density of 1.74 g/cm^3 in its solid state. During the present research activity, the attention was focused on the mechanical and deformation properties of Mg alloys that are relevant to correctly design lightweight components [15]. For this reason, it is important to fully understand in which scenario the material under investigation is contextualised.

1.1. Mg and its alloys

Mg and its alloys are the lightest structural metals available for engineering use, characterized by an exponential and continuous growth in terms of their engineering use. The increase in the use of magnesium and its alloys can prove to be an interesting opportunity, thanks to the low density combined with a high specific strength and availability.

Mg and most of its alloys show a low Young's Modulus (about 45GPa) and low resistance to fatigue, creep and wear. In order to overcome these limitations in the mechanical properties addition of alloying elements can be used leading to markedly increased properties. On the other hand, Mg and many of its alloys possesses better damping, i.e. ability to absorb energy among metals. Increased vibration absorption capacity provides for quieter operation of equipment when magnesium castings are used for housings and enclosures.

Another important aspect is represented by the ratio between the economics and technological aspects. The Mg alloys are currently more expensive if compared to the Al alloys. However, in recent years, the cost difference is slightly reduced due to an increased use of the Mg alloys.

Furthermore, recyclability of Mg, as for other metals and alloys, is a growing factor that motivates the adoption in automotive applications, since nowadays it is possible to recycle up to 99% of parts and pieces manufactured with Mg alloys. This aspect, in addition to the economic reasons, is fundamental in order to comply with the international standards about environmental concerns.

In addition, the lower density of Mg alloys can greatly increase the efficiency of most of the components. After steels and Al alloys, they appear to be the most commonly used alloys for structural applications. International automotive producers such as GM, Ford, Volkswagen and Toyota are just a few of the largest automobile industries employing Mg alloys to produce vehicles parts.

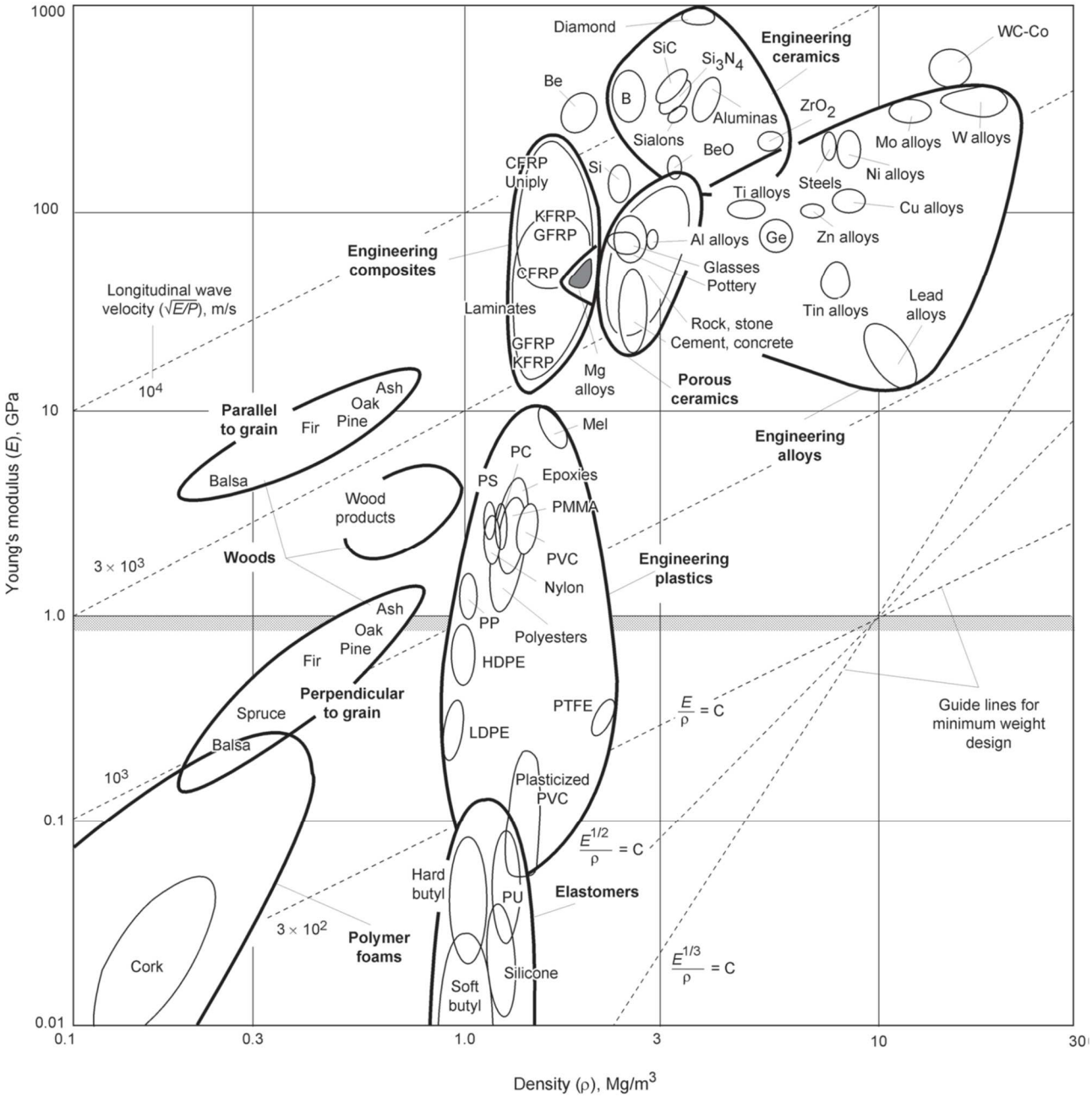

Figure 1 Ashby diagram for materials selection.

Ashby diagram of Young's modulus (E) plotted against density, for various engineered materials is shown in Figure **1**. This plot constitutes a good reference to observe the position of different materials, based on both E and density values, in comparison to the other type of alloys usually adopted in the main industrial sectors.

The position at a corner of the triangular shape representing all engineering alloys and its position shared by engineering composites highlight the special qualities of Mg alloys [16]. Mg has a density that is about two-thirds of Al and only slightly higher than that of fiber-reinforced plastics. The melting temperature is very close to that of Al (650°C) and, at room temperature, the Mg alloys are difficult to deform due to their HCP crystal structure, as shows in Figure 2.

The HCP structure has two parallel planes with atoms both at the vertices and in the centre of hexagon separated by an additional plane including three atoms and placed in the middle position.

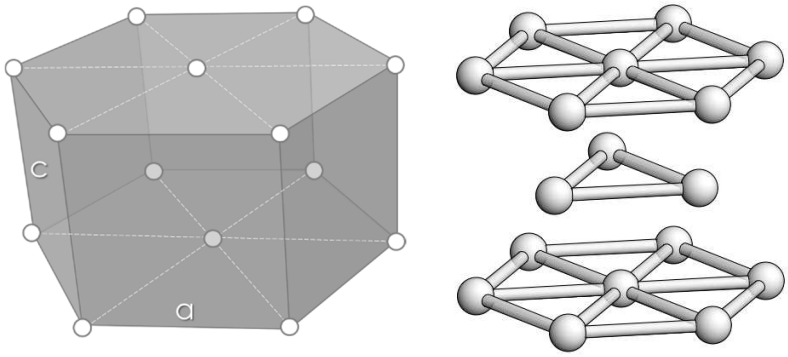

Figure 2 Scheme of HCP.

Five independent active slip systems are required for a polycrystalline material to exhibit ductile behaviour according to von Misses criterion[17]. Magnesium circumvents this criterion due to the activities of the twining systems. Figure 3 shows the different deformation modes in HCP crystals. "Slip" is the process by which a dislocation moves and causes a plastic deformation in the material. The "slip direction" is the direction along which the dislocation moves, that is the direction of the Burgers vector for dislocations. These densely populated planes and directions constitutes "slip systems". The number of such 'slip systems' determine the ability of the metal to deform, i.e. the deformation capacity. HCP systems possess only 2 independent slip systems that are operative at room temperature as compared to high values, i.e. 24 in FCC crystals. An additional and alternative deformation mechanism is represented by the twinning that operates in HCP magnesium. This phenomenon causes a reorientation of a portion of the crystal lattice, accommodating deformation by shear.

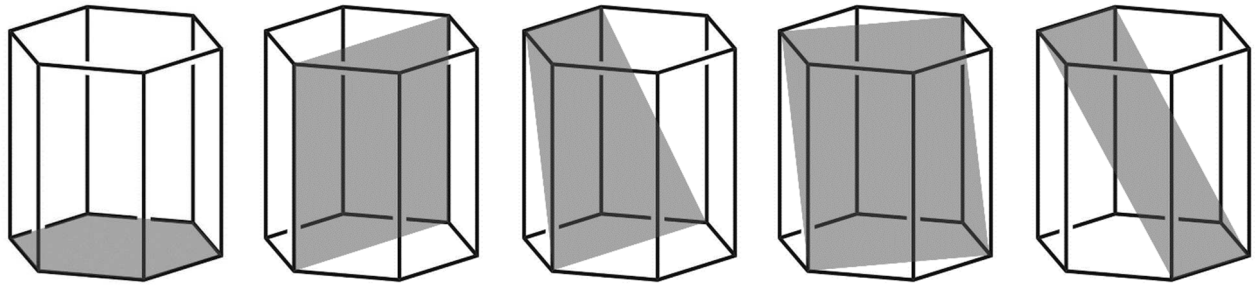

(a) (b) (c) (d) (e)

Figure 3 Deformation systems in magnesium: (a) basal slip system, (b) prismatic slip system, (c) and (d) pyramidal slip systems, (e) tensile twin system.

Macroscopically, twinning is identified by a distinct response in the stress-strain curve: softening after yield followed by a high work hardening rate [18–20]. High work hardening rate in magnesium is simply due to the larger 'core size' of dislocation as a result of relatively low Stacking Fault Energy (SFE) level.

The adoption of elevated temperatures increases the formability of Mg and its alloys. When temperature reaches about 225°C additional slip systems, i.e. the prismatic and pyramidal systems also become operative. Usually, the industrial plastic deformation processes are therefore conducted at temperatures above 225°C up to 450°C depending on the alloy type [21]. As is the case for other structural metals, pure Mg is not used to manufacture aerospace and automotive components. In order to be used in manufacturing, it is alloyed with other metals. Some of the most common alloyed elements in commercial alloys are Lithium (Li), Al, Tin (Sn), Strontium (Sr), Silver (Ag), Yttrium (Y), Zinc (Zn), Neodymium (Nd), Zirconium (Zr), Manganese (Mn), Thorium (Th) and Cerium (Ce). The rare-earth elements are collectively related to as REs, and - in some cases - they are used as mixtures under the name of "mischmetal".
Magnesium is amenable to essentially all casting methods and good mechanical properties can be obtained, provided that a proper microstructural state is achieved, i.e. a low level of porosity and inclusion content, and a fine grain structure.
Further characteristics which favour the use of casting techniques are the good fluidity of the majority of Mg alloys, the high thermal conductivity and the low latent heat of melting.
A fundamental requirement of an alloying element is represented by a sufficiently high solubility in Mg. A sufficiently high solubility is required to strengthen the alloy by means of the solid solution. Further benefits can be obtained if the alloying element in concern also form useful precipitates (as in age hardenable systems, i.e. coherent and/or semi-coherent precipitates). Some alloying elements, e.g. Ca or Si, may be prohibitive due to the casting method employed. For example, die sticking becomes an issue when metal molds are used. Therefore, the selection of the alloying elements is a function of both the manufacturing process condition and requirements of the finished product [21,22].
A more detailed description on the effects of the different alloying elements is proposed in the Chapter 2. Among all Mg-based alloys commercially available, Mg-Al alloys are one major group. In fact, the addition of Al increases the alloy castability and consequently promotes the pressure die casting. Albeit, Al decrease the creep resistance of the alloy due to the formation of $Mg_{17}Al_{12}$-β precipitates. In reference to the alloys in the Mg-Al system, a particularly interesting one is the AZ31 Mg alloy, due to its combination of strength, ductility and corrosion resistance [23].

1.2.Mg alloys applications

Magnesium alloys have replaced engineering plastics in many applications because they have a comparable density but are stiffer, more recyclable, and provide magnetic shielding. Magnesium is strong and light, making it an excellent choice for aerospace applications. Magnesium is also used in a number of other products such as hand-held devices (chain saws, power tools, hedge clippers), in cars (steering wheels and columns, seat frames, transmission cases, crank case, camshaft sprocket, gearbox housings), and in audio-video-computer-communications equipment (laptop computers, camcorders, TV sets, cellular telephones). In particular cast magnesium alloys have specific design and manufacturing

advantages: (i) castings can be made with thinner walls respect to the Al alloy; (ii) castings cool more quickly due to a reduced latent heat of fusion per unit volume; (iii) high gate pressures can be achieved using moderate pressures due to the low density of magnesium; (iv) iron based casting dies has low reactivity with magnesium alloys, which reduces any tendency to die soldering, and increases die life [24].
Figure 6 shows some examples of industrial applications for Mg alloys.

(a) (b) (c)

Figure 4 Mg alloys applications: (a) accessories, (b) sport equipment and (c) structural parts.

1.2.1.Mg alloys in automotive and aeronautic applications

Referring to the automotive field, Mg alloys (particularly in sheet form) offer new opportunities to the lightweight components manufacturing, particularly in the car body, chassis, interior and engine component. Possible applications for automotive application are listed in Table 1.

Component type	Component weight of Mg, kg
Roof cross member (b-pillar)	2.0
Roof cross member (a- and c-pillar)	0.6
Instrument cross-member	3.0
Seat shell	1.0
Cover parcel shelf	1.2
Door inner part	2.5
Front wall	2.0
Back wall	4.0
Bottom plate loading space	1.0
Window management	0.4
Bay gain	0.5
Decorative components such as hide	0.5
Tailgate (inside / outside)	3.5/2.0
Hood (exterior / interior)	4.5/3.0
Roof outside	7.0
Roof cover for rht	5.0

Table 1 List of possible Mg components for automotive application.

In reference to the automotive sector, actually, the adoption of Mg alloys is still marginal, if compared to that of Al alloys. However, as shown in FIG, considering that in 2010 the alloys of Mg covered only 1% of all metal parts of the car, recent market surveys have underlined that in the next twenty years this use will become around 5%.

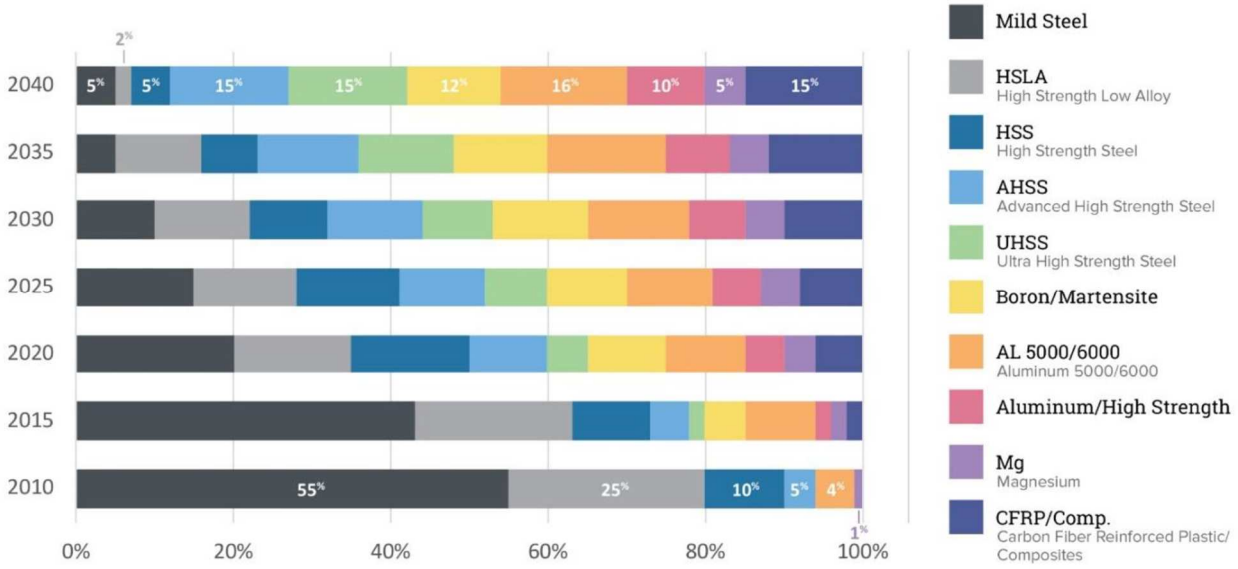

Figure 5 Material Distribution in the U.S. Fleet (Body-in-White Plus Closures), 2010 to 2040.

Magnesium was commonly defined as the metal of airborne construction. Historically, magnesium was used in aircraft since the thirties of the last century. In the fifties, magnesium went through a "boom" when it was broadly used in aircraft structures and components. Military aircrafts and helicopters that were built in that period included hundreds of kilograms of Mg products [25].

(a)

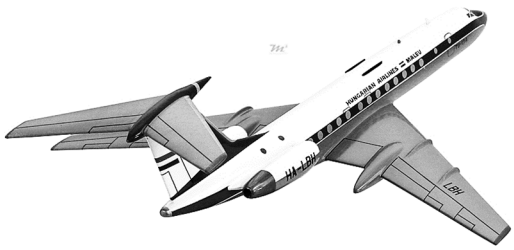

(b)

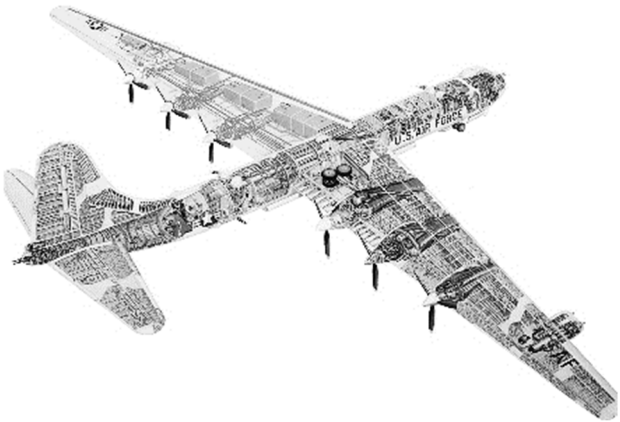

(c)

Figure 6 Examples of Mg alloys application on aircraft sector: (a) Sikorsky S-56, Westland Aircraft Ltd. (1950): 115 kg of Mg; (b) Convair B-36, total 8600 kg of magnesium: 5555 kg of magnesium sheet, 700 kg of forging; (c) Location of magnesium components (in red) in Tupolev TU-134 [26].

Mg alloys were widely used in aircrafts up to the 1950s. Due to some major drawbacks such as high corrosion sensitivity and flammability, other materials, both metals and plastics, have increasingly replaced magnesium.
Boeing 727, produced between 1962 and 1984, had 1200 different magnesium parts including leading and trailing edge flaps, control surfaces, actuators, door frames, wheels, engine gear boxes, power generation components and structural items (not primary).
Parts produced by casting are widely used in the aeronautical field. In fact, as documented by Magnesium Elektron (British chemical company which produces Mg alloys), several parts on Mg alloys can be obtained and implemented in the aircrafts.
Gear Box for MD500 and MD600 were manufactured using WE43. Additionally, main transmission castings are in WE43 for the Sikorsky S92. Rolls Royce RB211 gearboxes are manufactured adopting EZ33A.

1.2.2.Mg alloys in biomedical applications

In certain biomedical applications, especially fixators such as bone plates, screws, pins and stents, biomedical devices are required to stay inside the human body only for a restricted period, e.g., until fractured bones heal.
Thus, materials that ideally degrade in the same period as natural bone heals are highly desired to be utilized for these temporary devices. Biodegradable materials thus allow circumventing cumbersome second surgery for the removal of the temporary implants.
Besides complications and distress for the patient, the secondary surgery also increases insurance costs.
Classic metallic materials such as steels and titanium are not biodegradable and, if not removed, lead to long-term complications, as local inflammations due to the potential release of cytotoxic ions as a consequence of corrosion or wear processes.
It is therefore very attractive to identify materials that degrade in the same period as bone heals, dissolving entirely after complete healing. In this process, these materials must not cause any toxic, allergic, inflammatory or cancerous effects [27].

Properties	Natural bone	Stainless steels	Ti alloys	Co-Cr alloys	Mg alloys
Density, gcm^{-3}	1.7-2.0	7.9-8.1	4.4-4.5	8.3-9.2	1.74-2.0
Young's Modulus, MPa	3-20	189-205	110-117	230	41-45
Tensile strength, MPa	80-150	480-620	930-1140	900-1540	170-270
Compressive yield strength,	130-180	170-310	758-1117	450-1000	65-100
Elongation to failure, %	1-7	30-40	8-15	30-45	6-20
Fracture toughness, $MPam^{1/2}$	3-6	50-200	55-115	100	15-40

Table 2 Mechanical properties comparison between natural bone and typical metal alloys adopted to manufacture prosthetic implants [28–31].

However, since the mechanical properties of metals differ greatly from those of human bone, they are not always suitable for medical devices (Table 2).
The bigger the difference in elastic modulus, the higher the potential for stress-shielding, which is a phenomenological consequence of stress distribution changes. Biodegradable implants for the treatment of complex bone fractures, efficient in bearing the load of the body, showing good biocompatibility and suitable degradation properties matching the tissue healing are still lacking. These needs have led to the consideration of Mg and its alloys as very promising candidates for the development of temporary, degradable implants [31–34]. In fact, they are characterized by excellent biodegradability and biocompatibility as well as by suitable mechanical compatibility with human bone. In Figure 7 some examples of Mg alloys applications for biomedical needs are reported.

(a) (b) (c) (d)

Figure 7 Some examples of Mg alloys biomedical applications for biomedical needs: (a) Bone plates, (b) Nerve guide, (c) Bone screws and (d) Stents.

1.3. Mechanical behaviour and deformation characteristics at high temperature

The strength, hardness and Young's modulus of Mg-based alloys decrease with temperature. On the other hand, the elongation increases with rising temperature up to just below the melting point where it drops to nearly zero.
According to the chemical composition and the manufacturing process adopted to obtain Mg-based alloys or parts, these properties could also change drastically.
Taking into account Mg-alloys applications at elevated temperatures, such as the power train compartment of automobiles, it is fundamental to consider mechanical properties at the reference temperatures.
Due to the relatively low melting point of about 670°C and high diffusion rates in magnesium, the commercial alloys are necessarily confined to use at only moderately elevated temperatures. Clearly, as for the Al alloys, the safe operating temperatures for magnesium alloys are strongly less than those of steels. Depending on the chemical composition, the melt temperature can range from about 360 to 650°C. The softening of the conventional Mg-based alloys starts at exposure to temperatures as low as 95°C. Despite the

advantageous properties of Mg alloys, one of the hard challenges is represented by the difficulty of manufacturing complex shapes via sheet metal forming. Essentially, Mg alloys are suitable for any manufacturing processes such as machining and casting [35]. However, automotive body panels are typically manufactured from sheet materials using traditional deformation processes such as die stamping.

Mg alloys, including AZ31, do not exhibit enough ductility at room temperature. Formability of AZ31, measured by means of tensile tests as elongation to rupture, is strongly affected by temperature. In fact, considering an elongation equal to 15% at room temperature, an increase up to 400% can be obtained at 450°C and low strain rate values [36].

There exist studies [37] analysing the work hardening behaviour of AZ31 Mg alloy sheets in a range of temperature from the room one and 400°C and considering a strain rate of 0.045 s^{-1}.

As depicted in Figure 8, yield stress and maximum flow stress decrease with increasing temperature from 256 MPa at room temperature to about 47 MPa at 350°C for the yield stress and from 330 to about 52 MPa at 350°C for the maximum stress. The ductility of the alloy increases with temperature above 100°C, reaching to about 100% at 400°C. The work hardening rate also decreases with increasing temperature. It becomes very close to zero at temperatures between 350 and 400°C, which can be attributed to an increase in the activity of non-basal slip systems.

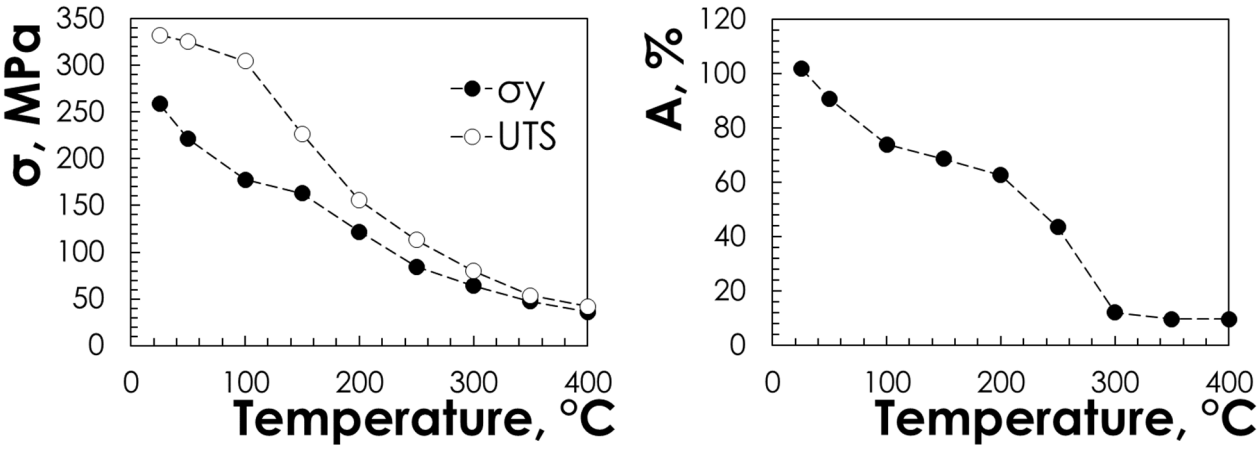

(a) (b)

Figure 8 (a) Yield stress (σy), Ultimate Tensile Strength (UTS) and (b) Elongation to fracture (A) according to the temperature.

The registered behavior suggests that complex shapes can be manufactured by means of sheet metal forming processes if high temperatures are employed. In addition, considering that an increase of the strain rate (for example equal to 0.001 or 0.0001s^{-1} allows to obtain a marked increase of the total elongation to fracture, strains greater than 100% could be achieved).

As previously mentioned, the activation of additional slip systems, i.e. prismatic and pyramidal, are required for a polycrystalline magnesium material to improve its formability drastically. The stress required to initiate slip in those additional slip systems depends on

the changes in the Critical Resolved Shear Stress (CRSS) level with temperature. CRSS is lowered at elevated temperatures beside that of the main slip system (i.e. the basal system) which improve formability drastically [38]. Improvements in terms of the number of active slip systems with increasing temperature allows to obtain high elongation-to-fracture ratios as shown in Figure 8.

Clearly, a drastic increase in deformation capability of the material is not enough to obtain a sound component with high complexity. In fact, in some cases, traditional stamping process are not able to achieve this goal. Unconventional sheet metal forming techniques, such as SPF and SPIF could be a good solution to overcome this limitation.

In reference to the SPF process, superplasticity can be associated to the capability of some polycrystalline metals to manifest very high deformation capacity in terms of elongation before the necking with the adoption of both high temperature and low strain rates. One of the most important conditions for some metallic alloys to exhibit superplastic properties, is represented by a high value of the strain rate sensitivity index, m. Since the extraordinary elongation of superplastic materials is related to the diffuse necking which, in turn, is affected by the strain rate sensitivity, the m-value can be considered as a formability index [39]. In addition, superplastic behavior can be obtained with the adoption of extremely low strain rate values (less than $0.001s^{-1}$) and temperatures higher than half the melting temperature of the alloy [40].

For materials with a fine grain size, typically less than 10μm, deformation results primarily from Grain Boundary Sliding (GBS) creep. GBS creep is associated with a high strain-rate sensitivity, m, equal about 0.5. On the contrary, at high strain rate values and very low m-values (0.2), the predominant creep mechanism active is the Dislocation Climb (DC) [41].

1.4.Unconventional sheet metal forming processes

As previously mentioned, unconventional sheet metal forming processes cold be a good solution to overcome the limitation of the traditional sheet metal forming process in order to manufacture complex parts for several industrial and biomedical sectors. In particular, to correctly design and manufacture the different geometries selected in the present research two unconventional techniques, such as SPF and SPIF, were adopted with particular emphasis on the first one.

1.4.1.Super Plastic Forming (SPF)

SPF is a sheet metal forming technique particularly adopted for obtaining complex lightweight metal components with high accuracy, which is achieved at a particular range of strain rates and temperatures. If the process is correctly designed, SPF is able to fabricate complex parts in a single operation with a great surface finish.

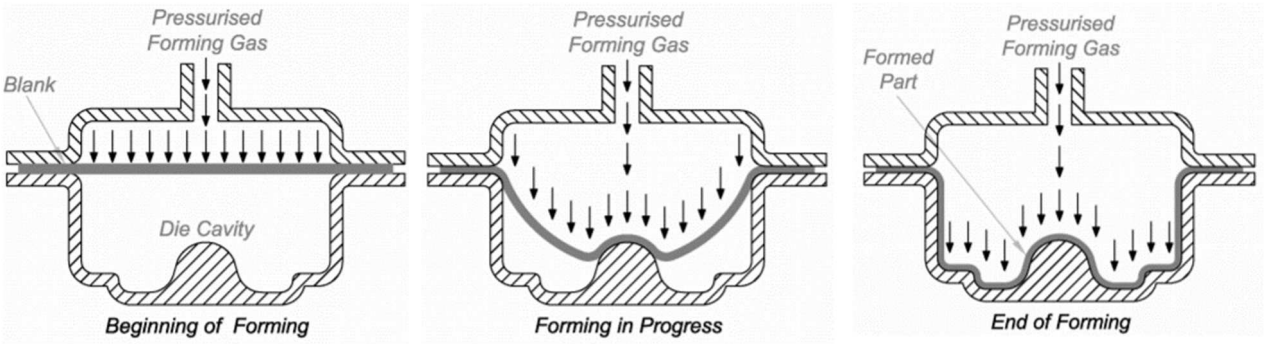

(a) (b) (c)

Figure 9 SPF process schematization: (a) Beginning of Forming, (b) forming in progress and (c) end of forming.

During a SPF test, as schematically shown in Figure 9, a metal sheet is clamped between a blankholder and a die with different geometries. The same sheet is deformed by a flexible media represented by a pressurized inert gas (usually Argon or Nitrogen). A proper Blank Holder Force (BHF) is applied to avoid the sliding of the sheet into the die cavity. Adopting the correct combination of temperature, strain rate and starting microstructure, many metals become superplastic, enabling them to be deformed into complex die shapes in a single operation using low pressure air and low-cost tooling.

Blow forming and vacuum forming are probably the two most frequently used methods of SPF, and are very similar to each other, in principle. This approach is widely used to manufacture different types of parts. Specifically, during the two variants of SPF, a pressure difference between the two sides of the sheet is imposed, allowing it to completely take the geometry of the mold. In vacuum forming, the applied pressure is, at most, equal to atmospheric pressure and, therefore, has limited capacity. On the contrary, during blow forming (or free inflation test) the pressure is applied directly on the sheet through an inert gas with variable pressures.

1.4.2.Single Point Incremental Forming (SPIF)

SPIF of metal sheets is a cheap, flexible process that allows manufacturing sheet metal components without the need for expensive, dedicated tools. Fundamentally, SPIF is a sheet metal forming technique applied mostly for small batch and custom-made products of various shapes and dimensions. Compared to conventional sheet processes it offers many advantages, especially in terms of flexibility and material formability.

The configuration reported in Figure 10 shows a scheme of the experimental setup commonly used in a SPIF process.

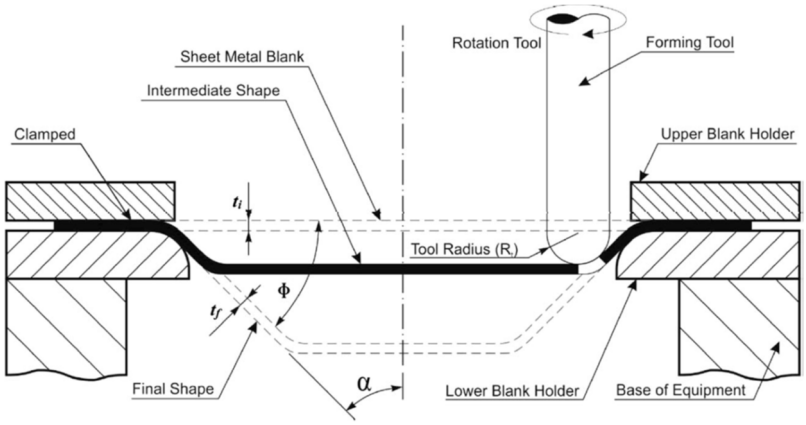

Figure 10 SPIF process schematization [42].

SPIF process is performed exploiting three-axis CNC machine. During the SPIF process, a sheet is clamped between a clamping plate and a backing plate. The bottom part of the sheet does not contact with any supporters in order to be freely deformed by a rotating tool with a spherical tip that has a single-point contact with the sheet metal blank. The backing plate is used to decrease spring-back problems in forming process.
The main process parameters that affect the accuracy and the surface quality of formed part are: (i) the tool diameter, (ii) the Spindle speed, (iii) the feed rate and (iv) the step down. Therefore, a proper choose of these parameters associated to the optimization of the tool path trajectory happens to be the determining factors to achieve a good quality of SPIFed parts [43–45].
Usually, SPIF process is conducted at room temperature. In fact, the friction developed during the experimental procedure allows to drastically increase the sheet temperature with high benefit in terms of formability (especially for materials with low deformation properties at room temperature). However, considering the very low formability for Mg alloys at room temperature, several researchers adopted heating systems to perform tests at warm temperature [46].

1.5. The role of numerical modelling for Mg alloys

The importance of numerical simulation in the design of a manufacturing process is clearly known. The adoption of a robust numerical modelling correlated by constitutive models is nowadays capable to predict truthfully both macroscopic aspects (mechanical properties, such as yield stress, UTS and deformation behaviour) and the microstructural evolution of the material subjected to manufacturing processes.

1.5.1. Material constitutive models overview

Several material constitutive models are proposed in literature with reference to the AZ31B Mg alloy; these differ significantly from those commonly used for metallic materials. In fact, traditional models, such as Johnson & Cook (JC) model, Steinberg & Guinan (SG) model, and Zerilli & Armstrong (ZA) model do not consider specific micro-mechanisms of dynamic

deformation of magnesium alloys [47].
In particular, material models able to predict the AZ31B Mg alloy deformation behaviour are valid at high temperature and correlate stress with the strain rate by creep laws. Material models available in literature are related to experimental data coming from tensile and compression tests. The usual procedure followed by researchers is based on the evaluation of the behaviour after mechanical tests at high temperature, followed by supplementary microstructure observations by means of light and/or electronic microscopes.
Modelling of the deformation behaviour of a magnesium alloy is rather complex. In fact, both hardening and softening are strongly affected by temperature, strain and strain rate [48,49]. As confirmation of this marked dependence, most of the available material models refer to a creep law based on the Arrhenius equation, which expresses stress as a function of both temperature and strain rate [36,50]:

$$\dot{\varepsilon} = A(\sigma/E)^n \exp\left(-Q/(RT)\right) \qquad \text{Equation 1}$$

where A and n represent two characteristic constants of the creep mechanism, E is the Young's modulus related to a fixed value of temperature (T), R is the gas constant and, finally, Q is the activation energy for the creep.
Based on Equation 1, different material models were developed for AZ31B Mg alloys. Q value of 145 kJ/mol were found by Nourollahi et al. [51]: a model based on the Arrhenius law, considering the effects of temperature and strain rate on deformation behaviour by means also the Zener-Holloman parameter, was proposed.
Another important aspect to be considered is the stress-strain dependence from the grain size: generally, the Hall–Petch law correlates the material grain size with the yield stress value. As suggested by Armstrong et al. [52] , the yield stress can be expressed as:

$$\sigma(\varepsilon) = \sigma_0(\varepsilon) + k(\varepsilon)d^{-1/2} \qquad \text{Equation 2}$$

where $\sigma_0(\varepsilon)$ is the flow stress within the grain, directly connected with the dislocations accumulated in dislocation boundaries, $k(\varepsilon)$ is a strength contribution due to additional resistance caused by the presence of grain boundaries. Clearly, d represents the grain size.
Starting from this consideration and using samples of AZ31 Mg alloy with ultrafine grains obtained by means of Equal Channel Angular Pressing (ECAP), Kim [53] demonstrated that $\sigma_0(\varepsilon)$ increases with the strain. However, it has found that $k(\varepsilon)$ decrease during the forming steps, suggesting that new and mobile dislocations are generated during deformation.
Another important contribution to AZ31 Mg alloy deformation behaviour modelling at high temperature is represented by the Garofalo's equation. This equation is a general form of the power law equation describing slip creep controlled by DC and therefore by diffusion processes:

$$\dot{\varepsilon} = Ae^{\frac{-Q}{RT}}(\sinh(\alpha\sigma))^n \qquad \text{Equation 3}$$

where the additional terms respect to the Arrhenius law are A, n and α (Garofalo's

parameters). Equation 3 describes the material behaviour at high strain rate values, where tendentially the DC creep is predominant.
The mechanisms of plastic deformation in a Mg AZ31 wrought alloy sheet at 450°C across strain rates from 10^{-4} to 10^{-1} s^{-1} are identified as GBS creep and DC creep. GBS creep is subject to hardening from grain growth, and DC creep produces texture-dependent plastic anisotropy [14]. In addition, for fine grain size materials (about less than 10μm) deformation results primarily from GBS creep [54]. As described by Langdon [55], GBS is a creep process in which the grains exhibit no significant elongation but they become displaced with respect to each other so that there is a net increase in their number lying along the tensile axis.
The last equation to be considered involves directly the strain rate sensitivity index (m) [56]:

$$\sigma = K\varepsilon^{n}\dot{\varepsilon}^{m} \qquad \text{Equation 4}$$

where, considering the constant K describing the active creep mechanism, the stress is represented as a function of both strain and strain rate raised to respectively the strain hardening exponent (n) and m.
Related to the case of a bulge test (fundamental for the present research activity) and the last equation 4, a first approach was proposed by Jovane [56], which proposed an analytical model with different assumptions: (i) isotropic material, (ii) volume constancy, (iii) negligible elastic strains, (iv) ratio between sheet thickness and diameter small, (v) negligible bending effects and, finally, (vi) the sheet can be assumed, during all forming steps, as part of a thin sphere subjected to internal pressure.

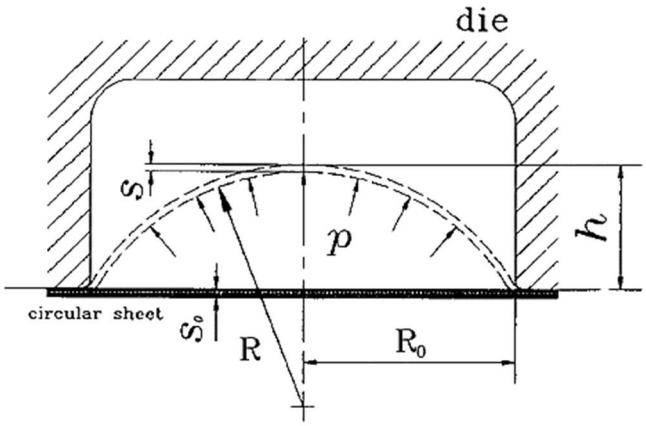

Figure 11 Gas forming scheme.

In the bulge test scheme proposed in Figure 11 most important geometric variables that affect the process are visible: many of these will be fundamental for both constitutive model calibration and correct design of the test. Expressions for stress and strain state model provided by Jovane were based on membrane theory and geometrical considerations. In fact, with reference to the previous scheme in Figure 11 and according to the Jovane's assumptions, next equation 5 can be considered as valid in the dome apex of the sheet. In fact, considering stress equilibrium in a bulge pole one can obtain a classical relation between effective stress in the apex of a dome (σ) and applied pressure (P):

$$\sigma = \frac{P\rho}{2s} \qquad \text{Equation 5}$$

where ρ is the curvature radius and s is the actual dome apex thickness.
Based on the Jovane suggestions, Enikeev and Kruglov [56] ,determined by means equation 6, the material strain rate sensitivity index as a function of both pressure and time:

$$\mathrm{m} = \ln\left(\frac{\mathrm{p_1}}{\mathrm{p_2}}\right) / \ln\left(\frac{\mathrm{t_2}}{\mathrm{t_1}}\right) \qquad \text{Equation 6}$$

where t_1 and t_2 represent the forming times at constant pressures p_1 and p_2, respectively. Finally, the K parameter may be obtained from the following expression:

$$\mathrm{K} = \frac{\mathrm{p_f R_0}}{2\mathrm{s_0}} \left[\frac{\mathrm{t_f}}{2\mathrm{I_m}(\pi/2)}\right]^{\mathrm{m}} \qquad \text{Equation 7}$$

where t_f is the forming time at constant pressure p_f; $I_m(\pi/2)$ is fundamentally an integral depending from geometrical aspects [56] of the dome with a value fixed value of m.
K and m values can be used to predict the material behaviour.
Instead, considering the first three equations previously reported, the constitutive material model considered for the present research activity was the one suggested by Carpenter et al. [14]. In particular, this model takes into account all variables that affect the material behaviour. In fact, the stress is considered according to strain, temperature, strain rate and microstructure evolution (both static and dynamic grain growth were considered).
As reported by Carpenter et al., the calibration of the suggested constitutive material models was performed by means of tensile tests and considering anisotropic effects. To consider both static and dynamic effects in terms of grain growth, respectively the undeformed grip region and the deformed area of the different tensile samples were analysed to determine the mean grain size. Other materials constants were determined by minimizing the error between experimental and analytical results.
As anticipated, the adopted material model took into account both the static and the dynamic grain growth together with the stress and strain condition:

$$\mathrm{d_s} = (\mathrm{d_0^n} + \mathrm{Ct})^{1/\mathrm{N}} \qquad \text{Equation 8}$$

being d_0 the grain size in the as-received condition, while C and N are constants determined by means of experiments. In addition, the dynamic effect on the grain size, as suggest by Sato et al. [57] was described as a function of d_s and true strain, ε:

$$\mathrm{d} = \mathrm{d_s}\exp(\alpha\varepsilon) \qquad \text{Equation 9}$$

being α an additional material constant.
Finally, the effects of GBS and DC creep were modelled according to the law reported in

equation 10 [14]. Material constitutive model suggest by Carpenter et al. accounts for normal anisotropy by means of separate quadratic Hill stresses [58] for GBS creep and DC creep, each of which exhibits different degrees of plastic anisotropy.

$$\dot{\varepsilon} = \frac{A_{GBS}}{d^{p}} \sigma_{GBS}^{nGBS} + A_{DC} \sigma_{DC}^{nDC} \qquad \text{Equation 10}$$

where A_{GBS}, n_{GBS}, A_{DC} and n_{DC} are material constants referring to the two different creep (GBS and DC) types mechanism, while d is the mean grain size affecting the GBS contribute according to the exponent p. As shown in the last equation, the DC creep mechanism is not affected by grain size.

Another important contribution - in terms of material modelling – was provided by Miao et al. [13]. Miao et al. demonstrated that, during isothermal or isochronal annealing, the grain size of an AZ31 Mg alloy produced by hot rolling always increased according to the time and temperature and the effect of annealing temperature on grain size was more significant than that of annealing time. In addition, grain growth kinetics can be expressed by the following equation:

$$D^{n} - D_{0}^{n} = kt \qquad \text{Equation 11}$$

where D_0 is the starting grain size before annealing, D is the grain size after annealing for a period of time t, and k is a constant depending on the annealing temperature T.
The grain growth rate constant k (Equation 12) is a function of both temperature and activation energy, Eg:

$$k = k_0 \exp\left(-E_g/RT\right) \qquad \text{Equation 12}$$

where k_0 is the pre-exponential term, R is the gas constant and T is the absolute temperature of annealing.

2. Methodologies and facilities adopted

In the present chapter, methodologies and facilities adopted to achieve main research objectives is proposed are summarized. All experimental activities were conducted exploiting primarily skills and facilities available in the Polytechnic University of Bari; in addition, thanks to consolidated international cooperation, a part of the experimental activities was carried out at the University of Mugla (Turkey) and the University of Girona (Spain).

2.1. Main research objectives

According to the aspects discussed above in chapter 1, the main objectives of the present research activity were represented by the design of both new Mg alloys and unconventional sheet metal forming process with the aim to focus on the deformation behaviour of the investigated alloys and capability of the manufacturing process to obtain final shape that best fit the theoretical one.

For greater clarity, it is possible to divide the present study in three different parts, as suggested below: (i) New Mg-based alloys manufacturing (chapter 3); (ii) Innovative methodology for characterization (chapter 4); (iii) Complex shaped parts manufacturing (chapters 5 and 6).

Procedure and facilities adopted to develop the three different aspects are illustrated and explained in the present chapter.

To achieve the objectives related to the first point (new Mg alloys design), starting from literature review about the effect of the different alloying elements, several different innovative Mg alloys were manufactured and subsequently tested at room, warm and high temperatures. A scheme of the different steps followed are proposed in previous Figure 12. Considering the best performing Mg alloy obtained experimentally, the same was compared – through bulge tests - with the commercial AZ31B-H24 Mg alloy, expressly recognized as one of the most performing in terms of its hot deformation properties. Among the different Mg alloys manufactured and subsequently tested, a new ternary Mg alloy (Mg-2Zn-2Ce) was selected as the best one. Then, the Mg-2Zn-2Ce alloy was compared with the AZ31B Mg alloy: experimental results, obtained by means of hardness, tensile and bulge tests, showed performances of the innovative Mg alloy comparable to those of AZ31B Mg alloy.

As anticipated in the introduction, the (many) existing models refer to commercially available Mg alloys, specifically with reference to the AZ31 Mg alloy. For this reason, since results coming from the comparison between Mg-2Zn-2Ce and AZ31B shown good matching, the subsequent research activity steps were conducted adopting the AZ31B. In addition, since the experimentally obtained alloys were manufactured through the casting

process, manufacturing times and samples preparation via Electro Discharge Machining (EDM), for the subsequent phases were not compatible with the research time.

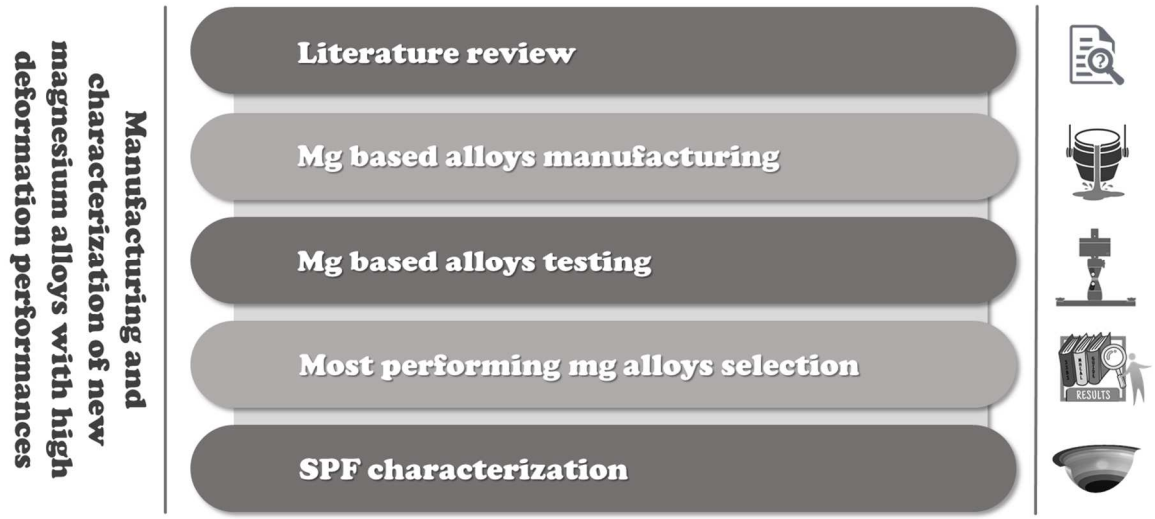

Figure 12 Scheme of approach adopted to manufacture and evaluate a new high performing Mg alloy.

As abovementioned, in addition to a new material design, during research activities, the attention was also focussed on unconventional (SPF and SPIF) manufacturing process design. In particular, new solutions to manufacture two different cases study were proposed (Figure 13).

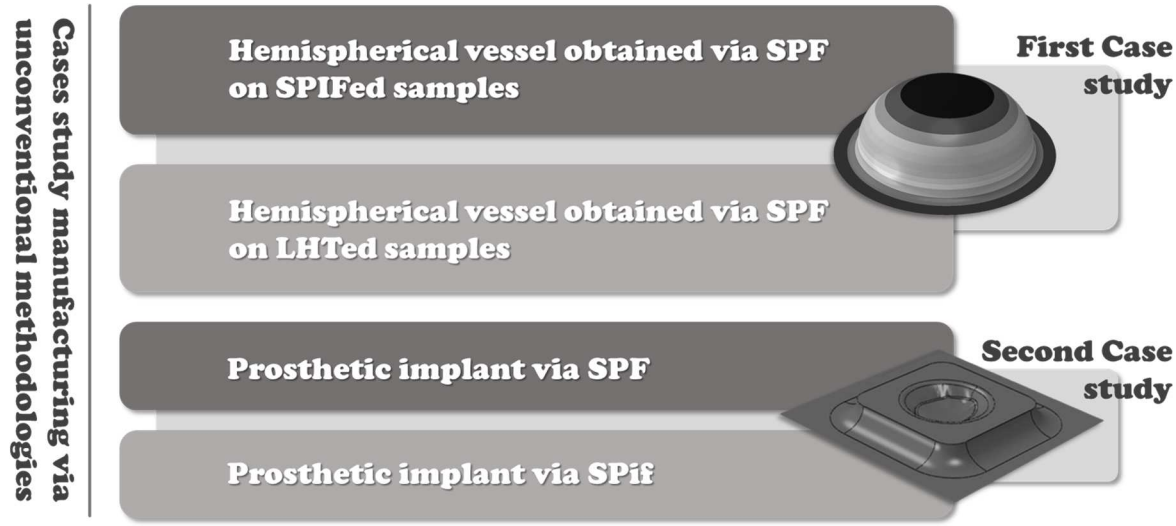

Figure 13 Scheme of sheet forming process design.

The first case, related to an automotive application (spherical vessel), was performed by using hybrid methodologies aimed at optimizing the thickness distribution after forming, thus overcoming one of the most negative aspects of the SPF process: (i) SPF performed using a Mg alloy blank with optimized thickness by means of SPIF process; (ii) SPF performed on samples modified with localized microstructural modification by LHT. The

second case study, differently, was represented by a cheekbone prosthesis implant obtained both via SPF and SPIF. Considering SPF methodology, a numerical/experimental approach was purposed to design all forming process involved as robustly as possible. For a correct process design, a numerical modeling, based on constitutive material models which enable prediction of the deformation and microstructural behavior of the alloy with great accuracy, must be adopted. Three different constitutive material model were implemented in numerical simulations (suggested by Enikeev and Kruglov, Carpenter et al. and Miao et al.). To correctly design the manufacturing process via SPF of a spherical vessel, for the two innovative approach proposed a numerical/experimental approach was used. For this purpose, the material constitutive model suggested by Carpenter [14] and Miao [13] were implemented in numerical models. Instead, related to the second case study, exclusively prosthesis obtained by means of SPF process was performed with a numerical/experimental method. In particular, the material constitutive model adopted to perform numerical analyses were suggest by Enikeev and Kruglov [56]. SPIF process optimization were achieved thanks an experimental approach based on a Central Composite Designs (CCD) experimental plan. Comparison in terms of thickness distribution were proposed to evaluate the effect of SPF process starting from SPIFed or LHTed blanks respect to the one in "as received" condition. It is important to emphasize that all numerical analyses were performed adopting the commercial code ABAQUS (2017). Furthermore, to evaluate microstructure changes, all experimental tests were supported by metallographic analyses.

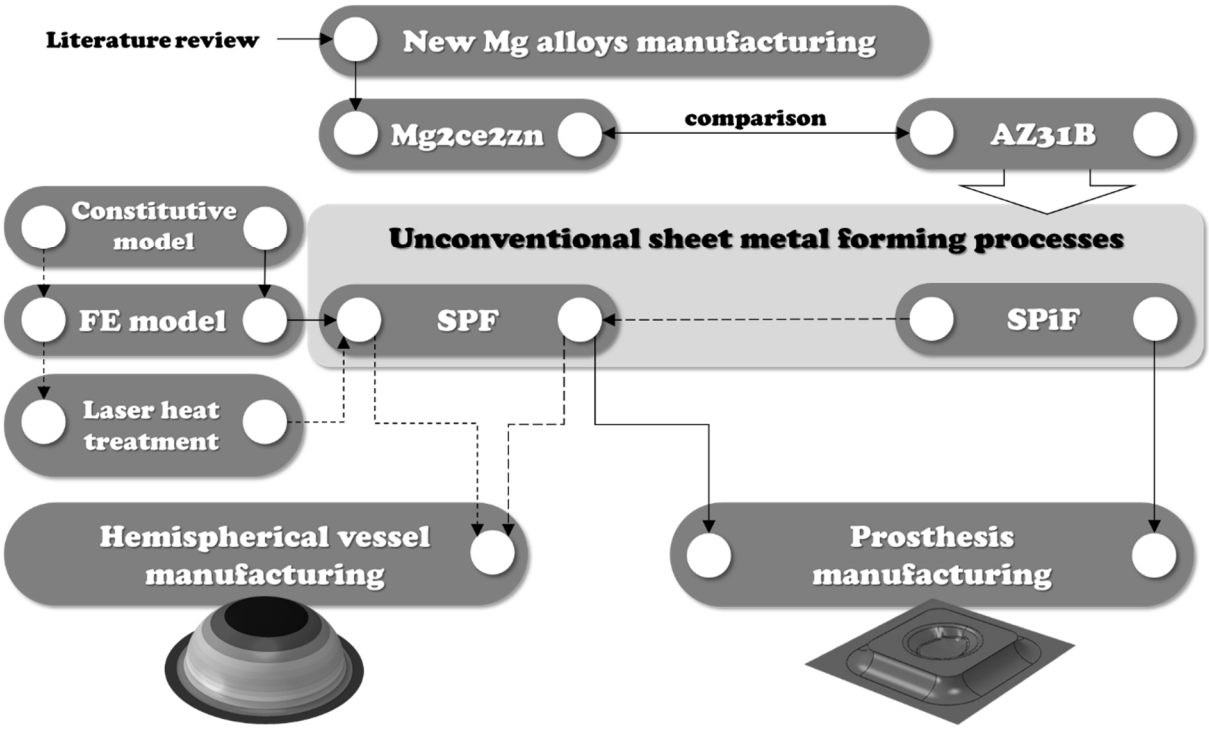

Figure 14 Scheme of the methodology adopted during the research activity.

General methodology used in the present research activity is summarized in Figure 14. This methodology involved different aspects such as literature review, (traditional and innovative) experimental trials coupled with numerical simulations.

2.2. New Mg alloys manufacturing and characterization

The first step of the research activity was represented by the innovative Mg-based alloys manufacturing. Exploiting results available on the literature, several Mg alloys were manufactured and then tested in order to evaluate the best performing alloy able to be considered as promising in the adoption for complex parts obtained via sheet metal forming.
The best alloy, finally, was compared with the commercial AZ31B-H24 Mg one adopted for the subsequent research steps.

2.2.1. New Mg alloys manufacturing

Several new Mg Alloys were prepared under argon atmosphere using pure metals and/or suitable master alloys in an electric furnace under the protective atmosphere of argon at about 3atm pressure.
The equipment shown in Figure 15 was adopted to produce all Mg-based alloys subsequently analysed.

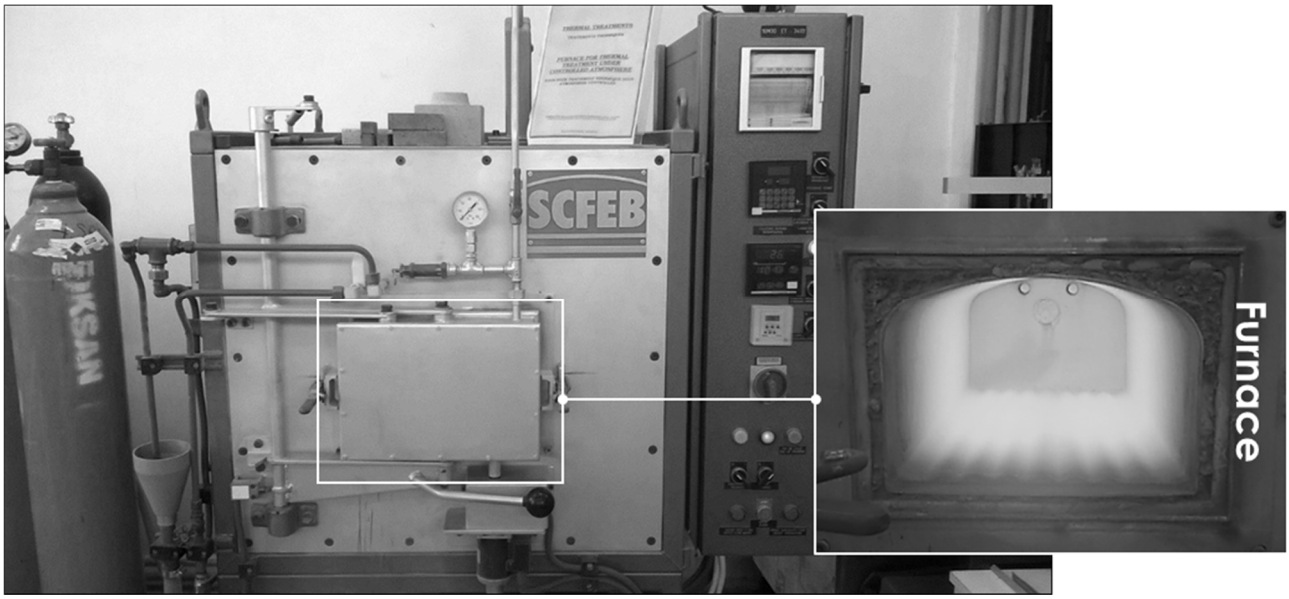

Figure 15 Experimental facilities adopted.

Depending on the desired chemical composition, the different alloy elements were added to the pure Mg using the "master alloys", containing a known quantity of the element (or elements) needed. After each weighing (Figure 16a), all elements characterizing the final alloy were placed in a square shaped melting container made of steel (Figure 16b) for the subsequent steps in furnace.

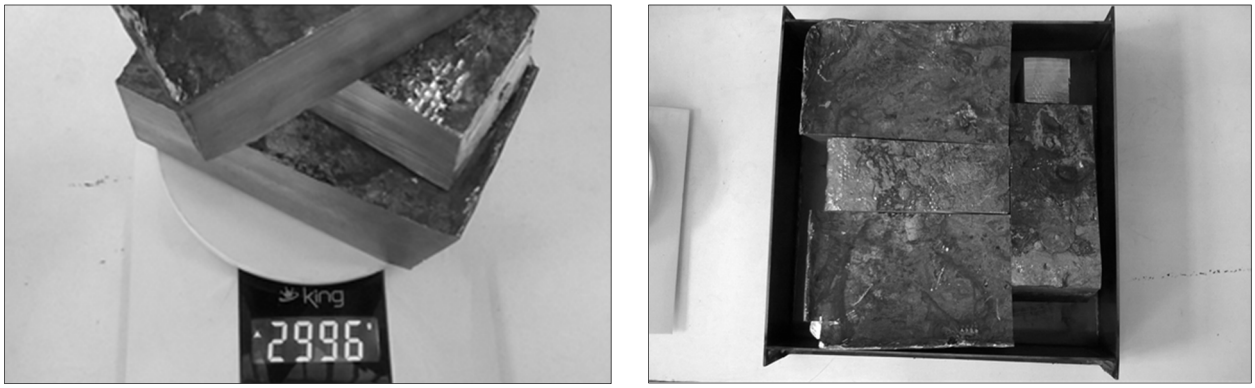

(a) (b)

Figure 16 Example of weighing phase (a) and steel melting container with all the needed master alloys (b).

After a preheating step in another furnace at 220°C for 15 minutes, when the temperature in the furnace (shown in in detail of Figure 15) was steady, the melting container with all elements needed for the final Mg-based alloy was put inside the furnace.
Considering a melting point equal to 650°C for the Mg alloys, the temperature was sets at 790°C.

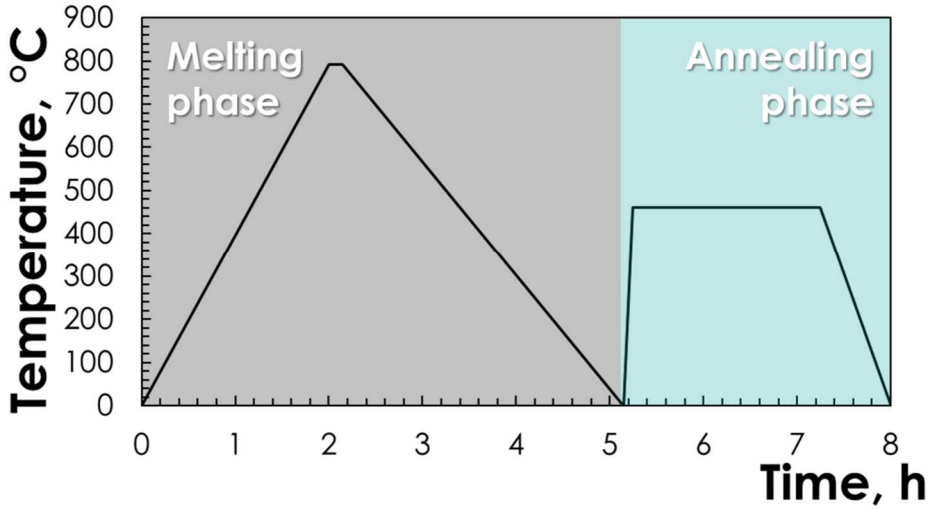

Figure 17 Thermal cycle adopted: Melting (a) and annealing (b).

As reported in Figure 17, the maximum temperature (790°C) was reached in 2 hours and kept constant for the following 15 minutes.
Finally, the cooling phase was 3 hours longer up to the room temperature.
In order to reduce residual stresses and increase alloy ductility, when the temperature was equal to the room temperature, a homogenization annealing treatment was performed (blue area in Figure 17); in this case, the temperature increase in about 6 minutes up to 460°C and then, after a 2 hour long maintenance phase, cooled to room temperature in 45 minutes.

Figure 18 Obtained cast after melting and annealing phases.

2.2.2. Mechanical characterization of new Mg alloys

Mechanical characterization of the produced Mg alloys was carried out by means of metallographic analyses, hardness and tensile tests (at room, warm and high temperature). In addition, the best performing alloy deriving from abovementioned tests was tested under superplastic conditions via bulge tests, investigating both temperature and gas pressure effects.

2.2.2.1. Metallographic analyses

EDS of FEI NOVANANO SEM 650 was used to perform metallographic analyses. This facility offers the most extensive set of integrated tools, including a 16-bit on-board digital pattern generator and dedicated patterning software, a high-speed electrostatic beam blanker and gas-injection systems for direct electron beam writing of nanostructures. In addition, the SEM stage is powered by piezomotors for producing finer, predictable and repeatable XY movements over a range of 150 mm.

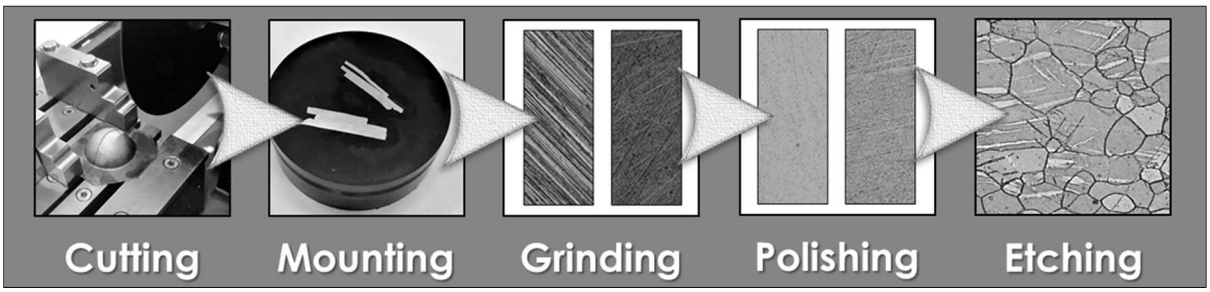

Figure 19 Adopted methodology to properly prepare samples for microstructure analyses.

In order to evaluate the microstructure, for all Mg-based alloys manufactured samples were extracted, cut, mounted, properly grinded and etched by immersing the sample for 5 sec in

Acetic-Picral (5 ml Acetic Acid, 6 g Picric Acid, 10 ml Water, 100 ml Ethanol). To avoid corrosive effects and then negative preparation results, the use of water was avoided in the last stage of grinding and in all polishing steps. The scheme of metallographic preparation of a Mg alloy sample is depicted in Figure 19.

2.2.2.2. Mechanical characterization by means of tensile and hardness tests

After a first screening via Brinell Hardness (HB) tests, mechanical and deformation behaviour of the most performing manufactured Mg alloys were evaluated by means of tensile tests at warm and hot conditions.
Mg alloys characterization via tensile tests was carried out using a properly equipped 200 kN universal INSTRON testing machine with the experimental setup shown in Figure 20.
Temperature after and during each test was guarantee thanks to the EASYHEAT Induction Heating System (made by AMBRELL®), that is a solid-state induction heating system able to convert three-phase line voltage to 10kW terminal power output over a range of radio frequencies and voltages. This energy is delivered to a remote series-resonant circuit - including coil - where a precisely controlled magnetic field is created closed to the sample. To both control and acquire the temperature during the experimental activity three different K-type thermocouples were implemented on the sample, as schematized in Figure 20 (Right zone). The central thermocouple is controlled in feedback, in order to keep the temperature constant and equal to the predetermined one.

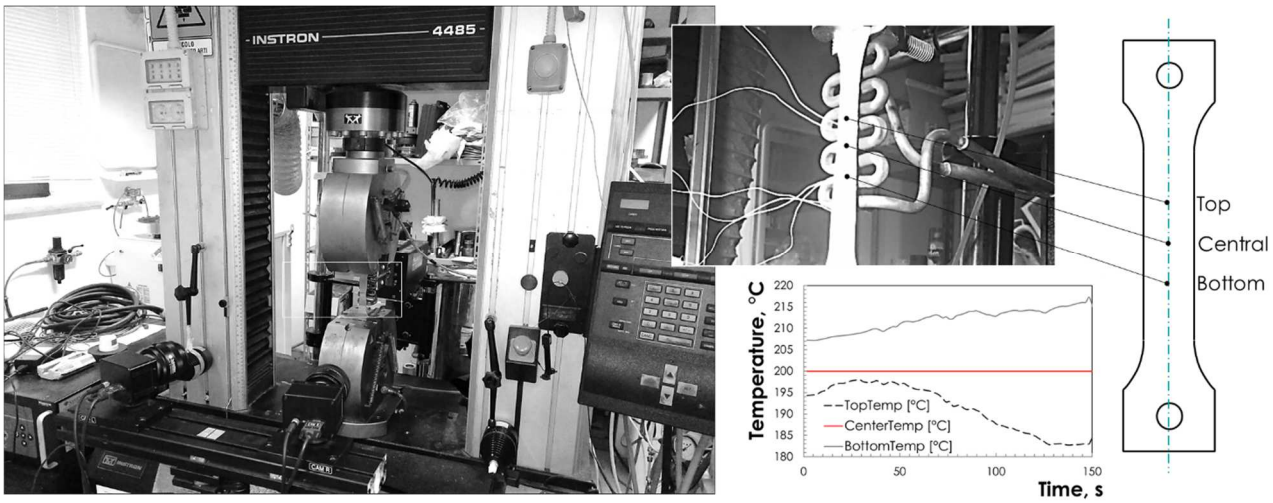

Figure 20 Experimental setup adopted to perform tensile tests.

The experimental setup, as designed, leads a not constant temperature distribution along the longitudinal direction of the sample, due to the simultaneous presence of the heating system and the cooled grips. Therefore, to avoid negative effect on the results, tensile tests were assisted by the Digital Image Correlation (DIC) system ARAMIS (GOM®), able to continuously acquire the strain map on the sample during the test.

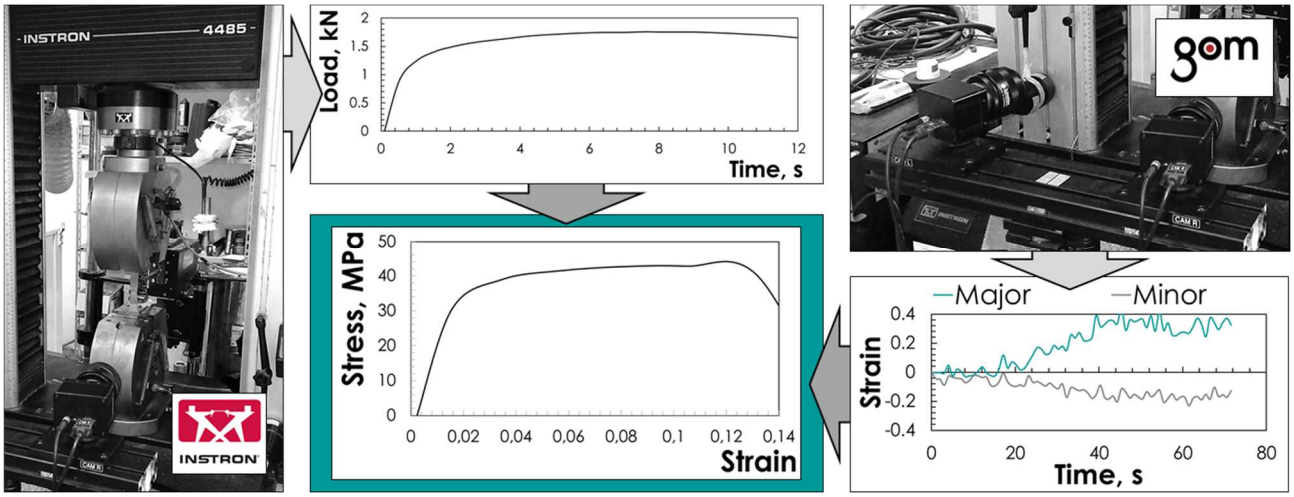

Figure 21 Data processing steps.

Before each test, the sample was sprayed with a white matte layer to avoid reflections and then a random distribution of black dots was superimposed: the resulting pattern could thus be recognized by the two cameras as a virtual grid making possible the local evaluation of the strain in any point of the specimen. In such a way, it was possible to obtain the output desired values analysing locally the strain map, as shown in Figure 21.

2.2.2.3. Superplastic characterization by means of bulge tests

As below discussed later in chapter 3, results coming from previous mechanical characterization allowed to determine the best performing innovative Mg alloy. Then, deformation behaviour of the selected alloy was evaluated in a gas-forming process. In addition to the metallographic investigation performed both on hot-rolled and hot-formed condition, results of an extensive experimental campaign, based on two different methodologies of bulge tests end adopting different values of both temperatures and pressures, were conducted.

2.2.2.3.1. Bulge test

Bulge tests were carried out at different temperatures and pressures using a properly equipped universal INSTRON 4485 testing machine, as reported in Figure 22.
During each test, a circular sample, clamped between a blank-holder and a cylindrical die (with a diameter and an entry fillet radius equal respectively to 45 and: 3mm), was heated by exploiting an electric furnace with three controlled zones.
Due to the argon gas pressure the sample was freely deformed into the die and both the temperature and the Dome Height (DH) were continuously acquired using a 6mm diameter K-type thermocouple in contact with the dome apex area and directly connected to a magnetostrictive sensor.
The circular Mg alloy samples (diameter and thickness equal respectively to 75 and 1mm) were cut from the as-cast blocks by means of Wire Electrical Discharge Machining.

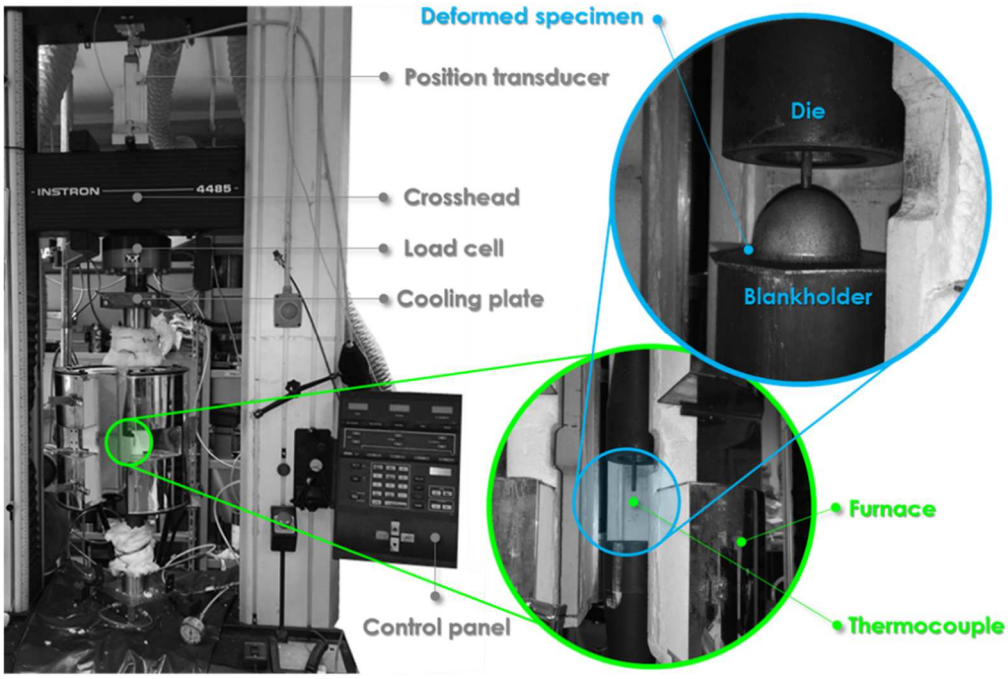

Figure 22 Experimental setup adopted to perform bulge tests.

In order to avoid both gas leakages and sheet metal sliding, the sample was firmly clamped between the Blank-Holder and the die with a proper Blank-Holder Force (BHF), as schematized in Figure 23.

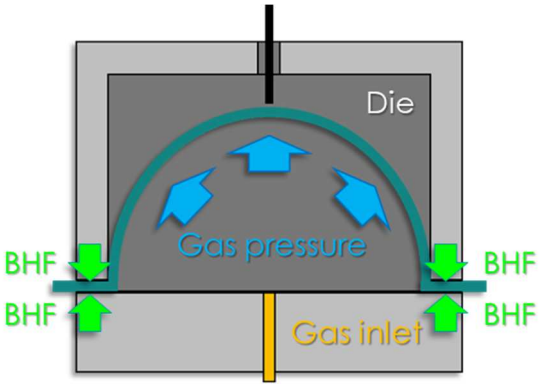

Figure 23 Bulge tests scheme.

Bulge tests were conducted employing two different methods: (i) setting a Constant Pressure (CP tests) of the argon gas for each test; (ii) by alternatively switching between two different pressure levels during the same test (Jump Pressure tests- JP tests) [59].
Finally, in order to associate the deformation behaviour with microstructural aspects, interrupted CP tests at increasing heights (40%, 65% and 90% of DH at rupture) were conducted.

2.2.2.3.2. Hot rolling tests

Due to the prohibitive geometry of the dome shaped samples to obtain flat samples, the behaviour of the alloy in terms of deformation texture was studied on planar samples

extracted from hot rolled parts. Hot rolling was conducted on plates 100mm long with an initial thickness of 5mm and going down to 1mm at 5 steps at 400°C. Inter-pass heating periods were 5 minutes long.

2.2.2.3.3. Metallographic investigations

Bulge test samples were cut in half for the metallographic analysis exploiting the axial-symmetry of the dome-shaped deformed sample, so that the cross section could be analysed starting from the dome apex, which experiences the maximum strain level as being stretched in all principal directions, down to the flanged area, which remains undeformed due to clamping.
Metallographic samples were prepared by following the same steps reported in Figure 19: cross sections were ground and polished according to the conventional metallographic preparation techniques.

2.3. An innovative method to characterize an AZ31B Mg alloy

As previously described and as will be highlighted in results discussion (chapter 3), the best performing innovative Mg based alloy showed good property in terms of both mechanical properties and deformation behaviour.
Comparison with the commercial AZ31B-H24 Mg alloy allowed to assert that the innovative Mg alloy obtained can be considered as promising in sheet metal forming processes aimed to complex parts manufacturing.
However, due to both supply time (due to casting process) and extraction procedure of samples (performed by Electro Discharge Machining, EDM), from this point forward the efforts were focused on the commercial AZ31B-H24 Mg alloy.
Therefore, in this section a new approach able to characterize the material behaviour was developed and evaluated. In particular, considering the material model suggested by Carpenter et Al., as usually occurs, material model constants are calibrated exclusively on tensile tests.
In the present study, on the contrary, a new approach based exclusively on bulge tests was proposed in order to both characterize the material and correctly calibrate the material model.
As know, the constitutive material model (described in chapter 1) is influenced by several terms (**C**, **N**, $\boldsymbol{\alpha}$, $\mathbf{A}_{GBS}$, $\mathbf{n}_{GBS}$, **p**, $\mathbf{A}_{DC}$ and $\mathbf{n}_{DC}$); all terms were calibrated experimentally, as documented in chapter 4.

2.3.1. Investigated material

Circular specimen with a diameter equal to 75mm and adopted to conduct experimental bulge tests were obtained by cutting a single Mg alloy (AZ31B-H24) sheet with an initial thickness equal to 1 mm.

Chemical composition of the material is shown in Table 3.

	Al	Zn	Mn	Ca	Cu	Fe	Ni	Si	Others	Mg
Min	2.50	0.70	0.20	-	-	-	-	-	-	Balance
Max	3.50	1.30	1.00	0.04	0.05	0.005	0.005	0.05	0.30	Balance

Table 3 AZ31B-H24 Mg alloy chemical composition.

2.3.2. Experimental methodology to calibrate the material model adopted

As done for the previous characterization under superplastic condition and related to the innovative Mg alloy, also for the AZ31B-H24 characterization via bulge tests was carried out using the testing machine and experimental setup shown in Figure 22. All experimental tests were conducted at 450°C adopting seven different gas Argon pressure values (0.2, 0.3, 0.4, 0.7, 1.0, 1.3 and 1.6MPa). In addition, each condition of pressure was performed interrupting the test at a specific value of strain (0.36, 0.5, 0.65 and 0.84). Therefore, the forming time, as wells as the final height of the spherical component, changed according to the level of the adopted strain rate (pressure level). Results obtained from each experimental test was exploited for constitutive model constants determination and to validate the capability of FE model to predict the Mg alloy behaviour. Experimental plan performed is summarized in Table 4.

	0.2MPa	0.3MPa	0.4MPa	0.7MPa	1.0MPa	1.3MPa	1.6MPa
ε=0.36	•	•	•	•	•	•	•
ε=0.50	•	•	•	•	•	•	•
ε=0.65	•	•	•	•	•	•	•
ε=0.84	•	•	•	•	•	•	•

Table 4 Experimental conditions investigated by means of bulge tests.

To measure the evolution of the grain size due to both static and dynamic effects, each sample was again cut, mounted, properly grinded and etched by immersing the sample for 5 sec in Acetic-Picral (5 mL Acetic Acid, 6 g Picric Acid, 10 mL Water, 100 mL Ethanol).
The mean grain size was evaluated according to the ASTM Standard [60]: samples extracted from both the flange (static grain growth) and from the dome (static and dynamic grain growth) were observed using an Eclipse MA200 Nikon light microscope.
To correctly calibrate the material model, the minimization of the error between experimental results and results coming from analytical equations characterising the material model was adopted as optimization method.
Considering equations 8, 9 and 10, the calibration started with the determination of both d_s and d values by means metallographic analyses; these values, obtained for each experimental condition investigated, are necessary to determine C, N firstly and subsequently α respectively from equation 8 and equation 9.
At this point, to obtain the value of the remaining constant affecting the GBS and DC creep mechanisms, the true stress determination for each test condition is fundamental. The true

stress based on experimental test can be achieved thanks the shell theory (equation 5) adopted by Jovane et al. [12].
Also this terms can be determined experimentally: in fact, the final thickness in correspondence of the dome apex (s) was measured by means of a caliper; the term p is the gas pressure; finally, the curvature radius (ρ) of the shape obtained was determined by means of light microscopy (as shown in Figure 24).

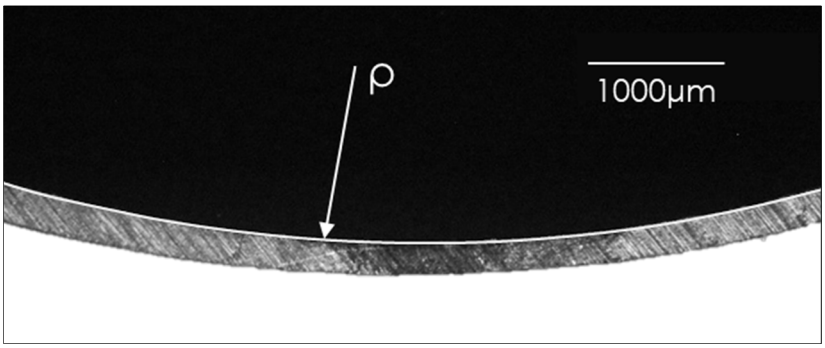

Figure 24 Example of curvature radius acquisition via light microscopy.

True stress determined for all tests condition can be exploited to achieve the remaining constant (A_{GBS}, n_{GBS}, p, A_{DC} and n_{DC}) material model by minimizing the error between experimental and analytical results using equation 10.

2.3.3. Experimental bulge tests design

In the proposed approach, in order to significantly limit the number of experimental tests necessary to both characterize the material and calibrate the material model, the sheet thickness in correspondence of the dome apex is assumed to be related linearly with respect to the dome height normalized by curvature radius and the entry fillet [61].
In fact, keeping in mind the bulge tests scheme reported in Figure 11, thanks to the equation 5 and assuming the dome as a spherical shape, the curvature radius can be expressed as follows:

$$\rho = \frac{H^2 + (R_0 + \rho_0)^2}{2H} \qquad \text{Equation 13}$$

where H represents the actual dome height; R_0 and ρ_0 represent respectively the radius and the entry radius fillet of the die cavity.
At this point, considering the two previous equations, in order to predict the actual thickness at the dome apex by knowing geometrical variables of the experimental facility and the dome height, equation 14 can be adopted:

$$s = s_0(1 - BH/(\rho + \rho_0))$$
$$= s_0(1 - \frac{2BH^2}{H^2 + (R_0 + \rho_0)^2}) \qquad \text{Equation 14}$$

where B is a constant in a range between 0.5 and 1, depending on material properties and s_0 is the initial sample thickness.
From an experimental point of view, starting from a single test (up to rupture or interrupted) and knowing both dome height and die geometry, the B value, according to the gas pressure, can be determined.
Graph in Figure 25 shows the obtained trend of B as a function of gas forming pressure adopted: the experimental value of B ranges from 0.68 to 0.79 in agreement with the range suggested by the literature [61].
Starting from this value, it is possible to predict with high accuracy the final thickness at the dome apex and consequently, considering the logarithmic ratio between initial and final thicknesses, to determine the strain.

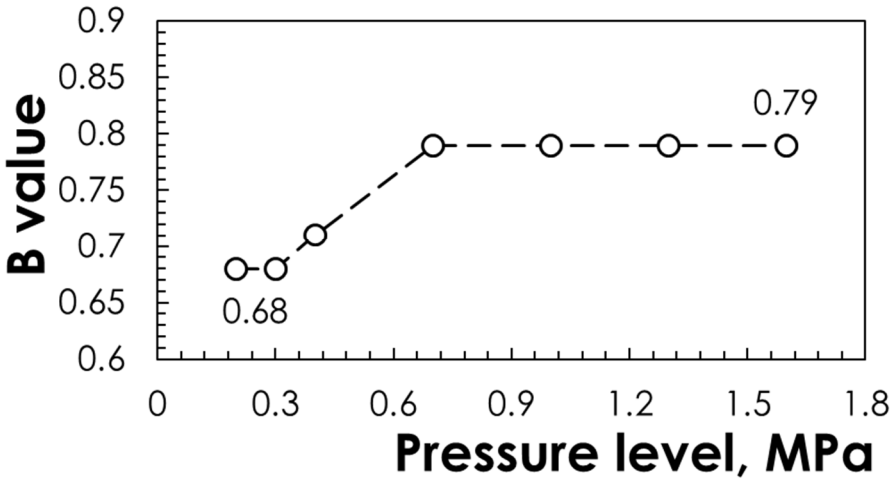

Figure 25 Value of B according to the gas forming pressure.

At this point, thanks to determination of the strain involved in equation 9 and necessary to determine the α value, the Carpenter's material model can be calibrated.

2.3.4. Numerical model of the bulge test

With the aim to evaluate the capability of the material model calibrated with the new methodology to predict correctly the AZ31B-H24 Mg alloy behaviour, the same was implemented in a Finite Element (FE) model. Numerical simulations were performed considering bulge tests conditions.

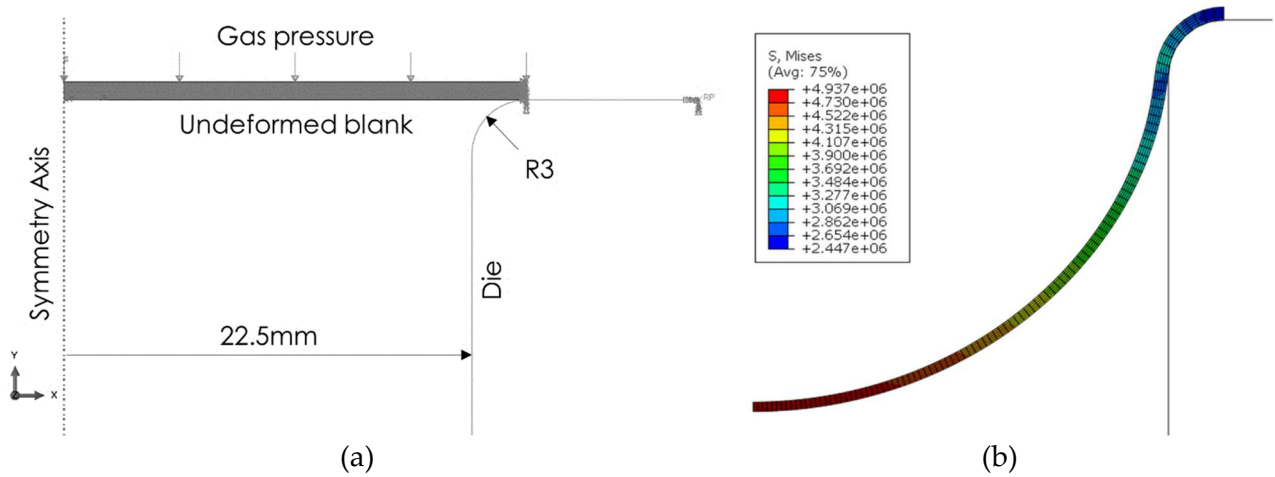

Figure 26 Scheme of FE model for producing spherical vessel: (a) after and (b) before forming step.

To properly replicate experimental SPF test conditions, FE model shown in Figure 26 was created using the commercial code ABAQUS (v 6.17) for simulating the same experimental test conditions (different pressure values at 450 °C). In particular, the numerical model capability to predict the deformation behaviour according to the microstructural one was evaluated by focusing the attention on the tests conducted up to a nominal final strain equal to 0.84 (last row in Table 4).
In addition, in order to reduce the computational cost, a 2D axial-symmetric model was adopted: the cylindrical die cavity was assumed to be a rigid surface, while the blank was modelled as a deformable part (initial thickness: 1 mm) and meshed with 0.2 mm 4 nodes axisymmetric elements.
As shown in Figure 26a, a uniformly distributed pressure was applied on the upper part of the sheet with a magnitude equal to the pressure level. The blank was modelled with a radius equal to 25.5mm, deriving from the sum of the die cavity radius and the entry fillet radius; in addition, blank was blocked in the peripherical zone in order to avoid movements along the x axis and rotations around the y and z axes.
Finally, the microstructural evolution due to both strain and time exposure to temperature was taken into account implementing the proposed model through a FORTRAN subroutine.

2.4. Manufacturing of complex shaped parts

From a manufacturing point of view, in the last part of research activity the attention was uncentered on two different cases study (a spherical vessel and a temporary cheekbone prosthesis) fabricated via unconventional techniques (SPF and SPIF).
With the aim to optimize and/or change locally the thickness distribution of the final part, vessel manufacturing process was design following two distinct approaches: (i) SPF process on SPIFed samples with optimized thickness distribution; (ii) SPF process on LHTed samples. In both cases a numerical/experimental approach was used.
Instead, related to cheekbone prosthetic implant manufacturing process design, numerical/experimental approach was adopted exclusively for SPF; in fact, SPIF process were optimized by means of experimental trials, based on a CCD experimental plan.

2.4.1. Investigated material

Square samples with a side length equal to 150mm were extracted from a single AZ31B-H24 Mg alloy sheet with an initial thickness equal to 1 mm. Chemical composition of the material is the same shown in Table 3. The choice of the abovementioned sheet dimension took into account the experimental SPIF equipment layout (Figure 28 and Figure 29). In the case of the spherical vessel, SPIFed samples were further cut to obtain circular shape necessary for subsequent SPF tests. For each SPIFed sheet four circular (d=75mm) samples useful for the SPF process were extracted.

2.4.2. A spherical vessel manufacturing combining SPIF and SPF

This first approach aims at investigating the combination of SPF and SPIF processes in order to produce a Mg alloy component characterised by a constant thickness. Numerical simulations using the commercial ABAQUS (v.2017) code of the SPF process were implemented to produce the final spherical part; in particular, the simulation analysis was iteratively conducted changing the thickness distribution of the starting blank (before the SPF step) by means of a Genetic Algorithm in order to minimize the thickness variation in the final component. SFP tests were thus performed in order to validate the numerical results: in order to obtain the initial optimized thickness distribution calculated by numerical simulation, the SPIF process was adopted. The tool trajectory was determined using the sine law to predict the values of the wall inclination angle able to determine the proper thickness values along the blank and SPIF tests were conducted changing the step down and the federate according to a full factorial design. SPIFed circular blanks having the thickness distribution close enough to the numerical prediction were obtained for all the process parameters combinations. The AZ31B-H24 samples adopted to produce the final component was extracted from the same blank from which the samples for the cheekbone prostheses manufacturing were obtained.

2.4.2.1. Thickness distribution optimization by numerical simulations

It is well known that, according to the deformation mechanism of the SPF process, the strain mainly occurs in the thickness direction (being the border of the blank clamped between the heated tools). For this reason, one of the most widely adopted solution to obtain a uniform thickness component at the end of the SPF step is to start from a blank with a specific initial distribution of thickness. The design of the initial distribution is not trivial, and the numerical approach is indeed a viable solution to avoid unbearable material and time wasting: in the case here described, the definition of the initial thickness distribution can be regarded as an optimization problem based on the satisfaction of a properly defined objective equation. For this reason, a 2D axisymmetric Finite Element (FE) model reproducing the experimental facility adopted to perform experimental tests (schematized in Figure 31) was created with the commercial code Abaqus CAE [62] and coupled with the

integration platform modeFRONTIER within an automatic procedure managed by a multi-objective genetic algorithm. Material behaviour was modelled according the Norton Bailey power law implementing the material constants calculated applying the model proposed by Enikeev [56] on bulge tests carried out at two different levels of constant pressure. The initial thickness distribution (t) was approximated by a parabolic distribution with the radial position (r) expressed by Equation 15:

$$t = Ar^2 + C \qquad \text{Equation 15}$$

where C parameter was set at the constant value of 1 (equal to the initial thickness of the sample) while A was defined as the input parameter to be calculated in order to minimize the error function defined as the difference between the maximum and the minimum thickness value along the radial direction. The improved version of the MOGA genetic algorithm (MOGA-II) was used as the optimization evolutionary algorithm once having set the initial DOE population and the total number of successive generations.
As previously mentioned, once defined the input variable of the problem, an initial population of 50 individuals – where the term "individual" refers to a single numerical run – was created with the Sobol algorithm, able to uniformly distribute the individuals within the design space avoiding clustering phenomena. Adopting the common operators of the genetic algorithm (mutation and crossover), 20 successive generations were created thus a totality of 1000 simulations were run.

2.4.2.2. Experimental tests performed by means of SPIF

Experimental SPIF tests were conducted at room temperature on preheated square sheets.

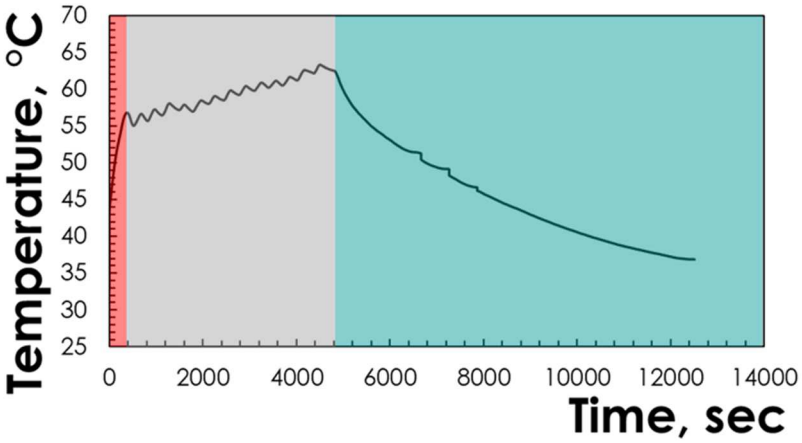

Figure 27 Heat treatment of the undeformed sheet.

Heat treatment was acquired by a thermal imager. The thermal cycle performed (shown in Figure 27) consists in a heating phase equal to 400s up to an average temperature of 60°C, followed by 90 minutes of maintenance and then cooled in the same furnace.
The experimental setup adopted to perform both heat treatments and SPIF tests are reported in Figure 28. A Kondia HS1000 Vertical machining center proper equipped was used.

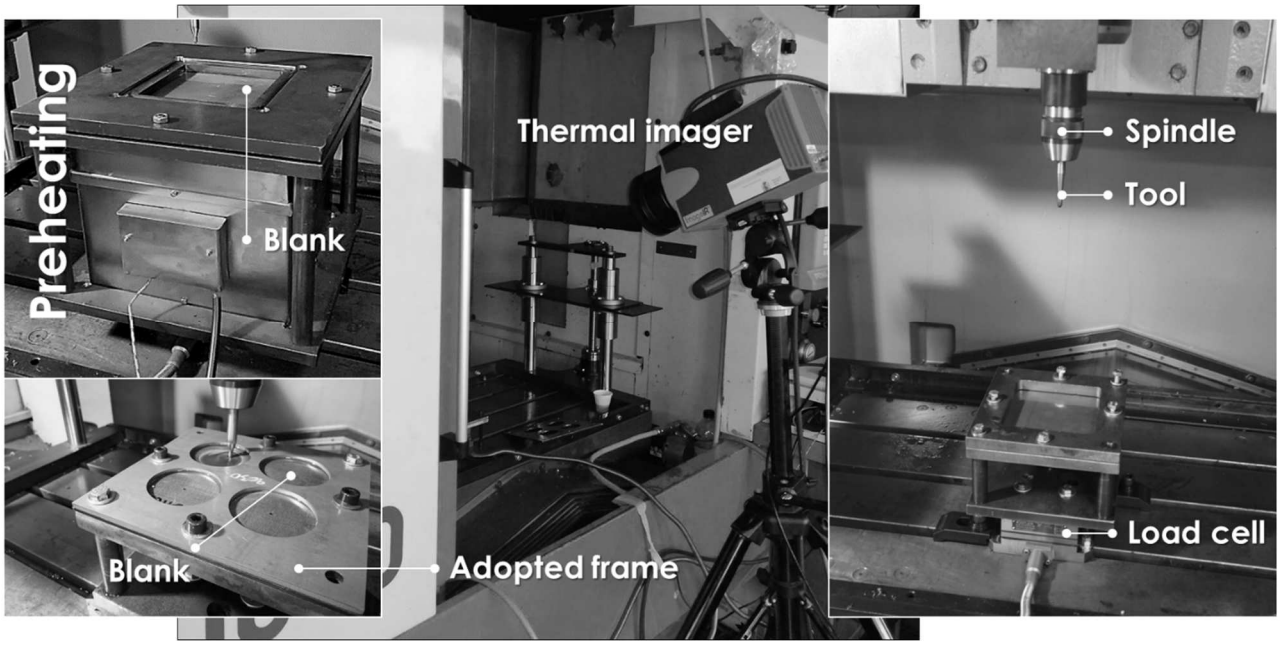

Figure 28 Heat treatment of the undeformed sheet.

Since the dimension of the final shape was very small, to minimize waste in terms of unprocessed areas of the blank, four different tests were carried out for each blank. In addition, to reduce effect of spring-backs, an optimized backing plate (Figure 29b) was designed to efficiently support the blank during the forming process. In the same way, also the clamping plate (Figure 29a) was designed aimed to manufacture four prostheses on the same blank.

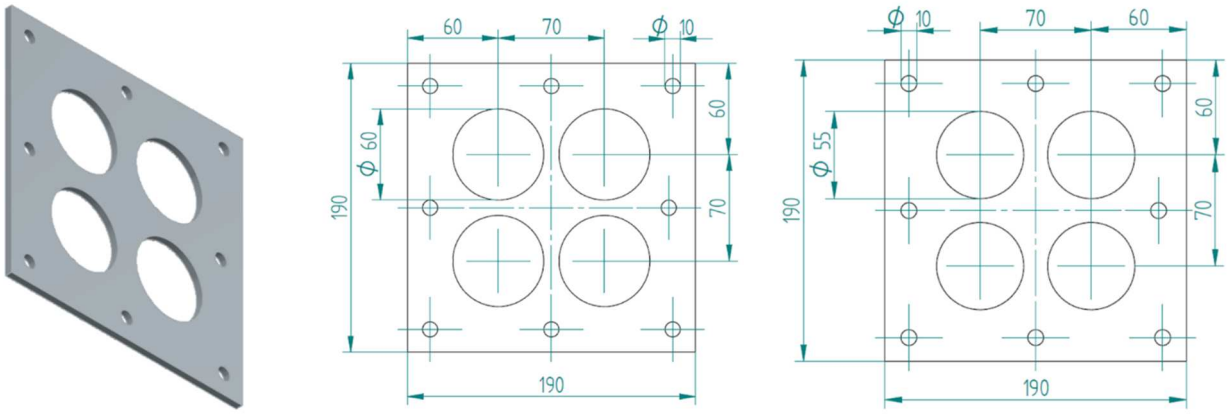

(a) (b)

Figure 29 Clamping (a) and Backing (b) plates designed to carry out experimental SPIF test.

Differently from what was done for the SPF process, in this case an experimental plan, obtained by adopting the Central Composite Design (CCD) method and based on three different process parameters (Feed Rate, FR, Spindle Speed, SS and Step Down, SD), was proposed.

Based on the numerical results, the starting point for the experimental step was represent by the optimization of SPIF tool trajectory aimed at experimentally reproducing the

thickness radial profile resulting from the previous optimization procedure.
As shown in Figure 30, the approach used for designing the SPIF trajectory was derived from the so-called "Sine law"; in fact, this law, considering the volume constancy and simple geometrical assumptions, allows to predict the sheet thinning after SPIF:

$$t = t_0\left(\frac{\pi}{2} - \alpha\right) \qquad \text{Equation 16}$$

where t is the current sheet thickness, t_0 is the initial thickness, and α is the inclination angle of the formed part, as imposed by the tool trajectory [63].

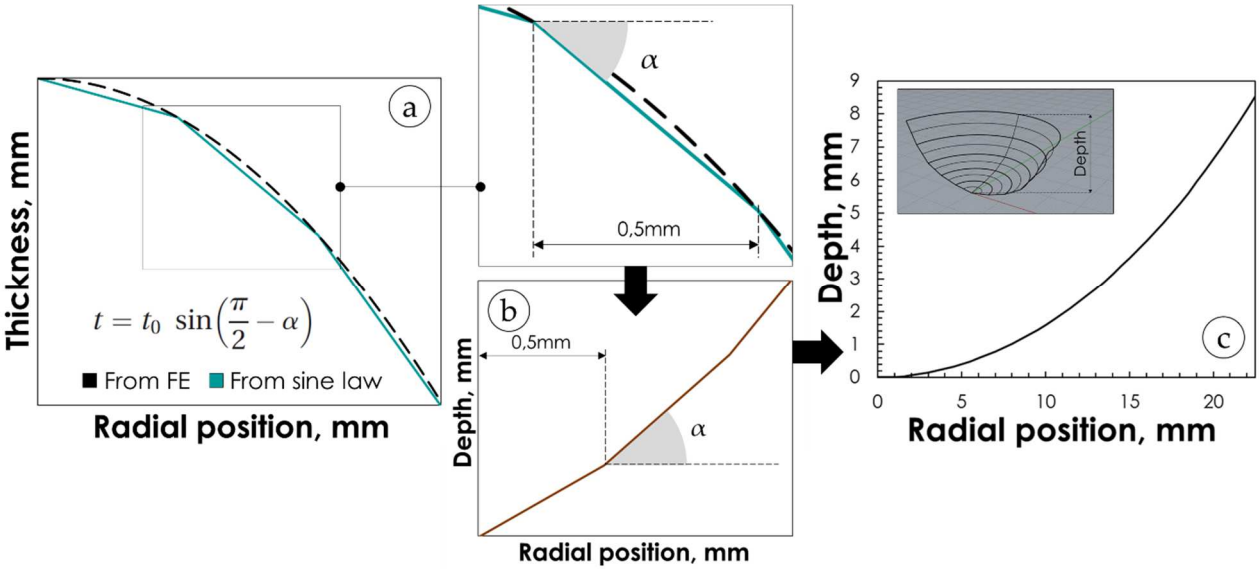

Figure 30 Depth profile determination starting from the initial thickness calculated by the FE simulation.

Then, the initial thickness distribution to be obtained by means of SPIF process was discretized with a step of 0.5mm along the radial direction and, applying the sine law equation, different wall angle values were calculated for each step by minimizing the error between the targeted thickness distribution deriving from the FE simulation and the one determined by the application of the abovementioned law.
Figure 30c shows the resulting geometry from this procedure (a dome type), and, the corresponding values of the tool depth versus the radial position that has to be reached to achieve the designed thinning.

2.4.2.3. Experimental tests performed by means of SPF

The facilities adopted to conduct all experimental SPF tests are reported in Figure 22.
A hemispherical die cavity with a 3mm entry radius fillet (Figure 31a) was used to reproduce perfectly the final shape desired.
In addition, the temperature in correspondence of the center of the sample was continuously acquired during the tests thanks to a K-type thermocouple. A scheme of the procedure

adopted is reported in Figure 31b.
Since results in terms of dome height, roughness and thickness distribution were analyzed and discussed, the first output was acquired by means of the same k-type thermocouple directly connected to a magnetostrictive linear sensor position, while roughness surface measures after SPF process were performed using a Mitutoyo Surftest SJ-400 Surface Roughness Tester.

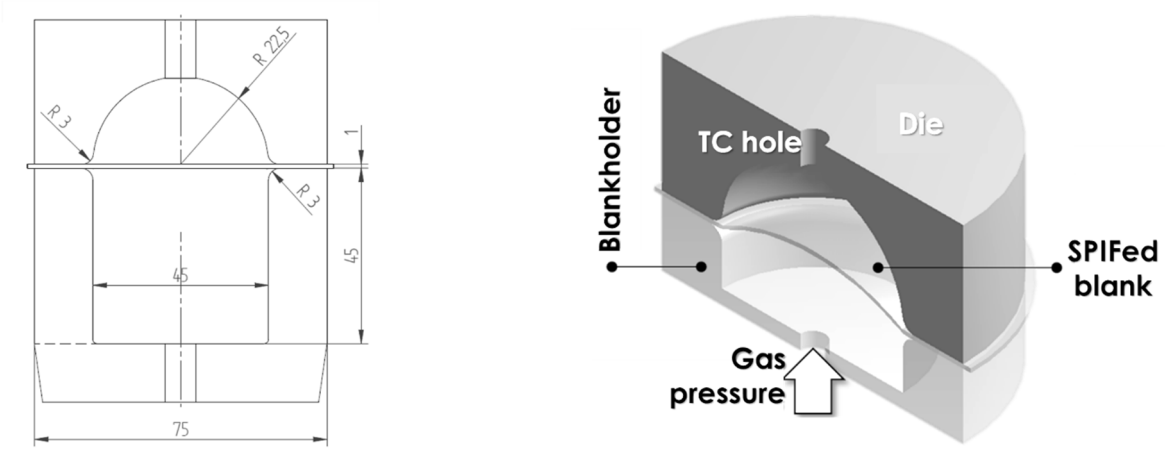

(a) (b)

Figure 31: Main dimension of metallic die (a) and a scheme of procedure (b) adopted to perform experimental SPF tests.

Finally, thicknesses were measured thanks a Mitutoyo 573-701 Absolute Digimatic Offset Caliper. All instruments adopted are reported in Figure 32.

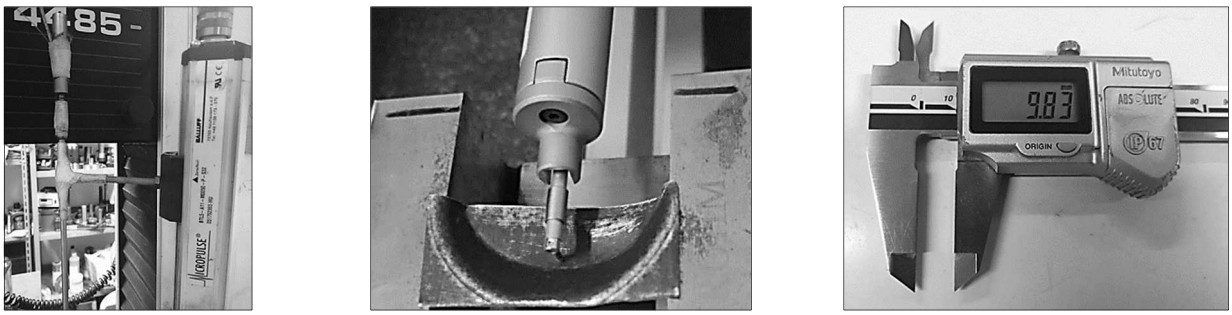

(a) (b) (c)

Figure 32: Facility adopted to perform experimental measurements: (a) magnetostrictive linear sensor position directly connect with the thermocouple; (b) Mitutoyo Surftest SJ-400 Surface Roughness Tester; (c) Mitutoyo 573-701 Absolute Digimatic Offset Caliper.

2.4.3. Manufacturing a spherical vessel via SPF on LHTed samples

2.4.3.1. LHT experimental tests

A CO_2 Laser source with a maximum power equal to 2500 W (Figure 33a) was used to perform LHT tests. The experiments were conducted using a lens having a focal length

equal to 95.2mm which produced a square spot area (100 mm^2) with a top-hat intensity distribution (Figure 33b). Keeping the spot stationary in the center of a sample for 20 seconds, two different power values (200 and 250 W) were investigated. Since the sample was heated only in the central area, this was affected by a thermal gradient along the radial direction.

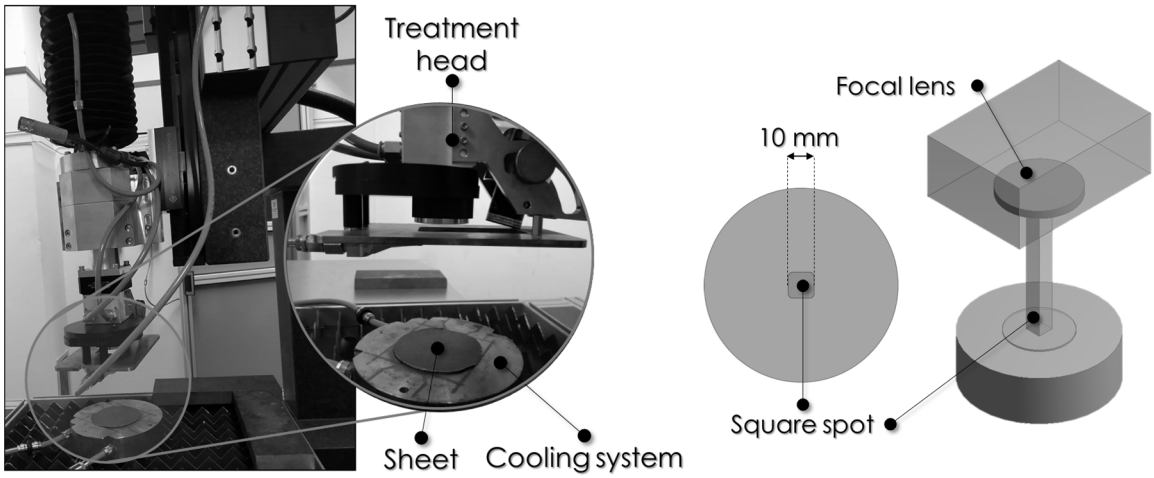

(a) (b)

Figure 33: Experimental facility (a) and setup (b) adopted to perform LHT tests.

The temperature gradients were provided by an infrared camera. In order to determine the microstructure evolution in terms of grain average size according to the temperature, each sample was cut along the radial direction, properly prepared, etched and finally analyzed using a light microscope (Eclipse MA200 Nikon).

2.4.3.2. LHT numerical modelling

To conduct FE simulations, the commercial code ABAQUS (v2017) was used. Implementing the temperature distribution experimentally obtained, the numerical model was calibrated. Constitutive model proposed by Miao et al. [13] was adopted to predict the microstructure evolution due to the LHT. Such a material model was implemented using a Python script which allowed to calculate the map distribution of the grain size according to Miao's model.

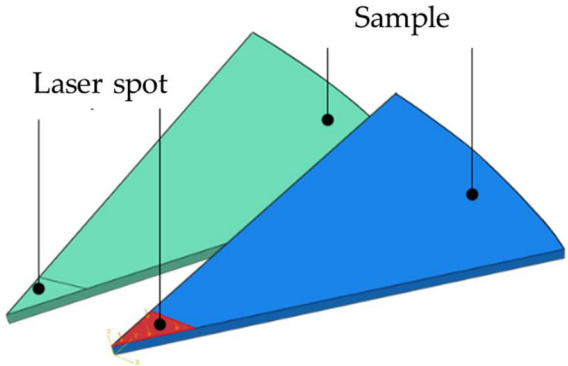

Figure 34: FE model of the localized LHT process.

Considering the geometry of both sample (circular) and laser radiation distribution (square), in order to reduce the total computational costs, one eighth of the circular sheet was modelled (Figure 34).

2.4.3.3. Experimental SPF on LHTed samples tests

Starting from the obtained results, next step was aimed at implementing the grain size dimensions into the simulation of the manufacturing of the spherical part via SPF.
From an experimental point of view, considering tests performed to calibrate the material model suggest by Carpenter, the intermediate gas pressure value (0.7MPa) was adopted. In fact, at this pressure - as previously demonstrated – the most performing fitting between experimental and numerical results was achieved.
Experimental setup adopted is depicted in Figure 22. Both LHT conditions were tested two times and adopting a constant gas pressure (0.7MPa). Results in terms of dome height, thickness distribution and grain size distribution were evaluated and discussed.

2.4.3.4. SPF on LHTed samples Numerical modelling

FE model used is the same in section. Exploiting mean grain size distribution previously obtained, the microstructural evolution due to both strain and time exposure to temperature was taken into account implementing Carpenter's material model through the FORTRAN subroutine.
As shoved in Figure 35, the initial radial grain size distribution (Figure 35a) change according to the forming time (Figure 35b). The two experimental grain size distribution obtained changing the laser power were approximated by means of a sixth-degree polynomial.

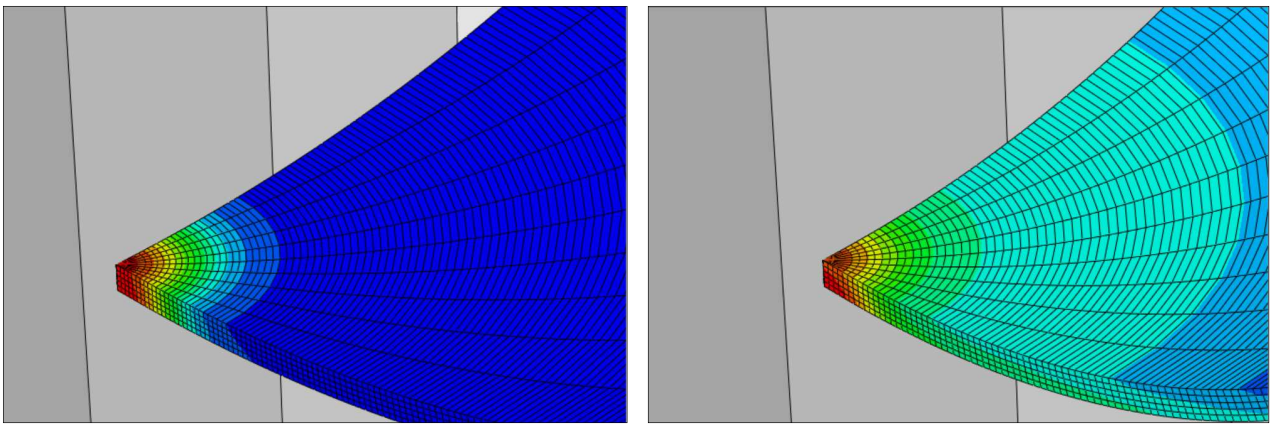

(a) (b)

Figure 35 FE modelling of grain distribution: (a) initial grain size distribution; (b) node coordinates change during forming. Red for highest grain size and blue for grain size in the as-received condition.

2.4.4. Manufacturing of a resorbable cheekbone implant by advanced sheet metal forming processes (SPF and SPIF)

The second case study investigated, depicted in Figure 36 below, was represented by a customized Mg alloy cheekbone prosthesis; this type of prosthetic implant, thanks to the capability to be absorbable into the human body, could be very useful to repair small damages without any additional surgery step.
The proper design of a prosthetic implants starts from the correct identification of the damaged area to be replaced; the huge progress in terms of made computer graphics hardware and image processing since 1980s have improved the potentialities of the three-dimensional Computed Tomography (CT) scanning techniques in the pre-operative planning step: the reconstruction of the bone damaged area is nowadays demanded to the mirroring technique based on the definition of the prosthesis geometry starting from the healthy side so the symmetry after implantation is entirely preserved [64,65].
In this study, the geometry was defined using data from Digital Imaging and COmmunications in Medicine (DICOM) images, properly manipulated and used to reconstruct the geometry of a defected area or to be integrated in a bone region of the patient.
The first step was characterized by the damage identification (Figure 36a): the damage was created by means of drilling of radiopaque material skull. The DICOM acquisition allowed to digitalize the area of interest (Figure 36b).

(a) (b)

Figure 36 Procedure adopted to digitalize the damage to be repair: (a) damage area identification and (b) results from DICOM acquisition.

Starting from the DICOM acquisition and taking advantage of mirroring techniques, the CAD geometry was optimized thanks to the adoption of the surfaces tangent to the damaged area (Figure 37).

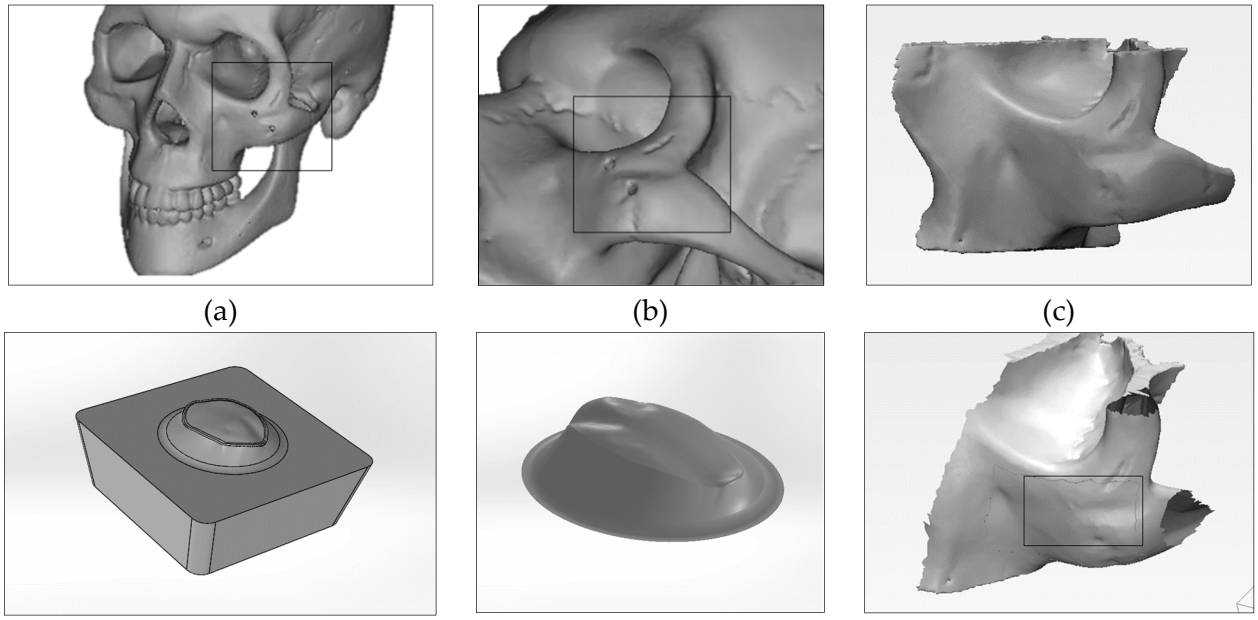

Figure 37 Surface repair and zone of interest extraction: (a) starting CAD model, (b) repairing, (c) CAD model repaired, (d) prosthetic surface extrapolation, (e) and (f) final shape according to SPF die.

2.4.4.1. Experimental prosthesis manufacturing via SPF

To fabricate cheekbone prostheses via SPF, square blanks with length side equal to 150mm and obtained by cutting a single AZ31B-H24Mg alloy sheet with an initial thickness equal to 1 mm were used. Gas pressure profiles deriving from FE model (results are discussed below in chapter 5) and able to maintain a constant strain rate of 0.001 and $0.0005s^{-1}$ were implemented to perform experimental tests. Each strain rate condition was replicated three times. To perform experimental tests, the equipment shown in Figure 38 was used.

The 2500 kN electro-hydraulic press machine, specifically designed in collaboration with the Gigant Industries company, is particularly suitable for superplastic forming tests, being equipped with heated tools for hot conditions (up to 1000°C). Argon gas was adopted to conduct all experimental tests.

To correctly carry out the manufacturing process, a die design according to prosthesis geometry and process characteristics must be performed. Clearly, in order to avoid localized zone of the sheet subjected to high deformations (i.e. due to very small radius fillet), the shape deriving from the prosthesis design was appropriately connected to the flat area of the SPF die. Furthermore, since high temperatures are necessary during the SPF process, it is crucial to design the die also considering the different linear shrinkage coefficients of die and sheet.

From an economic point of view, as reported both in the left box in Figure 38 and in Figure 39, to drastically reduce the total costs associated with the forming process, an expendable insert was designed and produced.

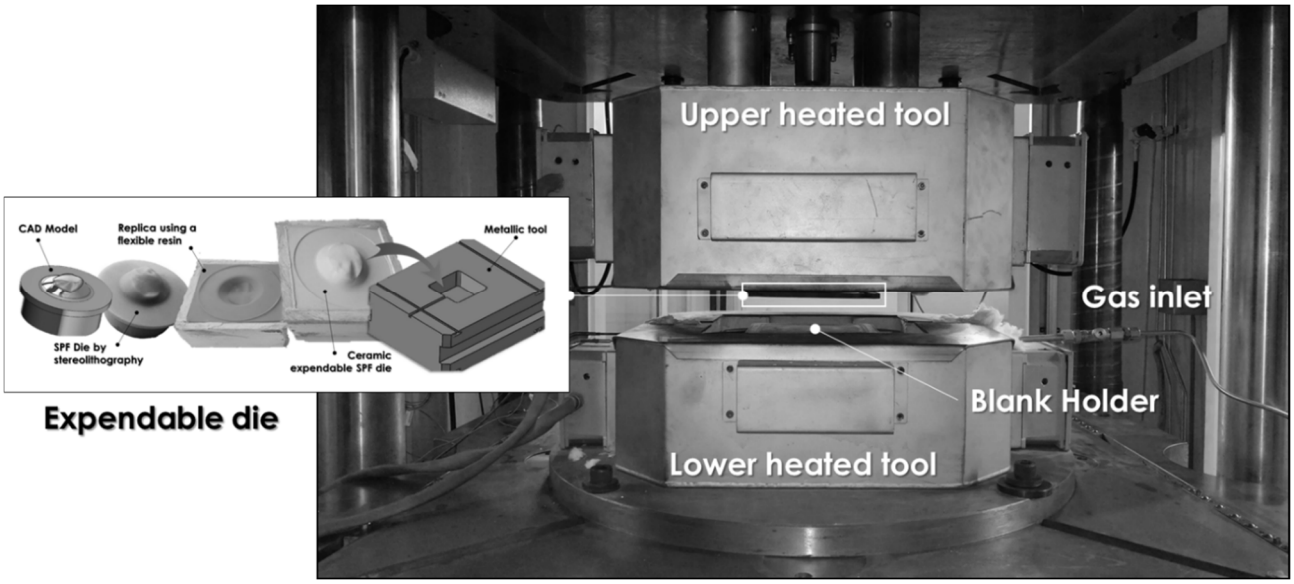

Figure 38 Experimental facility for SPF tests.

The main steps of the adopted procedure can be summarized as follows: (i) Expendable die geometry (interfaced with the cavity of a standard metallic tool) manufacturing starting from a stereolithography model (step 2 and 3 in Figure 39); (ii) Manufacturing of a resin pattern replica, able to reproduce complex geometries (even with undercuts) and sufficiently flexible (step 4 in Figure 39); (iii) Fabrication of the expendable die using the obtained resin replica (step 4 in Figure 39).

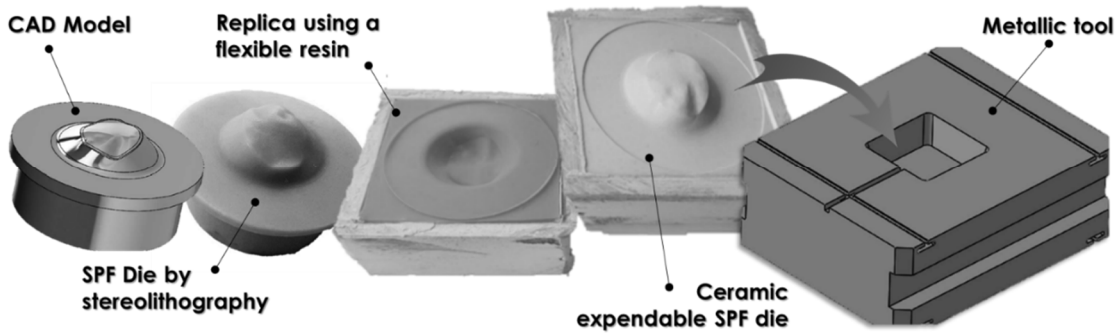

Figure 39 Methodology adopted for creating expendable SPF die.

2.4.4.2. Numerical modelling of prosthesis manufacturing via SPF

FE model was based on constant material obtained by means of Bulge tests.
The material constitutive model adopted to perform numerical analyses were suggest by Enikeev and Kruglov [56].
Starting from four experimental bulge tests performed at 450°C and adopting 0.2, 0.3, 0.4 and 0.7MPa as gas pressure, the m and K values were determined by applying equations 6 and 7 (Table 5).

Gas pressure, MPa	K	m	Eq. strain rate, s^{-1}
0.2 – 0.3	1937.32	0.65	0.0001
0.3 – 0.4	653.932	0.53	0.0005
0.4 – 0.7	140.475	0.34	0.001

Table 5 Obtained values of K and m exploiting experimental tests.

In the last column of Table 5 values about the equivalent strain rate were reported. Approximating the strain rate of each test as that obtained from the constant slope curve, the values listed in table were obtained as average between the two curves considered to determine K and m values. An example is reported in Figure 40.

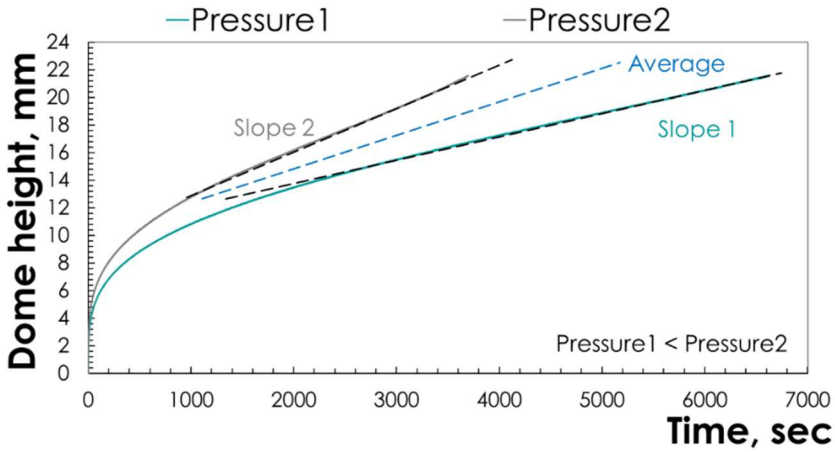

Figure 40 Equivalent strain rate determination.

The experimental setup for the SPF tests was reproduced in the FE Abaqus/CAE environment. The die was modelled as a rigid body and meshed with shell elements, while the blank was modelled as a deformable shell body and meshed with S4R elements. The modelled assembly is shown in Figure 41.

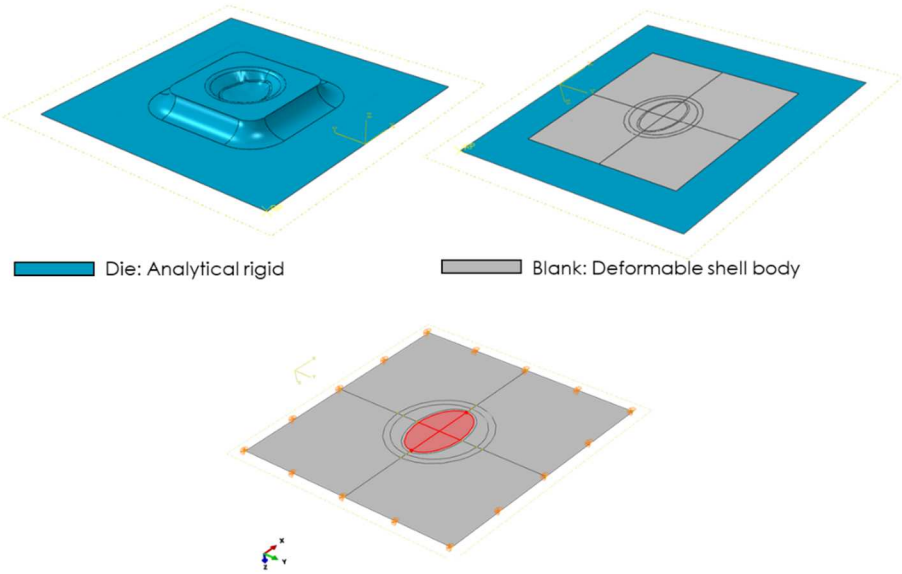

Figure 41 FE model of the SPF process for producing the case study.

Blank outer region is pinned (all the translational degrees of freedom are blocked).
The gas pressure is modulated to induce the predefined strain rate target level (according to the three different strain rate target levels reported in Table 5) in the blank portion highlighted in red (that approximately corresponds to the final prosthesis geometry).
Considering the three equivalent strain rates reported in Table 5, three different pressure profile were obtained.

2.4.4.3. Experimental prosthesis manufacturing via SPIF

Experimental tests were performed exploiting the same SPIF facilities and experimental setup adopted to manufacture the preform for the vessel manufacturing via SPF. In this case, process parameter investigated to optimize SPIF response in terms of thickness distribution were SD, FR and SS.
For each variable three different levels were selected according to the previous case study results (spherical vessel) and machine characteristics. In addition, since the dimension of the part to manufacture was small and excessive bending effects were recorder in a preliminary test adopting a tool diameter of 2mm, a tool with a diameter equal to 4mm was adopted to perform all experimental tests.

	FR, mm·min^{-1}	SS, rpm	SD, mm
Min	120	2500	0.0150
Max	600	7500	0.0900

Table 6 Experimental limits adopted for the three input variables.

For each input parameter the highest and the lowest levels were determined according to the limits of the experimental facilities and reasonable cycle times (Table 6).

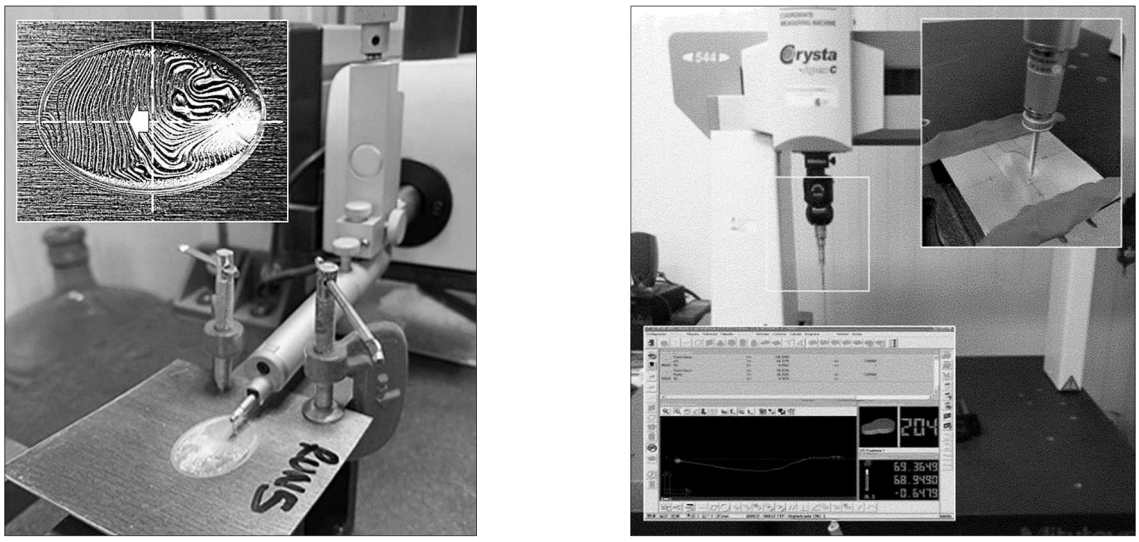

(a) (b)

Figure 42 Experimental setup to measure surface roughness (a) and experimental setup adopted and methodology to calculate the shape accuracy (b).

Mitutoyo Surftest SV1000 was used to measure Surface Roughness, Ra. Ra measures were performed starting from the center of each sample to the peripherical zone along the longitudinal central path of the prosthesis shape (Figure 42a).
Shape profile of the cheekbone prostheses were acquired using the Coordinate-Measuring Machine (CMM) Mitutoyo Crysta-Apex C544, shown in Figure 42b.

3. Manufacturing and characterization of new Mg alloys with high deformation performance

The first part of the present research activity was focused on the alloy manufacturing by casting with the aim to obtain a new Mg alloy with high mechanical-deformation capacity comparable to the commercially available Mg alloys.

In order to achieve a high-performance alloy, selection of the alloying elements in this research activity were made based on the known-through-the literature effects of some alloying elements on Mg and the Stacking Fault Energy (SFE) levels in Mg.

An ideal alloy design strategy for a better deformation capacity should pursue such alloying elements that do not facilitate the already very active basal plane, i.e. the basal slip, but instead the pyramidal and/or prismatic slip systems.

This way, not only the deformation capacity of the Mg alloy would increase but the texture tendency would diminish as well. The same approach would also be expected to improve the potential of at least the deformation hardening mechanism and possibly of the grain refinement following recrystallization.

A broad review on the effects of alloying elements used is beyond the scope of this study, and therefore we will limit our scrutiny to the effects of the alloying elements used in the present research (more comprehensive reviews on Mg-RE and Mg-Zn-RE systems have been reported by other authors [66,67]).

It has been long known that Zn imparts strengthening, and Ce, more precisely rare-earth elements, increases deformation capacity while also providing strength [66–70].

A well-known commercial alloy, WE43 may be given as an example, which shed light on the effects of REs. The increased ductility [18,71–73] even at room temperature via activating additional twinning planes and pyramidal slip plane, improved strength [70] and reduced texture are all well-established [74] and attributed to the presence of Yttrium and REs.

Cerium has the lowest solubility in Mg compared to the other RE elements. Due to Ce addition, deformation becomes more homogeneous as compared to pure Mg and deformation and annealing textures weakens up to 0.03% Ce addition beyond which concentration this effect levels out [75].

Compared to many alloying elements, including Zn, used in Mg, Ce has the greatest segregation tendency to twin boundaries [68]. Although Zhang et.al. [76] pointed out some of the outcomes of this important finding, it also begets the question of what the already present in the as-cast condition, if any, Ce atoms (as well as Zn) on the twinning planes do prior to the twinning itself.

The answer should be sought in the changes in SFE of those planes due to the presence of Ce solute atoms. All RE elements lower all types of SFEs in Mg, the degree of drop relatively lessens as the atomic number of the RE element increases [76]. Through this influence on SFE, the dislocation as well as deformation characteristics change.

Zn is an alloying element of the commercially available AZ series in which Zn acts as a more effective [77] solid solution strengthened as compared to Al (almost twice in concentrated solutions [78] while also imparting grain refinement [79]).
Tin (Sn) and lead (Pb) have a relatively high solubility in Mg at the eutectic temperature,14.5wt% and 41.9wt%, respectively, which reduces significantly at ambient temperature. Both Sn and Pb have a favourable size factor for forming a substantial solid solution in the Mg matrix.
Alloying elements Sn and Pb also affect the lattice parameter and the generalized SFE of Mg. Additions of a small amount of Pb enhances the ductility of Mg–Al and Mg–Sn alloys, and can modify the microstructure and improve the mechanical properties of Mg-based alloys [80].
Again, the addition of Sn is also known to reduce the degree of segregation formed during twin-roll casting, which has become the most efficient fabricating process for Mg alloy sheets [81].
A first analysis, aimed at reducing the total number of obtained alloys to be analysed, was carried out by means of Brinell Hardness (HB) tests and metallographic observation of the samples extracted.
After this first skimming phase, tensile tests at warm (200°C) and hot (400°C) conditions were conducted to determine which of the manufactured ones had the best deformation performance, without neglecting the mechanical properties.
In addition, also strain rate effect were evaluated for the two best performing Mg alloy (both ternary) varying it from 0.00125 to $0.0125s^{-1}$.
Finally, the best one was selected to perform bulge tests under superplastic forming conditions to calculate the strain rate sensitivity index (m value) and compare its results with the commercial Mg alloy AZ31B-H24, one of the most adopted in the aeronautical and automotive sectors due to high deformation properties at elevated temperatures.
All experimental activities previously depicted were supported by metallographic analyses with both light and scanning electron microscopy (SEM).
The experimental trials were performed in cooperation with the Mugla Sıtkı Kocman University (Turkey); in particular, exploiting facilities and skills present in the abovementioned university, the manufacture of alloys and their subsequent micro / macrostructural characterization (through SEM and Brinell hardness analysis) were conducted jointly in Politecnico di Bari and Mugla S.K. University in Turkey by involvement of the present author in both institutions.
Remaining experimental activities documented in this chapter were performed using facilities of the Polytechnic University of Bari (Italy) alone.

3.1. Innovative Mg alloys manufactured

Following the casting procedure described in chapter 2 (section 2.2.1) and starting from the considerations abovementioned, fourteen different Mg-based alloys were prepared under argon atmosphere using pure metals and/or suitable master alloys in an electric furnace.

Each Mg alloy type is listed in Table 7 with the respective nomenclature adopted to distinguish the same from each other.
As possible to see from the same table, experimental Mg-based alloys differ from each other based on the type, quantity and number of alloying elements.

3.2. Microstructural analyses

To analyse the performances of the different Mg alloys manufactured (particularly in terms of deformation behavior), microstructural analyses were carried out using light microscopy as well as SEM imaging.

Mg alloy number	N. of alloying elements	Name	Nominal compositions
1	2	YS	Mg-2Y-2Sn
2	2	ZY	Mg-2Zn-2Y
3	2	ZC	Mg-2Zn-2Ce
4	2	YP	Mg-2Y-1Pb
5	3	ZYC	Mg-2Zn-2Y-2Ce
6	3	ZYS	Mg-2Zn-2Y-2Sn
7	3	SY1P	Mg-2Sn-2Y-1Pb
8	3	ZYP	Mg-2Zn-2Y-1Pb
9	3	SY2P	Mg-2Sn-2Y-2Pb
10	4	ZSYC	Mg-2Sn-2Y-2Zn-2Ce
11	4	ZCY1P	Mg-2Ce-2Zn-1Pb-2Y
12	4	ZCY2P	Mg-2Ce-2Zn-2Pb-2Y
13	5	ZYSCP	Mg-2Zn-2Y-2Sn-2Ce-1Pb

Table 7 Nominal compositions of the alloys as obtained via semi-quantitative SEM-EDS (weight%).

Table 7 gives the alloy compositions prepared based on different area analysis at small magnifications (large area selection) using EDS of FEI NOVANANO SEM 650.
After having proper prepared each sample by means of cutting, mounting, grinding, polishing and etching operations, micrographs were obtained by using the same experimental facility adopted to obtain chemical composition.
Results achieved are depicted from Figure 43 to Figure 45 (subdivided by alloying elements number).
The predominant grey/black colour in each micrograph represents the Mg (due to low number of back scattered electrons from Mg), while the white parts (high atomic numbers) are representative of the secondary phases, for which a more detailed investigation was needed to establish their nature.

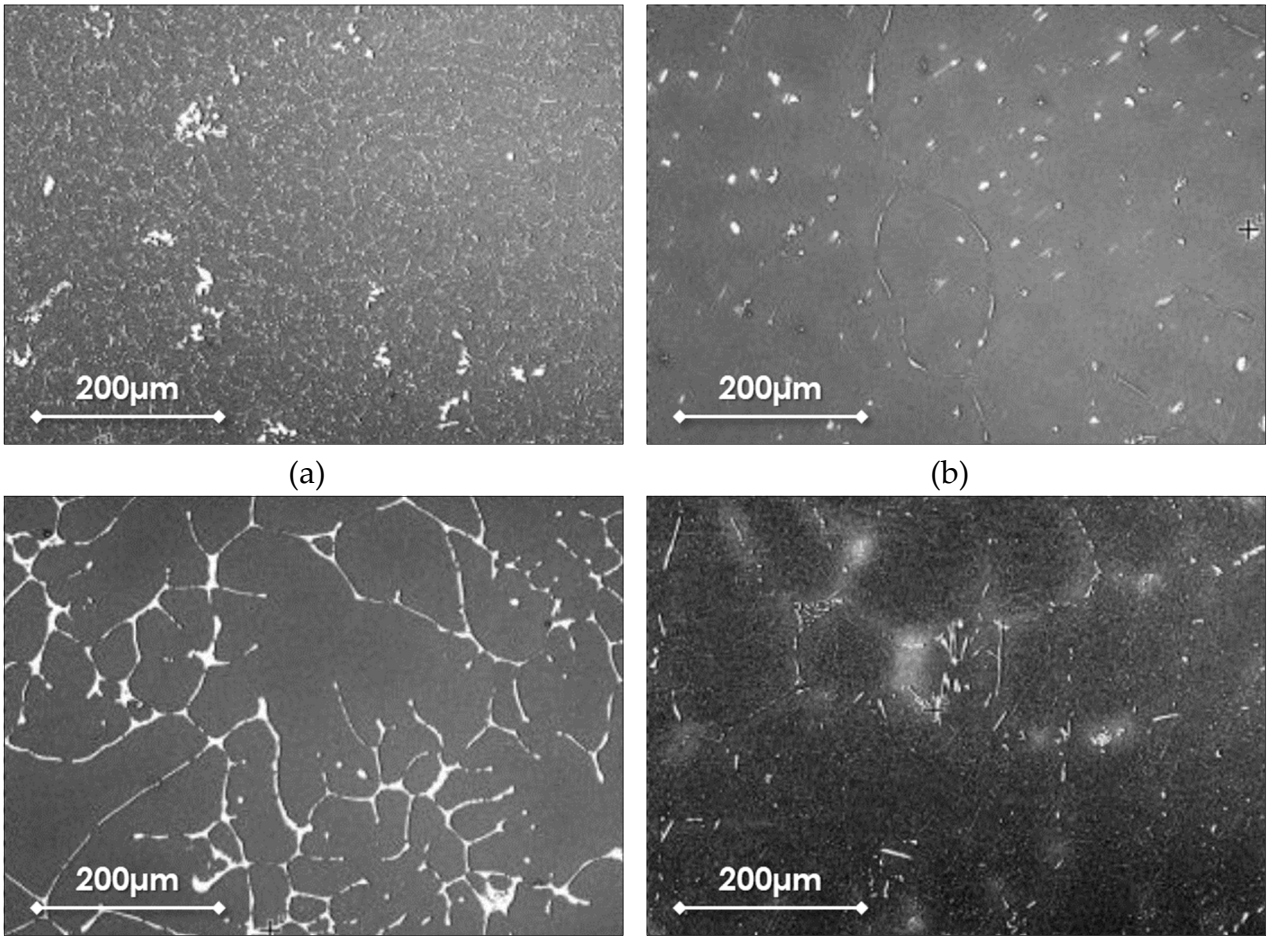

(a) (b)

(c) (d)

Figure 43 SEM-Back scattered electron (BSE) micrographs of the as-cast microstructures of the experimental Mg-based alloys with two alloying elements: (a) YS, (b) ZY, (c) ZC and (d) YP.

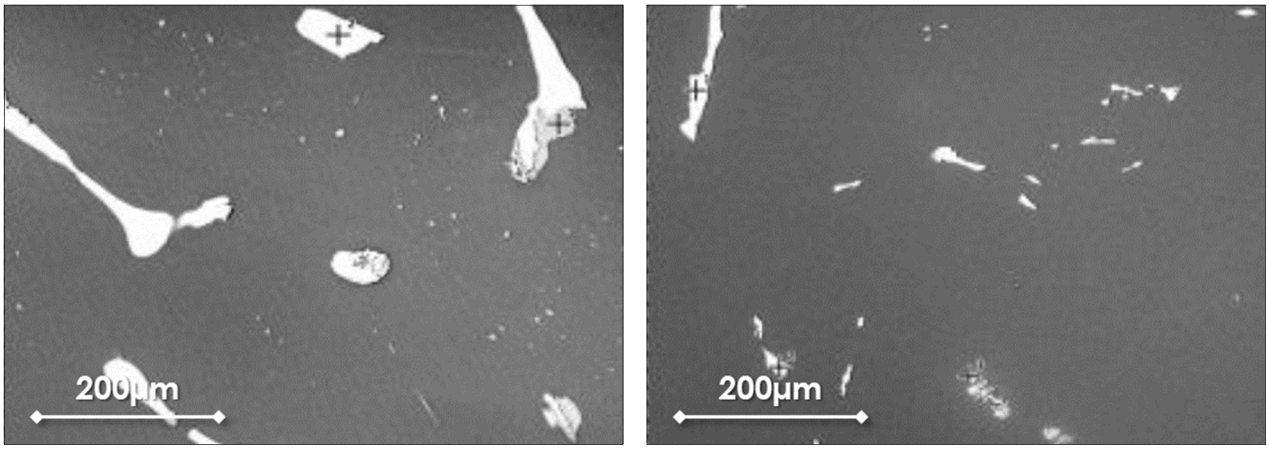

(a) (b)

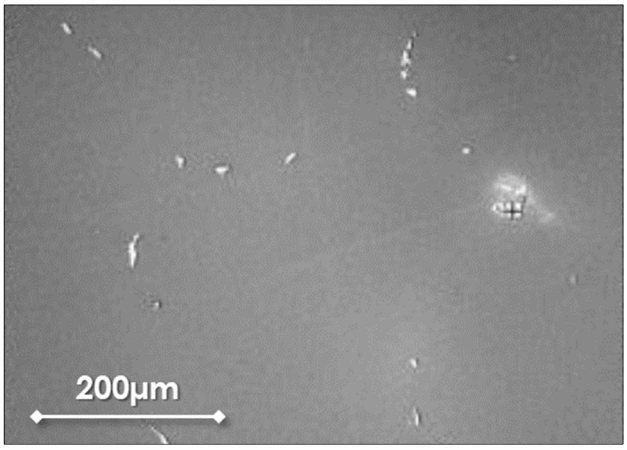

(c)

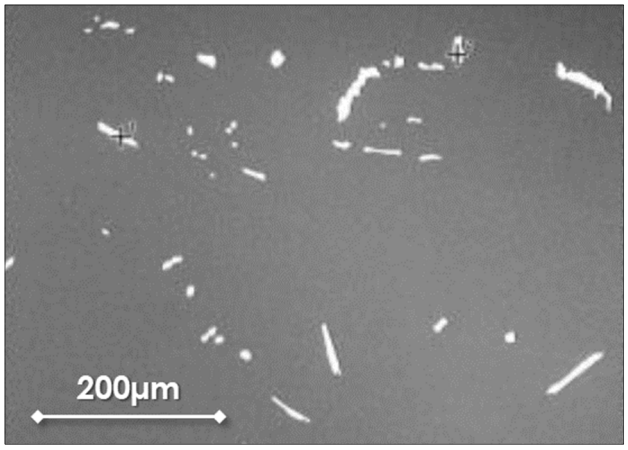

(d)

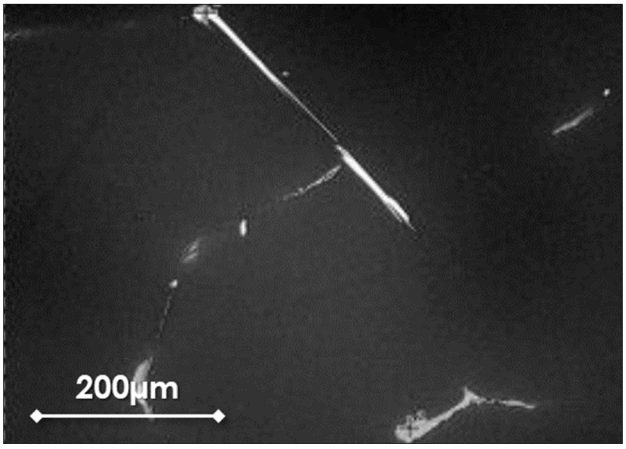

(e)

Figure 44 SEM-BSE micrographs of the as-cast microstructures of the experimental Mg-based alloys with three alloying elements: (a) ZYC, (b) ZYS, (c) SY1P, (d) SY2P and (e) ZYP.

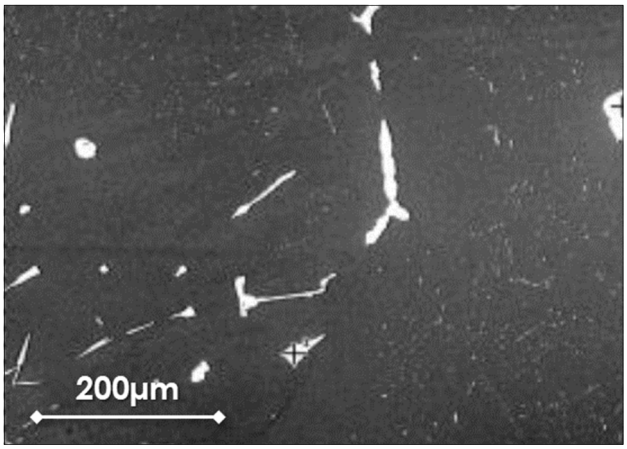

(a)

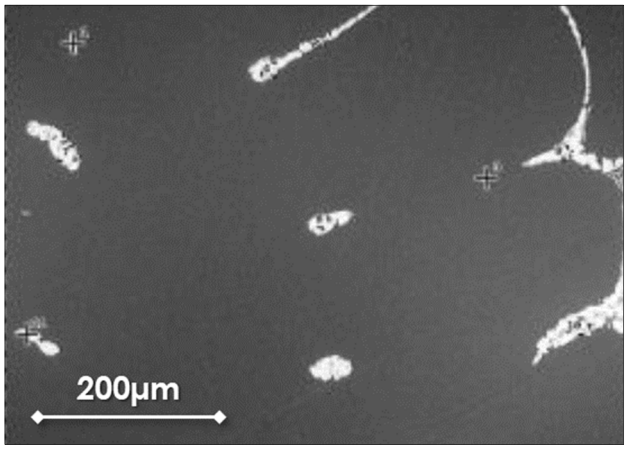

(b)

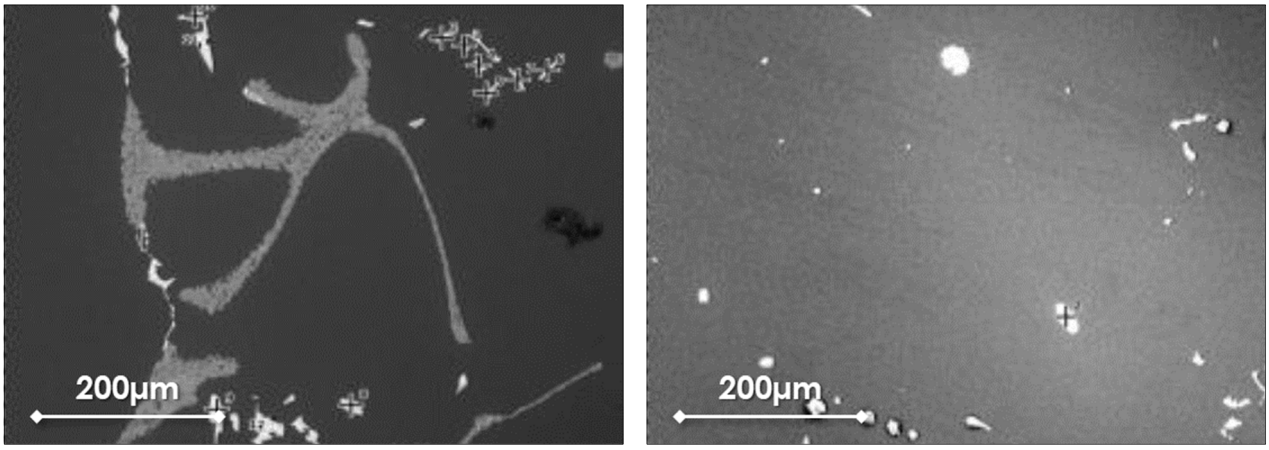

(c) (d)

Figure 45 SEM-BSE micrographs of the as-cast microstructures of the experimental Mg-based alloys with four or five alloying elements: (a) ZSYC, (b) ZCY1P, (c) ZCY2P and (d) ZYSCP.

Chemical compositions of the different phases seen in the microstructures were determined for all Mg alloys prepared via Energy-Dispersive X-ray Spectroscopy (EDS). Chemical compositions associated with the micrographs are listed from Table 8 to Table 20.

Element number	Element symbol	Element name	Concentration	Error
12	Mg	Magnesium	97.8	0.2
50	Sn	Tin	1.1	7.1
39	Y	Yttrium	1.1	7.4

Table 8 YS composition from EDS analysis

Element number	Element symbol	Element name	Concentration	Error
12	Mg	Magnesium	96.4	0.2
39	Y	Yttrium	1.5	2.1
30	Zn	Zinc	2.1	8.2

Table 9 ZY composition from EDS analysis.

Element number	Element symbol	Element name	Concentration	Error
12	Mg	Magnesium	96.7	0.2
58	Ce	Cerium	1.6	6.1
30	Zn	Zinc	1.7	9.8

Table 10 ZC composition from EDS analysis.

Element number	Element symbol	Element name	Concentration	Error
12	Mg	Magnesium	97.8	0.2
82	Pb	Lead	1.2	1.1
30	Y	Yttrium	1.1	7.4

Table 11 YP composition from EDS analysis.

Element number	Element symbol	Element name	Concentration	Error
12	Mg	Magnesium	96.4	0.2
30	Zn	Zinc	2.3	6.8
58	Ce	Cerium	1.0	8.9
39	Y	Yttrium	0.3	21.0

Table 12 ZYC composition from EDS analysis.

Element number	Element symbol	Element name	Concentration	Error
12	Mg	Magnesium	96.7	0.2
30	Y	Yttrium	1.3	5.9
50	Sn	Tin	0.7	9.5
30	Zn	Zinc	1.3	11.9

Table 13 ZYS composition from EDS analysis.

Element number	Element symbol	Element name	Concentration	Error
12	Mg	Magnesium	97.3	0.2
39	Y	Yttrium	1.0	6.5
82	Pb	Lead	1.1	9.0
50	Sn	Tin	0.6	9.9

Table 14 SY1P composition from EDS analysis.

Element number	Element symbol	Element name	Concentration	Error
12	Mg	Magnesium	97.9	0.2
39	Y	Yttrium	0.7	9.8
82	Pb	Lead	1.0	10.0
50	Sn	Tin	0.4	14.7

Table 15 SY2P composition from EDS analysis.

Element number	Element symbol	Element name	Concentration	Error
12	Mg	Magnesium	97.0	0.2
39	Y	Yttrium	0.9	7.6
82	Pb	Lead	1.0	9.6
30	Zn	Zinc	1.2	11.6

Table 16 ZYP composition from EDS analysis.

Element number	Element symbol	Element name	Concentration	Error
12	Mg	Magnesium	95.8	0.8
58	Ce	Cerium	1.1	8.0
50	Sn	Tin	0.8	8.3
30	Zn	Zinc	1.8	8.1
39	Y	Yttrium	0.6	10.9

Table 17 ZSYC composition from EDS analysis.

Element number	Element symbol	Element name	Concentration	Error
12	Mg	Magnesium	97.2	0.3
58	Ce	Cerium	0.8	13.7
39	Y	Yttrium	0.4	19.3
82	Pb	Lead	0.6	20.9
30	Zn	Zinc	0.9	20.6

Table 18 ZCY1P composition from EDS analysis.

Element number	Element symbol	Element name	Concentration	Error
12	Mg	Magnesium	89.5	0.3
30	Ce	Cerium	3.2	2.7
82	Pb	Lead	2.4	3.2
39	Y	Yttrium	1.2	2.4
58	Ce	Cerium	8.9	8.4

Table 19 ZCY2P composition from EDS analysis.

Element number	Element symbol	Element name	Concentration	Error
12	Mg	Magnesium	96.5	0.2
39	Y	Yttrium	0.8	8.6
58	Ce	Cerium	0.8	10.5
50	Sn	Tin	0.6	11.7
30	Zn	Zinc	0.9	16.7
82	Pb	Lead	0.5	19.0

Table 20 ZYSCP composition from EDS analysis.

3.3. Mechanical characterization of the manufactured Mg alloys

Mechanical characterization of the manufactured Mg-based alloys can be divided in three steps: (i) Brinell hardness (HB) tests conducted for all produced alloys aimed to discharge the worst one; (ii) Tensile tests at warm and high temperature on the most performing alloys deriving from the previous skimming step; (iii) Characterization via bulge test of the most performing Mg alloy. In this way, results coming from experimental tests could be compared with those related to the commercial AZ31B-H24 Mg alloy. Experimental facilities and procedure described in section 2.2.2 were adopted.

3.3.1. Brinell hardness tests results

As anticipated, the first step was represented by HB tests. Results coming from these tests are divided according to the number of alloy elements. As possible to observe in Table 21 and Figure 46, the two best performing alloys (in terms of HB value) among those with three elements are the ZY (with an HB equal to 53.4) and the ZC (with an HB of 38.6).

Alloy type	R1	R2	R3	R4	R5	Average	Std. Dev.
ZC	40.4	38	37.9	38.8	37.7	38.6	1.0
ZY	51.2	59.1	53.2	50.6	53	53.4	3.0
YS	30.5	26.9	35.3	37.8	30.5	32.2	3.9
YP	30.9	29.7	30.8	30.1	33	30.9	1.1

Table 21 HB values obtained for Mg-based alloys with two alloying elements.

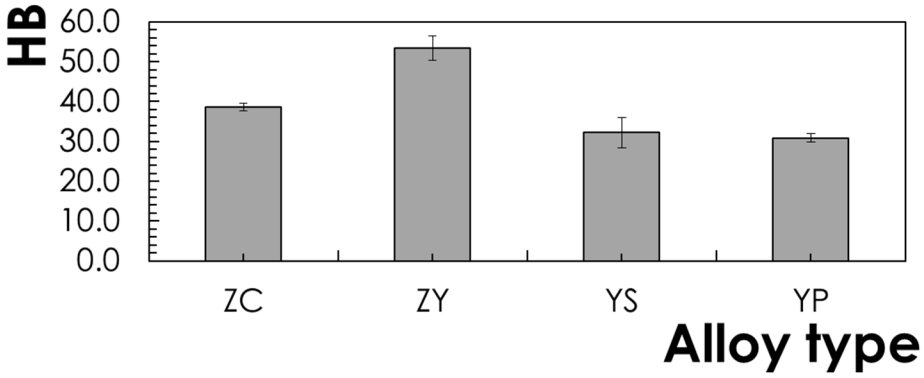

Figure 46 HB values obtained for Mg alloys with two alloying elements.

Related to the ZC alloy the minimum value of the standard deviation was recorder highlighting a good homogeneity following the casting process.
The same analyses were performed also for the Mg-based alloys with three, four and five additional elements. The obtained results are listed below.

Alloy type	R1	R2	R3	R4	R5	Average	Std. Dev.
ZYC	49	51	46.1	46.2	48.1	48.1	1.8
ZYS	37.9	40.2	42.2	42.4	38.1	40.2	1.9
SY1P	37.8	34.3	36.1	41.7	38.7	37.7	2.5
SY2P	34.4	35.8	36.2	35.7	35.6	35.5	0.6
ZYP	43.4	38.8	41.6	44.7	39.2	41.5	2.3

Table 22 HB values obtained for Mg-based alloys with three alloying elements.

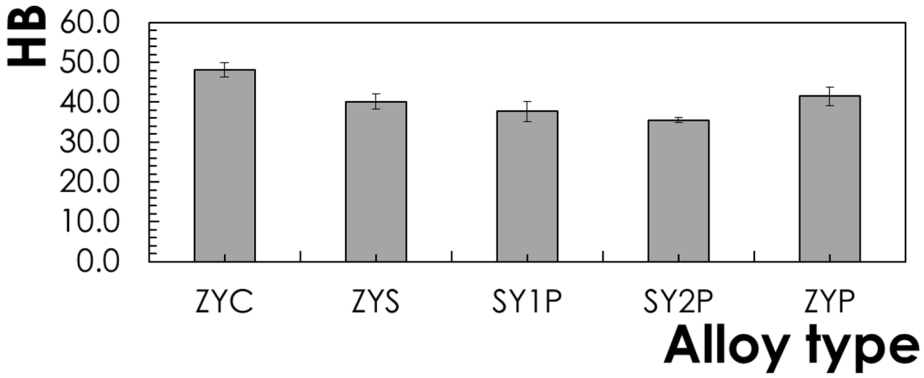

Figure 47 HB values obtained for Mg alloys with three alloying elements.

When quaternary Mg based systems (three alloying elements) were considered, the best performances were observed with the ZYC (48.1HB) and the ZYP (41.5HB) alloys. On the other hand, the lowest HB value obtained was 35HB for the SY2P alloy. Comparing the two alloys in which Pb was present, it emerges that, although the content of the latter has been doubled, no advantage in terms of hardness was recorded.
Finally, the comparison of the HB results for the remaining Mg-based alloy showed a substantial similarity between all the alloys investigated; in fact, the HB values range between 36.3 (ZSYC) to 41.1 (ZYSCP), as reported in Table 23 and Figure 48.
From a global comparison, the two best alloys in terms of recorded hardness are the ZY and the ZYC with respectively 53.4 and 48.1HB.

Alloy type	R1	R2	R3	R4	R5	Average	Std. Dev.
ZSYC	38.8	34.4	35.6	36.4	36.1	36.3	1.4
ZCY1P	40.4	40.5	39.2	40	39.8	40.0	0.5
ZCY2P	39.6	42.2	36.6	39	36.5	38.8	2.1
ZYSCP	39.5	38.8	39.8	41.5	45.7	41.1	2.5

Table 23 HB values obtained for Mg-based alloys with four or five additional alloying elements.

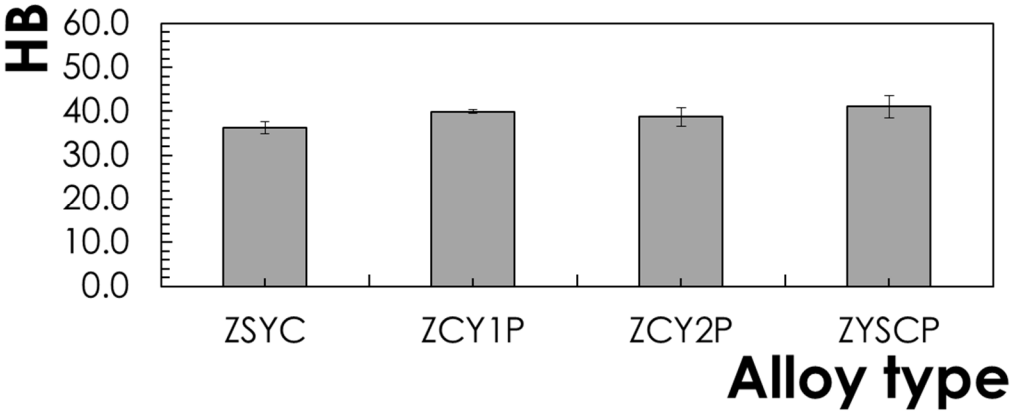

Figure 48 HB values obtained for Mg alloys with four or five additional alloying elements.

3.3.2. Tensile tests at warm and high temperature results

The subsequent tensile tests were carried out focusing the attention on a part of the starting Mg-based alloys. Considering the previous hardness results, the for each group of alloys the best performing ones were subjected to tensile tests.
In particular, the two Mg-based alloys (ZY and ZC) with the highest values of HB were considered to perform tensile tests.
Referring to the quaternary Mg alloys (Figure 47), since the difference in terms of HB for SY1P and SY2P according to the standard deviation can be considered statistically not significant, the SY2P was not considered for the tensile tests.
As possible to observe from Figure 48, the ZSYC and ZCY2P were discarded due to both the lowest HB value and the negligible effect of Pb improvement as compared to ZSYC and ZCY2P alloys

Tensile tests were performed considering two different values of temperature (200 and 400°C) for all Mg-based alloys. In addition, for only the ternary Mg-based also the effects of strain rates (0.0125 and 0.00125s^{-1}) were evaluated. In Table 24 all experimental tensile tests performed are summarized.

Alloy type	200°C-0.0125s^{-1}	200°C-0.00125s^{-1}	400°C-0.0125s^{-1}	400°C-0.00125s^{-1}
ZC	•	•	•	•
ZY	•	•	•	•
YS	•	•	•	•
YP	•	•	•	•
ZYC	•		•	
ZYS	•		•	
SY1P	•		•	
SY2P	•		•	
ZYP	•		•	
ZSYC	•		•	
ZCY1P	•		•	
ZCY2P	•		•	

Table 24 Experimental tensile tests performed.

As previously depicted in Figure 20 and Figure 21, thanks to the articulated experimental setup and the matching between the different outputs facilities was possible to reach all needed outputs coming from the experimental tests: Elongation to failure (εf), Yield stress (σy) and Ultimate Tensile Strength (UTS) according to the temperature.
Results for the Mg-based alloys with two alloying elements (ZY and ZC) are reported from Figure 49 to Figure 51.

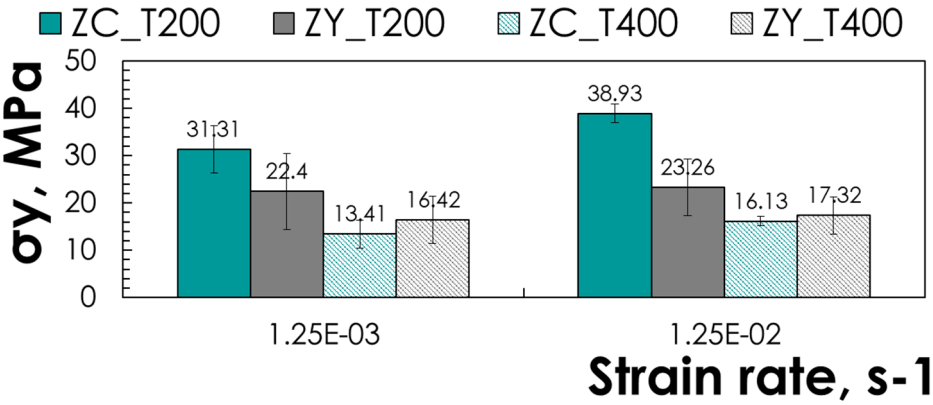

Figure 49 σy according to strain rate and temperature for Mg-based alloy with two alloying elements.

With regard to the ZY alloy, the value of the yield stress is not particularly affected both by the strain rate and by the temperature. More pronounced appear to be the effect of the temperature when the ZC alloy was considered: in fact, increasing the temperature from

200 to 400°C, a decrease in terms of σy equal to 57.2% and 58.6% for strain rate equal to respectively 0.00125s^{-1} and 0.0125s^{-1} was obtained.

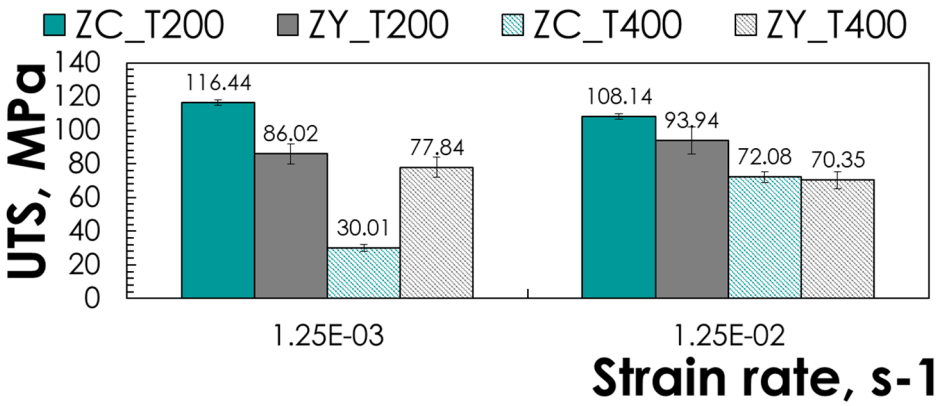

Figure 50 UTS according to strain rate and temperature for Mg-based alloy with two alloying elements.

On the contrary, related to the UTS, the only substantial effect registered can be associated with the strain rate for the ZC alloy: a marked increase equal to 42.07MPa occurs passing from 0.00125 to 0.0125s^{-1}.

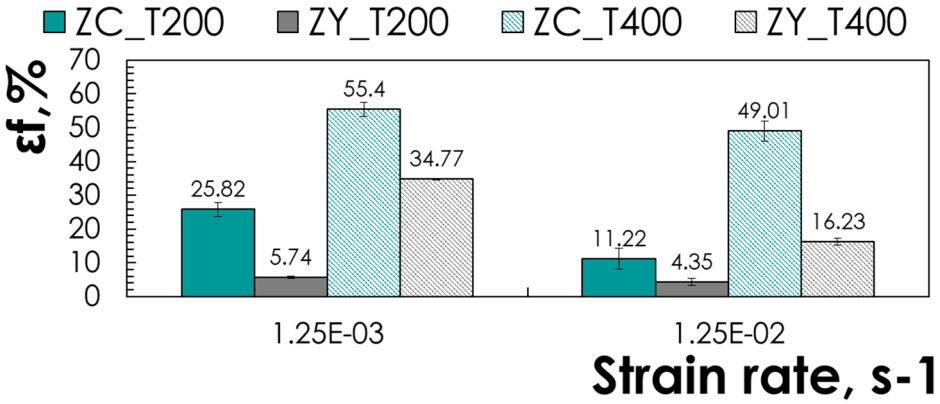

Figure 51 εf according to strain rate and temperature for Mg-based alloy with two alloying elements.

Considering both tests conducted at 200°C, marginal effects were recorded for the ZY alloy in terms of εf: in fact, low values of εf were obtained (5.74 and 4.35 respectively for 0.00125 to 0.0125s-1). Passing to 400°C, the effects of strain rate increasing causes, as expected, a significant reduction in terms of maximum elongation (from 34.77 to 16.23MPa) equal to 53.3%. Instead, very interesting appear to be the results obtained from the ZC Alloy: in all cases, high values of εf were obtained (from a minimum of 11.22 to a maximum equal 55.4). The best condition is attributable to the test performed at 400°C and 0.00125 totally in accordance with the expected deformation behavior due to a temperature increase coupled with a decreasing in the strain rate. Considering the results obtained through the tests carried out on the previous ternary alloys, all the remaining tensile tests for the alloys with

several (more than two) alloying elements were carried out by adopting the most favourable condition in terms of strain rate, analysing the only temperature effect.
Results for the quaternary alloys (ZYC, ZYS, SY1P and ZY1P) are reported in the graphs listed from Figure 52 to Figure 54.

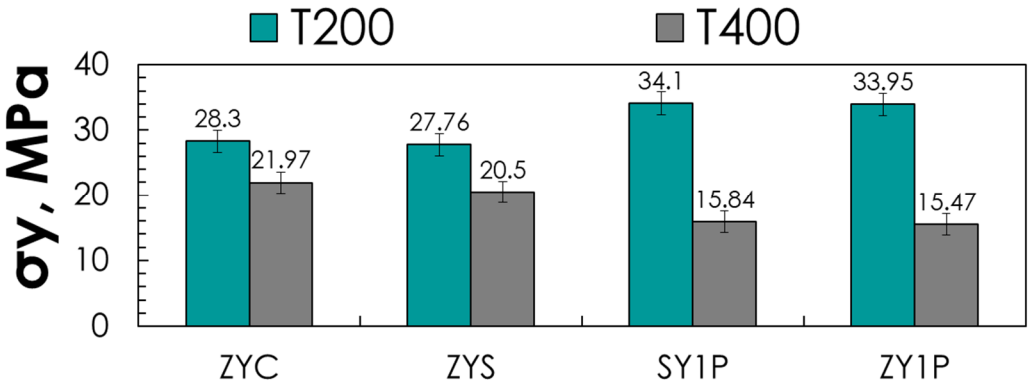

Figure 52 σy according to temperature for Mg-based alloy with three alloying elements.

In all the cases analysed, a reduction in the yield stress was found following an increase in temperature; this experimental evidence is particularly marked when the two alloys containing Yttrium and Lead (SY1P and ZY1P) are considered.

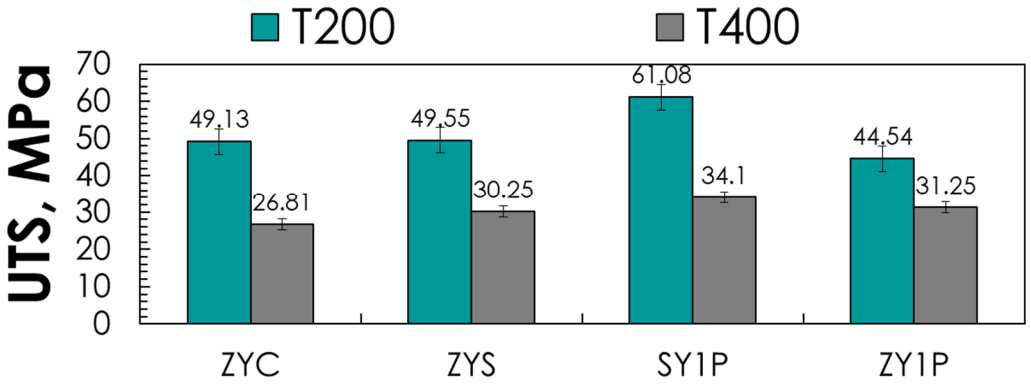

Figure 53 UTS according to temperature for Mg-based alloy with three alloying elements.

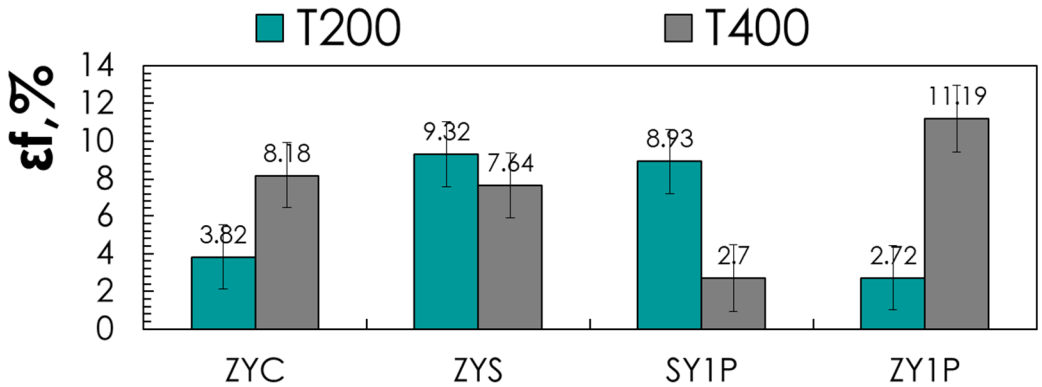

Figure 54 εf according to temperature for Mg-based alloy with three alloying elements.

Similar results can be associated with the UTS values according to a temperature increase from 200 to 400°C. In addition, it is possible to observe the much higher value for the SY1P alloy when a temperature of 200°C is considered.
Results for the Mg-based alloys with four or five alloying elements (ZCY1P and ZYSCP) are reported in the Figure 55 and Figure 56.
Analysis of σy for these two alloys showed a behaviour not dissimilar to each other: in fact, in both cases the difference between the two alloys is less than 1%. The UTS values are independent of temperature and, in any case, the highest ones refer to the ZYSCP alloy. Good elongations can be associated with the ZCY1P alloy (up to 20.18).

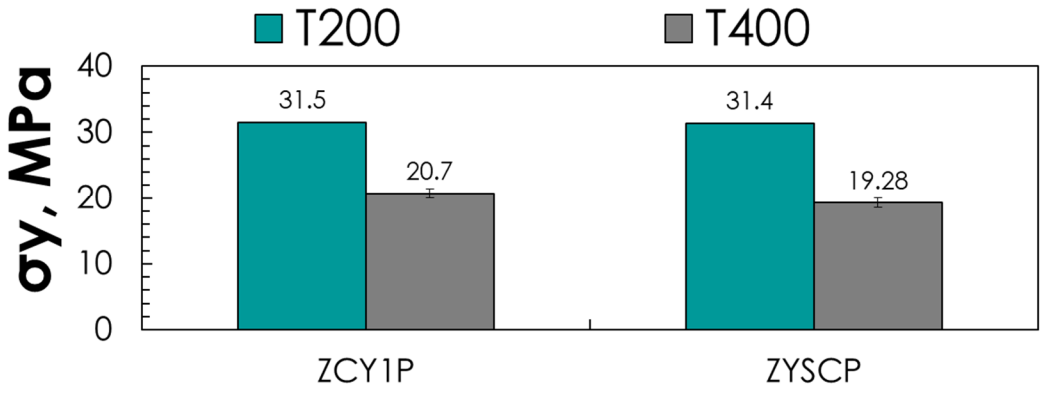

Figure 55 σy according to temperature for Mg-based alloy with three alloying elements.

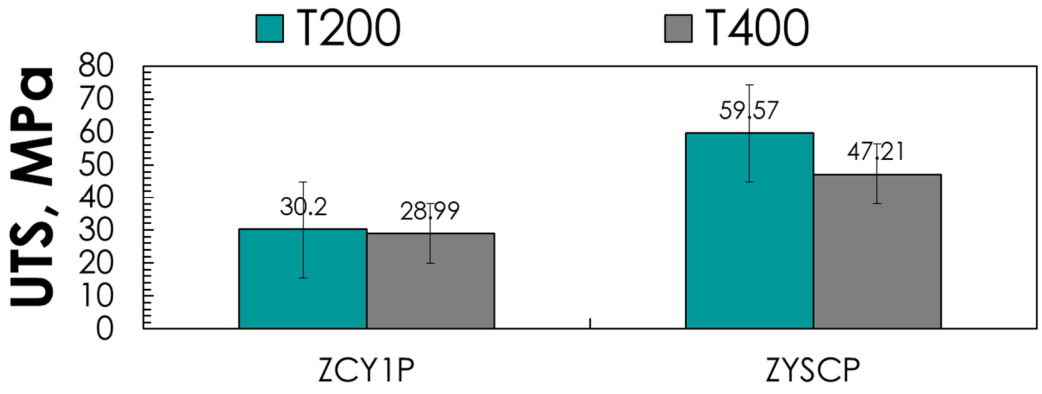

Figure 56 UTS change with temperature for Mg-based alloy with three alloying elements.

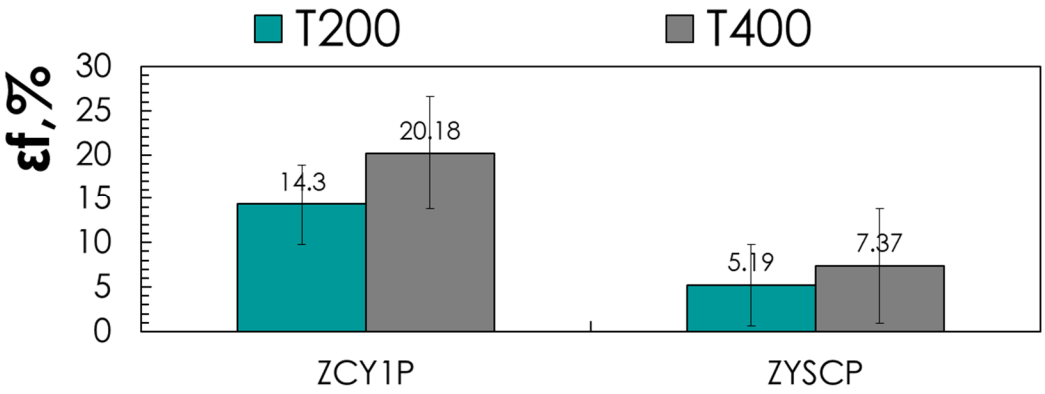

Figure 57 εf change with temperature for Mg-based alloy with three alloying elements.

Finally, results for the all alloys tested are reported in the following three figures (from Figure 58 to Figure 60).

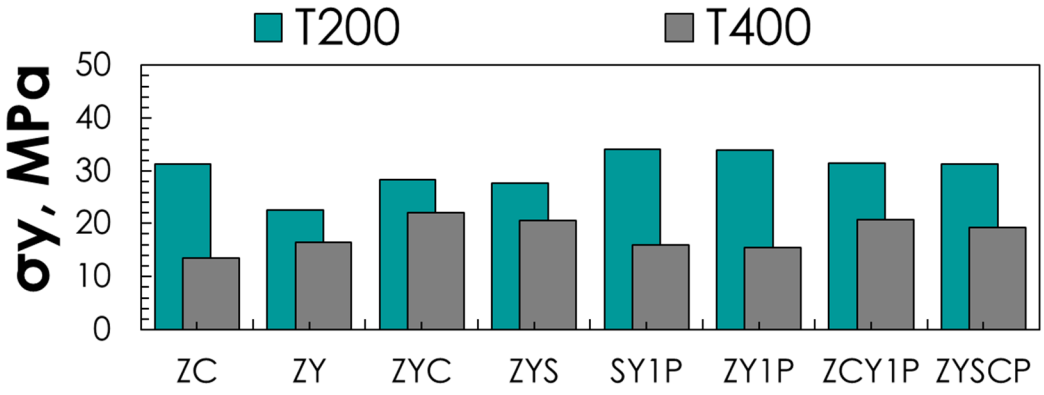

Figure 58 σy change with temperature for all Mg-based alloys investigated.

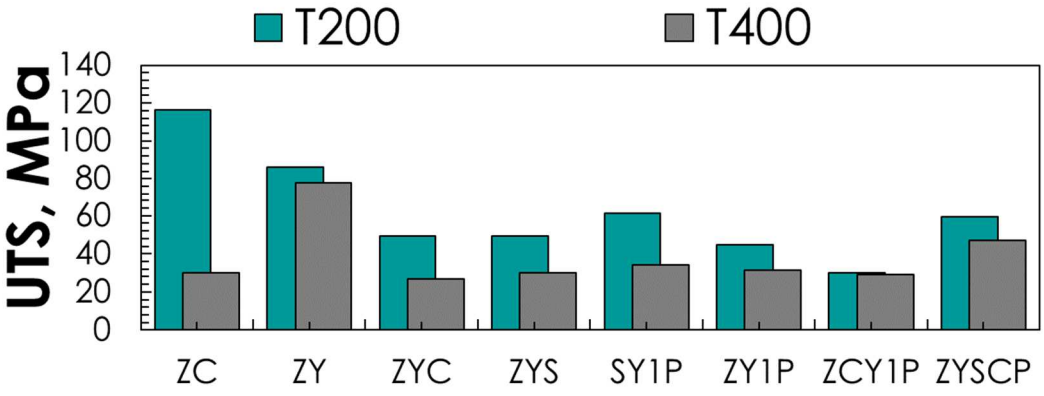

Figure 59 UTS change with temperature for all Mg-based alloys investigated.

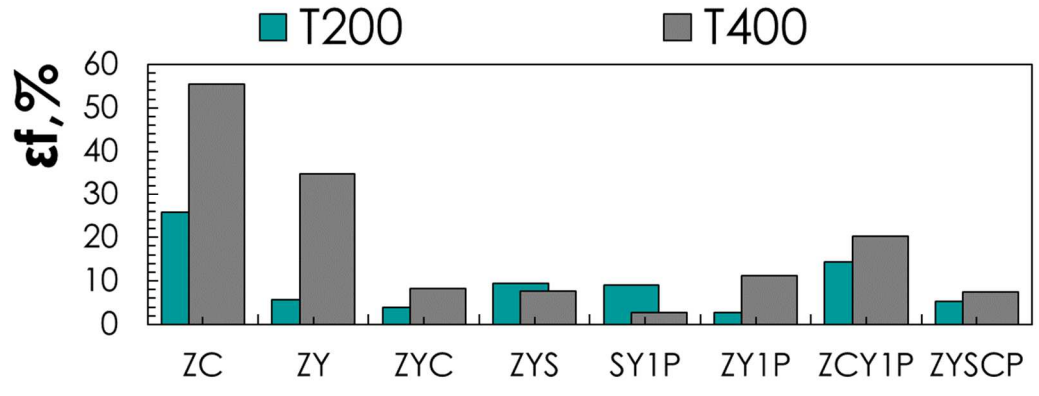

Figure 60 εf change with temperature for all Mg-based alloys investigated.

By observing all graphs reported, it is possible to assert that the best (in terms of mechanical property and deformation behaviour) Mg-based alloy manufactured is the ZC.
The results obtained according to temperature and strain rate for this alloy are listed in Table 25.

Temperature, °C	Strain rate, s-1	σy, MPa	UTS, MPa	εf
200	0.00125	31.3	116.4	25.8
200	0.0125	38.9	108.1	11.2
400	0.00125	13.4	30.0	55.4
400	0.0125	16.1	72.1	49.0

Table 25 Experimental results (UTS, σy and εf) obtained for the ZC Mg-based alloy.

3.4. Superplastic forming characterization via bulge tests results

In this section, experimental results coming from bulge tests in terms of both metallographic analyses and experimental tests output (dome height according to the forming time, thickness distribution and m value with respect to the different tests condition) are summarized. Methodology and experimental facilities used were discussed in section 2.2.2.3.

3.4.1. Microstructure analyses

A SEM micrograph of the as-cast structure of Mg-2Ce-2Zn alloy is given in Figure 61.

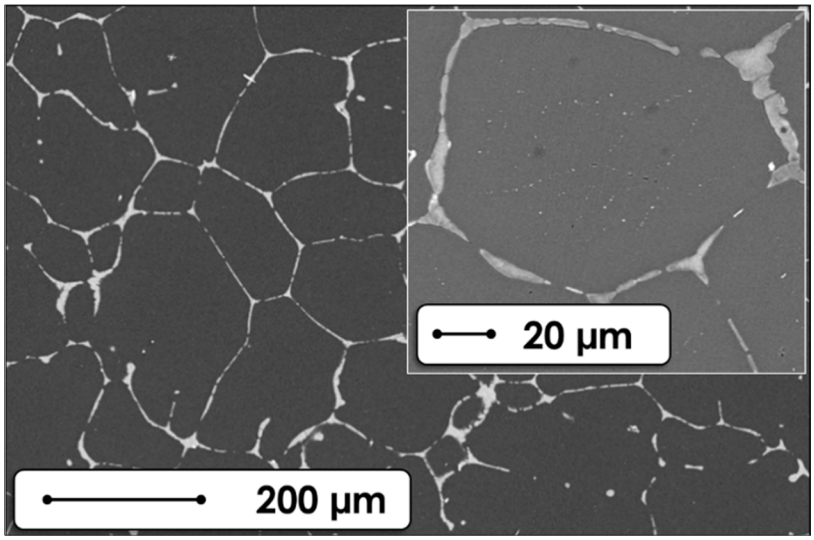

Figure 61 SEM micrograph of the as-cast structure. The inset shows presence of intra-granular fine precipitates.

It can be seen that Mg-2Zn-2Ce alloy has three types of secondary phases: the coarse type decorating the grain boundaries apparently is composed of two, grey and white contrast, phases. The grey contrast portions of the coarse precipitates at grain boundaries has an approximate stoichiometry of $Mg_{2.5}X_{0.5}$(Zn, Ce), and relatively the much finer type, the portions with white contrast, located inside the coarse precipitates has an average stoichiometry of $Mg_{1.5}X_{0.9}$(Zn, Ce).

The very fine precipitates with less than 1µm in size located within the interiors of the grains showed an approximate stoichiometry of Mg4X0.04(Zn, Ce) as determined by EDS analysis

given in Figure 62. Ling-Fei Hu et al., also reported such a coarse secondary phase in Mg-Ce-Zn-Zr system, albeit with a different stoichiometry, that is $(Mg, Zn)_{12}Ce$.

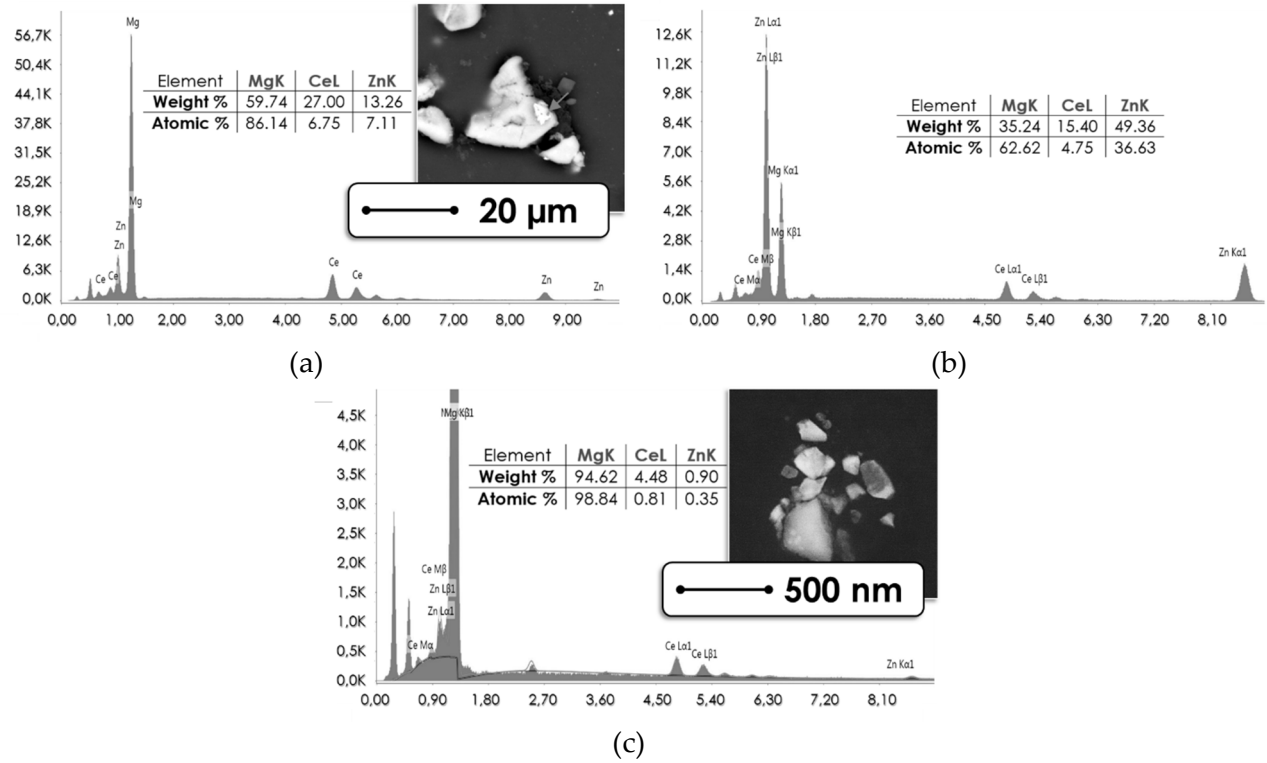

Figure 62 SEM-EDS microanalysis results from the precipitates at the grain boundaries: (a) coarse areas of grey contrast, and (b) finer areas of white contrast indicated with the arrow; (c) the fine precipitates located in the interiors of the grains in the as-cast structure.

The XRD spectra from the hot-rolled state and the as-cast structure have been given together in Figure 63, with possible peak positions of α-magnesium indicated. The changes in some of the peak heights have been interpreted as due to weak texture in the hot rolled state.

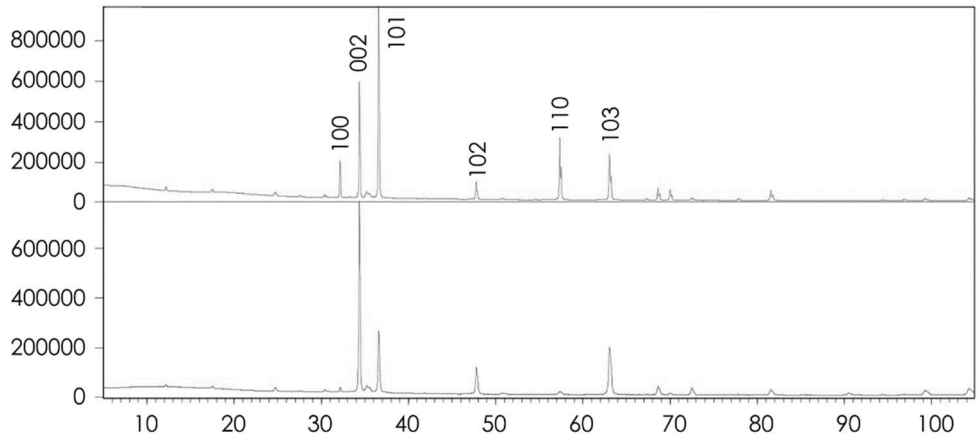

Figure 63 XRD spectra of (a) the as-cast, and (b) the hot-rolled structure.

It is worth noting that the stress states in bulge and rolling are different, the former corresponding to a more complex and multi axial stress states. Thus, the deductions made from hot rolled samples based on XRD data have been tentatively translated in this part of the research activity to the bulge samples in the following fashion: it may be possible to envisage relatively weaker texture and greater non-basal slip in bulge samples compared to those observed in hot rolled one due to multi-axial stress state in the former.

3.4.2. Evaluation of deformation behaviour

Evaluations of mechanical properties associated to microstructural aspects were carried out following two different test strategies: (i) bulge tests up to failure able to determine da maximum value of dome height according to different pressure and temperature conditions; (ii) interrupted tests to correlate strain value with microstructural evolution.

3.4.2.1.Bulge tests up to failure

As anticipated in the chapter 2 about the methodology adopted to perform experimental bulge tests, three different temperatures, 350°C, 400°C and 450°C, were adopted for the bulge tests up to failure, either using the CP and the JP methodology. The pressure levels were chosen in accord with temperature so that excessively low strain rates especially at lower temperatures were to be avoided. Thus, CP tests were conducted adopting the following pressure levels: 1.00 MPa, 1.25 MPa, 1.50 MPa and 1.85 MPa at 350°C; 0.50 MPa, 0.65 MPa, 0.75 MPa, 1.00 MPa and 1.25 MPa at 400°C; 0.20 MPa, 0.25 MPa, 0.35 MPa, 0.50 MPa and 0.65 MPa at 450°C.

	CP tests			JP tests		
Pressure, MPa	**350°C**	**400°C**	**450°C**	**350°C**	**400°C**	**450°C**
0.20			•			•
0.25			•			•
0.35			•			
0.50		•	•		•	
0.65		•	•		•	
0.75		•	•			
1.00	•	•		•		
1.25	•	•		•		
1.50	•					
1.85	•					

Table 26 Experimental bulge tests performed.

Since a large enough quantity of jumps must be performed during the JP test, JP tests were conducted choosing the two lowest pressures levels for each temperature: 1.00 MPa, 1.25 MPa, at 350°C; 0.50 MPa, 0.65 MPa, at 400°C; 0.20 MPa, 0.25 MPa at 450°C.

In order to have large enough durations, JP tests were conducted changing the pressure alternatively every 100s. All bulge tests performed are summarized in the experimental plan scheme purposed in Table 26.
Three replications were performed for each test condition; for each temperature and pressure level, the following outputs were evaluated: (i) the maximum dome height, (ii) the thickness profiles along the radial path of the formed samples and (iii) the m-value.
As concerning to m-value, two different approaches were adopted: for CP tests, m-value was calculated using the Enikeev and Kruglov formulation (equation 6 in chapter 2). For JP tests, on the contrary, formulation proposed by Sorgente et al. was used [82]:

$$m = \ln\left(\frac{p_2}{p_1}\right) / \ln\left(\frac{\dot{h}_2}{\dot{h}_1}\right) \qquad \text{Equation 17}$$

where the subscript refers to one of two pressure levels adopted ("1" for the low gas pressure level and "2" for the high level); $\dot{h}_1$ and $\dot{h}_2$ are the derivatives with respect to time of dome height at a fixed level of pressure.
By applying the first equation, for each temperature level investigated, the m-value was calculated using data from the tests conducted at the two lowest pressure levels.
Results from CP tests have been resumed in the next three figures (from Figure 64 to Figure 66) in terms of dome height evolutions (the tests were stopped when the rupture occurred). It should be noted that the DH at which the sample failed increases when increasing the temperature and decreasing the pressure.
For example, the dome height at failure increased up to 100% when the temperature was increased from 350 to 450°C and the pressure was reduced from 1.85 to 0.20MPa.

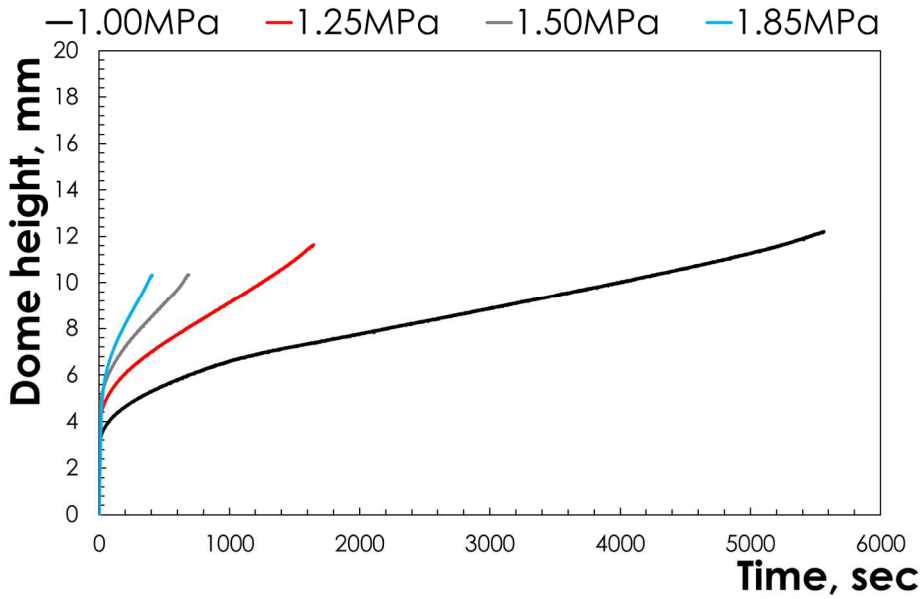

Figure 64 Dome height vs time curves for CP tests at 350°C.

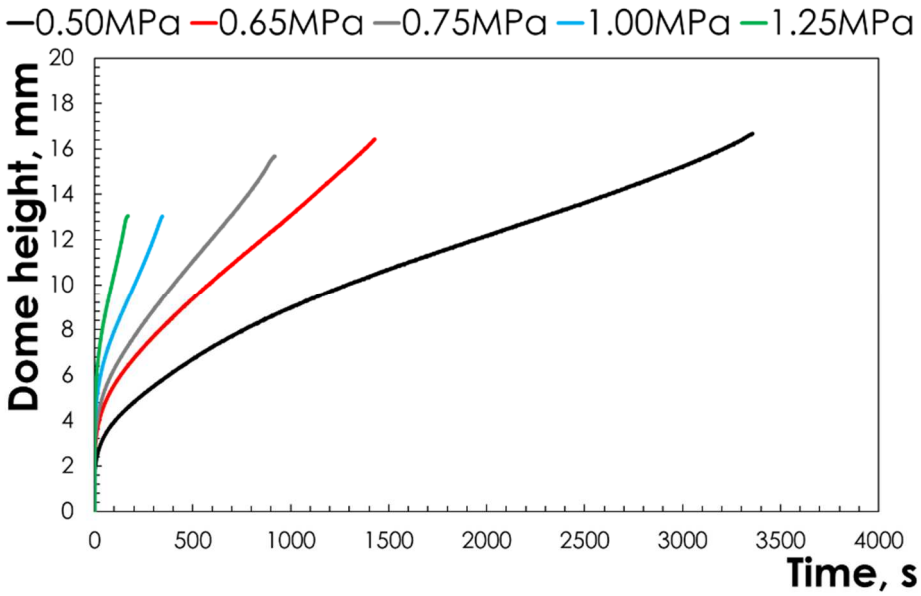

Figure 65 Dome height vs time curves for CP tests at 400°C.

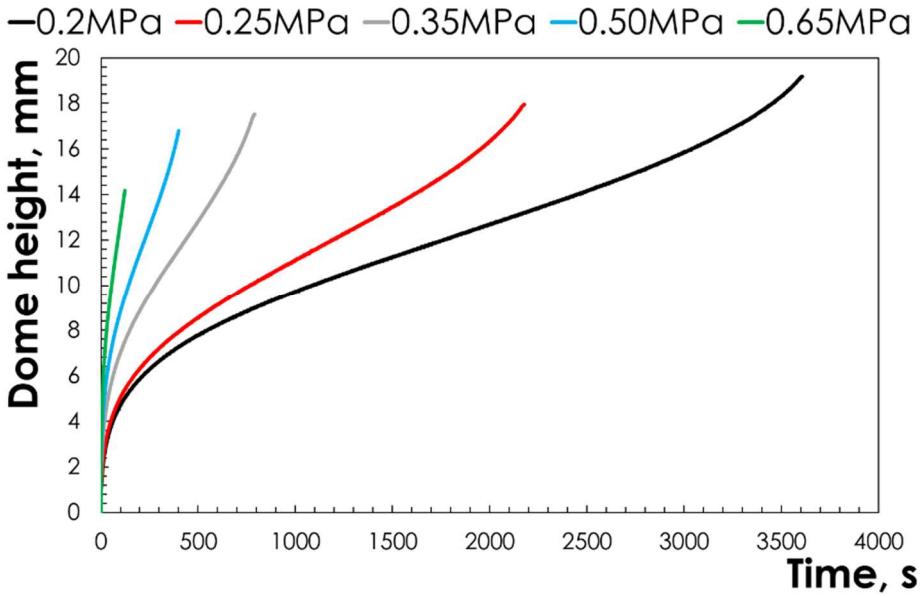

Figure 66 Dome height vs time curves for CP tests at 450°C.

Figure 67 shows a typical dome-shaped free-inflation test sample possessing a characteristic "orange peel" surface for all the test temperatures.

It should be noted that the DH at which the sample failed increases when increasing the temperature and decreasing the pressure.

For example, the dome height at failure increased up to 100% when the temperature was increased from 350 to 450°C and the pressure was reduced from 1.85 to 0.20MPa.

The typical failure mode in free-inflation tests were punctures at locations of coarse inclusions or pores formed due to cracking of the coarse secondary phase and concomitant pressure drop.

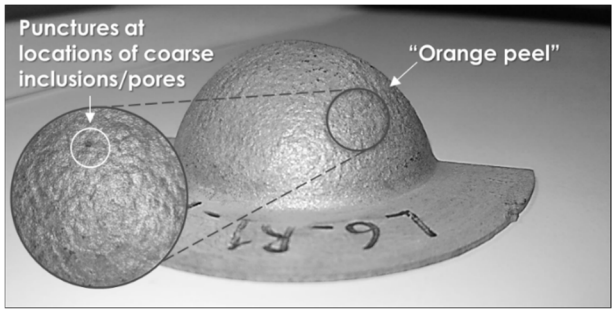

Figure 67 Photomicrograph showing the external surface of a dome with orange peel appearance and failures at punctures.

Results in terms of m-value coming from CP tests are summarized in Figure 68.

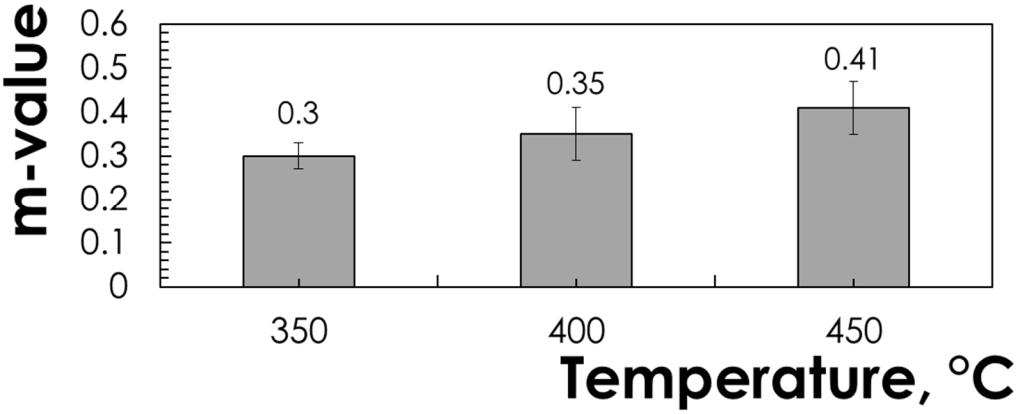

Figure 68 m-value obtained from CP-tests.

It is evident that an increase in temperature allows to obtain increasing sensitivity index values (from 0.3 to 0.41). These results also show a tendency of the Mg-2Ce-2Zn alloy to exhibit superplastic behaviour, when high temperatures and low strain rate (gas pressure) values were adopted.

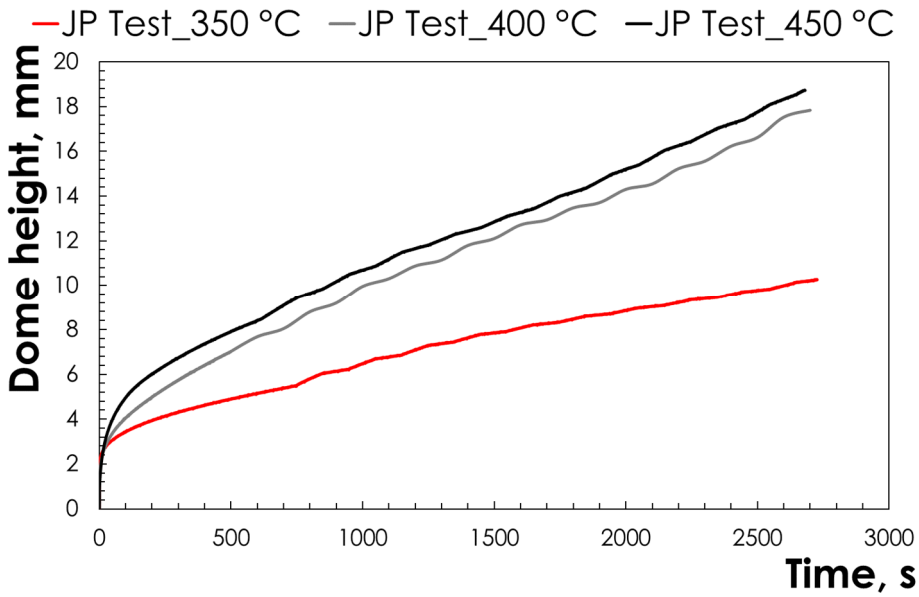

Figure 69 Dome height vs time curves for CP tests at 450°C.

The dome evolutions concerning JP tests have been plotted in Figure 69: the jumps between the two pressure levels are clearly visible; in addition, it can be seen that the maximum dome height was obtained at 450°C.
The temperature improvement from 350 to 400°C causes a marked increase of the dome height according to the time; in addition, the difference between these two curves is much more pronounced than the one obtained passing from 400 to 450°C.
For JP tests, the m-value was determined using eq. 2 at each jump. A graph showing the evolution of the strain rate sensitivity index versus time has been given from Figure 70 to Figure 72. In the same figures, the m-values at each temperature (obtained averaging all values but excluding the first and the last pressure jump, i.e. the ones immediately after the initial pressure application and the ones just before the rupture) have also been shown with the dashed green line.

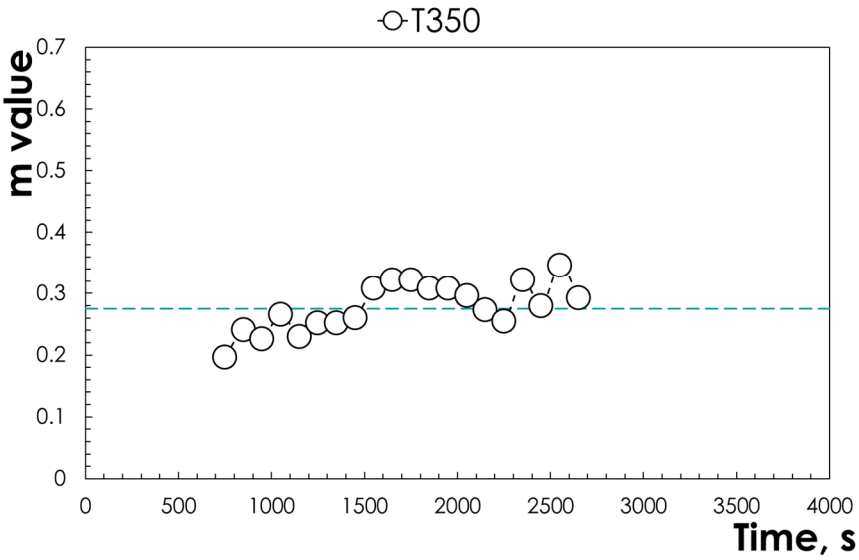

Figure 70 m-value at each jump for the tests conducted at 350°C.

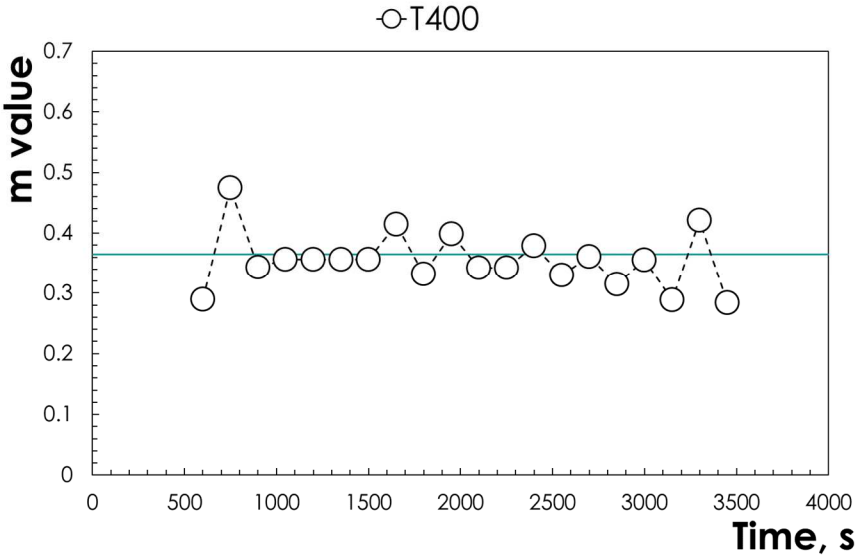

Figure 71 m-value at each jump for the tests conducted at 400°C.

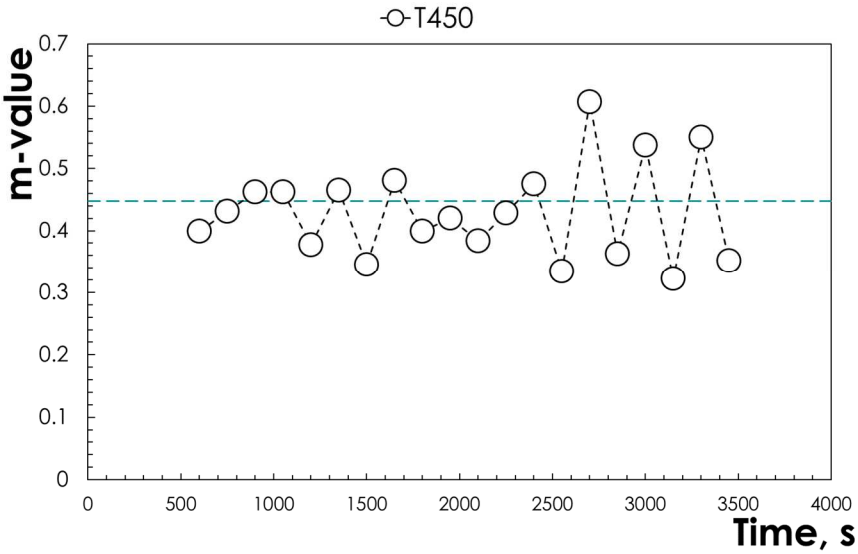

Figure 72 m-value at each jump for the tests conducted at 450°C.

In any case, results in terms of m-value according to temperature and coming from JP tests are summarized in Figure 73. Experimental results in terms of m-value obtained from JP-tests confirm what was already predicted by the CP-tests. In fact, going from 300 to 400°C, the obtained value increases considerably. It is worth noting that the standard deviations are quite low.

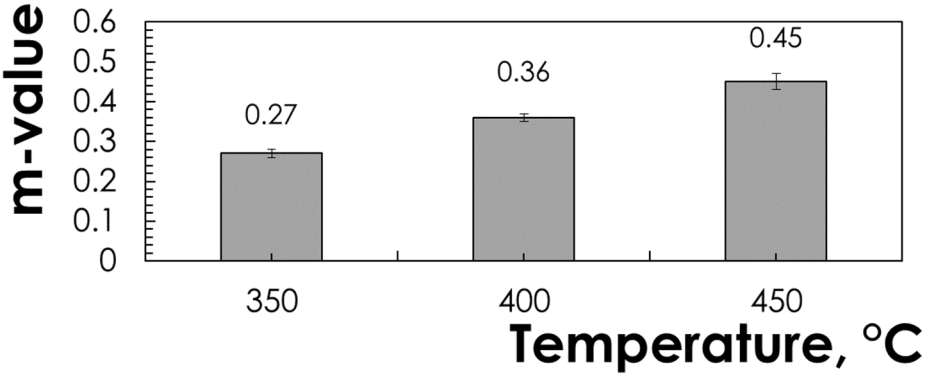

Figure 73 m-value obtained from JP-tests.

From the comparison (Table 27) of m-values calculated using the two approaches (CP tests and JP tests) it can be noted that: (i) irrespective of the adopted methodology, the values are very similar; (ii) with respect to temperature m-values appear to increase with a linear trend (R^2 = 99.96 % for m-values from CP tests; R^2 = 99.94 % from JP tests).

Temperature, °C	m-value from CP-tests	m-value from JP-tests
350	0.30±0.03	0.27±0.03
400	0.35±0.06	0.36±0.01
450	0.41±0.06	0.45±0.02

Table 27 m-value (obtained with the two methodologies) comparison.

The experimental conditions (temperature and gas pressure) able to determine the highest m-value obtained are very close to those measured on a commercial Mg alloy (AZ31B-H24) as demonstrated by Palumbo et al. [83].
In this work, the authors investigated the m-value of the commercial AZ31B-H24 Mg alloy under typical superplastic condition by means of bulge tests at 410, 460 and 520°C with different gas pressure levels (from 0.3 to 0.8MPa with a step equal to 0.1).
The highest m-values were found both for the low-pressure levels (between 0.2 and 0.3 MPa) at the highest temperatures investigated (460 and 520°C). In fact, by calculating the mean m- value on the same pressure levels and at various test temperatures, this alloy exhibits the greater mean value of m at 460°C, certifying what was achieved in the present research activity regarding the new Mg ternary alloy.
Therefore, the results obtained indicating the good suitability of the Mg-based alloy as proposed in the present research activities.
In addition, these results are even more important considering that the samples tested were obtained by casting process (instead of a rolling product).
It can reasonably be suggested that with the same alloy composition a material free from casting defects, e.g. an extrusion product, would give an even better value.

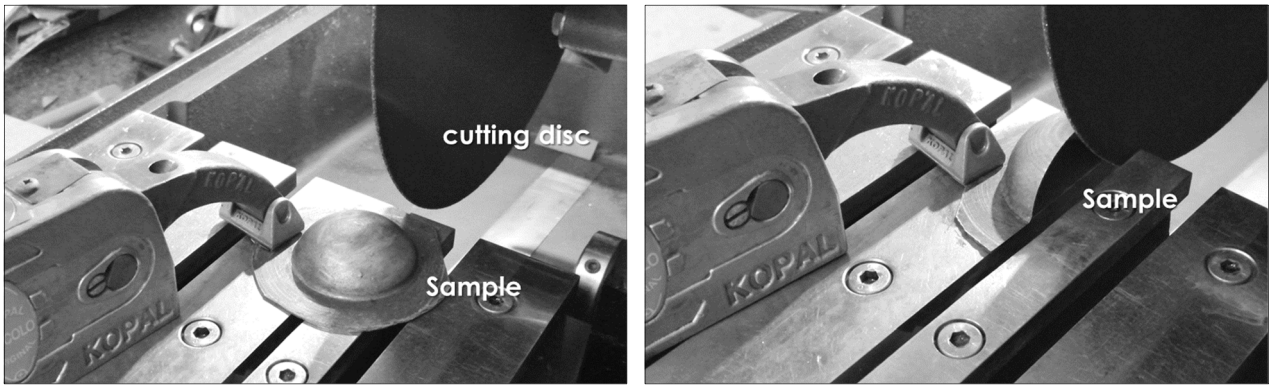

(a) (b)

Figure 74 Procedure aimed to the radial thickness measurements: (a) Before and (b) After cutting.

Referred to CP-tests, in order to determine both strain rate (according to the pressure level used during the tests) and thickness distribution along the radial direction of the tested samples, additional analyses were performed.
The thickness values were measured along the dome radial cross path of each formed sample. Specifically, the samples were cut along the abovementioned direction (as depicted in the next Figure 74) and polished to avoid any burrs that could compromise the subsequent measurement by means of calibre.
For all test conditions the minimum thickness was obviously located at the dome apex, where the material experiences a biaxial stretching state.
Therefore, the equivalent strain at the dome apex could be easily calculated using the thickness measurements (as the natural logarithm of the ratio between the initial thickness and the one measured at the dome).
In Figure 75, the maximum equivalent strain at the dome of the samples tested using the CP methodology has been plotted as a function of pressure and for all temperature levels.

It can be noted that the strain linearly decreases when increasing the pressure; on the other hand, the trend is reversed when the temperature effect is considered.

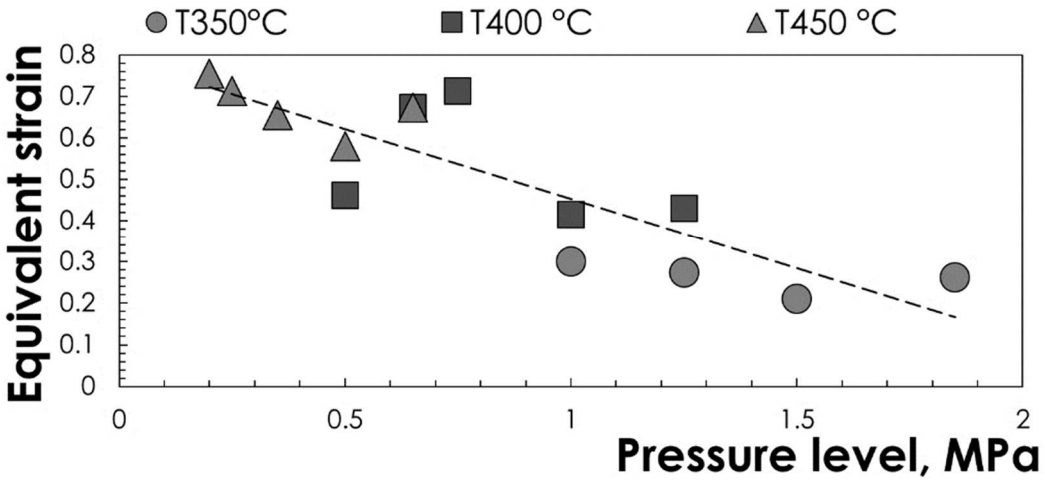

Figure 75 Equivalent strain at the dome apex according to temperature and pressure for CP method.

Finally, the thickness distributions along the radial path of the samples from the tests performed at all temperature levels employing different pressure values are shown from Figure 76 to Figure 78.

It should be noted that the lower the pressure, the higher strain (Figure 75) achieved. It is also worthy of notice that, when decreasing the forming pressure, a greater thinning is observed along the deformed sheet (Figure 76). This is consistent with the greater dome height achieved in the sheet formed at the lowest pressure values.

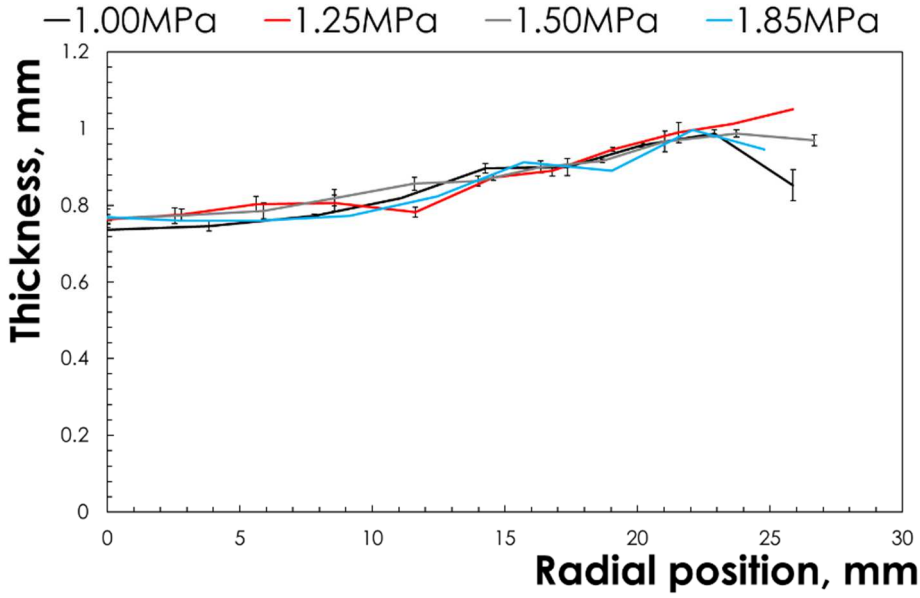

Figure 76 Thickness variations along the dome radial cross-sections for CP method at 350°C.

The difference between the tests performed at 350°C, if compared with those obtained at the other two temperatures investigated, are less evident. With reference to the tests at 400 and

450°C, the effect of the gas pressure appears to be much more marked: as the pressure increases, a lower thinning is recorded contrary to the lower equivalent strain obtained, as previously observed in Figure 75).

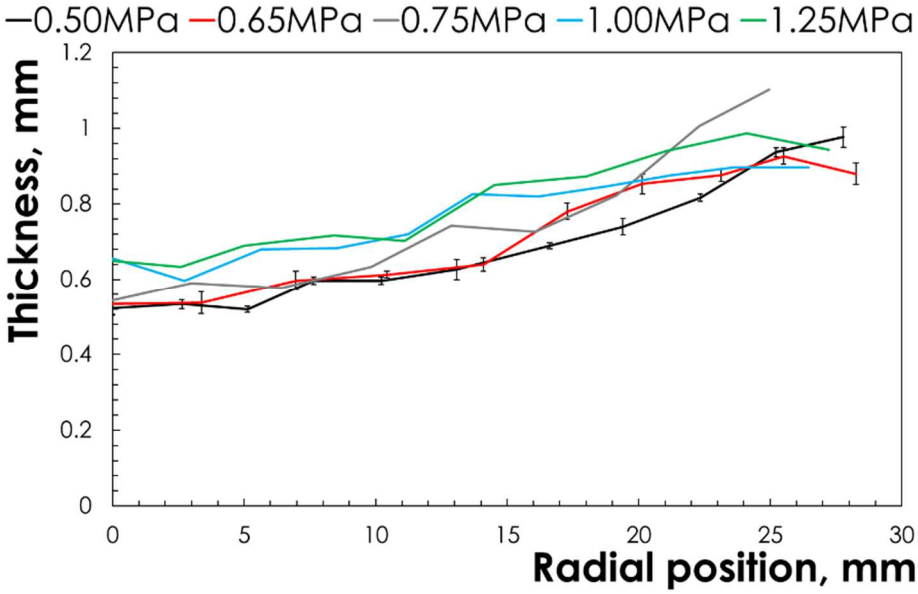

Figure 77 Thickness variations along the dome radial cross-sections for CP method at 400°C.

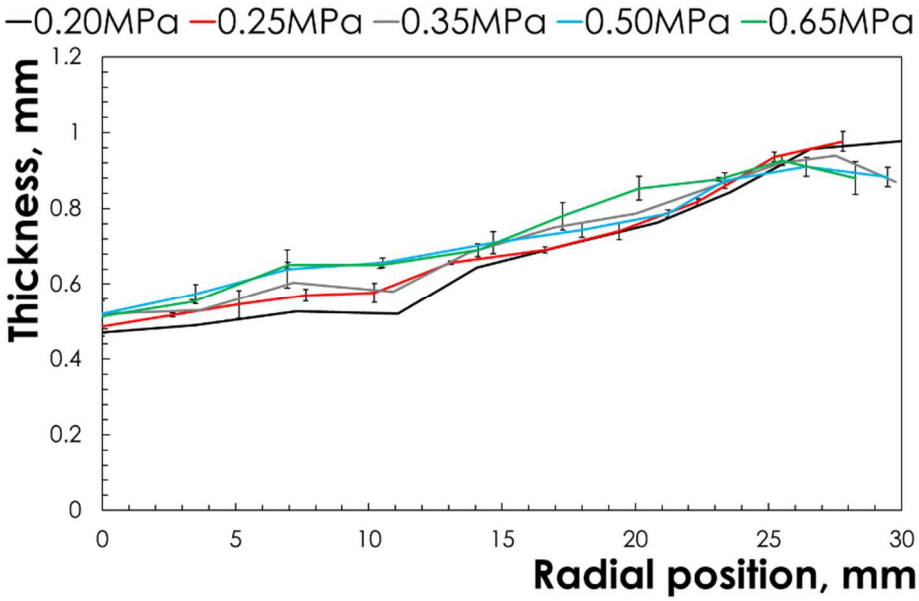

Figure 78 Thickness variations along the dome radial cross-sections for CP method at 450°C.

In addition, a greater uniformity in the thickness distribution was found, especially in the region close to the dome apex, in the specimen deformed with the lowest pressure value. This behaviour could be related to the effect of the strain rate on the m-value and, consequently, on the capability of the material to exhibit a diffuse necking and a higher ductility. Thus, it can be speculated that, at specific temperature of 400 and 450°C, the material has the highest m-value at the lowest strain rate values explored.

3.4.2.2. Interrupted bulge tests

Considering the results deriving from the previous analysis of thicknesses, the attention was focused on the two highest levels of temperature investigated (400 and 450°C). Interrupted CP-tests were used to determine the thickness distribution and to observe the evolution of the microstructure at different strain levels. They were conducted up to intermediate levels of the dome height at rupture (40, 65 and 90%) and setting two different process conditions (temperature/gas pressure): 400°C/0.75MPa and 450°C/0.5 MPa.

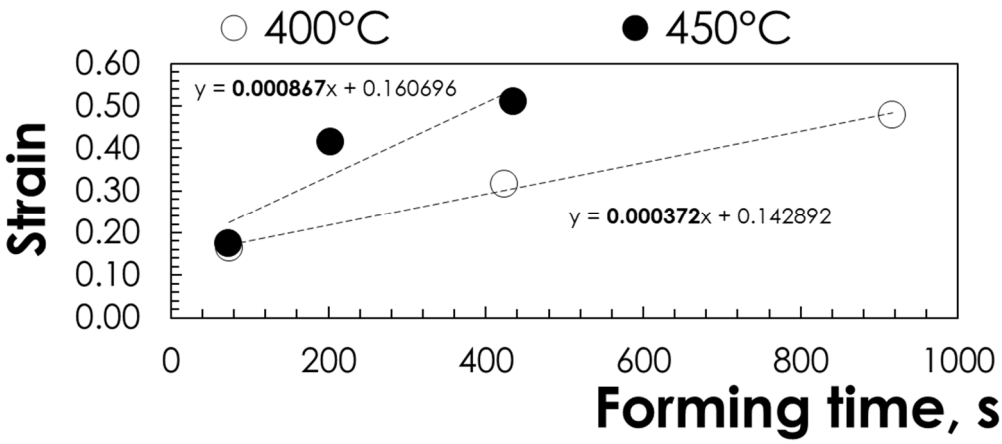

Figure 79 Strain measured in correspondence of the dome apex and according to the forming time for the three different values of dome height at 400 and 450°C.

As depicted in Figure 79, the strain evolution as a function of the forming time reveals the trend according to which the deformation level increases during the test: the strain rate values in the tests conducted setting the two temperature levels (400 and 450°C) were thus assumed as the slope of the linear trend (3.72E-04 and 8.67E-04s^{-1}, respectively).

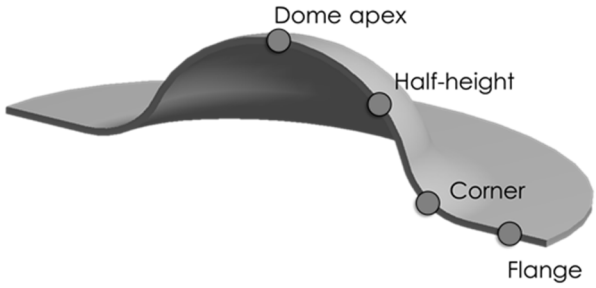

Figure 80 Scheme of the analysed points.

The microstructural evolution at three different deformation steps were followed at four different locations (as outlined in Figure 80) of the cross sections labelled as dome apex, flange (clamped region), half-height (the section between these two), and corner (where the material starts bulging during the tests (from Figure 81 to Figure 84).

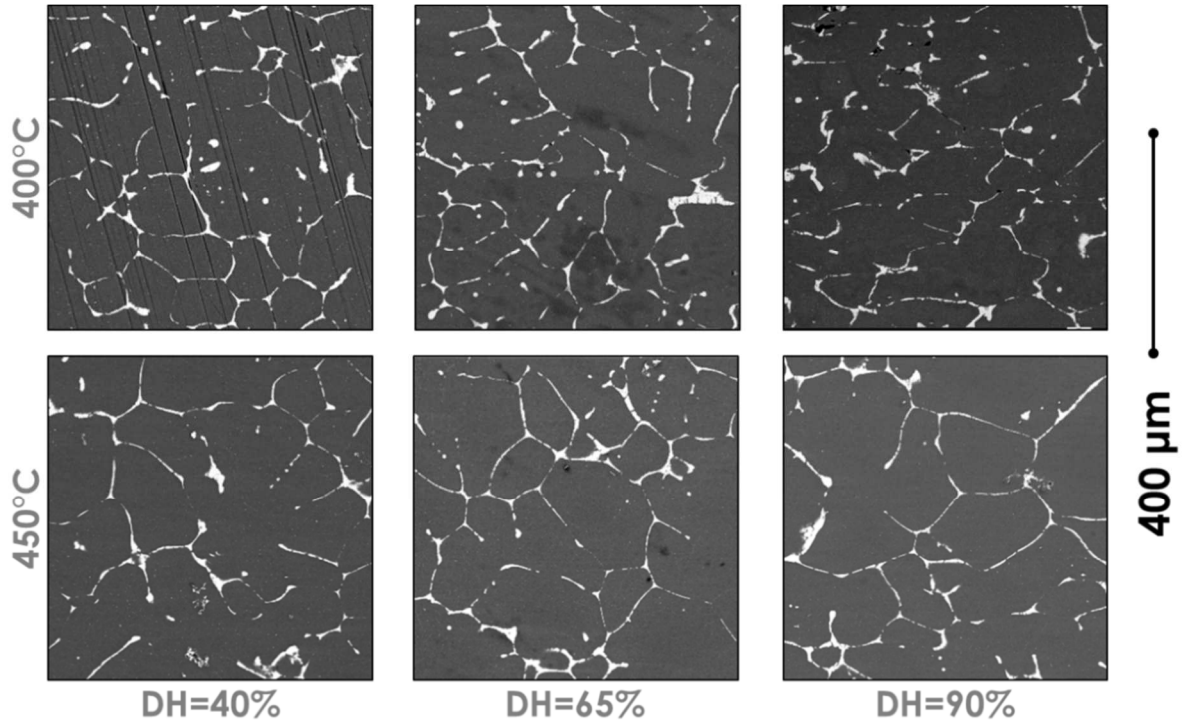

Figure 81 Micrographs concerning the region of the flange extracted from the samples tested at 400°C/0.75MPa and 450°C/0.5MPa up to different dome height (scale bar shown in the right).

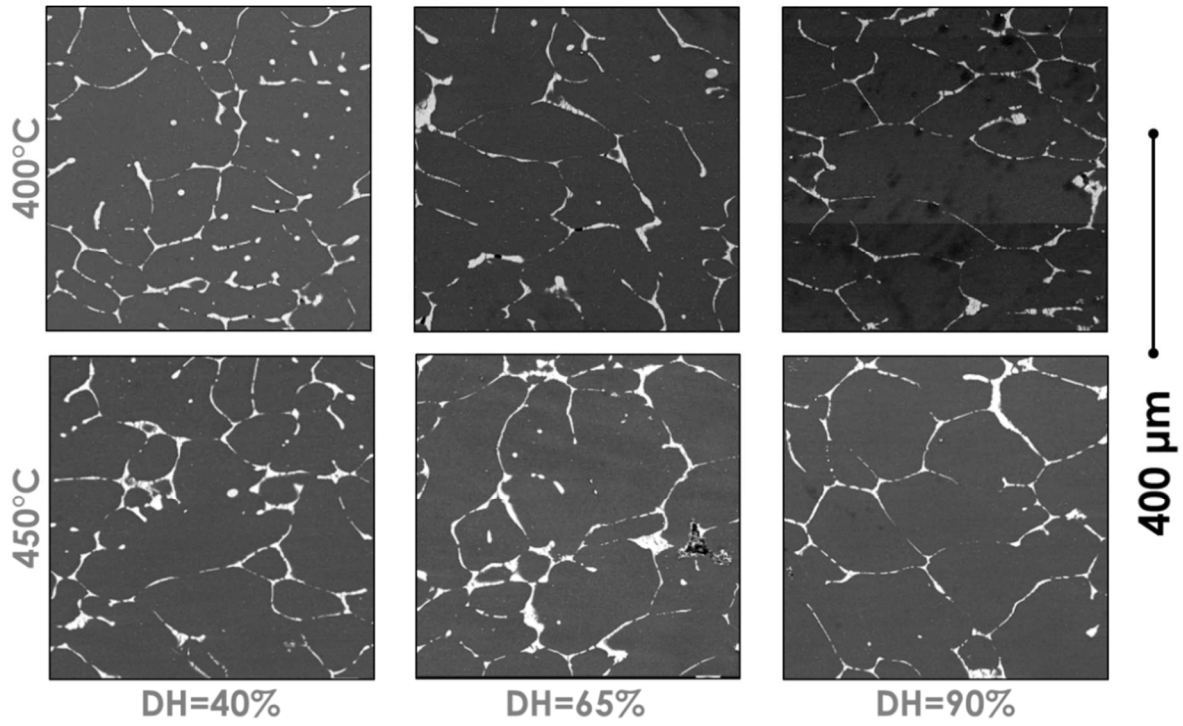

Figure 82 Micrographs concerning the region of the corner extracted from the samples tested at 400°C/0.75MPa and 450°C/0.5MPa up to different dome height (scale bar shown in the right).

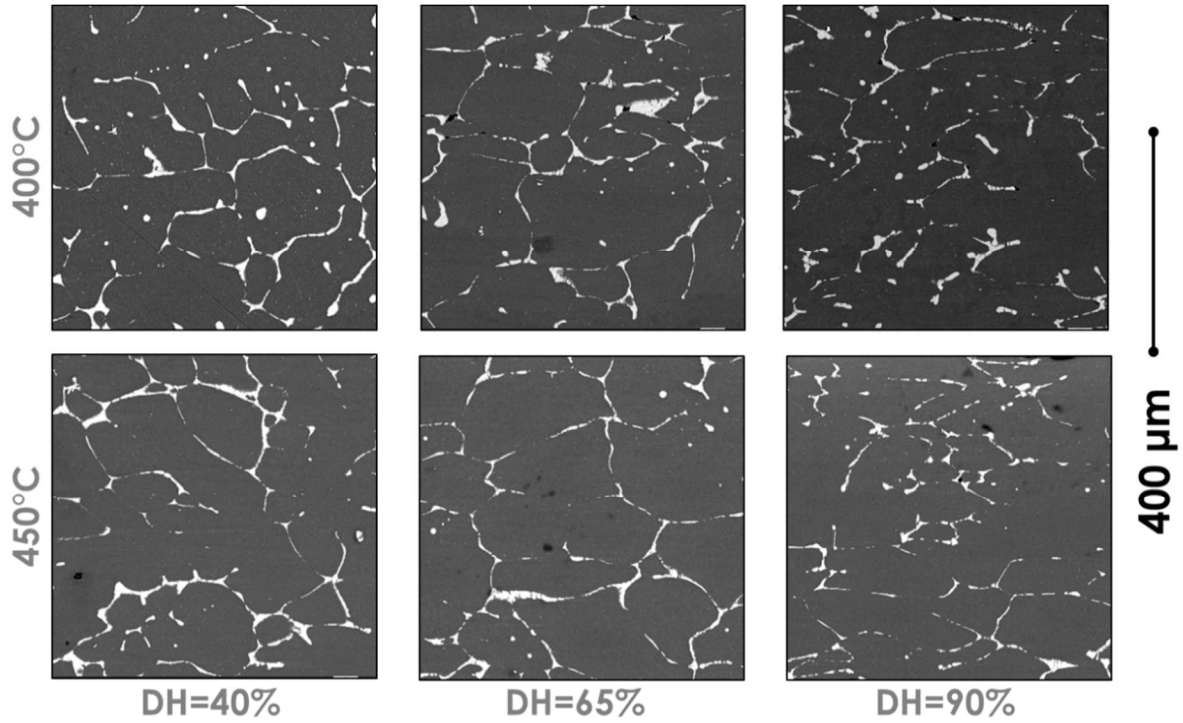

Figure 83 Micrographs concerning the region of the half-region extracted from the samples tested at 400°C/0.75MPa and 450°C/0.5MPa up to different dome height (scale bar shown in the right).

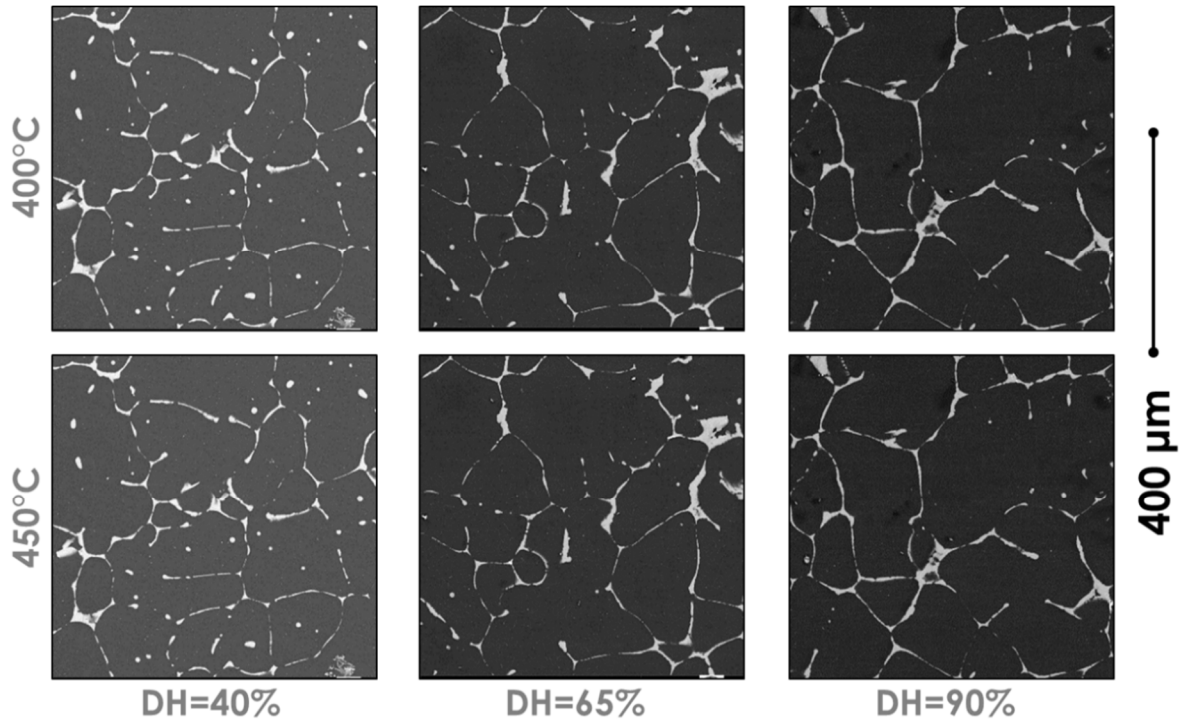

Figure 84 Micrographs concerning the region of the dome apex extracted from the samples tested at 400°C/0.75MPa and 450°C/0.5MPa up to different dome height (scale bar shown in the right).

The flange region was assumed to represent the original material where only small strains (due to the clamping force) occurred. The corner is a location where probably the most complex stress state prevails. The half-height of the dome and the dome apex are regions

where the material was subjected to gradually increasing strain levels, reaching the maximum at the apex. For each temperature investigated, it was observed that the secondary phase, $Mg_2X(Zn,Ce)$ decorating the grain boundaries in an almost continuous fashion, appeared to have fragmented during inflation. As evident in the SEM micrographs given in Figure 84, this phenomenon was much more pronounced at the apex region where greater deformation occurred, and was present even in the $Mg_4X(Zn,Ce)$ type intra-granular small precipitates. The brittle nature of this second phase was already apparent in the SEM micrograph of the as-cast structure given in Figure 61 as metallographic preparation introduced some cracking in the coarse grain boundary phase. In many areas between the fragments of this phase cavities (pores) were observed to have formed between the fragments of what was previously a single particle (Figure 85a).

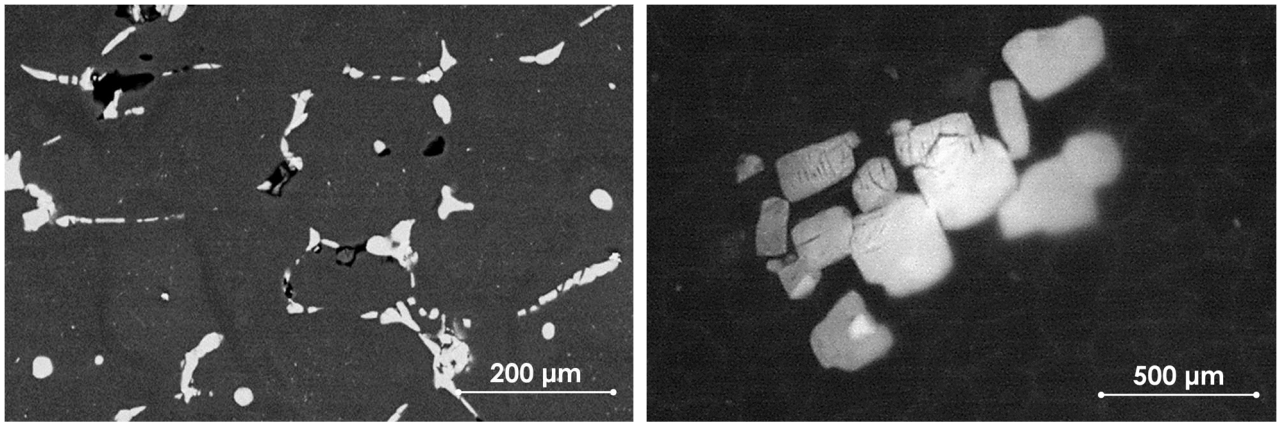

(a) (b)

Figure 85 SEM micrographs of the dome apex zones: (a) cavities generated between the fragments of the grain boundary second phase particles at 450°C and (b)fragmentation of the intergranular fine precipitates.

Twinning was not observed in any of the bulge or rolling samples. Moreover, considering different deformation temperatures employed, there was no discernible grain size change in any of the samples as compared to the initial as-cast state. It should also be noticed that the grains appeared to show little or no elongation, except for the apex region, in the direction of increasing deformation levels from flange to the dome apex.

3.5. Discussion

The manufacturing process of the Mg-based alloys was based on the literature and aimed to emphasize the deformation behavior of these alloys. The employed alloying elements, namely Rare Earths, Yttrium, Cerium and Zinc, proved to be correct for the purposes of this research activity [1-12].

The starting Mg alloys manufactured were tested by means of both tensile and Brinell Hardness tests in order to understand which was the most performing (in terms of mechanical and deformation properties) among all those produced. For this reason, a first screening of the batch analysed was performed by Brinell Hardness tests. Results allowed to reduce the total number of Mg alloy from the initial thirteen to eight. The latter, therefore,

were subjected to tensile tests at high temperatures (200 and 400°C).
Analysis of the results after these tests allowed to identify the ternary Mg-2Y-2Ce alloy as the most promising one for superplastic applications. In fact, the abovementioned Mg alloy is characterized by the highest deformation value obtained (55.4%) for a strain rate equal to $0.00125s^{-1}$ and a temperature equal to 400°C; the only Mg alloy comparable with the previous was the other ternary (Mg-2Zn-2Y) characterized by a maximum elongation to failure of 34.8% in the same test conditions. For the remaining Mg alloys the maximum recorded value was equal or less than 20%.
Therefore, the subsequent experimental characterization in the superplastic field was carried out exclusively on the ternary Mg-2Y-2Ce alloy.
In fact, this new ternary alloy showed interesting features. Despite the fragmentation of the coarse second phase particles located at grain boundaries, formation of cavities between those fragments and lack of twinning, the good deformation capacity in as-cast condition and the high m-value are issues that need to be addressed. All tests were terminated due to point-like punctures rather than tearing, most probably on oxide inclusions or expansion of the pores formed between the fragmented coarse second phase particles located along the grain boundaries.
Mg-Zn-Ce system was also studied by Mackenzie and Pekguleryuz [86]. Despite the compositional similarity of their material with the one used in the present research activity; they made no reference to the presence of secondary phase(s). They reported weakened and non-basal texture components revealed by EBSD. Contrary to our observations, they also claimed twins based on some light microscopy images obtained after deformation at 400°C. However, twins in the images given in that report are not discernible at all, casting doubt on the claim in terms of their existence. On the other hand, their report supports our findings in terms of a weak texture.
The texture behaviour of the composition studied may be assessed indirectly in this part of the research activity based on the XRD peaks of the α-magnesium matrix from the hot rolled sample (Figure 63). Having said that, it can be readily noticed that the peak heights appeared to have changed when spectra of the as-cast and the hot rolled samples are compared. For instance, the relative intensities of the (002) and (101) peaks reversed, while (002), (102) and (004) counts increased, the intensities of (100), (101) and (110) planes drastically reduced in the hot-rolled state.
Considerable increase in the intensity of the (002) basal plane can be taken as a strong indication for existence of a basal texture to some degree. Corresponding decrease in the intensities of especially (100) and (110) planes that make 90^0 with the basal planes further confirms the crystal orientations in general, indicating that the basal planes are aligned in the rolling direction and parallel to the sample surface describing texture. On the other hand, the dramatic decreases in the intensity of (101) pyramidal and (110) prismatic planes by about 80% and over 90%, respectively, seem difficult to explain with the increase in the intensity of (002) basal plane by only about 30%.
Even though evolution of this basal texture can account for some of the decrease in the intensity of (101) plane, a strong contribution due to accumulation of dislocations on these pyramidal and prismatic planes, thus bending of the crystal and taking these planes out of

diffracting condition, can also be envisaged. Therefore, non-basal dislocation mechanisms can reasonably be assumed to have operated as supported by others in the literature [16]. The observed deformation capacity of this alloy in free-inflation tests, despite the absence of twinning, can also be taken to testify for this suggestion.

Admittedly, the stress states in bulge and rolling are different, the former corresponding to a more complex and multi axial stress states. Thus, the deductions made from hot rolled samples based on XRD data may be tentatively translated to the bulge samples in the following fashion: It may be possible to envisage relatively weaker texture and greater non-basal slip in bulge samples compared to those observed in hot rolled ones.

The deformation capacity observed in the bulge tests apparently has some contribution from GBS mechanism as well. The high m-value also can be taken as a strong indication of this proposal.

However, further support can be found upon a close examination of the fragmented grain boundary precipitates as well. Cavities located between the fragments and the close morphological fitting of the fragment facets with some degree of rotations strongly suggested that the neighbouring matrix grains had made relative movements during free-inflation tests. Furthermore, the grain morphologies showed very little elongations except for the dome apex, where the maximum deformation took place. Considering also the absence of twinning, should the GBS was negligible as a deformation mechanism, prominent elongations in the grains would have been inevitable. In a parallel line of thinking, lack of readily noticeable grain elongations rules out bulk diffusion (viscous flow) as yet another deformation mechanism given the test conditions employed.

The high m-value of the experimental Mg-2Ce-2Zn alloy may be attributed to the short-range interactions of dislocations with the relatively larger size of the solute atoms Ce and Zn as compared to that of Mg, as well as to the presence of intra-granular fine precipitates. A comparison of the observed high m-value with that of a well-established alloy AZ31 may be indicative. El-Morsy et al. [87] reported a superplastic behaviour at a strain rate value of about 5E-04 s^{-1} for an AZ31 Mg alloy at 400°C. It should be born in mind that the strain rates during the tests conducted in our study was even faster than the conventional strain rates permitting GBS [22]. Although the investigated alloy was in cast-condition and having a coarse for superplastic behaviour grain size, namely about 100-200μm, it can be said that Mg-2Ce-2Zn alloy showed a good potential for superplastic deformation as also evident with the calculated m-value which was higher than the conventional limit of 0.3 [87].

Furthermore, the material's ability to maintain the grain size and shape were taken as indications that would support this ability.

The resistance to grain coarsening in this alloy can be attributed to the presence of grain boundary precipitates. This feature should also be considered highly useful in superplastic forming conditions.

In seeking ailments to the anomalous behaviour of Mg alloys, e.g. maintaining the deformation texture even after recrystallization, special processing conditions can also be helpful. For example, the forming method employed in this study, gas forming, would create a multi-axial stress distribution in the material. Especially, hot deformation methods, if coupled with alloy systems that promote random formation of recrystallized grains, can

be highly effective in eliminating the post-deformation texture. Although the texture of the bulge samples was not directly investigated, Mg-2Ce-2Zn system, in this regard, probably has little, if any, tendency to develop severe texture. Good deformation capacity of this alloy, even in the absence of twinning and predisposition for superplastic deformation mechanism, points out that initial random grain orientation of the as-cast structure was preserved. Furthermore, the presence of grain boundary as well as intra-granular precipitates could be considered as potential nucleation sites for the formation of randomly oriented new grains during a recrystallization process as a valuable feature of the alloy to eliminate texture, if born.

The effects of Ce and Zn have been well established in the literature. Less than 0.025 at. % Ce addition does not create solute solution strengthening while increasing deformation capacity considerably due to increased non-basal slip [16]. Low concentration, e.g. 0.2 mass percentage Ce addition, without changing the c/a ratio was still observed to give rise to increased ductility as well as yield strength. Ce also has been reported to delay dynamic recrystallization, possibly due to reduced diffusion rate, thus leading to lower ductility at high temperatures [17]. Some studies further indicated that Zn, in low concentrations, created Short Range Order (SRO) as an additional strengthening mechanism [76,89]. When in solid solution it is said to facilitate the prismatic slip [90] while suppressing twinning with its increasing concentrations [91]. Zn has also been reported to segregate to the existing twin boundaries, effectively pinning them [92]. According to the data presented in an *ab initio* study by Shang et.al., Zn has no direct influence on the *twinnability* of Mg [93]. Sandlöbes et.al. [85], based on the highly positive effects of Yttrium, when developing a similarity-to-Yttrium index for each alloying element addition to Mg, assigned a figure of 0.743 for Zn, in terms of increasing the SFE of the basal plane while reducing the SFE for the additional slip systems [85]. In the light of the above, despite the apparent lack of twinning, good deformation capacity of the alloy studied could reasonably be attributed to the presence of the alloying elements Ce and Zn. The mechanism of this enhancement can be related to the changes in SFE of the prismatic and perhaps the pyramidal slip planes. Thus, based on the literature as well, it can be said that both Ce and Zn enhance deformation capacity via promoting non-basal slip and weaken the basal texture.

4. An innovative methodology to characterize material behaviour and experimentally calibrate a material model of an AZ31B-H24 Mg alloy

Considering the commercial AZ31B-H24 Mg alloy, in order to both characterize the alloy and calibrate the constitutive material model suggested by Carpenter (model described in section 1.5 of chapter 1), results obtained applying a new methodology based on bulge tests (section 2.3 of chapter 2) are collected and discussed in the present chapter.

4.1. Bulge tests experimental results

Results in terms of final shapes obtained are reported in Figure 86. As possible to see, passing from 0.2 to 1.6MPa, the final height of the dome decreases.

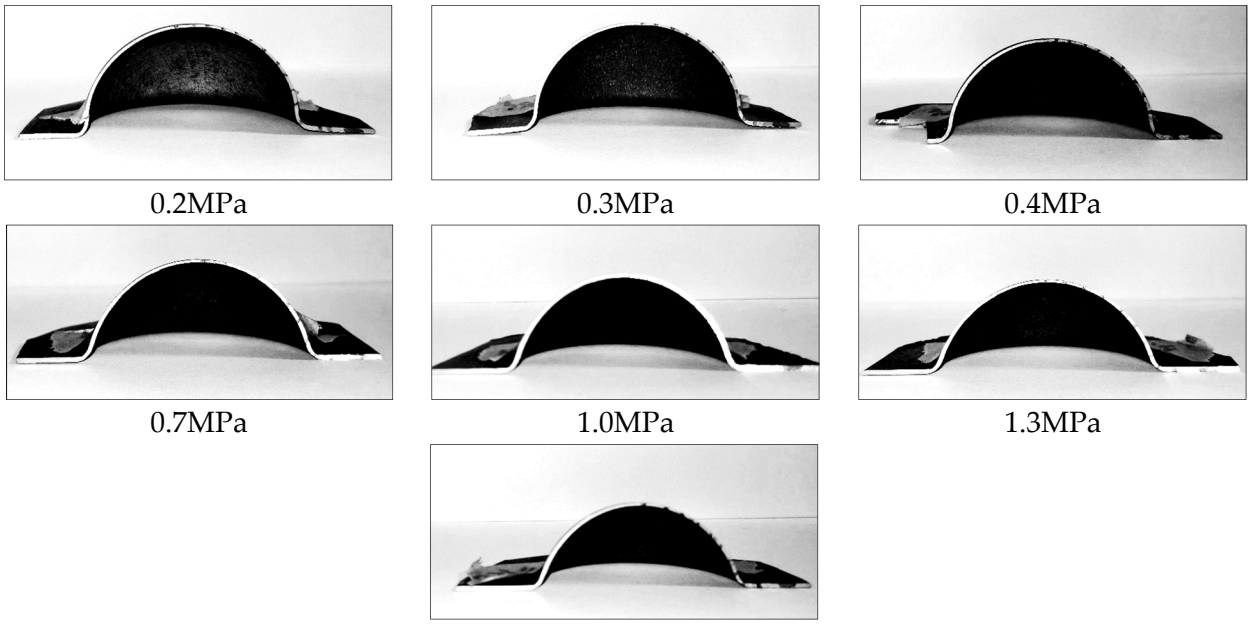

Figure 86 Samples obtained after forming process.

According to the argon gas pressure (or equivalent strain rate) value adopted to form the initial blank, comparison in terms of dome height as a function of the forming time are proposed in the next graphs (Figure 87 and Figure 88); in particular, in order to distinguish clearly the curves obtained, comparison is divided in two principal groups characterized by respectively low and high gas pressures.

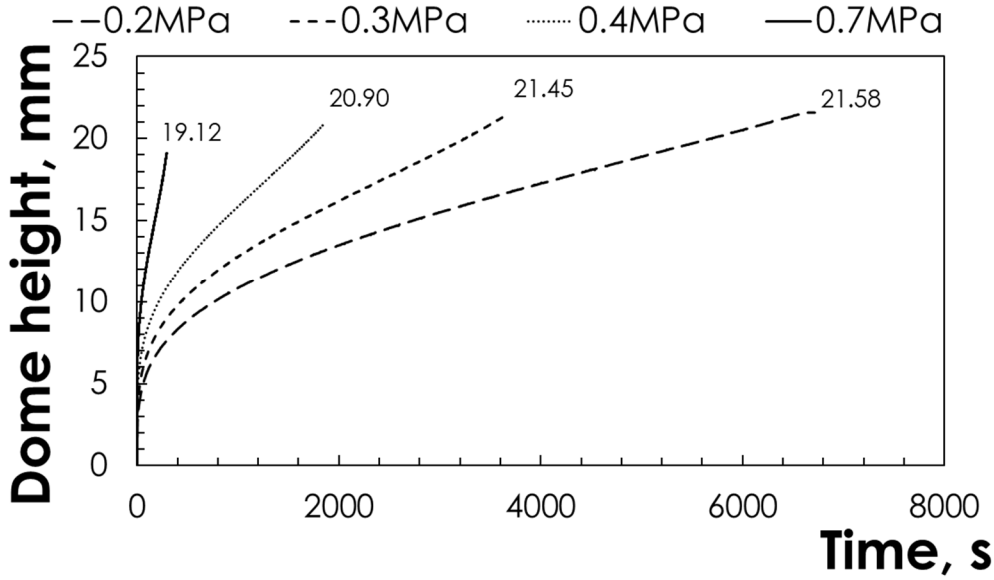

Figure 87 Dome height according to the forming time for low values of gas pressure.

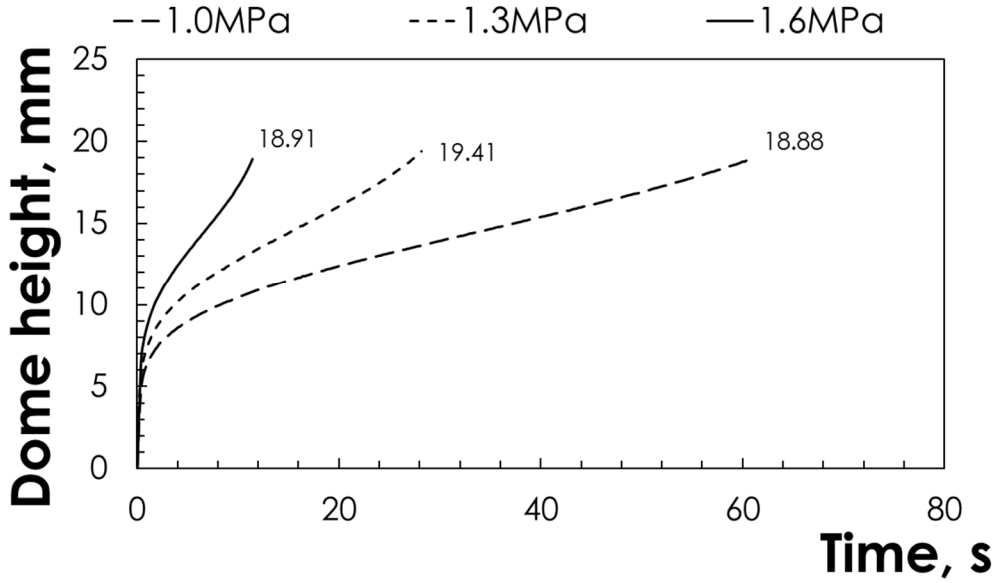

Figure 88 Dome height according to the forming time for high values of gas pressure.

It can be noted that dome height increases when the gas forming pressure decreases. For example, considering the extremes of the investigated range, a decrease of the pressure from 1.60 to 0.20MPa leads to obtain an increase up to 13% in terms of final dome height (from 18.91 to 21.58mm). As visible in the same graphs, this effect is absent for high gas pressure values: in fact, the three final dome height obtained for the three highest values of pressure are substantially unchanged.

To investigate the gas pressure effect in terms of thinning along the arc length, a comparison between the different thickness profiles (starting from the dome apex to the flanged area) are reported. Also in this case, for greater clarity, the experimental thickness profiles are depicted dividing the curves obtained at low pressure (Figure 89) from those related to higher pressures (Figure 90).

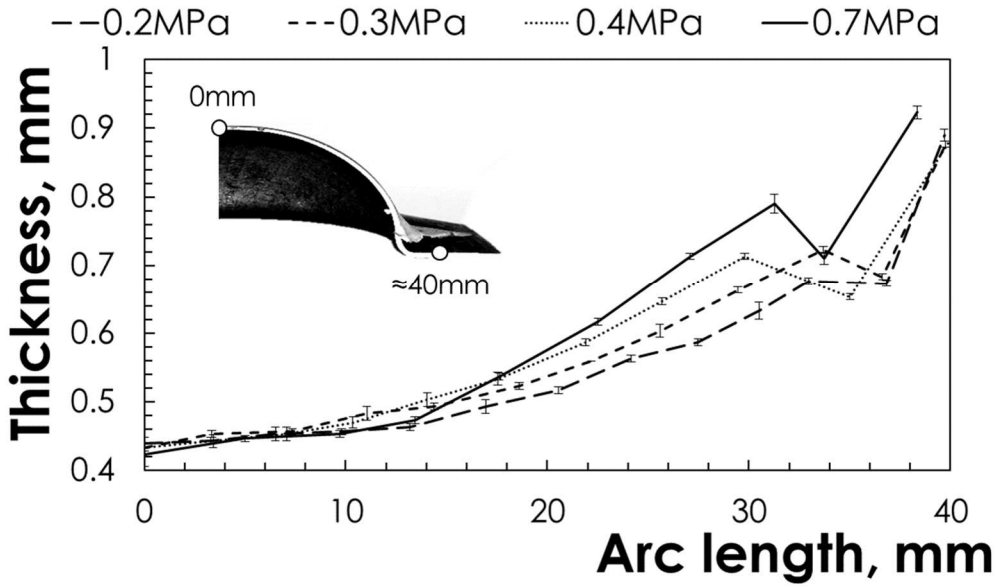

Figure 89 thickness distribution along the arc length for low values of gas pressure.

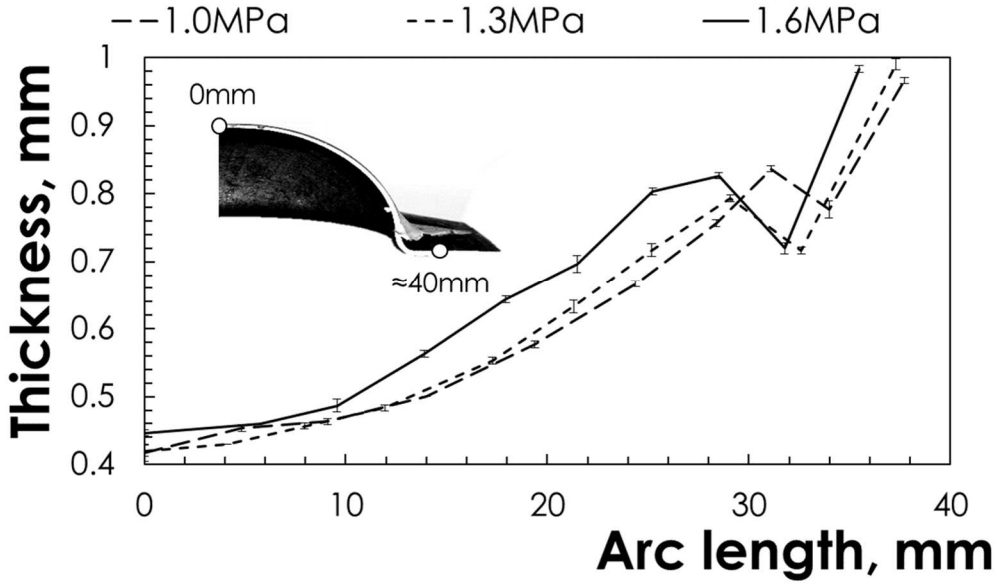

Figure 90 thickness distribution along the arc length for low values of gas pressure.

As shown in Figure 89 and Figure 90, a marked effect of the gas pressure was recorded: in fact, an increase of the thickness uniformity is obtained when low values of the pressure are adopted. Comparing the two extreme conditions (0.2 and 1.6MPa), marked differences for both final dome height and thickness distribution are registered. In particular, as reported in Figure 91, assuming as constant thickness the zone affected by a maximum variation equal to 2%, the extension of this area in the case of a pressure of 0.2MPa (black dashed curve) is about two times the one obtained in correspondence of 1.6MPa (black continues curve).

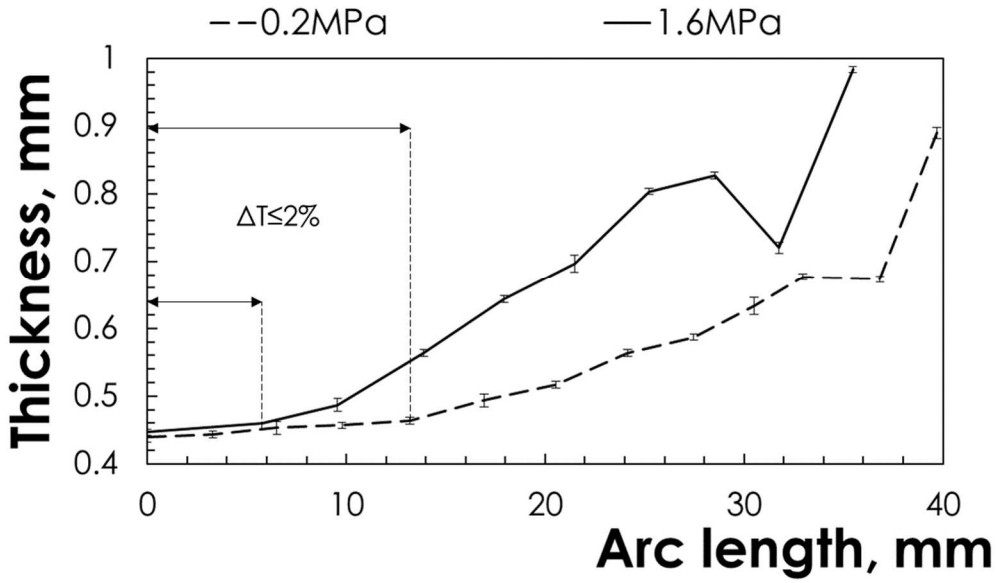

Figure 91 Thickness distribution along the arc length for the two extremes of the pressure range investigated.

4.2. Mean grain size measurements

After performing the experimental plan, all model constants (C, n, α, A_{GBS}, n_{GBS}, p, A_{DC} and n_{DC}) were determined. Firstly, the mean grain size was determined for the "As received" condition. The value obtained experimentally is equal to 10.8μm. Micrograph referring to this condition is reported in Figure 92.

Considering the first three constant characterizing static and dynamic grain growth (C, n and α), the optimized values were obtained minimizing the error between experimental and analytical results by means of equations 8 and 9. In particular, to determine C and N, metallographic analyses were conducted referring to the flanged area (subject to the only thermal load); on the contrary, the dome apex area were analysed to determine α value.

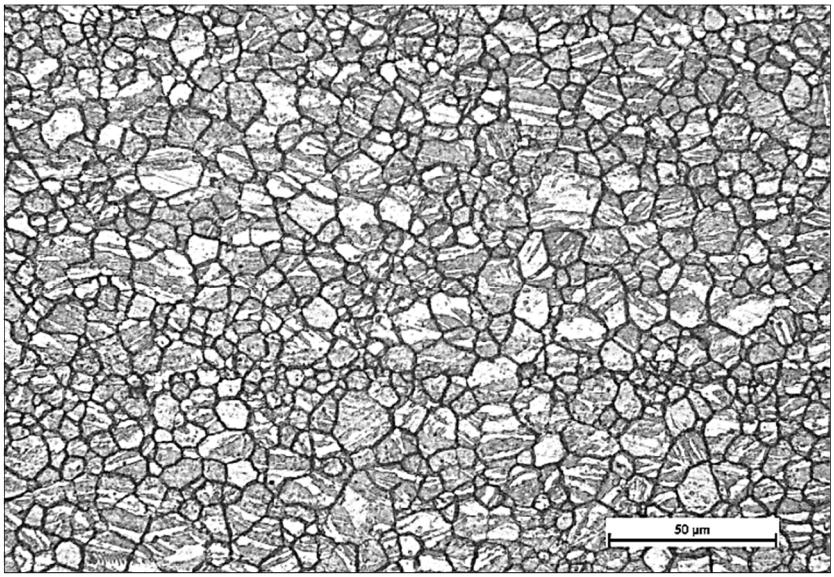

Figure 92 Microstructure of the "As received" condition.

Graphs in Figure 93 and Figure 94 show results from optimization procedure: circular marker indicates the experimental conditions, while the dashed black curve represents the analytical trend.

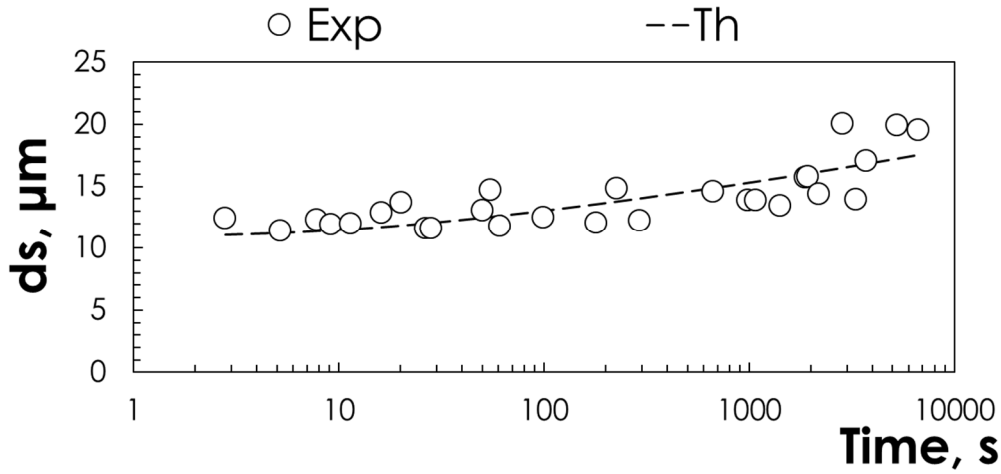

Figure 93 Static grain growth: comparison between experimental (circles) and analytical (dashed black curve) results.

When the gas pressure value increases by exceeding values of 0.7MPa (0.03 s^{-1}), abnormally large grains were observed; as abovementioned, in correspondence of these strain rate values the deformation mechanism is no longer due to the so-called GBS but is explained by the DC creep. As documented by Carpenter et al. [6]., differently respect to the GBS, DC creep is not affected by grain size. Therefore, tests performed with gas pressure values greater than 0.7MPa were not considered for the determination of α (Figure 94).

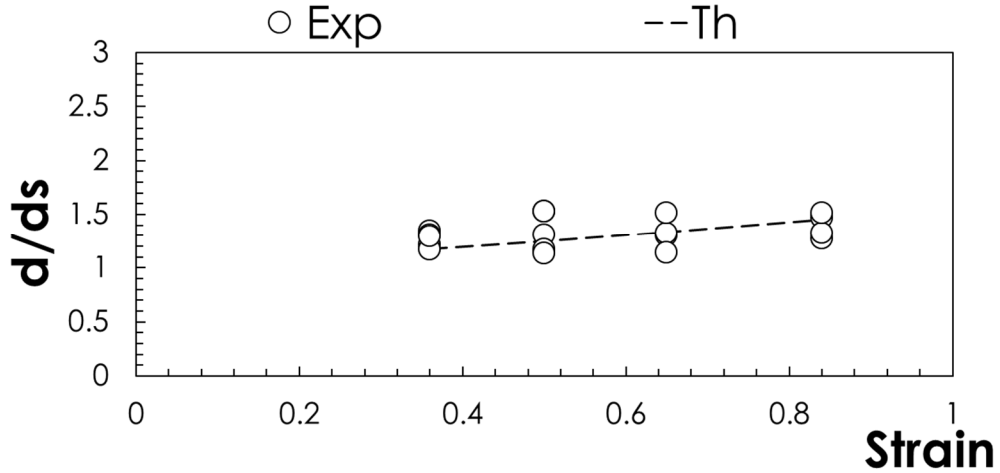

Figure 94 Dynamic grain growth: comparison between experimental (grey circles) and analytical (dashed green curve) results.

Figure 95a fully confirms what anticipated. In fact, considering all measures coming from deformed samples for a fixed strain value equal to 0.84 (the maximum value investigated), it is possible to observe how the static growth starts in correspondence of the low-pressure

values (this is clearly closely related to the longer permanence at high temperatures for the low pressures).

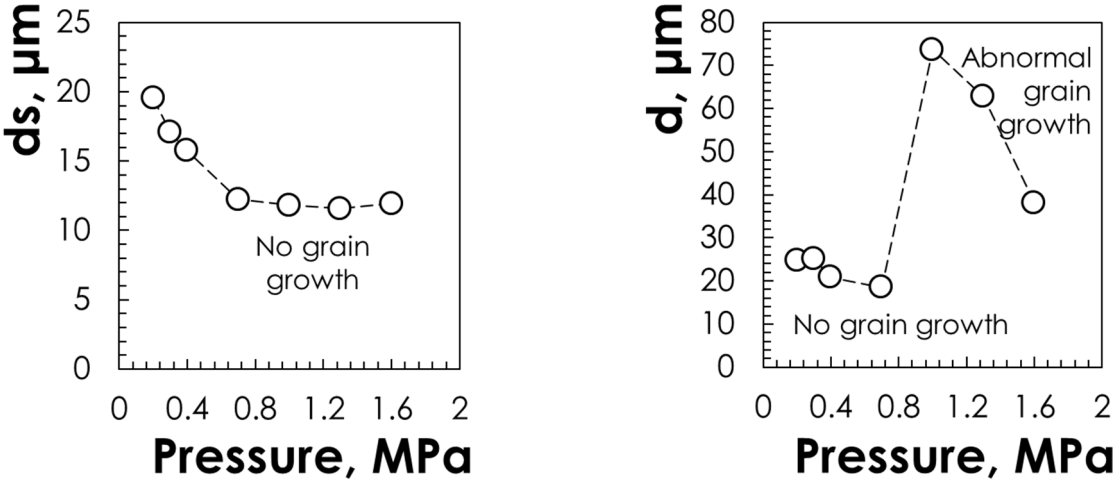

(a) (b)

Figure 95 Grain growth according to the gas pressure at fixed strain (84%): (a) static and (b) dynamic effects.

For all experimental conditions (in terms of strain and pressure) adopted, mean grain size due to both static and dynamic effects are listed respectively in Table 28 and Table 29.

Strain	0.2MPa	0.3MPa	0.4MPa	0.7MPa	1.0MPa	1.3MPa	1.6MPa
0.36	14.39	13.89	14.56	12.47	11.62	11.93	12.4
0.50	13.92	15.81	13.87	12.03	13.07	12.84	11.38
0.65	19.9	20.07	13.43	14.82	14.71	13.72	12.33
0.84	19.54	17.07	15.74	12.23	11.8	11.57	11.95

Table 28 Mean grain size due to the static effect (measures are in µm).

Strain	0.2MPa	0.3MPa	0.4MPa	0.7MPa	1.0MPa	1.3MPa	1.6MPa
0.36	19.41	16.85	19.12	14.62	15.06	80.21	54.31
0.50	21.29	20.66	21.18	14.11	14.81	88.14	63.01
0.65	25.96	26.51	20.3	16.91	70.9	76.76	56.43
0.84	24.85	25.14	20.88	18.53	73.66	62.75	38.17

Table 29 Mean grain size due to the dynamic effect (measures are in µm).

The abnormal dynamic grain growth obtained at high pressures are confirmed by the values in Table 29.

For the value of strain ranging from 0.50 up to 0.84, the abnormal growth regards pressures of 1.3 and 1.6MPa. For strain equal to 0.65 and 0.84, excessive grain growth was registered also in correspondence of 1.0MPa.

Micrographs obtained for all conditions listed in Table 28 and Table 29 are showed from Figure 96 to Figure 102.

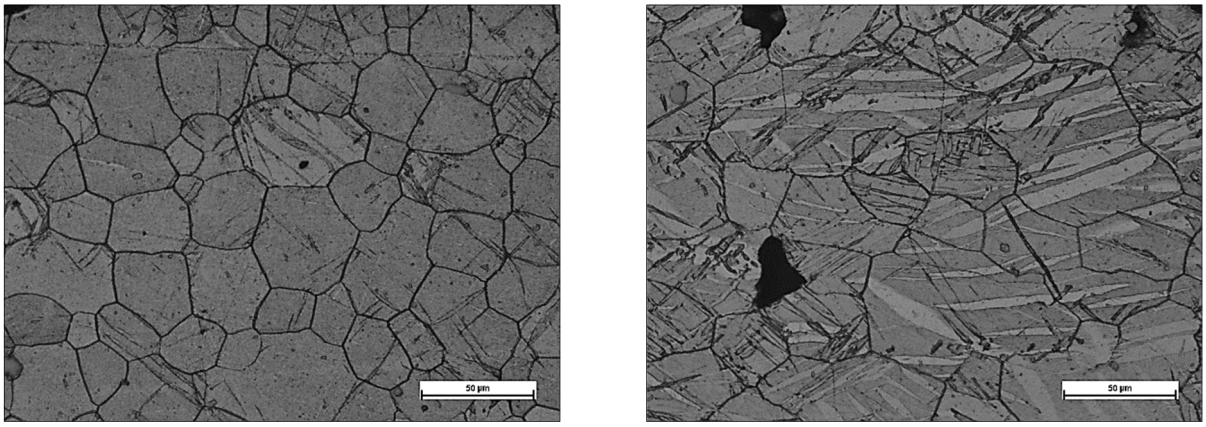

(a) (b)

Figure 96 Micrographs obtained at a strain of 0.84 and pressure equal to 0.2MPa: (a) flanged area and (b) dome apex.

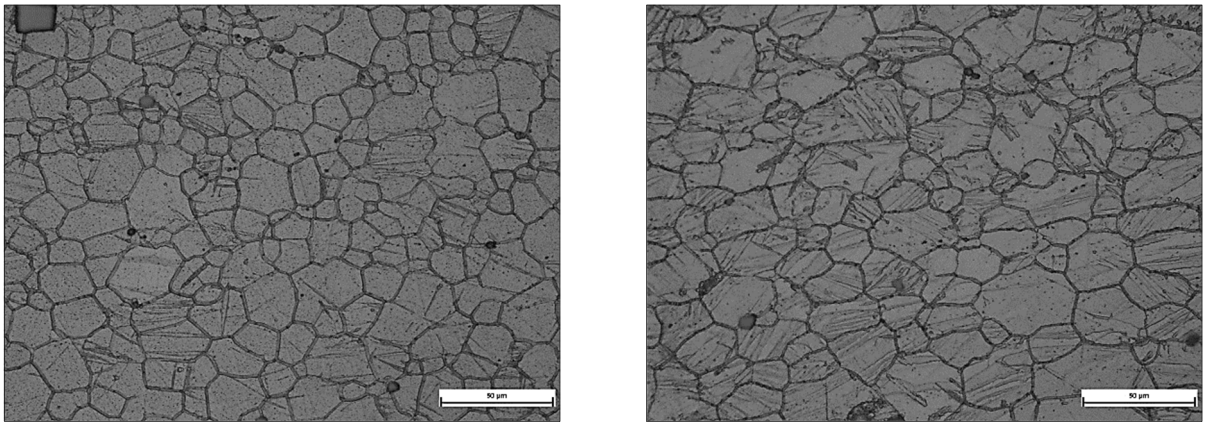

(a) (b)

Figure 97 Micrographs obtained at a strain of 0.84 and pressure equal to 0.3MPa: (a) flanged area and (b) dome apex.

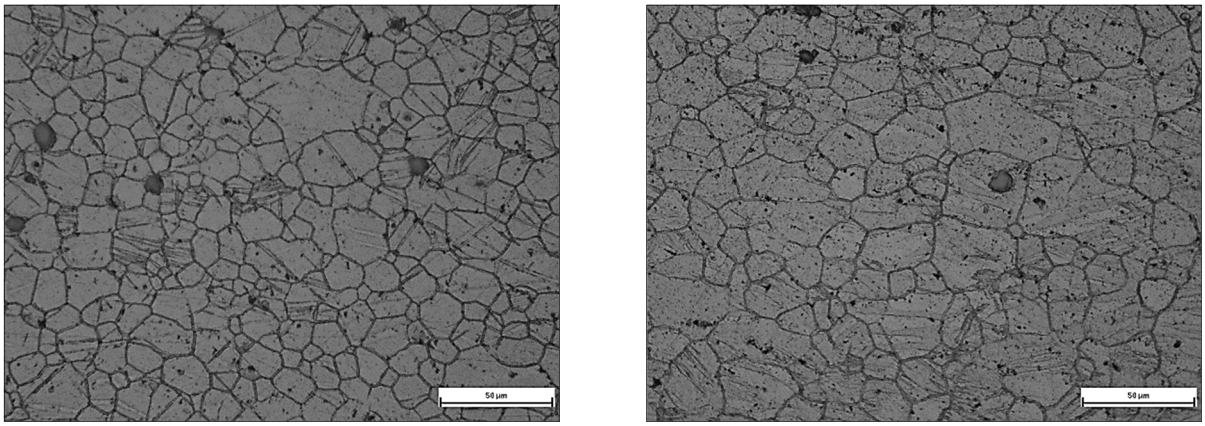

(a) (b)

Figure 98 Micrographs obtained at a strain of 0.84 and pressure equal to 0.4MPa: (a) flanged area and (b) dome apex.

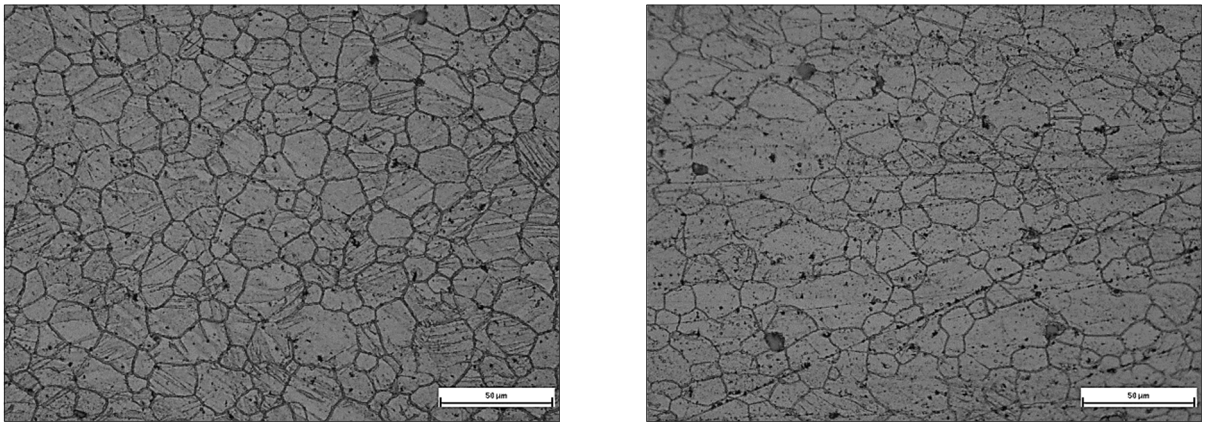

(a) (b)

Figure 99 Micrographs obtained at a strain of 0.84 and pressure equal to 0.7MPa: (a) flanged area and (b) dome apex.

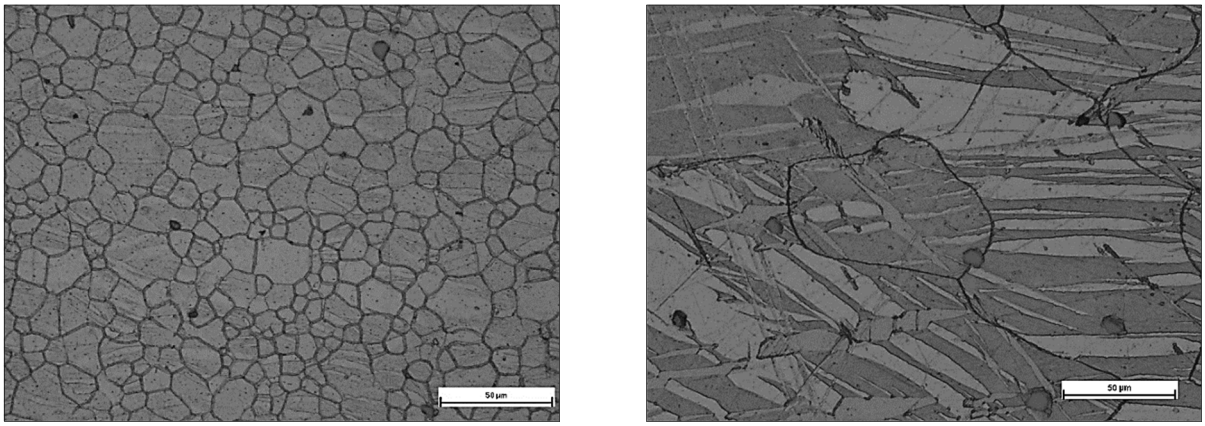

(a) (b)

Figure 100 Micrographs obtained at a strain of 0.84 and pressure equal to 1.0MPa: (a) flanged area and (b) dome apex.

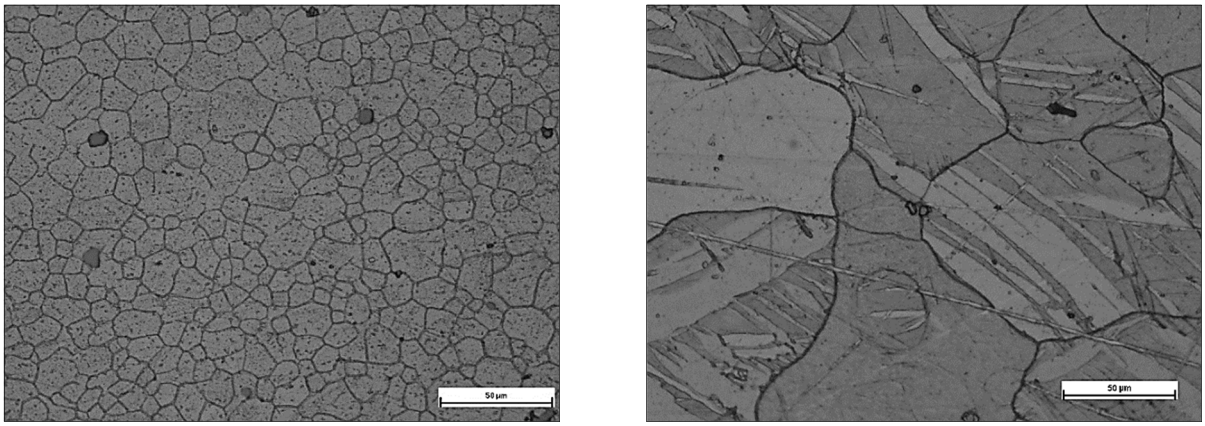

(a) (b)

Figure 101 Micrographs obtained at a strain of 0.84 and pressure equal to 1.3MPa: (a) flanged area and (b) dome apex.

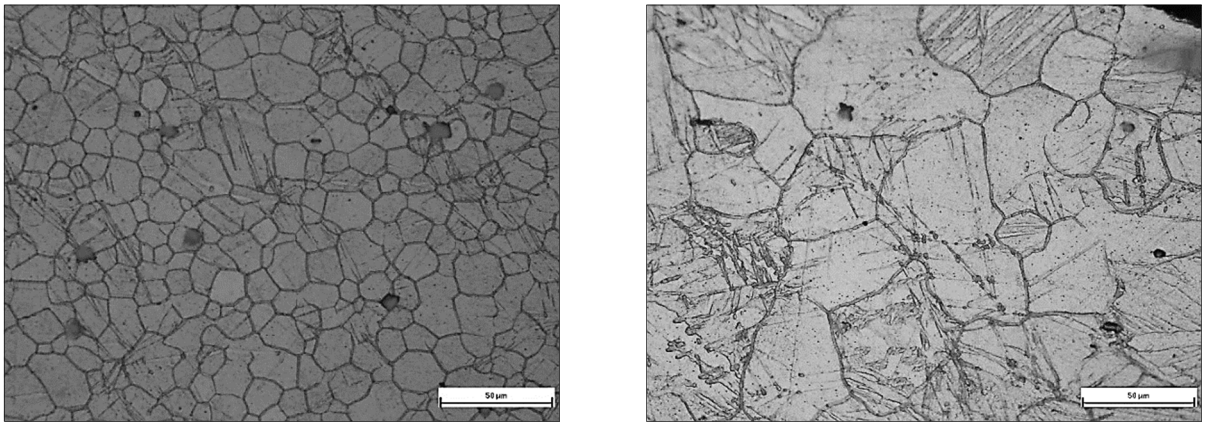

(a) (b)

Figure 102 Micrographs obtained at a strain of 0.84 and pressure equal to 1.6MPa: (a) flanged area and (b) dome apex.

Comparison of different pressure conditions related to the two distinct areas analysed (flanged and dome apex zone) shows marked differences. In fact, effect of static grain growth are visible exclusively in the flanged area, in witch (as also demonstrated in the graph of Figure 95a) the mean grain size appears to be visibly the same for pressure equal to 1.0, 1.3 and 1.6MPa (Figure 100a, Figure 101a and Figure 102a). This effect is directly connected to the permanence time at the test temperature (450°C). Total times for each test carried out up to a strain 0.84 are reported in Table 30.

	0.2MPa	**0.3MPa**	**0.4MPa**	**0.7MPa**	**1.0MPa**	**1.3MPa**	**1.6MPa**
Forming time, s	6617.6	3696.4	1862.2	296.6	61	28.2	11.4

Table 30 Forming time according the different test conditions.

No twinning phenomenon was observed in the area not affected by the gas pressure (flanged area); on the other hand, considering the dome apex (that is the one most stressed by the gas pressure), twinning phenomena are visible in all cases: the conditions in which they are most visible are associated both with high (0.2MPa) forming times and high pressure values (1.0, 1.3 and 1.6MPa). As previous underlined, abnormally large grains were observed for pressures greater than 0.7MPa; for these condition the deformation mechanism is no longer due to the GBS but is explained by the DC (not affect by grain size): this leads to the assertion that excessive grain growth should not significantly influence alloy deformation as also considered by Carpenter et al. [6]. Therefore, related to the abnormal grain growth at the dome apex (more deformed area), all values obtained starting from 1.0 MPa were not considered to determine α-value. Therefore, d_0, C, N and α values obtained after the optimization procedure are summarized in Table 31.

d_0, μm	**C, μm s^{-N}**	**N**	**α**
10.8	4.83E+13	14.106	0.456

Table 31 Constants obtained after the first step of the calibration procedure.

4.3. GBS and DC material constants determination

The determination of A and n for the two different creep mechanisms and p (that affects the GBS and typically ranges from 2 to 3) was based - as done previously for the other material model constants - exclusively by means of experimental bulge tests. Starting from experimental evidences (particularly regarding the curves of dome height according to the forming time), it was possible to determine a value of equivalent strain rate for each pressure condition: the zone of the curve with a constant slope was considered for this scope. All results are listed in Table 32.

	0.2MPa	0.3MPa	0.4MPa	0.7MPa	1.0MPa	1.3MPa	1.6MPa
Strain rate, s^{-1}	1.02E-04	2.02E-04	3.47E-04	2.04E-03	8.24E-03	2.33E-02	6.46E-02

Table 32 Strain rate values calculated for each gas pressure condition.

A s suggested by the literature, considering $0.01s^{-1}$ equal to the threshold value that divides between them the two different creep mechanisms, strain rates obtained indicate that up to pressures equal to 0.7MPa the predominant mechanism is GBS; on the contrary, for pressure greater than these values the DC creep predominates.

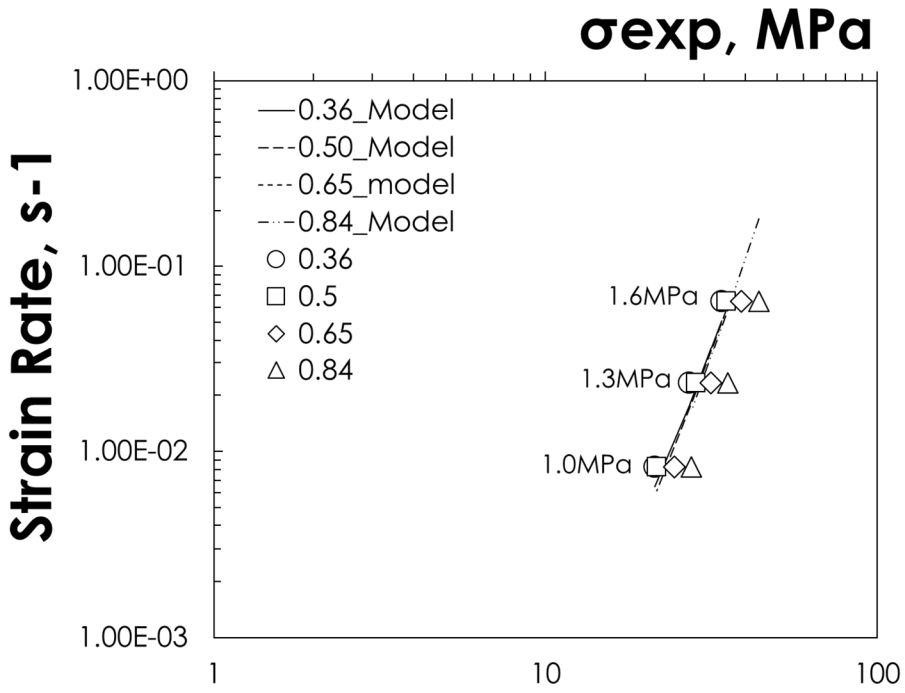

Figure 103 Comparison between analytical and experimental results in terms of the strain rate according to the stress for the highest values of pressure (1.0, 1.3 and 1.6MPa) investigated.

Calibration of material model aimed to obtain value of A and n for the two creep mechanisms was based on the minimization of the error between values predicted by the model and experimental data according to Equation 10.
To guarantee the physical plausibility of the solution obtained, the procedure was applied

in two different steps: firstly considering the conditions affecting the DC creep (1.0, 1.3 and 1.6MPa), aimed to determine the A_{DC} and n_{DC} values, and, than, considering all conditions evaluated (from 0.2 to 1.6MPa) in the experimental plan to determine A_{GBS}, n_{GBS} and p.

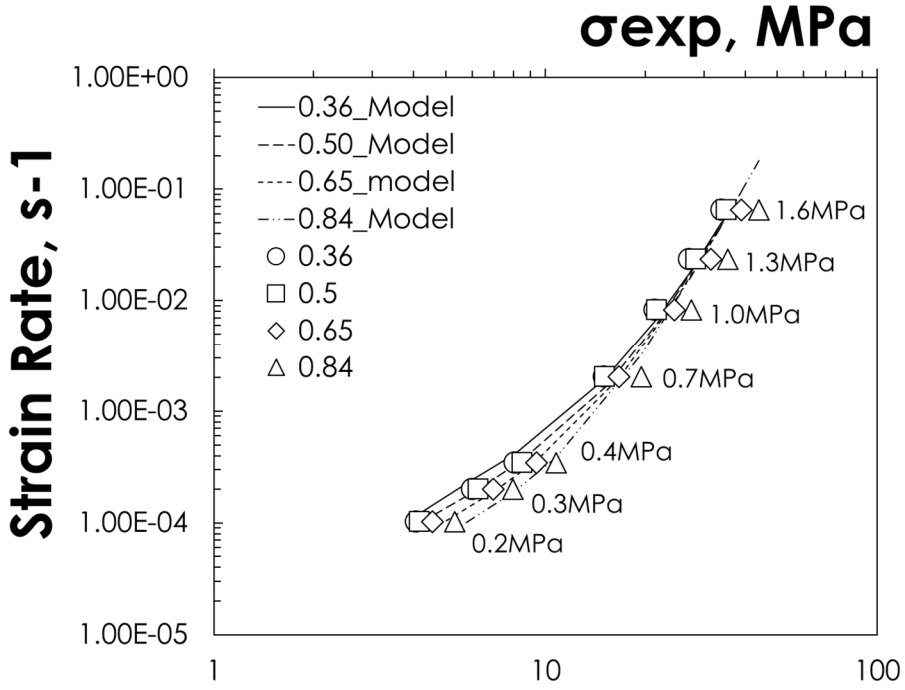

Figure 104 Analytical/experimental results comparison in terms of strain rate according to stress.

In Figure 103 and Figure 104 the logarithm of strain rate related to the logarithm of stress for respectively DC conditions and all bulge tests performed according to the four strain levels evaluated is plotted. As possible to see, the adopted procedure allowed to achieve the optimal matching between the experimental data (markers) and the material constitutive model (black curves) represented by equation 10.
Results obtained for the remaining material constant are listed in Table 33 together with those previously determined.

Constant model	Value
d_0, μm	10.8
C, μm s^{-N}	4.83E+13
N	14.106
A	0.456
A_{GBS}, $s^{-1}MPa^{-n_{GBS}}$ μm^{p}	2.22E-02
n_{GBS}	1.448
P	2.466
A_{DC}, $s^{-1}MPa^{-n_{DC}}$	3.100E-10
n_{DC}	5.325

Table 33 All constants (describing the material constitutive model) obtained after the calibration procedure.

4.4. Obtained results from numerical simulations

Exploiting constants material model and implementing these in the FE model (as described in section 2.3.4 of chapter 2), results in terms of (i) dome height according to the forming time, (ii) thickness distribution along the arc length and (iii) mean grain size were evaluated in this section. Dome height trends are reported in Figure 105 and Figure 106.

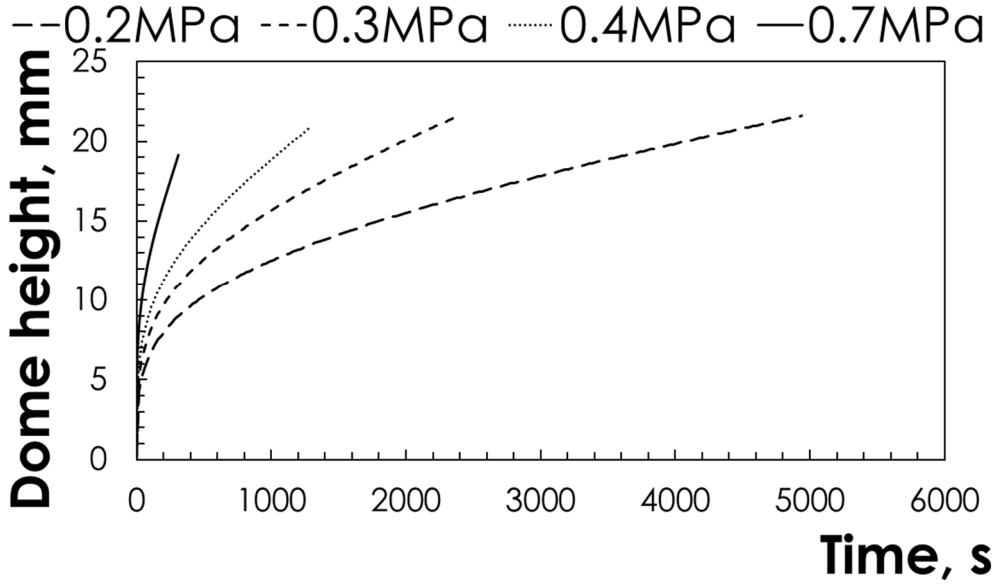

Figure 105 Dome height according to the forming time for low values of gas pressure.

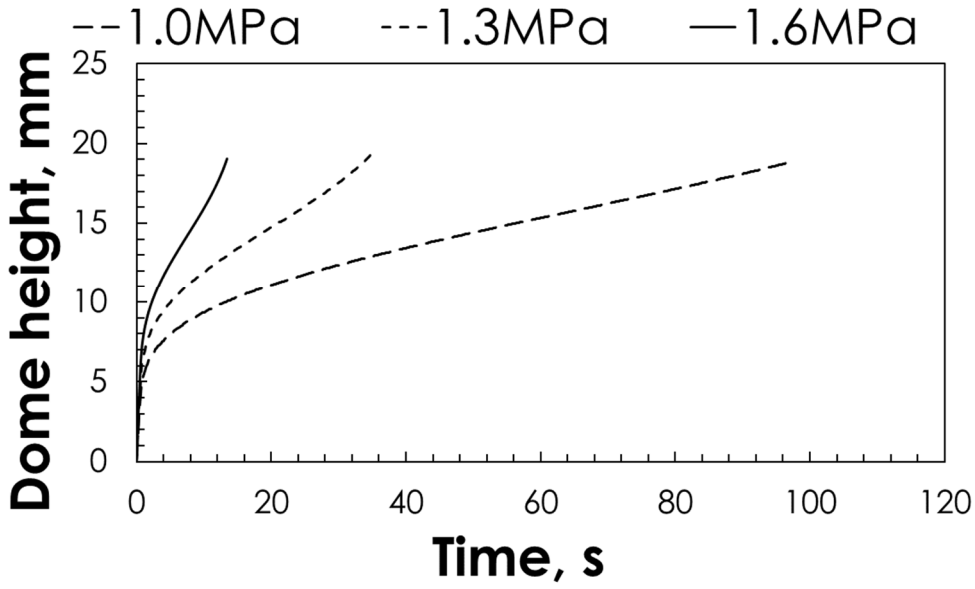

Figure 106 Dome height according to the forming time for high values of gas pressure.

As underlined for the experimental tests, numerical results show the effect of the gas forming pressure in terms of slope and length of the obtained curves: despite a reduction of the final dome height, an increase of gas pressure allows to achieve a marked reduction of the forming time. Numerical curves in Figure 106 show also that for pressure lower than

1.3MPa a strain equal to 0.84 can be obtained before recording a final drastic increase of the curve slope and, therefore, away from the necking.

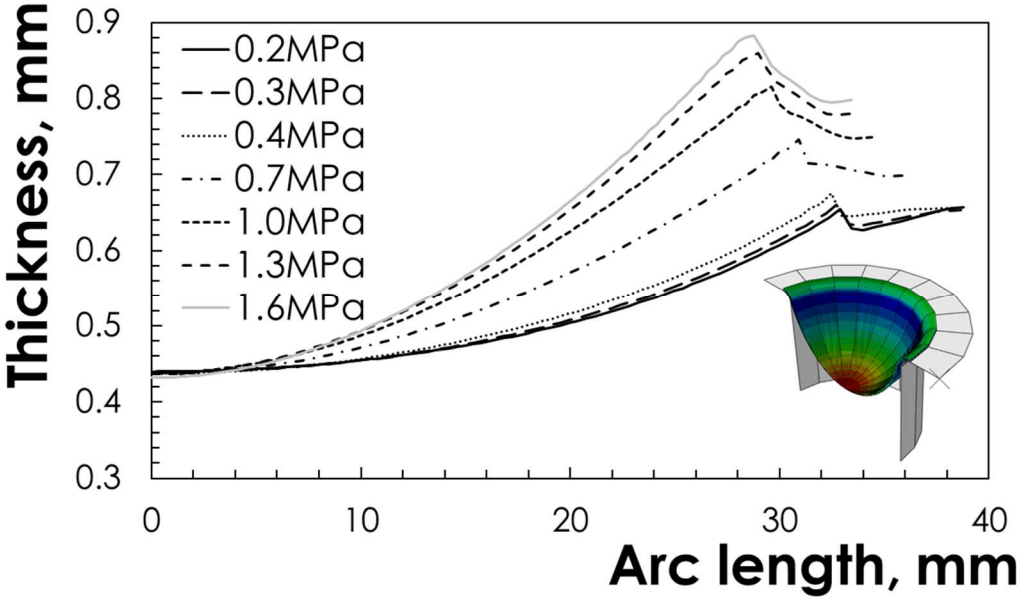

Figure 107 Thickness distribution along a radial path for all pressures investigated.

Numerical thickness distribution results are shown in Figure 107. As expected, considering the same value of strain at the dome apex (equal to 0.84) an starting from the low pressure (0.2MPa) value to the maximum (1.6MPa) one, the thickness distribution (plotted from the center of the sample to the flanged area) appears to be less gradual. In fact, as confirmed from previous experimental results, comparison between the two extremes conditions evaluated shows a marked difference in terms of thickness distributions: the extension of the zone assumable as constant in the case of 0.2MPa is about two times the one obtained with 1.6MPa.

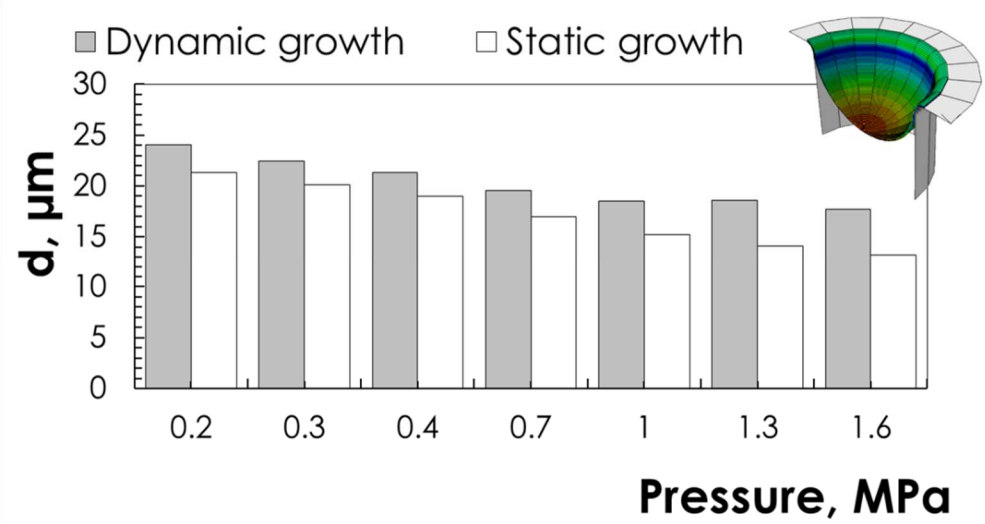

Figure 108 Numerical mean grain size due to static and dynamic effects.

The mean grain size in correspondence of both dome apex and flanged area are plotted in Figure 108. For high pressure values (1, 1.3 and 1.6MPa) the grain growth (particularly the dynamic one) can be considered negligible. Results coming from numerical simulations show a gradual decrease of the grain mean size from 24.03 to 19.54μm when the pressure passes from 0.2 to 0.7MPa corresponding to a difference equal to 18.68%.

4.5. Discussion

For each pressure adopted, numerical/experimental results comparison in terms of both dome height according to the forming time and thickness distribution along a radial path are summarized in the graphs from Figure 109 to Figure 115.

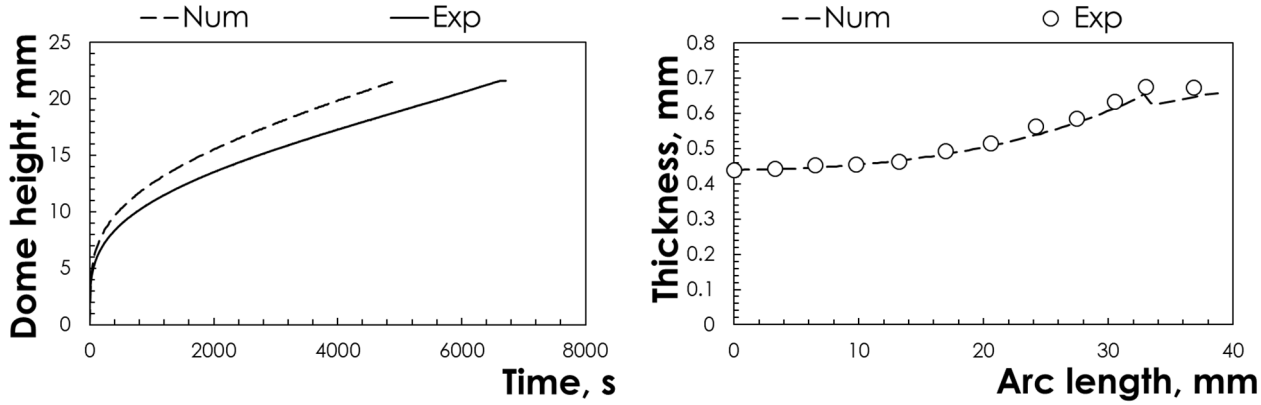

(a) (b)

Figure 109 Numerical/experimental comparison at 0.2MPa:
(a) dome height according to the forming time and (b) thickness distribution along a radial path.

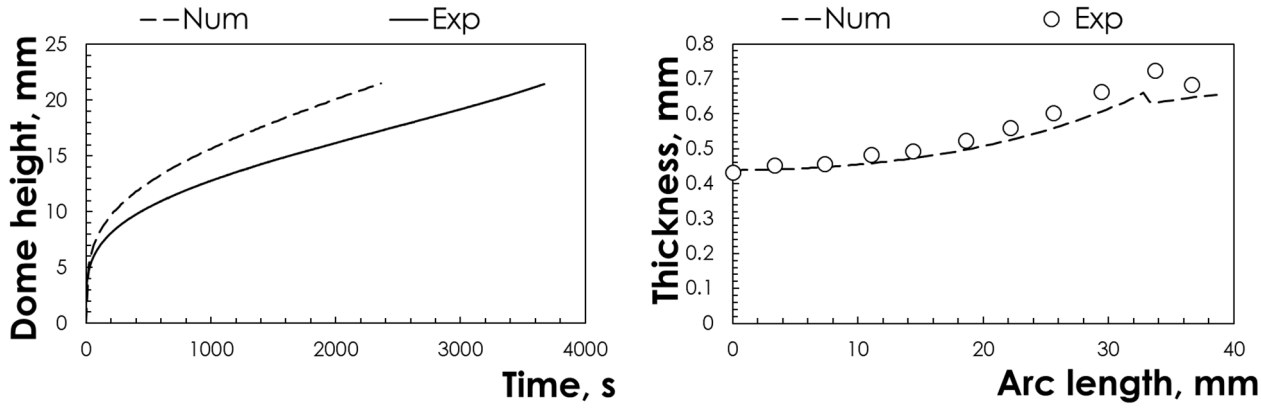

(a) (b)

Figure 110 Numerical/experimental comparison at 0.3MPa:
(a) dome height according to the forming time and (b) thickness distribution along a radial path.

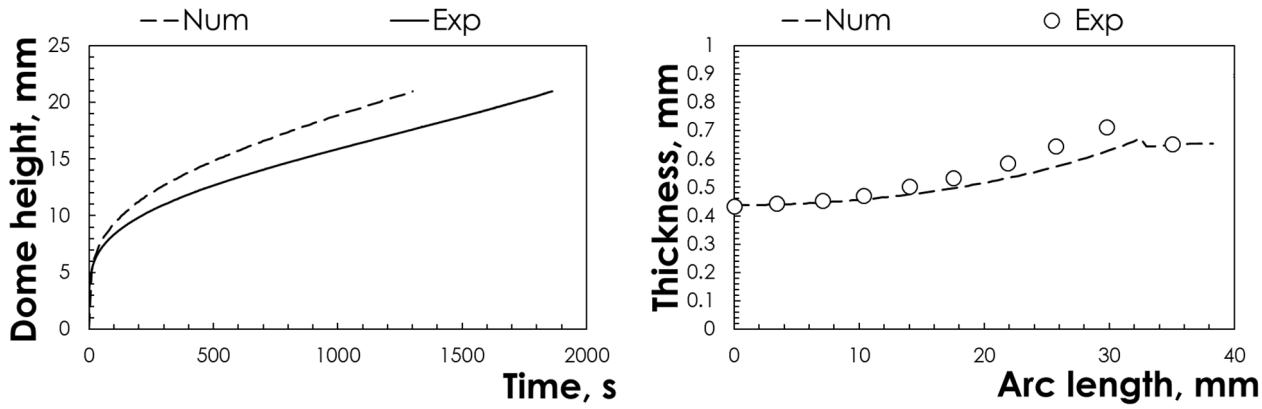

(a) (b)

Figure 111 Numerical/experimental comparison at 0.4MPa:
(a) dome height according to the forming time and (b) thickness distribution along a radial path.

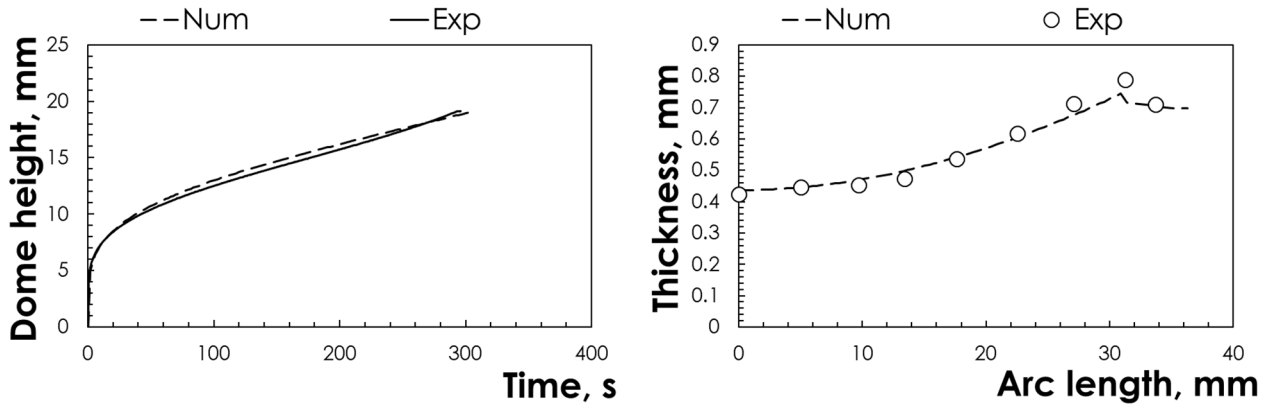

(a) (b)

Figure 112 Numerical/experimental comparison at 0.7MPa:
(a) dome height according to the forming time and (b) thickness distribution along a radial path.

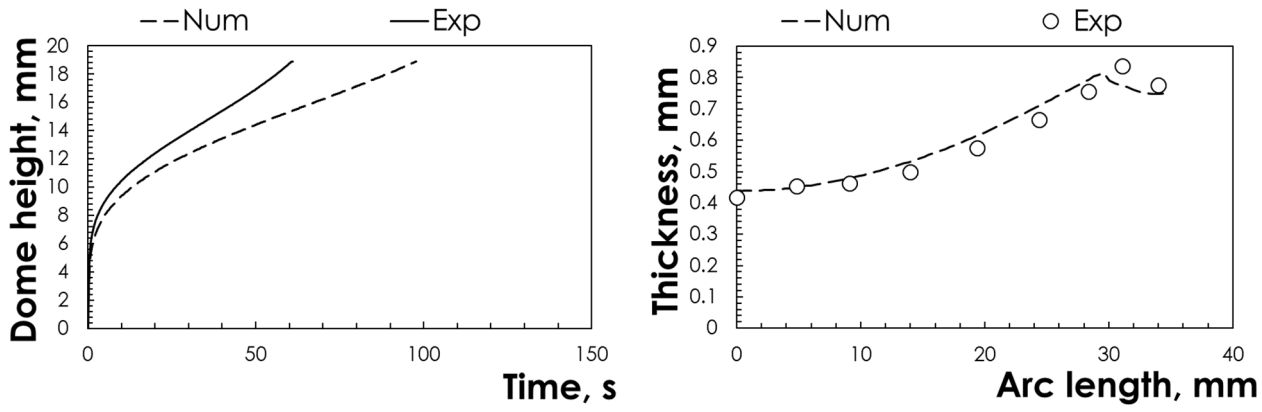

(a) (b)

Figure 113 Numerical/experimental comparison at 1.0MPa:
(a) dome height according to the forming time and (b) thickness distribution along a radial path.

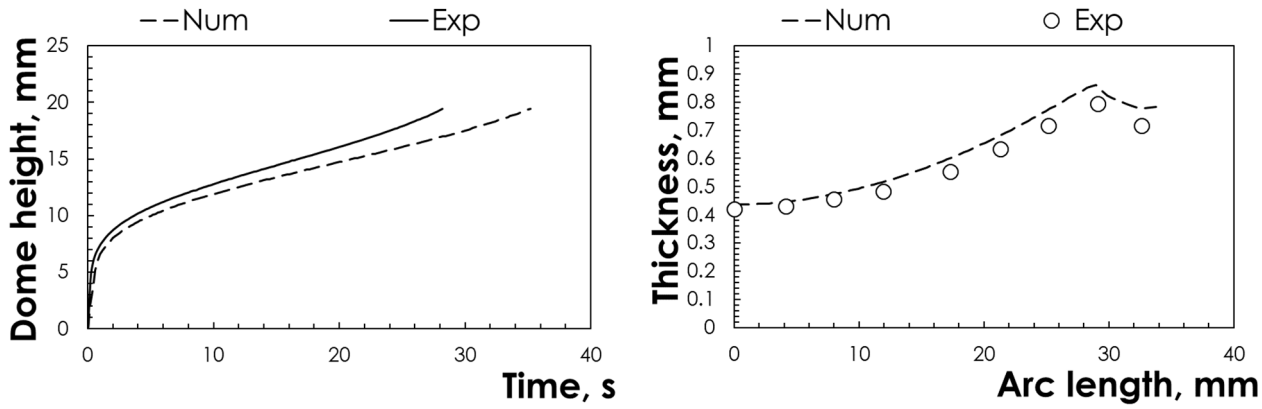

(a) (b)

Figure 114 Numerical/experimental comparison at 1.3MPa:
(a) dome height according to the forming time and (b) thickness distribution along a radial path.

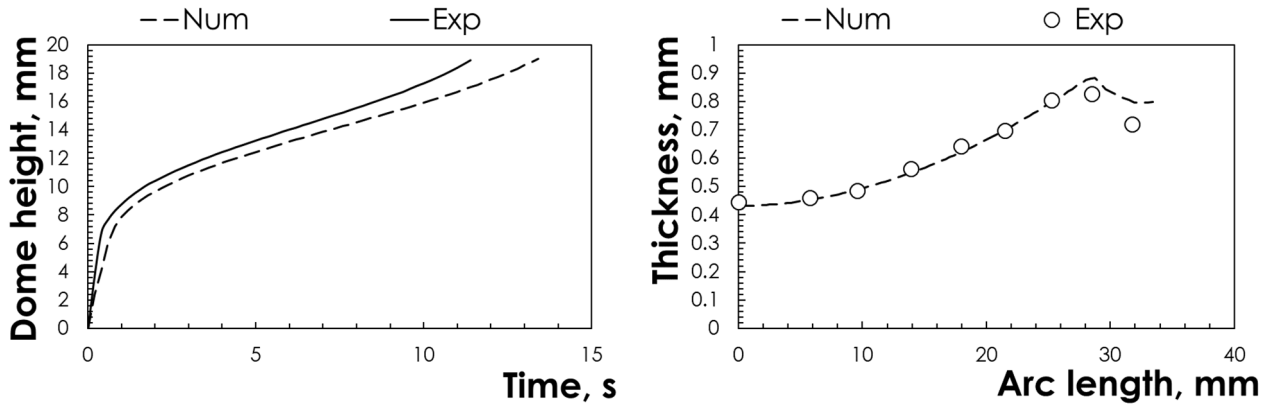

(a) (b)

Figure 115 Numerical/experimental comparison at 1.6MPa:
(a) dome height according to the forming time and (b) thickness distribution along a radial path.

As possible to observe in the previous graphs, numerical/experimental fitting of the obtained dome height curves is affected by a variable error changing with the pressure condition. In particular, the worst results are attributable to the low pressures (0.2, 0.3 and 0.4MPa). On the contrary, the best fitting is certainly associated with the test conducted at a constant pressure of 0.7MPa. Finally, although not perfectly superimposed, the model is able to predict the deformation behaviour of the material due to the three high-pressure values (1.0, 1.3 and 1.6MPa). Therefore, numerical simulations performed exploiting the material model described in this chapter predicts reasonably the deformation behaviour of the investigated Mg alloy. In fact, numerical-experimental comparison in terms of thickness distribution shows a good fitting between the theoretical distribution and the experimental one. This is true for all pressure values investigated, confirming the capability of the material model, calibrated exclusively by means of bulge tests, to reproduce conditions very close to those of SPF process.

In order to quantify the error between numerical and experimental results, the Root-Mean-Square (RMS) and Mean-Percent-Difference (MPD) errors were calculated and adopted to

describe the error between numerical simulations and experimental tests. Equations of the two error indicators adopted are listed below in Equations 18 and 19:

$$X_{RMS} = \sqrt{\frac{\sum_{i=1}^{n}\left(X_{exp} - X_{num}\right)^2}{n}} \qquad \text{Equation 18}$$

$$X_{MPD} = \frac{1}{n}\sum_{i=1}^{n} \left| \frac{X_{exp} - X_{num}}{X_{exp}} \right| 100 \qquad \text{Equation 19}$$

where n represent the number of comparisons between the two data sets, x_{exp} and x_{num} are respectively the single experimental measure and the corresponding FE model prediction.
Considering the same forming time for both numerical and experimental curves, the two types of error for both dome height and thickness distribution are summarized respectively in Table 34 and Table 35.
Obtained errors of DH, applying Equations 11 and 12, confirm that the most performing results in terms of capability to predict the material behaviour is represented by the gas pressure condition equal to 0.7MPa. In fact, error ranges from 0.4mm (2%) to 4.15mm (26%) in correspondence of a pressure of 0.3MPa.

Gas pressure, MPa	DH_{RMS}, mm	DH_{MPD}, %
0.2	2.38	15
0.3	4.15	26
0.4	3.56	21
0.7	0.40	2
1.0	1.92	13
1.3	1.24	8
1.6	1.32	10

Table 34 Obtained errors related to Dome Heights (DH).

These results confirm the lesser capability of calibration procedure to ensure a good prediction of the dome height according to the time for the conditions in which the GBS creep occurs. In support of this consideration, the maximum errors are located at the three lowest pressures. On the contrary, when the DC starts (0.7MPa) or is dominant (from 1.0 to 1.6MPa) the prediction accuracy improves considerably. Errors obtained for thickness distribution are listed in Table 35. Contrarily respect to the dome height errors, values of RMS and MPD related to the thickness distribution are very good for all conditions investigated. In fact, error value ranges from 0.02mm (2.13%) to 0.04mm (6.27%). The best conditions are attributable to pressure values equal to 0.2 and 0.7MPa; the worst one is represented by 1.3MPa.

Gas pressure, MPa	TD_{RMS}, mm	TD_{MPD}, %
0.2	0.02	2.13
0.3	0.03	4.94
0.4	0.05	5.80
0.7	0.02	2.98
1.0	0.03	4.74
1.3	0.04	6.27
1.6	0.03	3.52

Table 35 Obtained errors related to Thickness Distributions (TD).

As previous underlined, the adopted FE model was aimed at the prediction of both deformation behaviour and microstructural evolution of the AZ31B-H24 Mg alloy; therefore, results obtained from metallographic observations and from numerical simulations were compared in Table 36. In this case, the percentage error between experimental results and numerical ones was calculated considering both the heat input (measured in correspondence of the flanged area) and the combined effect of temperature and gas pressure (at the dome apex).

Gas pressure, MPa	Static Error %	Dynamic Error %
0.2	9.0	3.3
0.3	17.7	10.6
0.4	23.0	2.2
0.7	39.0	2.7
1.0	26.5	74.8
1.3	21.5	70.3
1.6	10.5	53.5

Table 36 Obtained errors related to mean grain size.

Clearly, as abovementioned, since abnormal grain growth occurs at highest gas pressures, the prediction (especially the one due to dynamic effects) is not good for DC creep conditions.
On the contrary, the model can correctly predict the evolution of the grain due to dynamic effects.
The marked errors, when static grain growth is considered, confirms the possibility of improving the calibration methodology of the material model especially in terms of grain evolution modelling (which clearly also affects the deformation behaviour of the material).
In fact, one of the future developments of the present innovative calibration procedure, aimed at the greatest possible reduction in terms of differences between numerical model and experimental evidence, is certainly represented by the extension of the starting experimental database by means of analytical extrapolation (therefore without further addition of experimental tests).

It is also necessary to reduce the dispersion of experimental data in terms of grain size due to both thermal and mechanical loads.
Finally, another possible strategy is represented by the adoption of an analytical expression that better fits the static grain growth. In fact, the experimental results showed an initial stationary phase (approximately equal to 500s) in which, contrary to what was predicted by Equation 5, the grain size remains almost constant (Figure 116).

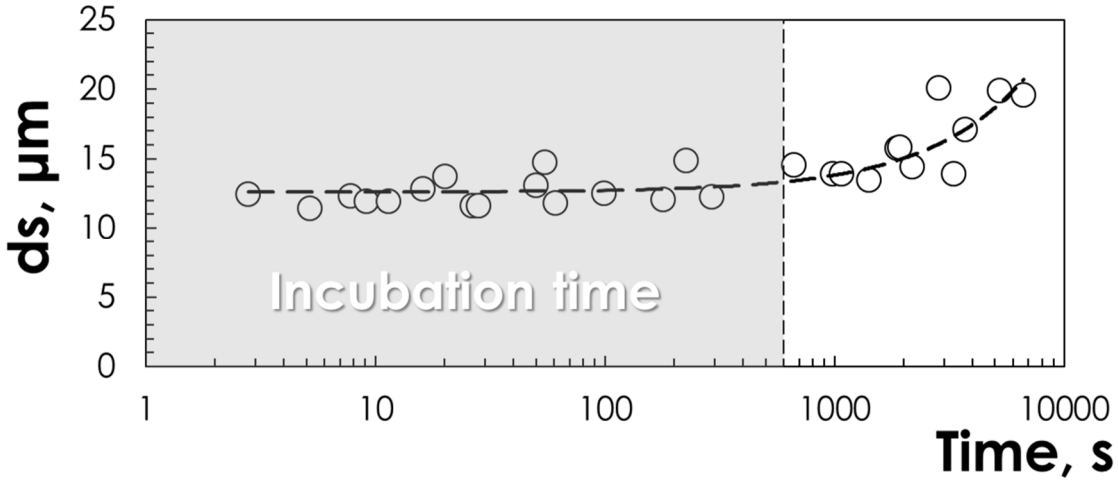

Figure 116 Experimental grain evolution according to time.

To support this consideration, as suggested by Yang [94], it is possible to assert that annealing time dependence of the mean grain size can be divided into three stages: (i) an incubation period of grain growth from 0 to 700s, (ii) a rapid grain coarsening from 700s to 70000s and, finally, (iii) a normal grain growths (Figure 117).

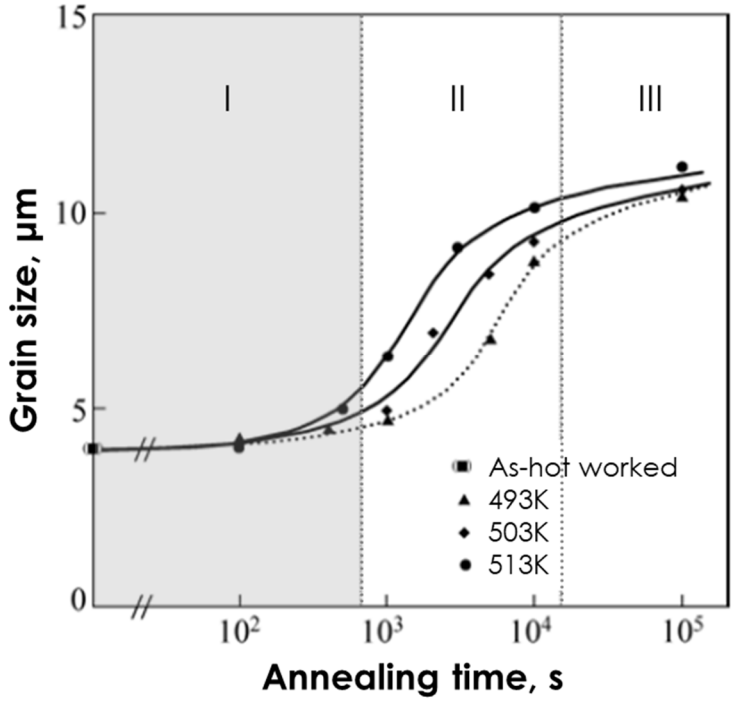

Figure 117 Effect of annealing temperature on mean grain size [94].

5. Manufacturing a spherical vessel with optimized/modified thickness distribution via unconventional techniques

Thickness distribution of a formed component is generally considered an indicator of quality during the post-forming investigations [95].
The possibility to predict, and thus control, a specific distribution at the end of the forming process becomes of first concern, especially if the component is required to ensure certain performance once put in exercise.
Such an aspect gets even more challenging when the shape complexity of the component increases or when the thickness distribution must be as uniform as possible (e.g. to guarantee the same corrosion for all parts of the prosthesis in the case of biomedical applications).
To accomplish such an ambitious goal, the research for the most suitable manufacturing process is still an open question: SPF process, despite being widely recognized as the ideal process to achieve higher final shape complexity, cannot ensure a final thickness uniformity due to the fact that the deformation occurs mainly by stretching with almost no drawing of the material into the die cavity. With reference to this scenario, as depicted in the chapter 2 (section 2.1.) the first of the two investigated cases study was represented by the manufacturing process of a spherical vessel aimed to optimize or influence the final thickness of the SPFed component. To pursue this, two different strategies were proposed.
The first approach was based on the possibility to efficiently combine the SPF process with the SPIF one in order to reduce as soon as possible the difference in terms of thickness between the center of the final shape (usually the more critical area) and the peripherical one.
Thanks to the local interaction between the rotating tool and the blank, SPIF is capable to provide a non-uniform sheet thickness distribution more suitable as a blank for a subsequent SPF process.
At the same time, in order to affect the thickness of the final component by previously changing the undeformed sheet, another promising approach investigated in the present research activities was represented by the adoption of LHT to modify locally the microstructure of the Mg alloy and thus the deformation behaviour during the forming process.
Vessel manufacturing process was designed exploiting a numerical/experimental approach: the laboratory equipment was modelled by Finite Element (FE), while the Mg alloy superplastic behaviour was modelled adopting the Enikeev and Kruglov material model and implementing experimental data from a previous characterization campaign.

In particular, for the numerical modelling of the LHT, FE simulations of the forming tests - using the grain-size dependent material constitutive model suggested by Miao [13] - were conducted.

5.1. A spherical vessel manufacturing combining SPIF and SPF techniques

Experimental and numerical results about the hybrid approach proposed are discussed in this section. Results coming from numerical optimization and modeling were fundamental for the design of the whole process.

5.1.1. Numerical optimization results

Considering the optimization procedure performed and documented in section 2.1.2.1 of chapter 2, results obtained from the optimization procedure were analyzed in terms of history charts, particularly useful to monitor the evolution of the input variable of the problem throughout the successive generations.
As shown in Figure 118a, the genetic algorithm converged toward a stable value of the A parameter around a value equal to 0.00045; correspondently, the difference between the maximum and the minimum final thickness (Figure 118b) settled around the minimum value of lower than 0.02 mm.

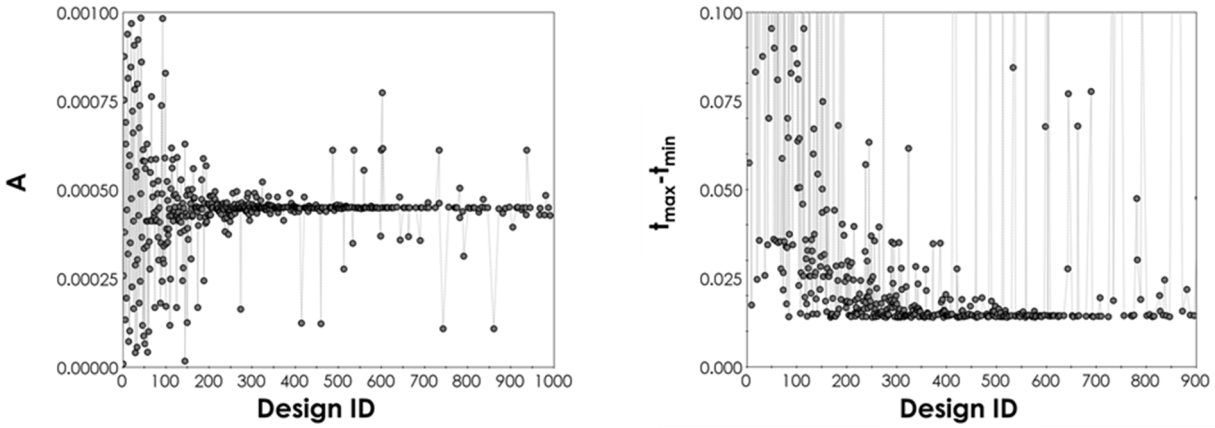

(a) (b)

Figure 118 History charts: a) A, b) difference between maximum and minimum thickness.

The best design, i.e. the one able to minimize the objective function, was characterized by an A value that allows to ensure a difference in the final thickness equal to 0.014mm. the optimized thickness profile obtained are showed in Figure 119a.

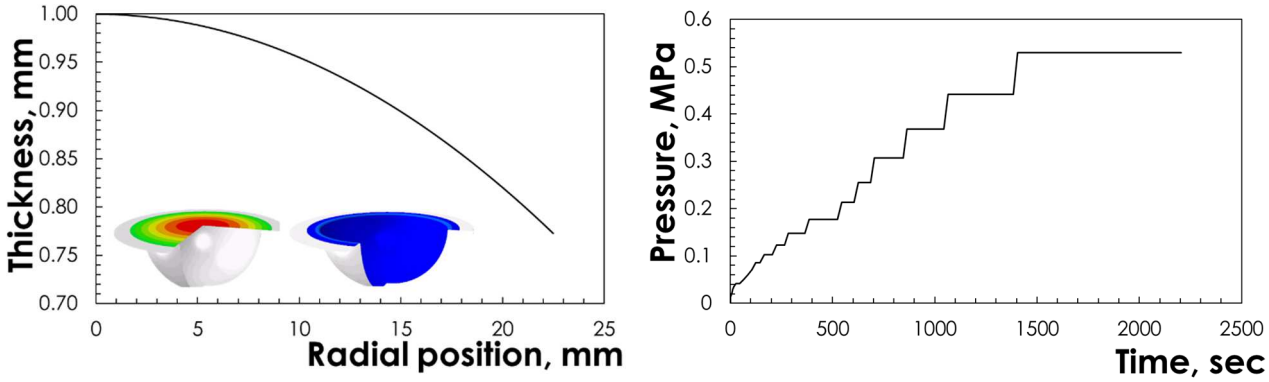

(a) (b)

Figure 119 Optimized initial thickness distribution (a) and gas forming pressure profile (b) obtained via FE model.

As depicted in the same figure, contour maps of the thickness distribution shown the variable thickness before forming (colours range from green in correspondence of the maximum value to the minimum placed in the sample center) and (with the blue colour) the quite constant thickness profile after forming.
At the same time, in order to guarantee high capability to fit very well the die shape in a reasonable cycle time, optimized gas pressure profile (Figure 119b) was obtained from FE model imposing a strain rate equal to $0.0005s^{-1}$ by adopting K and m value implemented in the material model suggested by Enikeev and Kruglov [56].
The FE model adopted was the same 2D-axisymmetric (section 2.3.4 in chapter 2) exploited to evaluate performances of the new methodology proposed to calibrate the Carpenter constitutive material model.

5.1.2. Results obtained after the SPIF step

Therefore, as abovementioned, to obtain a controlled thickness distribution along the radial direction, a dome-shape was designed according to the sine law (equation 16).

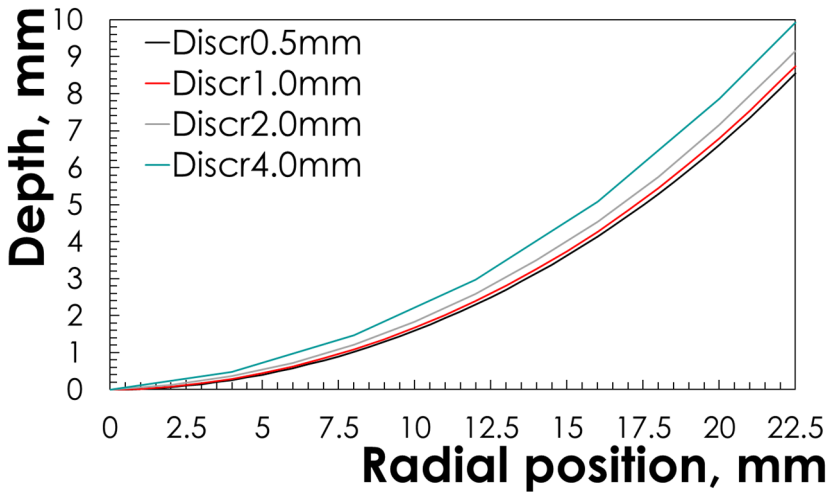

Figure 120 Depth according to the radial position as predicted by the sine law.

Considering numerical results (described in the previous paragraph), a procedure based on the minimization of the error between the initial shape of the blank (in terms of thickness distribution) and the actual distribution obtained applying the sine law was exploited: different values of α were determined by justifying a dome-shape as final geometry (Figure 120).
Depending on the alpha change according to the radial position, the geometry is strongly dependent from the discretization used for the radial position. For this reason, four different discretization values were selected, as depicted in Figure 120 and reported in Table 37.
The total radial length was fixed and equal to 22.5mm.

Discretization, mm	Max Alpha, deg	Max Depth, mm
0.5	39.41	8.546
1.0	39.41	8.747
2.0	39.41	9.157
4.0	39.41	9.923

Table 37 Different dome-shapes designed.

The highest variation concerns the maximum depth of the shape: for example, passing from a discretization of 0.5mm to 4.0mm, the maximum depth obtained ranges respectively from 8.546mm to 9.923mm.
Moreover, since the SPIFed component was needed for the vessel manufacturing by means of SPF process using a spherical cavity with a fillet entry radius of 3mm, the four geometries were designed with the same fillet radius in the peripherical zone (as depicted in Figure 121).

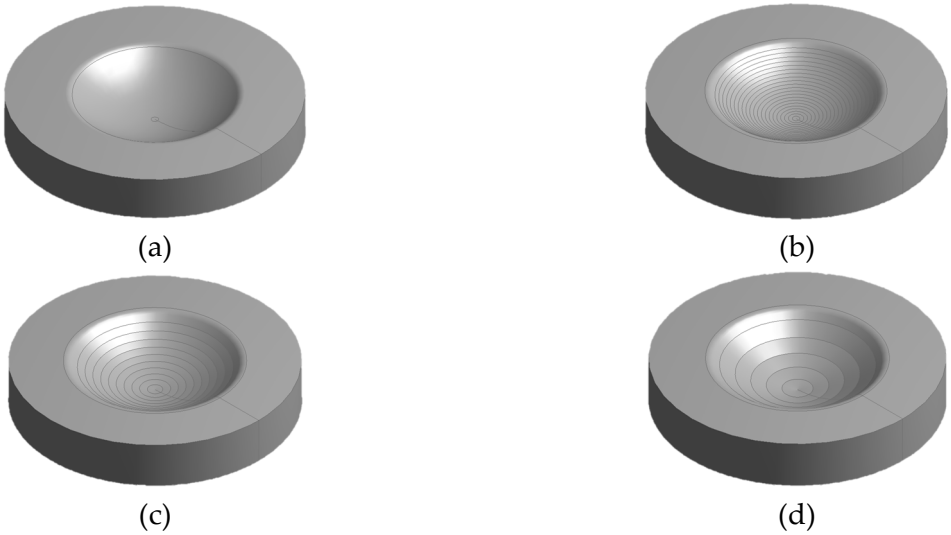

Figure 121: Dome-shapes performed by changing the discretization: (a) 0.5mm, (b) 1.0mm, (c) 2.0mm and (d) 4.0mm.

According to feasible limit of the used Kondia HS1000 Vertical machining center, the highest value of SS (10000rpm) available was adopted; in fact, this value allows to increase the temperature of the sheet during the test and consequently also the material formability. In addition, starting from previous work [96], FR and SD equal respectively to 400mm·min^{-1}

and 0.2mm, which allows to achieve acceptable cycle times, were used to perform preliminary tests.

The thickness distributions associated to the four samples subjected to SPIF process were then compared in order to evaluate the effect of the discretization. Graph reported in Figure 122 shows that a reduction of the discretization value allows to obtain a distribution of thickness very close to the target one. In addition, the peripherical zone on the right reverses the trend due to inevitable bending phenomena.

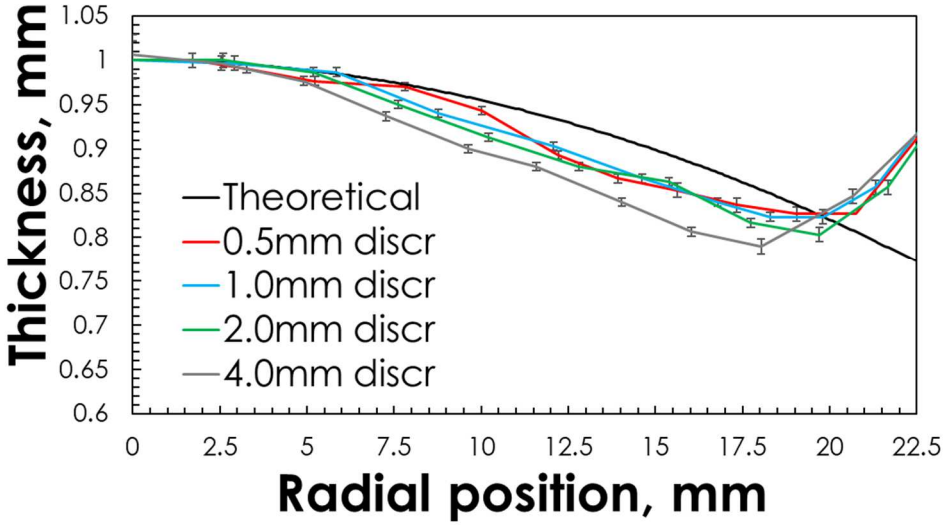

Figure 122: Thickness distribution according to discretization adopted.

According with the results summarized in Figure 122, adopting a discretization equal to 0.5mm (red curve), an experimental plan was conducted changing the values according to a Full Factorial Design (FFD) aimed at determining the optimal working condition (to achieve a thickness distribution very closed to the theoretical one).

Test number	SS, rpm	FR, mm·min^{-1}	SD, mm
1	10000	200	0.1
2	10000	200	0.2
3	10000	200	0.3
4	10000	400	0.1
5	10000	400	0.2
6	10000	400	0.3
7	10000	600	0.1
8	10000	600	0.2
9	10000	600	0.3

Table 38 Full factorial experimental plan performed.

The experimental plan was based on two input variables (FR and SD) and three levels for each. As previous anticipated, the SS was fixed at 10000rpm; regarding the levels for the other two variables, the preliminary test performed was considered as reference. For this reason, the full factorial experimental plan listed in Table 38 was performed. Each

experimental condition was performed three times at room temperature on preheated sheets (section 2.4.2.2) to increase Mg alloy formability.
Deformed samples obtained after SPIF process are depicted in Figure 123.

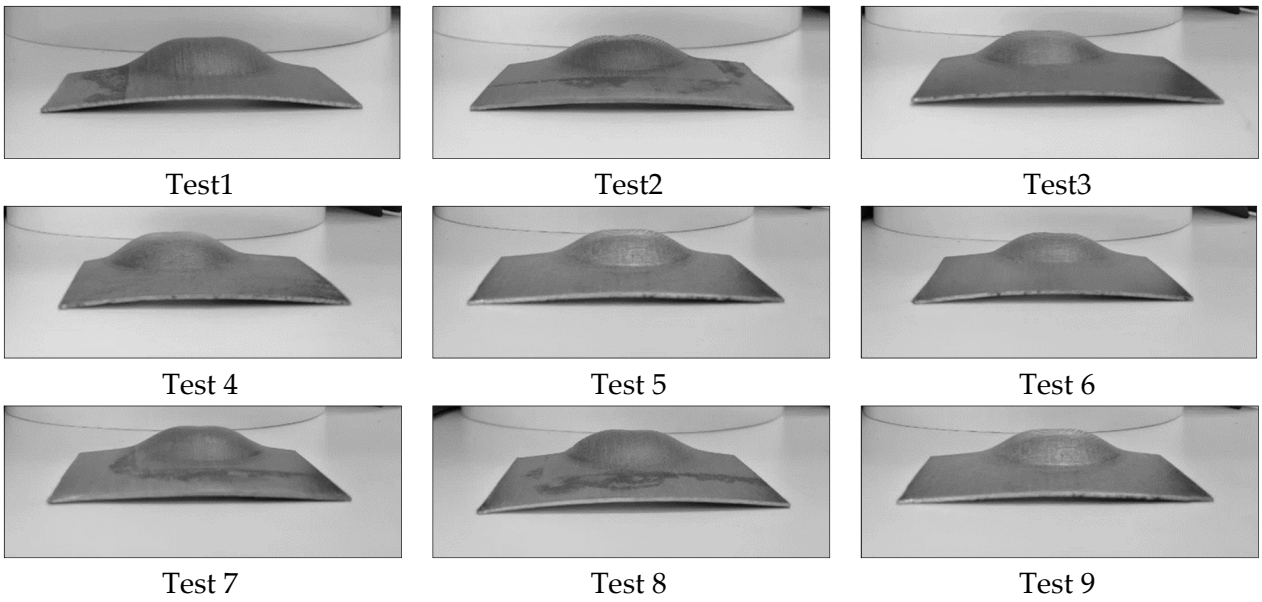

Figure 123: Samples deriving from the experimental plan.

Analyses in terms of thickness distribution and surface roughness (Ra) were carried out. If the thickness distribution represents the main objective, also the Ra (intimately related to the step down) can be considered essential to obtain sound components.
Thickness distributions are reported in the graphs from Figure 124 to Figure 126.

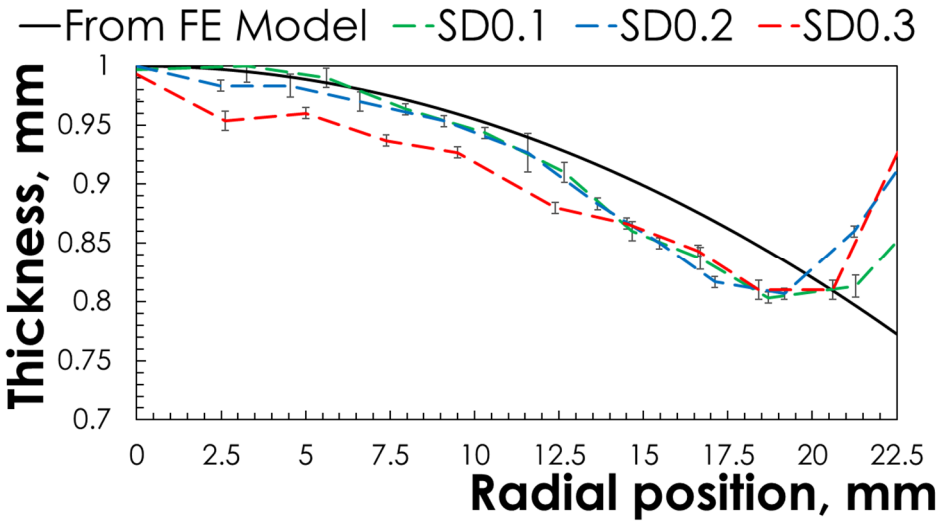

Figure 124: Thickness distribution according to SD investigated and at fixed FR (200mm·min^{-1}).

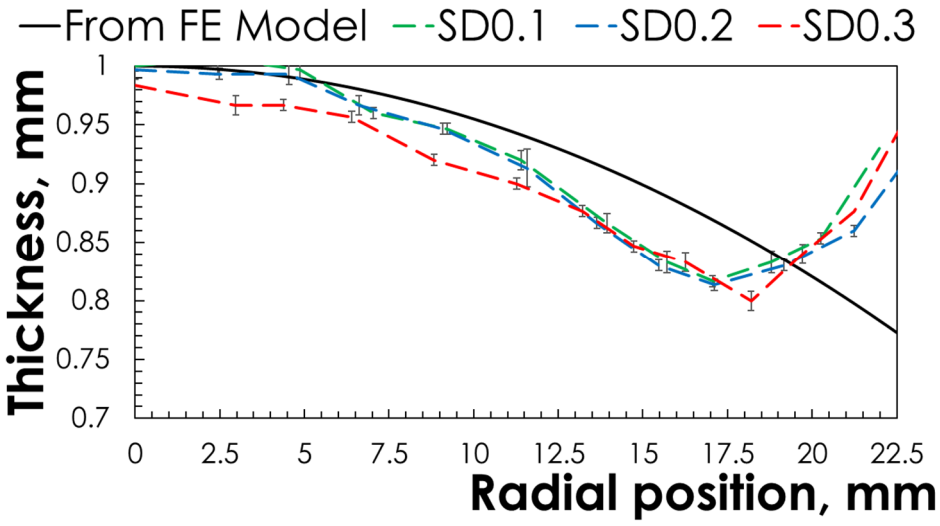

Figure 125: Thickness distribution according to SD investigated and at fixed FR (400mm·min^{-1}).

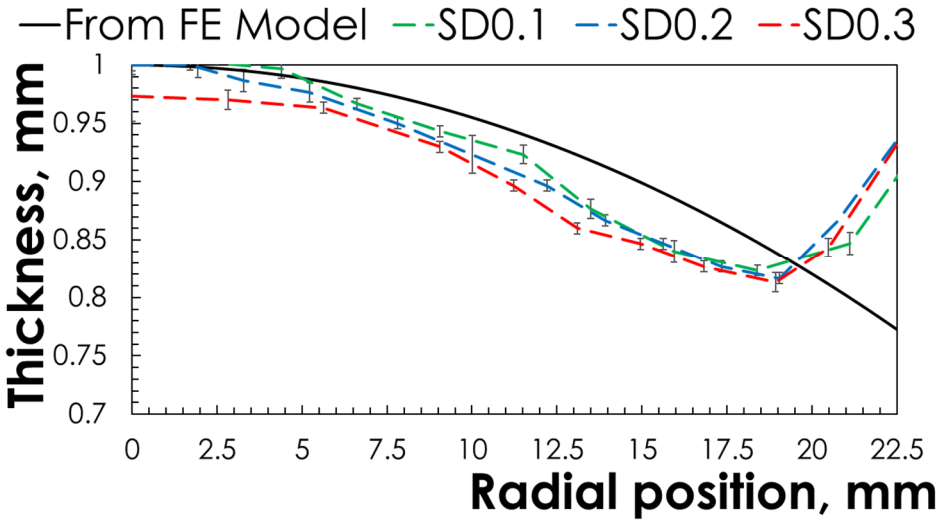

Figure 126: Thickness distribution according to SD investigated and at fixed FR (600mm·min^{-1}).

Considering a fixed value of FR, the difference between the experimental thickness distribution obtained and the theoretical one increase with the SD.
The dashed red curves related to the highest SD value (0.3mm) is always lower than the other two.
Albeit the difference between the curve obtained for a SD equal to 0.1 and 0.2mm appear to be reduced, the minimum value of error is attributable to the green dashed curve (0.2mm as SD). This last consideration is true for all FR considered.
The Mean-Percent-Differences (MPDs) assumed as indicator of errors - reported in equation 19 - for all investigated process conditions are summarized in Table 39.
The MPD increases with the SD and the FR; the increase due to the SD effect result to be greater than the one related to the FR.
Generally, the MPD recorded for the nine conditions ranges from 3.15 to 5.93%, suggesting that the application of the sine law coupled with a suitable discretization (0.5mm) according to the radial position could lead to satisfactory results in terms of thickness distribution of the SPIFed part.

Test number	SS, rpm	FR, mm·min^{-1}	SD, mm	Error, %
1	10000	200	0.1	3.15
2	10000	200	0.2	4.47
3	10000	200	0.3	5.42
4	10000	400	0.1	4.10
5	10000	400	0.2	4.67
6	10000	400	0.3	5.88
7	10000	600	0.1	4.28
8	10000	600	0.2	4.81
9	10000	600	0.3	5.93

Table 39 Average percentage errors for all investigated processing conditions.

Finally, as summarized in Figure 127, surface roughness tests (performed using a Mahr Micromar 40 EWR) showed a marked increase of the Ra with the SD. On the contrary, the FR effect appears to be negligible.

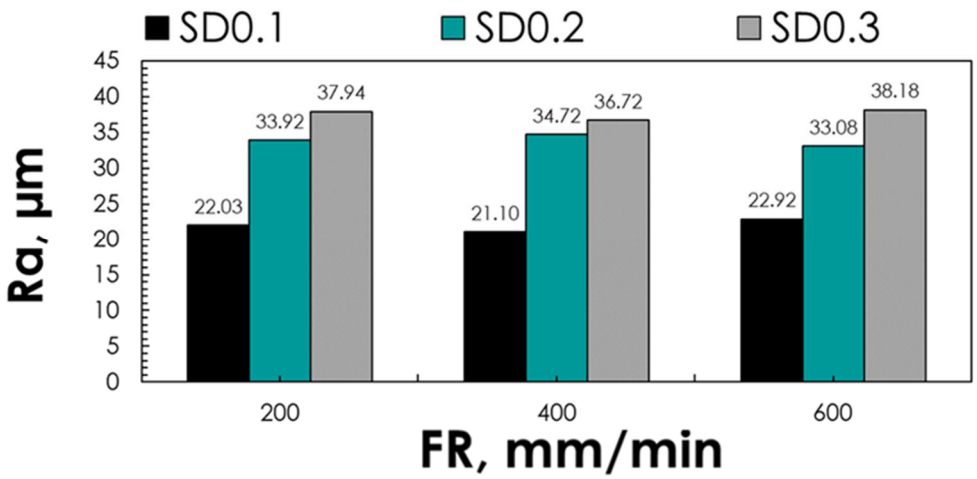

Figure 127: Ra according to SD and FR values investigated.

The Ra values obtained vary between a minimum equal to 21.10µm (SD and FR respectively equal to 0.1mm and 400 mm·min^{-1}) and a maximum of 38.18µm (SD and FR respectively equal to 0.3mm and 600 mm·min^{-1}).
Thus, neglecting the effect of the FR, an average value of Ra according to the SD alone can be calculated (Table 40).

SS, rpm	SD, mm	Ra, µm
10000	0.1	22.02±0.74
10000	0.2	33.91±0.67
10000	0.3	37.61±0.64

Table 40 Average Ra values according to the SD.

5.1.3. Results after the final SPF step

Based on the pressure profile determined numerically, experimental SPF tests were performed by exploiting the samples obtained from the SPIF experimental Full Factorial plan and applying the optimized gas pressure profile (able to guarantee a constant strain rate equal to $0.0005s^{-1}$) reported in the graph in Figure 119b. for each test - performed two times - a temperature and a BHF equal respectively to 450°C and 12kN were used.

(a) (b) (c)

Figure 128: Failure occurred in all samples deriving from the SPIF process with a SD of 0.1mm and a FR equal to (a) 200 $mm \cdot min^{-1}$, (b) 400 $mm \cdot min^{-1}$ and (c) 600 $mm \cdot min^{-1}$.

All tested SPIFed samples characterized by a Step Down equal to 0.1mm showed a premature rupture due to the presence of excessive thinning randomly located (underlined with the withes circles), as shown in
Figure **128**.

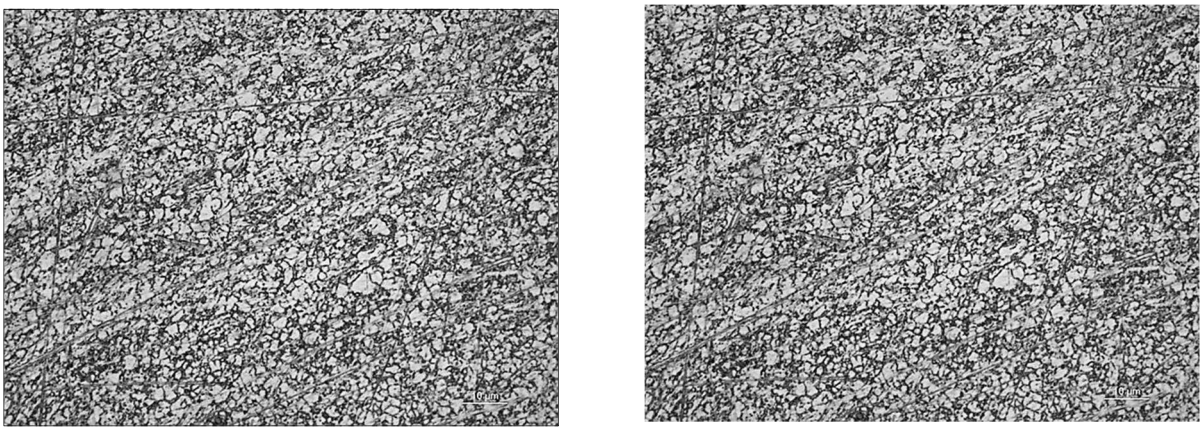

(a) (d)

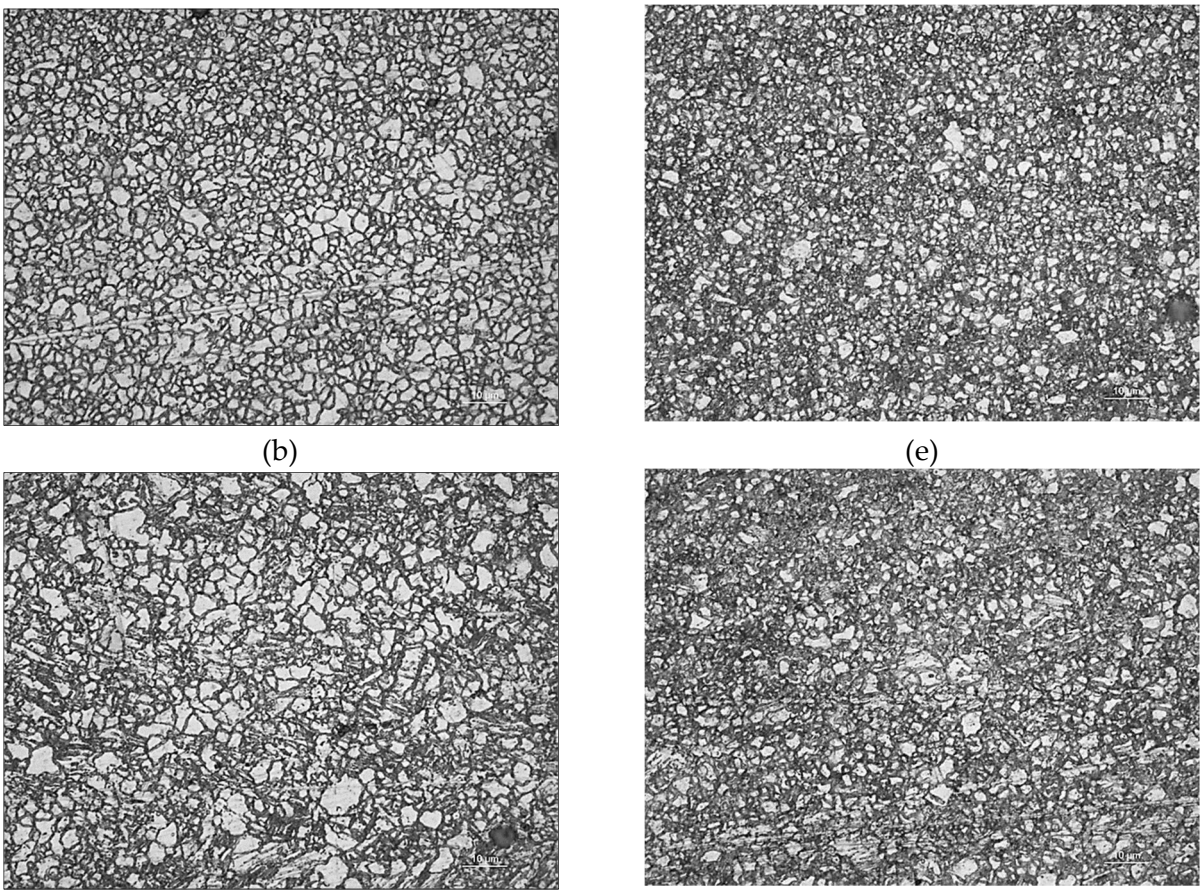

Figure 129: Microstructure of tested samples after SPF according to: (i) feed rate, 200 (a), 400 (b) and 600mm·min^{-1}, at a fixed step down of 0.1mm; (ii) step down, 0.1 (d), 0.2 (e) and 0.3mm, at a fixed feed rate of 200 mm·min^{-1}.

In order to evaluate the effect of microstructure, after SPIF step, on the premature rupture during SPF process, micrographs reported in Figure 129 show the grain size evolution according to respectively FR – from (a) to (c) – and SD – from (d) to (f).

Effect of FR, considering the three samples obtained by setting a step down equal to 0.1mm, appears to be very evident: the mean grain size grows markedly moving from 200 to 600mm·min^{-1}.

Considering the SD effect, although less marked, an inversely proportional growth to the SD value is recorded.

This phenomenon, as supported by literature [97], is due to dynamic recrystallizing in the contact area between the tool and sample: as know, recrystallization is a time-dependent phenomenon that causes microstructural reorganization with a marked reduction in the average grain size.

In addition to the microstructure observation, it is possible to assert that, when steps down adopted are very small, in correspondence of the higher slope values (peripherical zone) a greater overlap of contiguous tool trajectories happens.

This overlap causes excessive localized deformation (thinning).

Clearly, areas affected by excessive thinning become preferential zones of deformation concentration during the SPF process (up to eventually rupture).

Considering both aspects simultaneously, it is possible to associate the premature rupture of the SPIFed samples, obtained adopting a SD of 0.1mm, with the formability reduction (due to grain size reduction) coupled with presence of preferential rupture zones (due to excessive localized thinning caused by the tool trajectory overlap).
Regarding the other six conditions tested, all final shapes obtained were sound, as depicted in Figure 130.

Figure 130: Sound samples obtained from experimental SPF tests. Samples from (a) to (c) were obtained starting from the SPIFed blanks with a SD of 0.2mm and a FR equal to (a) 200 mm·min^{-1}, (b) 400 mm·min^{-1} and (c) 600 mm·min^{-1}. Samples from (d) to (f) were obtained starting from the SPIFed blanks with a SD of 0.3mm and a FR equal to (e) 200mm·min^{-1}, (d) 400mm·min^{-1} and (f) 600mm·min^{-1}.

Experimental dome heights according to forming time are reported in the graphs in Figure 131 and Figure 132.

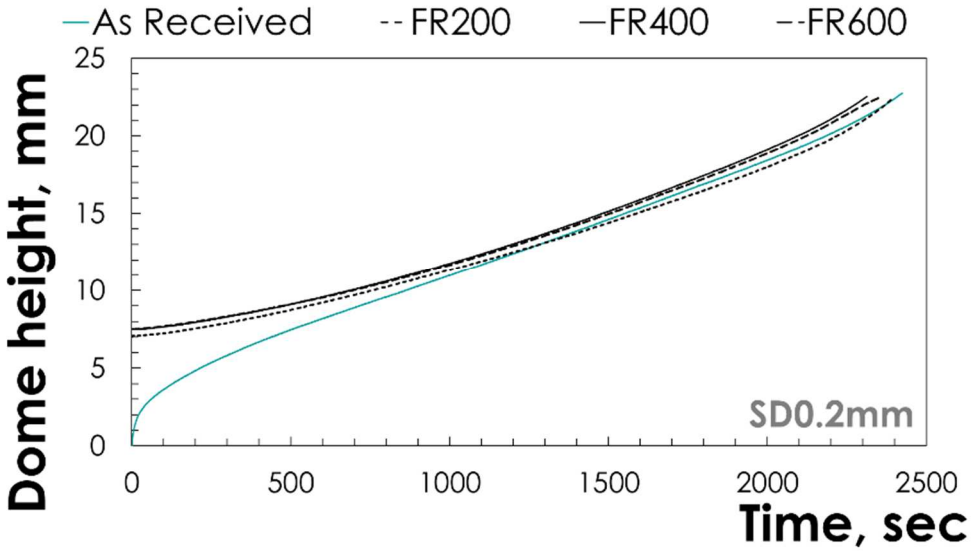

Figure 131: Dome height according to forming time using SPIFed blanks (SD0.2mm) with three different FR values.

Obtained results are compared with those obtained by testing an undeformed blank (in "as-received" condition) with a constant thickness of 1mm (green curve). It is evident that at the beginning of the experimental SPF test the height of the pre-processed samples via SPIF (black curves) is higher than the one in the "as-received" condition.
Regarding the tests conducted using SPIFed samples with SD equal to 0.2mm (Figure 131), all curves are almost overlapping each other. In addition, after about 1000s the trend of the three black curves are the same of the one related to the sample in "as-received" condition. The previous considerations are valid also for the results deriving from the SPIFed samples obtained with a SD equal to 0.3mm (Figure 132).

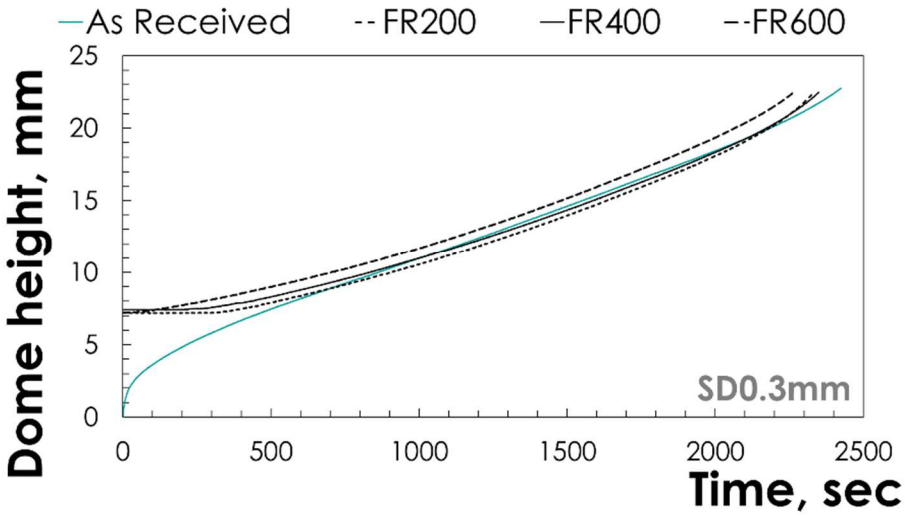

Figure 132: Dome height according to forming time using SPIFed blanks (SD0.3mm) with three different FR values.

Thickness distributions, obtained using again a Mitutoyo 573-701 Absolute Digimatic Offset Calliper and reported in the graphs in Figure 133 and Figure 134, are related to the curvilinear position: for this reason the total length plotted was greater than the SPF die cavity radius (equal to 22.5mm).

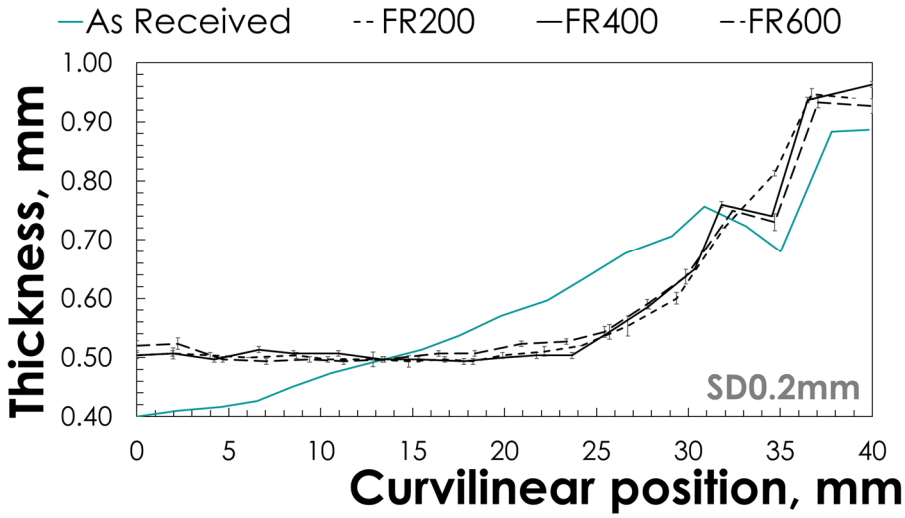

Figure 133: Thickness distribution using SPIFed blanks (SD0.2mm) with three different FR values.

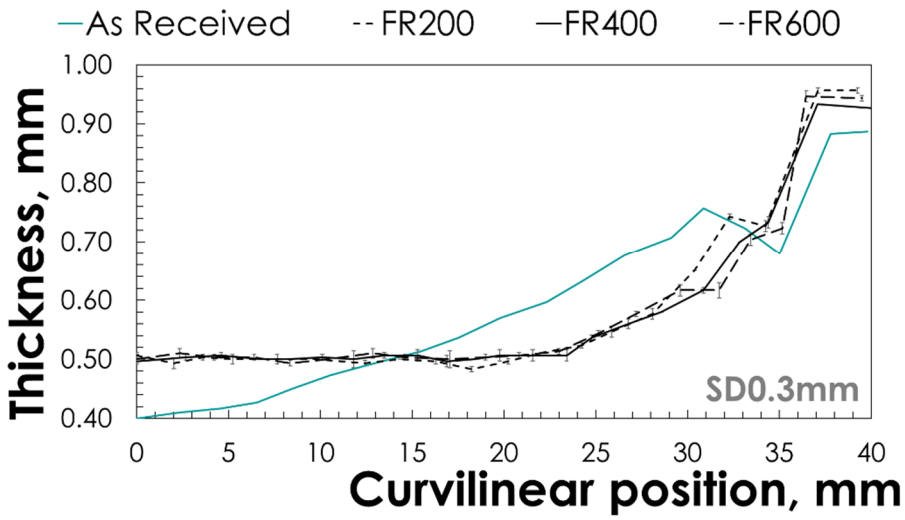

Figure 134: Thickness distribution using SPIFed blanks (SD0.3mm) with three different FR values.

For a fixed SD value, results with standard deviation bars are reported below and summarized according to the different FR investigated. In addition, for each graph, the comparison with the thickness distribution obtained in correspondence of the "as-received" condition (green curve) is proposed.
A good uniformity of thickness (about 65% of the total curvilinear length) was obtained.
If all thickness trends related to the samples previously modified by SPIF are compared with the results coming from the test performed using an undeformed sample, very marked differences are visible.
Regarding the comparison of results obtained for a SD of 0.2mm, the three curves appear to be very similar to each other. The same consideration is valid for the results obtained exploiting SPIFed blanks obtained with a SD of 0.3mm.
Analyses about the length of the constant thickness zone allow to obtain additional information about the effect of the investigated process parameters.

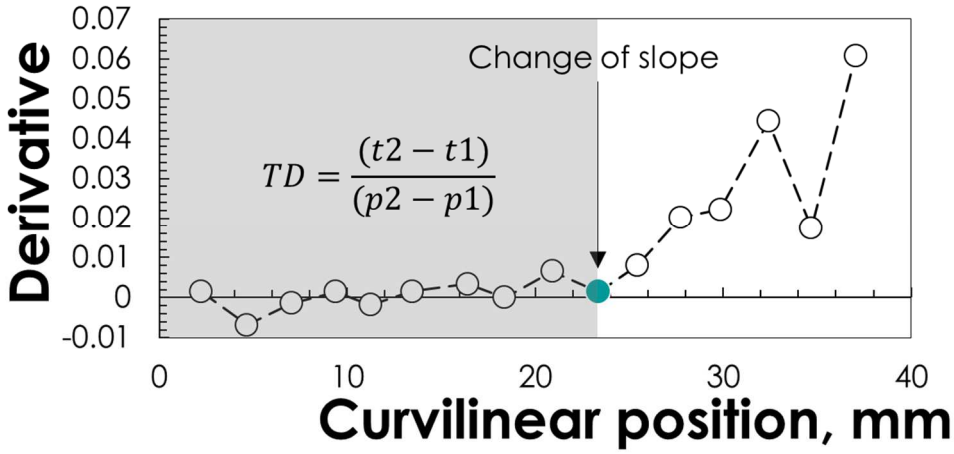

Figure 135: Constant thickness length determination: t and p represent respectively the thickness and the curvilinear position.

The curvilinear length with a constant thickness value was calculated for each sample tested considering the Thickness Derivative (TD) with respect to the curvilinear position.
When the curve slope of the derivative changes drastically, the thickness is no longer considered constant. The adopted criterion is reported Figure 135 as example for only one of the six samples analyzed.
Applying this methodology, results obtained in terms of Constant Thickness Length (CTL), which identifies the assumable constant length between the center of the sample and the point where TD grows dramatically, are summarized in Figure 136.

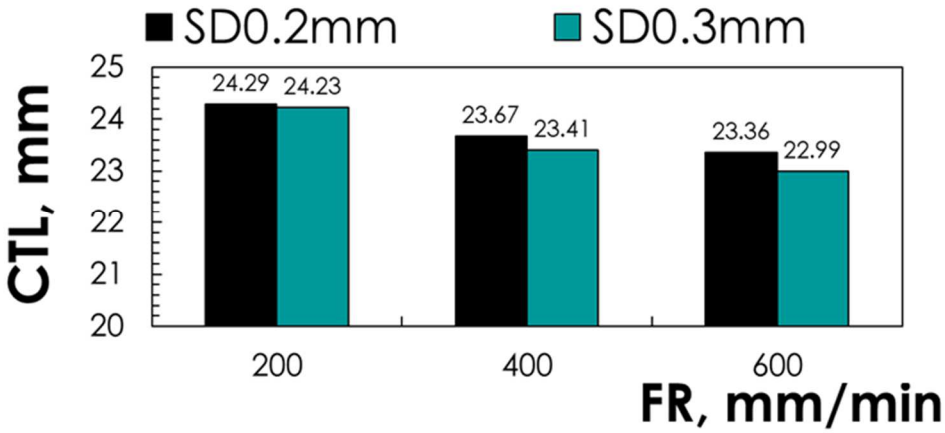

Figure 136: Constant Thickness Lengths (CTL) comparison.

As shown in the histogram in Figure 136, the predominant effect in terms of CTL can be associated with the FR. In fact, passing from 200 to 600 mm·min^{-1}, a decrease of 3.83 and 5.12% is recorded for a SD value respectively equal to 0.2 and 0.3mm.
The final experimental analyses performed regard the surface roughness. Despite the lowest values of Ra are attributable to the lowest SD investigated (0.1mm), a premature rupture of all samples characterized by this SD value occurred.
On the contrary, the other two conditions in terms of SD (0.2 and 0.3mm) allowed to obtain sound components.

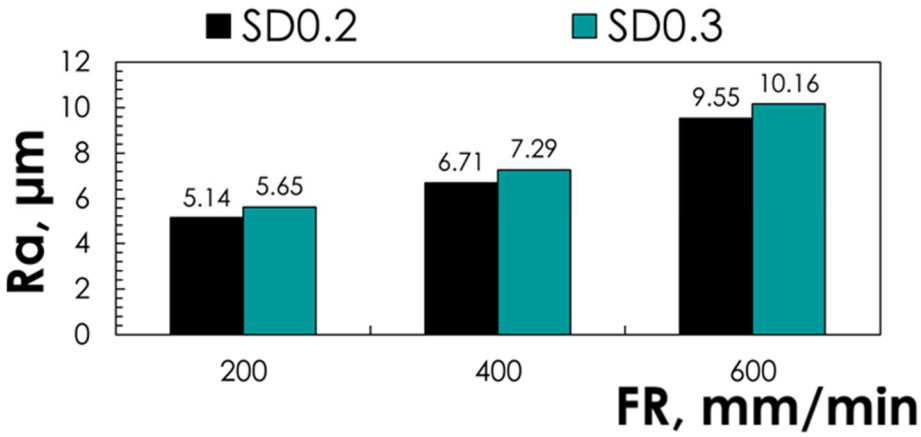

Figure 137: Ra comparison after SPF process.

Regarding the six experimental tests performed without any rupture, Ra measures after the SPF process were carried out and compared with those after SPIF.
Obtained results are summarized in the next two graphs (Figure 137 and Figure 138).
Contrary to the results about the CTL, both parameters of SPIF process investigated (FR and SD) seem to influence the Ra of the final component obtained by means of SPF process. In fact, considering a fixed value of FR and passing from 0.2 to 0.3mm as SD, the average Ra obtained shows an increase of about 0.5μm.
At the same time, passing from a FR of 200 to 600 mm·min^{-1}, an increase of 85.8 and 79.8% is registered for SD equal to 0.2 and 0.3mm respectively (Figure 137).
The last analysis purposed is represented by the comparison between the Ra values after SPIF and the ones after SPIF.

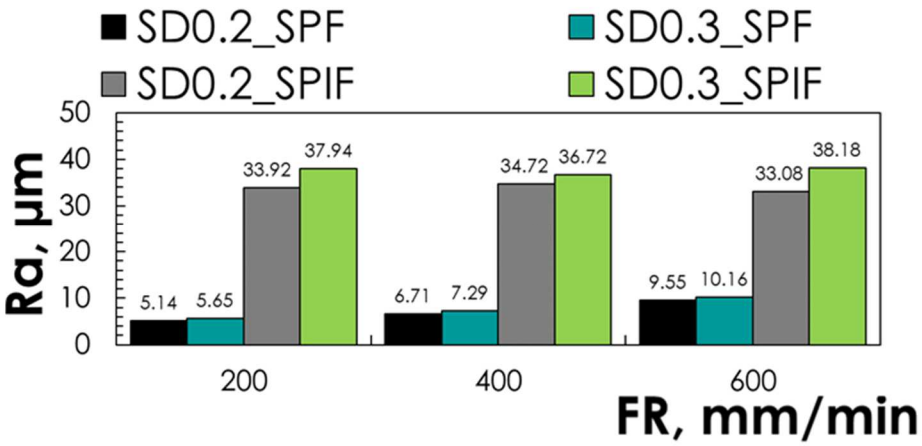

Figure 138: Ra comparison between samples from SPIF and SPF processes.

Ra values after SPIF and SPF are clearly different from each other (Figure 138). Generally, considering the obtained values after SPIF, the subsequent SPF step allows to reduce drastically the Ra: differences between SPIFed samples before and after SPF results are listed in the last column of Table 41.

SD, mm	FR, mm·min^{-1}	Ra from SPIF, μm	Ra from SPF, μm	Ra difference, μm
0.2	200	33.92	5.14	28.78
0.2	400	34.72	6.71	28.01
0.2	600	33.08	9.55	23.53
0.3	200	37.93	5.65	32.28
0.3	400	36.72	7.29	29.43
0.3	600	38.18	10.16	28.02

Table 41 Effect of SPF process in terms of Ra.

The Ra difference ranges from a minimum value equal to 23.53μm (SD and FR equal respectively to 0.2mm and 600mm·min^{-1}) to a maximum of 32.28μm (SD and FR equal respectively to 0.3mm and 200 mm·min^{-1}). The difference is inversely proportional to the FR and is more pronounced for the SD equal to 0.3mm.

5.2.Thickness distribution modification via localized LHT

In addition to the previous strategy able to modify the thickness distribution of the final component manufactured by means of SPF process, another approach proposed in the present research activity is represent by a localized change of the material properties prior to forming thanks to localized heat treatment.
In fact, as know, the grain growth can be strongly influenced by the initial grain size, particularly when dynamical recrystallization occurs [98].
Heat treatment represents an effective strategy to improve the properties of the Mg alloys. In fact, when the blank must be subject to a wide range of deformation conditions during the manufacturing process, a suitable strategy can be represented by the determination of variable properties within the undeformed sheet by means of localized heat treatment before the manufacturing process [5]. Therefore, localized LHT were performed by means of a CO_2 laser source on AZ31B-H24 Mg alloy blank for the SPF manufacturing of a spherical shape similar to the previous one (performed coupling SPIF and SPF process).
The approach analyzed in this section represent the first attempt aimed to evaluate the feasibility of the proposed methodology. The effect of LHT on AZ31B Mg alloy was investigated experimentally and numerically. In fact, starting from LHTed samples with different laser input parameters, the attention was focused on the microstructure evolution according to the temperature gradient on the samples tested. From a numerical point of view, the temperature distributions obtained by experimental LHT tests were adopted to calibrate the numerical model; subsequently, to predict the microstructure evolution, the constitutive material model suggests by Miao et al. [6] was implemented to perform LHT numerical simulations. Finally, LHTed samples were - numerically and experimentally – subjected to SPF process aimed to fabricate the spherical component. With reference to the FE modelling, the material model suggested by Carpenter and calibrated as explained in chapter 3 was again adopted to simulate SPF process.

5.2.1. Experimental LHT tests results

Experimental results were carried out using a CO_2 laser source with a maximum power equal to 2500 W. Experimental facility and a scheme of the experimental procedure adopted are both reported in Figure 33 (section 2.4.3.1).
Results concerning the two laser power levels investigated (200 and 250W) are summarized in terms of both micrographs and temperature/microstructure evolution respectively in Figure 139 and Figure 140.
Micrographs, reported Figure 139, are related to the as-received condition (a) and the two heat affected zones for LHTed sample with a laser power equal to 200 (b) and 250W (c).
Effects of the LHT are visible for both laser power conditions; in particular, difference between the as-received condition and LHTed samples at 250W is very marked. Considering that the average grain diameter for the as-received alloy condition (Figure 139a) is equal to 9μm, the maximum values obtained after the LHT are 9.7 (7% increase) and 13.1μm (45% increase) respectively for 200 (Figure 139b) and 250W (Figure 139c). at the same

time, the maximum values of the temperature (in the center of sample) are equal to 360°C (at 200W) and 410°C (at 250W).
Both the samples show grain size variations: however, this is much more pronounced when a laser power equal to 250W is applied. Also, the extension of the affected zone is much more pronounced for the highest power.

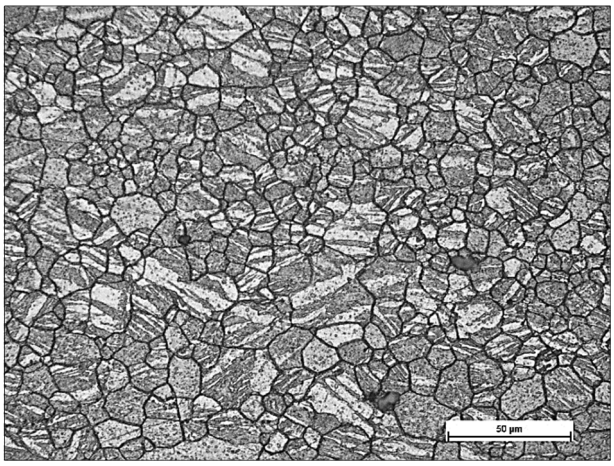

(a)

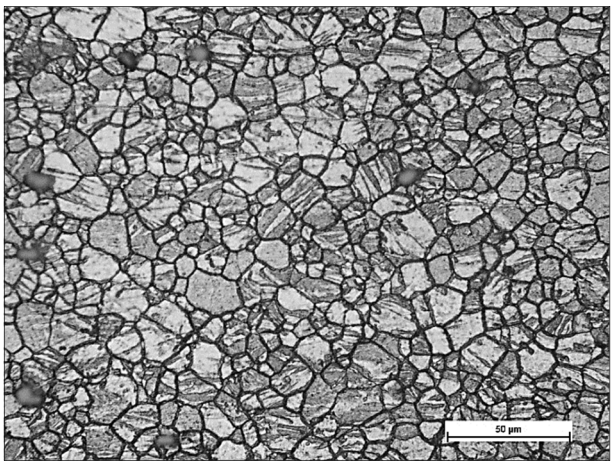

(b)

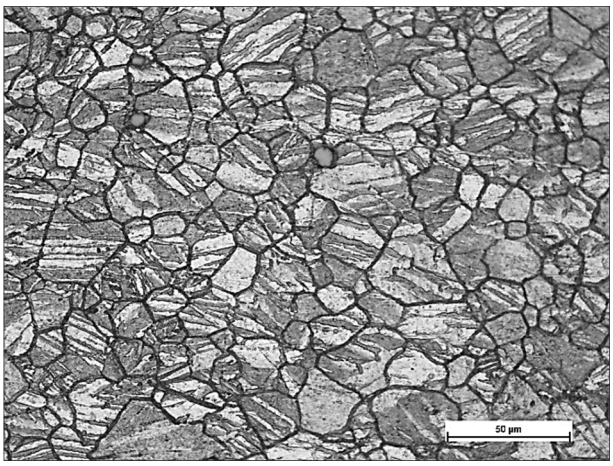

(c)

Figure 139: Microstructure related to (a) the as-received condition and affected zone LHTed samples tested at (b) 200W and (c) 250W samples.

In addition, in both samples the former twin boundaries, which formed during rolling of the sheet material, appear to have deteriorated as a result of recrystallization.
It may be tentatively said that the deterioration of the twin boundaries further progressed in the laser-treated regions for both the 200W and 250W samples.

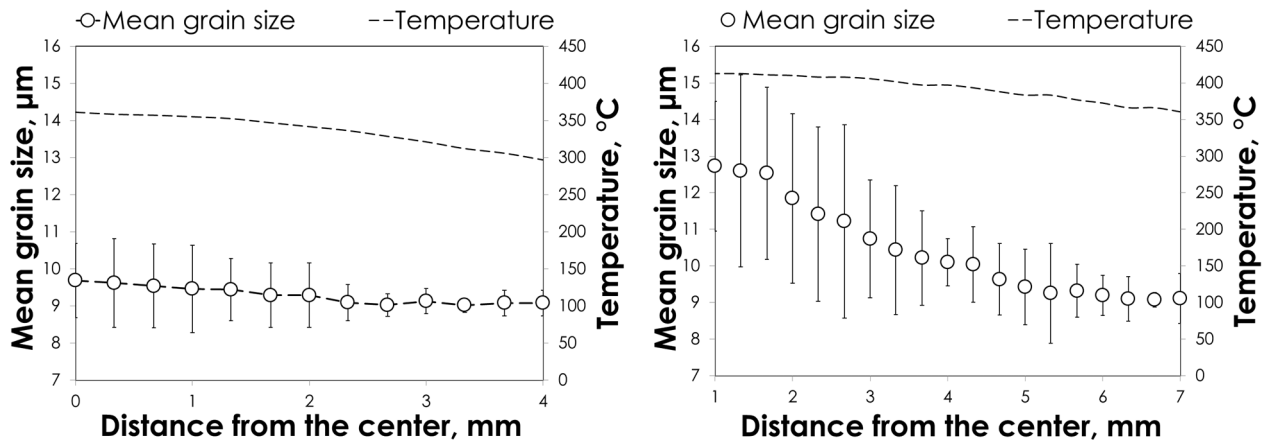

Figure 140: Experimental results: temperature and microstructure for 200 (a) and 250W (b).

5.2.2. LHT Numerical modelling results

Numerical/experimental comparison of the temperature distribution according to the radial path passing from the center of a side of the square laser spot is reported in Figure 141.

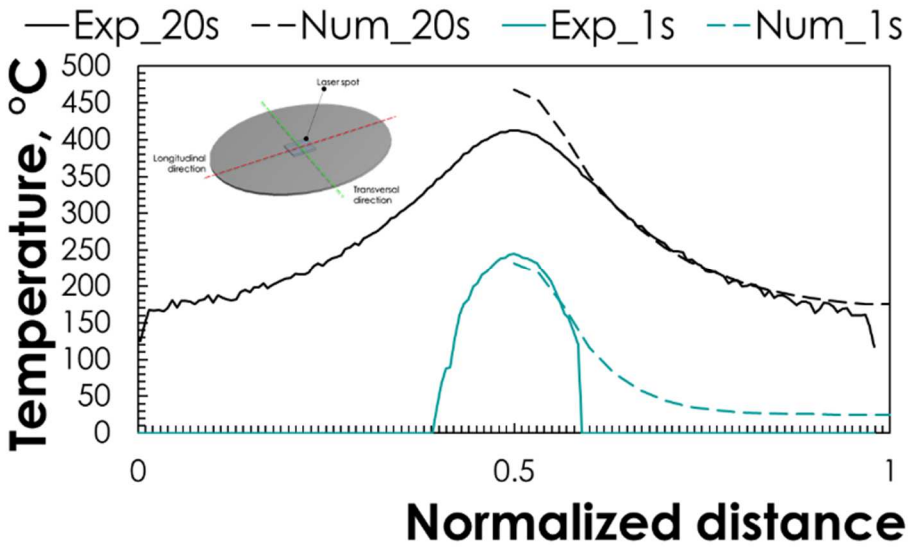

Figure 141 Numerical/Experimental temperature distribution comparison along a radial direction.

Temperature profiles reported are related to the first and the last second of interaction laser-material. Good fitting can be observed for both conditions; the only discrepancy is in correspondence of the sample center at 20s.
Results in terms of grain the average dimension according to the radial position could be thus compared with the experimental values obtained from LHT experiments. In Figure 142 numerical and experimental results in terms of grain size along the radial direction are compared. In particular, in Figure 142a data from the simulation and the experiments setting a laser power equal to 200W (t=20s) are plotted; on the contrary Figure 142b concerns the simulation and the experiments setting a laser power equal to 250W (for 20 seconds).

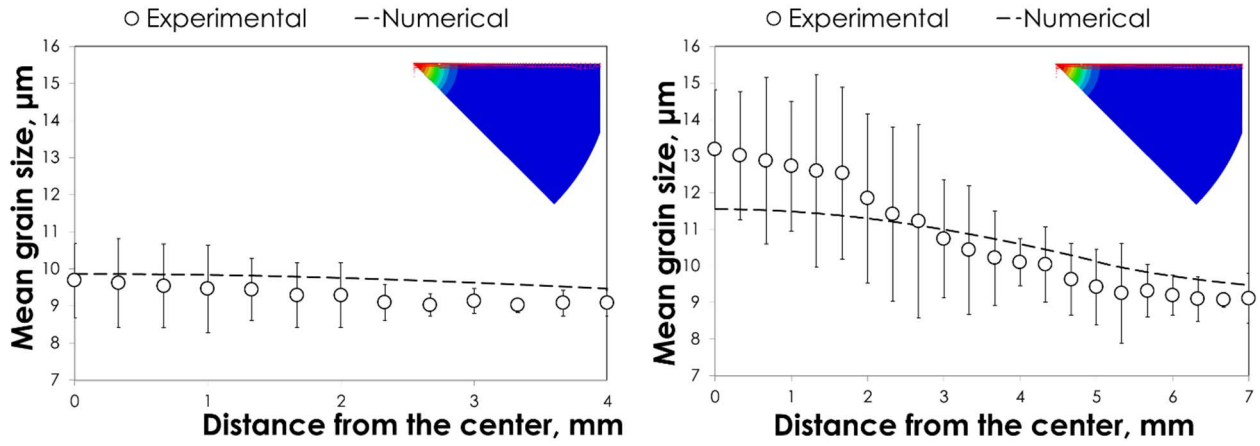

(a) (b)

Figure 142: Numerical/experimental comparison in terms of microstructure evolution for 200W (a) and 250W (b).

It can be noted that Miao's model implemented in the FE model predicts quite well the experimental trend, especially at the lowest level of the laser power.
Focusing the attention on the graph concerning the tests performed setting 250W as laser power, the model has well predicted the evolution of the microstructure except for the central area (about 2mm wide), in which a marked increase in grain size was observed (from 11.8 to 13.1 µm). LHT tests allow to effectively change the microstructure of the investigated Mg alloy in the center of sample due to the action of the laser. The microstructure evolution reveals to be much more pronounced when a laser power equal to 250W was applied.
A good numerical/experimental fitting is obtained for the low power laser and, except for the area closest to the center.

5.2.3. Results from experimental SPF tests on LHTed

Using the facility reported and discussed in section 2.4.3.3 (chapter 2), experimental SPF tests were performed adopting samples deriving from the previous LHT.

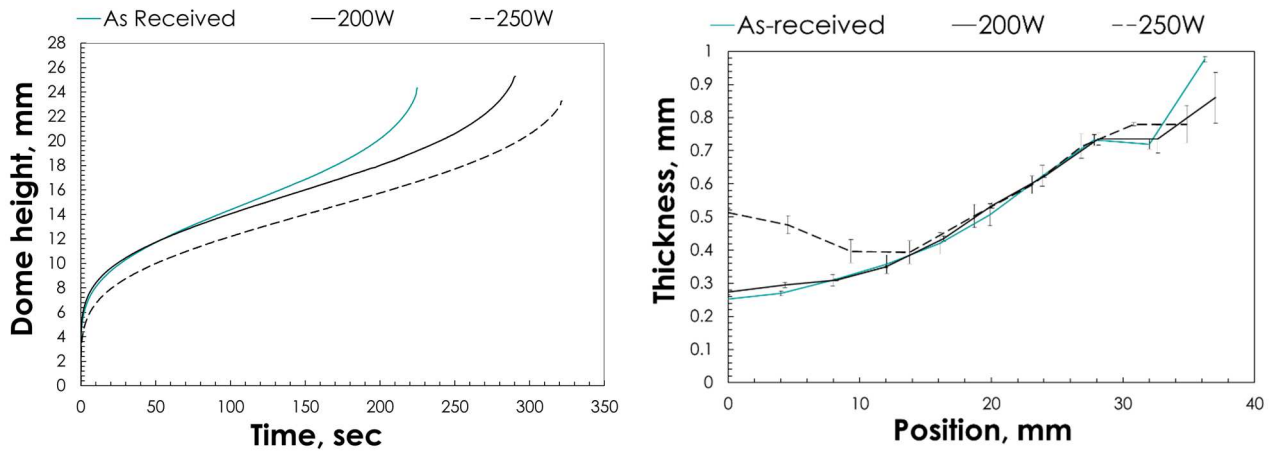

(a) (b)

Figure 143: Experimental results related to LHTed samples at 200 and 250W: (a) dome height according to time forming and (b) thickness distribution along a radial path.

Each condition was tested two times. Results in terms of dome height and thickness distribution are proposed in Figure 143. In addition, curves obtained are compared with the one deriving from test performed with the same condition (in terms of temperature and gas pressure) using an initial untreated Mg alloy sheet.
LHT improves the formability of the AZ31B Mg alloy when the lowest laser power level is adopted. The adoption of a 250W laser power, despite the dome height at rupture is the same respect to the as-received condition, change drastically the thickness distribution in center of the blank.

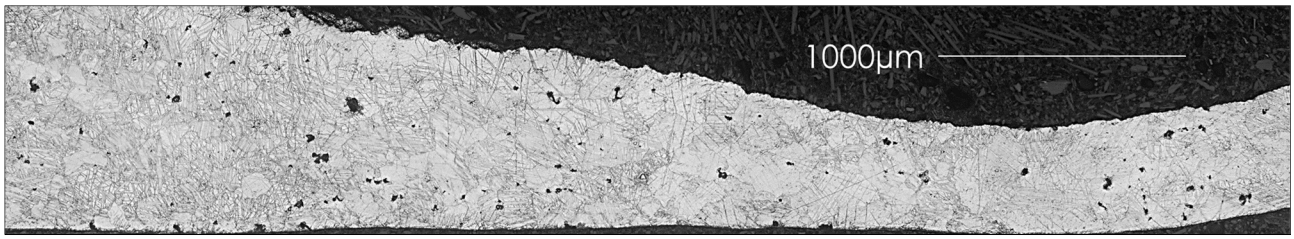

Figure 144: Microstructure evolution along a radial path of the spherical shape.

Observing the micrograph in Figure 144, marked difference between affected zone (on the left) and the rupture zone (on the right) occurred after forming of 200W LHTed sample. Cavitation effects are present randomly along the analyzed section; twinning is more concentrated in the area affected by the thermal treatment. Great difference in terms of thickness between the two areas is particularly evident.

5.2.4. Numerical modelling results

Comparison in terms of dome height and thickness distribution between numerical and experimental results (respectively in Figure 145 and Figure 146) show a non-negligible difference, especially if test performed using 200W LHTed sample is considered.

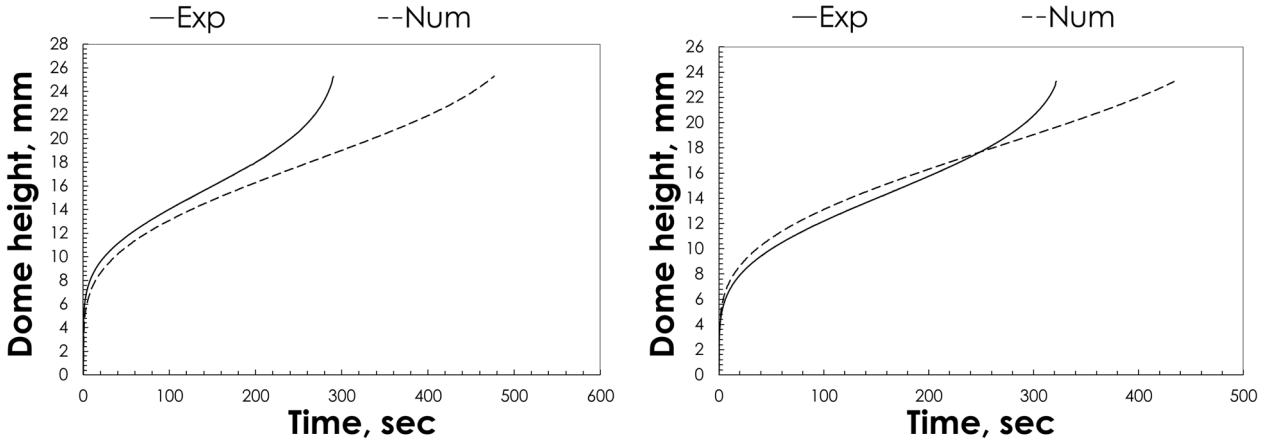

(a) (b)

Figure 145 Numerical/experimental dome height comparison for (a) 200 and (b) 250W as laser power.

As possible to see from graphs in Figure 146, in both cases, the trend of thickness distribution is quite well predicted. In particular, the main difference is located in correspondence of the peripherical zone for the test conducted using 200W LHTed sample; on the contrary, for 250W LHTed sample, the main discrepancies are attributable to the central zone, even if the trend is well predicted by the numerical model.
The green curves represent the experimental thickness distribution previously obtained to calibrate Carpenter material model exploiting the same gas pressure and sample in as-received condition (green curves in previous graphs): it seems evident that the numerical model in the peripheral zone cannot fully predict the effect of the pre-treatment performed before forming the sheet. Errors referring to both dome height and thickness distribution show values generally ranging between 5.44 and 10.80%.

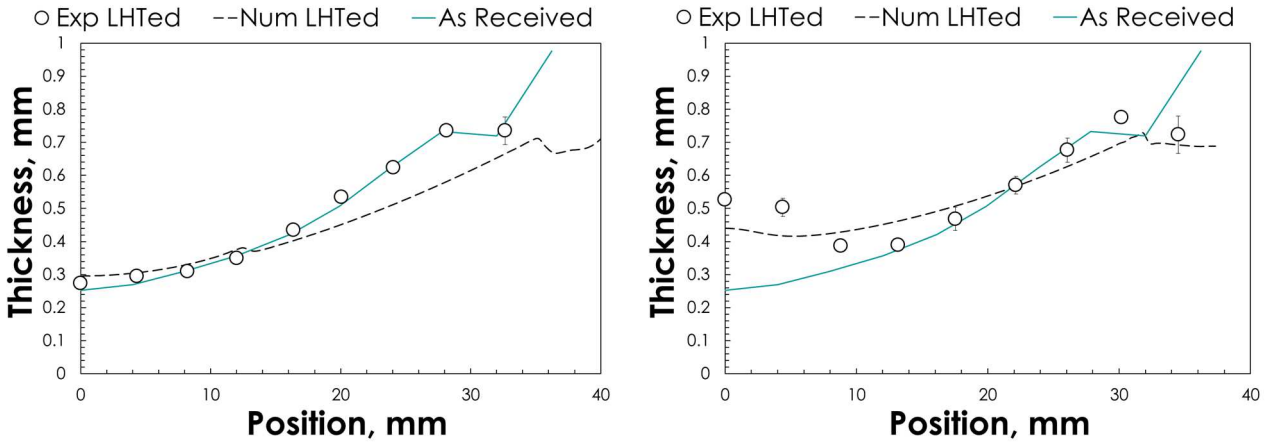

(a) (b)

Figure 146 Numerical/experimental thickness distribution comparison for (a) 200 and (b) 250W as laser power.

Specifically, as listed in Table 34, the dome height error is equal to 10.15 and 5.44% respectively for 200W LHTed and 250W LHTed samples, demonstrating a better capability of the FE model to predict the behaviour of the alloy when a more marked microstructural change (see Figure 143) was found.

LHT Power, W	DH_{RMS}, mm	DH_{MPD}, %	TD_{RMS}, mm	TD_{MPD}, %
200	2.07	10.15	0.32	10.24
250	0.72	5.44	0.25	10.80

Table 42 Obtained errors related to Dome Heights (DH) and Thickness Distribution (TD).

6. Manufacturing of a resorbable cheekbone implant by advanced sheet metal forming processes

As reported in literature, the scientific research has developed several biomaterials for bone repairing/regeneration [99]. The most used materials for implant cheekbone prostheses are Ti alloys and the Cobalt-Chromium alloys: in fact, they possess good corrosion resistance along with excellent load-bearing capabilities. However, when used for temporary solutions (such as plates, screws, wires) a second surgery step is required to remove the implant after the tissues have healed, which leads to increase the patient morbidity and healthcare costs [31,100]. Among different metallic materials, Mg alloys are currently attracting a great interest. In fact, due to its acceptable mechanical properties and to its good biocompatibility, Mg alloys can be considered as an optimal solution for removable cheekbone prostheses to be used in bone repairing/regeneration. To fulfil its restorative function, it is well known that the prosthesis must fit perfectly with the anatomy of the receiving patient; consequently, a high accuracy of the part is required. In this scenario, the geometry adopted - as discussed in section 2.4.4 - to manufacture a prosthetic implant, since it was extracted from a skull simulacrum, allowed to evaluate the potential of the SPF process by adopting AZ31B-H24 Mg alloy and refers to a small component with high shape details.
The subsequent comparison with the same component obtained by another promising unconventional process (SPIF process) allowed to further evaluate its effectiveness.

6.1. FE model results

Considering the three equivalent strain rates reported in Table 5 (section 2.4.4.2), deriving gas pressure profiles according to the forming time are reported in Figure 147.

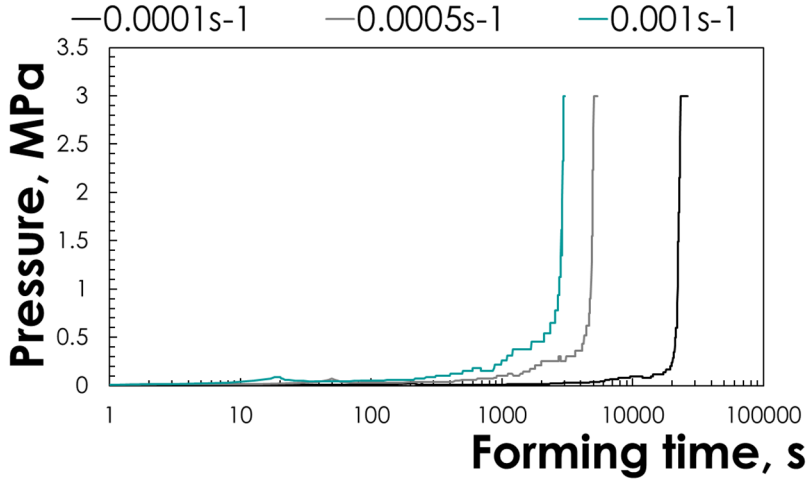

Figure 147 Gas pressure profiles from FE model.

Passing from 0.0001s-1 to 0.001s-1, the total forming time decrease from 26300s to 3023.5s. Results in terms of thickness distribution, coming from numerical simulations, according to the three different strain rates imposed are summarized in Figure 148.

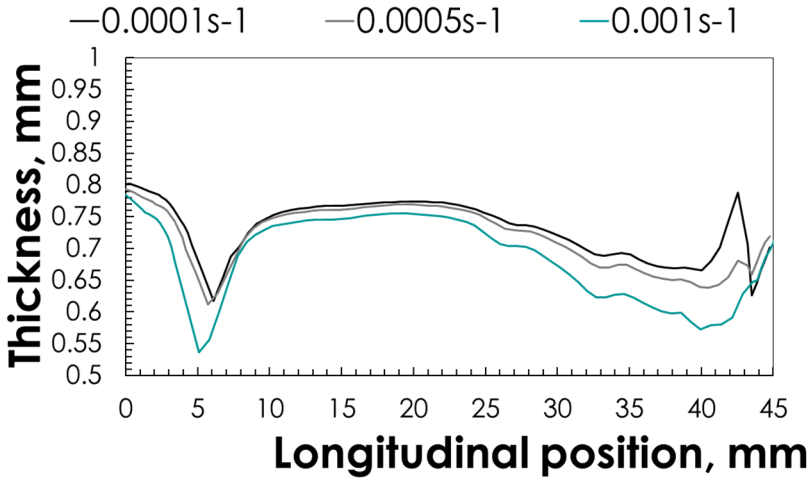

Figure 148 Thickness distributions from FE model.

As shown in Figure 148, strain rate improvement (reduction of the cycle time) causes a marked increase in terms of maximum thinning. In fact, at lower strain rates, more uniform thickness distribution is achieved.
The minimum thickness value ranges from 0.61mm at 0.0001s^{-1} to 0.54mm at 0.001s^{-1}.

6.2. Experimental SPF tests

To test the SPF process in condition attractive for industrial practice, the longer tests (strain rate equal to 0.0001s^{-1} and a total time greater than 20000s) cheekbone prostheses were fabricated by adopting the other two strain rate levels (0.0005 and 0.001s^{-1}). Prosthetic implant obtained via SPF are shown in Figure 149.

(a) (b)

Figure 149 Cheekbone prostheses obtained via SPF tests: Strain rate of (a) 0.0005 and (b) 0.001s^{-1}.

The prosthesis surface tested was the bottom one directly in contact with the die during the forming process. For this reason, the Ra value depends strongly from both die surface characteristics and process parameters. Experimental Ra values obtained were 1.80 and 2.57μm respectively for 0.0005 and 0.001s^{-1}.

Results coming from roughness surface measurement confirm the ability of the process to manufacture geometries with surfaces having high surface characteristics (depending from the die). The Ra value increase with the strain rate adopted.
Another important output of any manufacturing process is represented from the Shape Accuracy (SA) obtained, which quantifies the process capability to produce a shape that is as close as possible to the theoretical one. SA was calculated as reported in the equation 20:

$$SA = 1/\sum[\mathrm{abs}(h_t - h_e)] \qquad \text{Equation 20}$$

where h_t and h_e represent respectively the theoretical and the experimental values of the height.
The two profiles obtained by means of the CMM Mitutoyo Crysta-Apex C544 are plotted in Figure 150: also experimental tests confirm that, when high strain rates are adopted, an increase of thinning occurs.

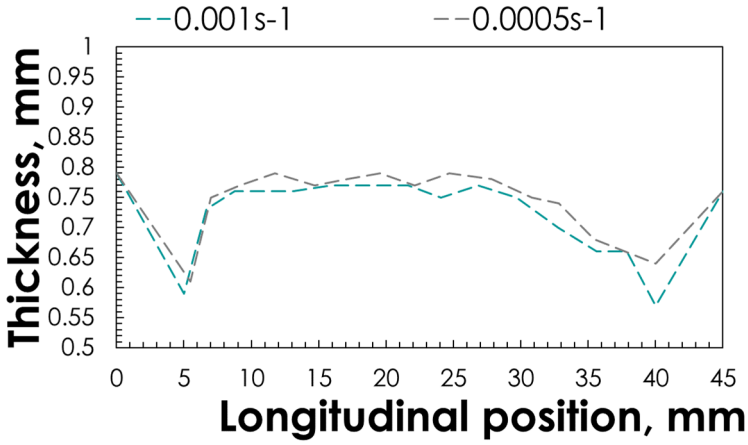

Figure 150 Thickness distributions from experimental tests.

Comparisons between numerical and experimental results are shown in Figure 151 and Figure 152.

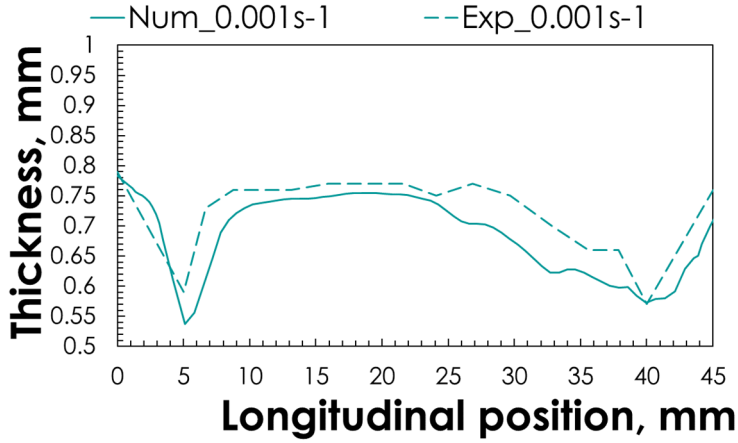

Figure 151 Numerical and experimental thickness distributions comparison at $0.001s^{-1}$.

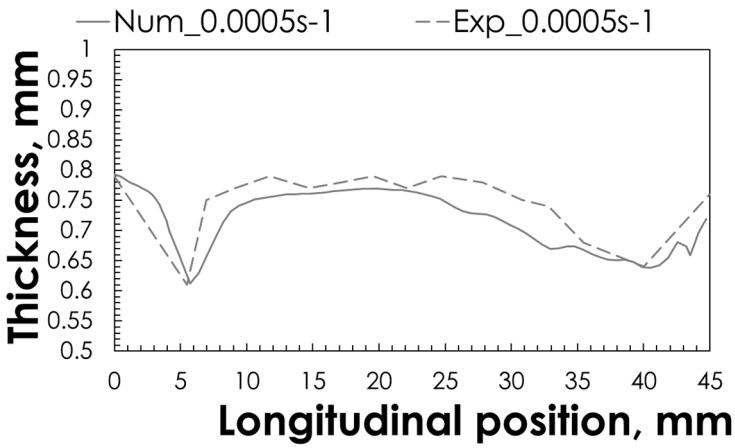

Figure 152 Numerical and experimental thickness distributions comparison at $0.0005s^{-1}$.

A good match was found in both cases; the numerical thickness distribution is continuously lower than the experimental one.
Considering the Mean-Percent-Differences (MPDs) between the numerical and experimental curves, the obtained values are equal to 0.039 and 0.034mm for 0.001s-1 and 0.0005s-1 respectively.

6.3. Experimental SPIF tests results

As previously discussed in section 2.4.4.3 of chapter 2, the CCD was obtained by adopting the modeFRONTIER multidisciplinary design optimization platform and is summarized in Table 43. Each test condition was performed two times.
Contrary to the full factorial experimental plan adopted for the spherical vessel, since the shape in this case appeared not too prohibitive in terms of deformation level, also the effect of SS was evaluated.

Test number	FR, $mm \cdot min^{-1}$	SS, rpm	SD, mm
1	200	3333	0.0275
2	200	3333	0.0775
3	200	6667	0.0275
4	200	6667	0.0775
5	520	3333	0.0275
6	520	3333	0.0775
7	520	6667	0.0275
8	520	6667	0.0775
9	120	5000	0.0525
10	600	5000	0.0525
11	360	2500	0.0525
12	360	7500	0.0525
13	360	5000	0.0150
14	360	5000	0.0900
15	360	5000	0.0525

Table 43 Experimental CCD plan performed.

Cheekbone prostheses obtained via SPF are shown in Figure 153.

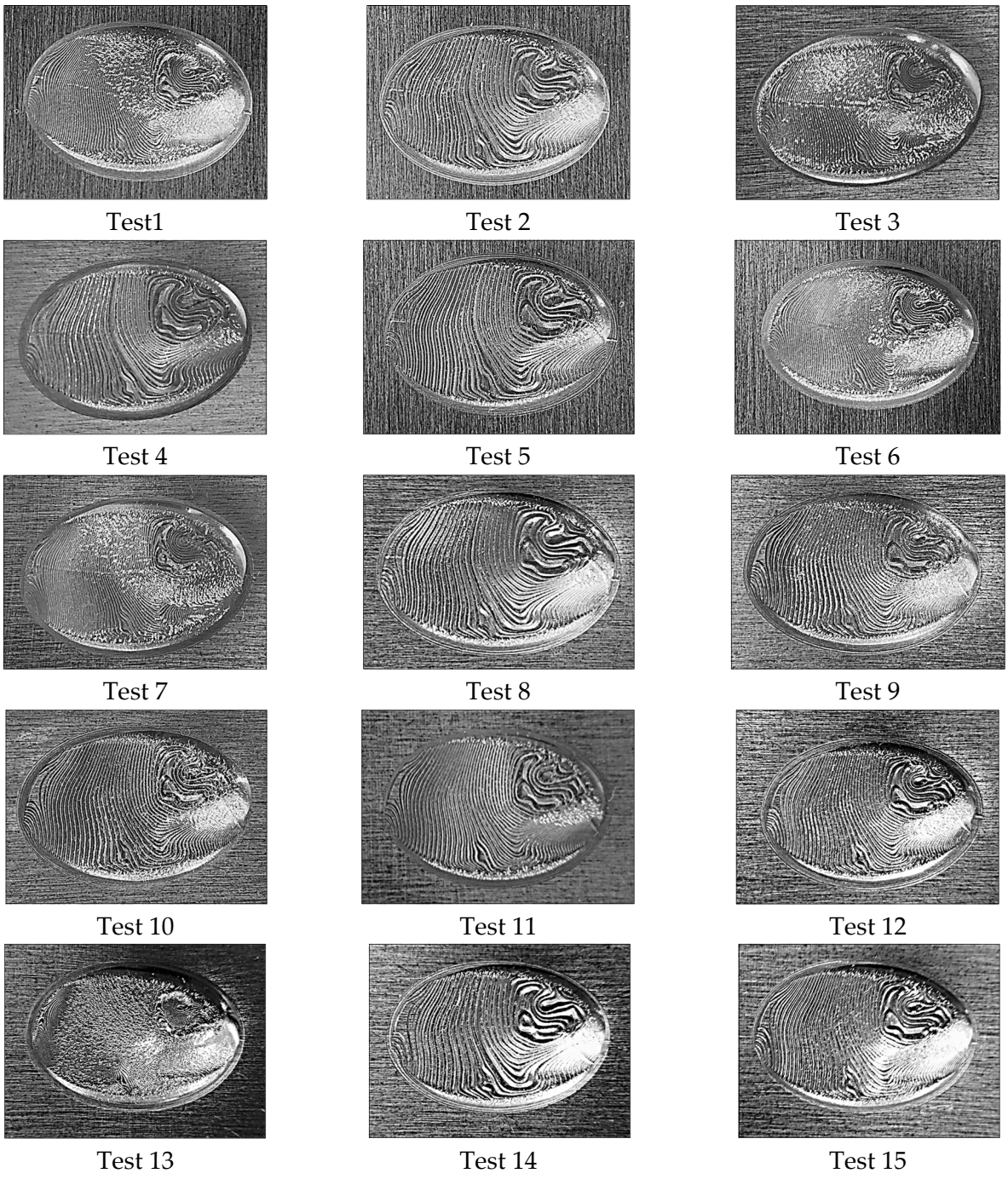

Figure 153 Cheekbone prostheses obtained after SPIF process.

Three different output variables (Ra, SA and Thicknesses) were selected and analyzed to optimize SPIF process.

Table 44 summarizes all values of Ra according to the different conditions analyzed with the CCD experimental plan. The Ra values range between 4.317 to 13.071µm.

Test number	FR, mm·min^{-1}	SS, rpm	SD, mm	Ra, μm
1	200	3333	0.0275	6.044
2	200	3333	0.0775	12.384
3	200	6667	0.0275	4.764
4	200	6667	0.0775	13.071
5	520	3333	0.0275	10.483
6	520	3333	0.0775	4.317
7	520	6667	0.0275	4.763
8	520	6667	0.0775	11.278
9	120	5000	0.0525	8.240
10	600	5000	0.0525	7.740
11	360	2500	0.0525	8.433
12	360	7500	0.0525	9.028
13	360	5000	0.0150	4.191
14	360	5000	0.0900	11.891
15	360	5000	0.0525	8.634

Table 44 Experimental Ra obtained

The contour plots reported in Figure 154 are useful to understand better the influence of the three input variables on the surface roughness; the three contour plots are related to different fixed values of Spindle Speed (2500, 5000 and 7500rpm).

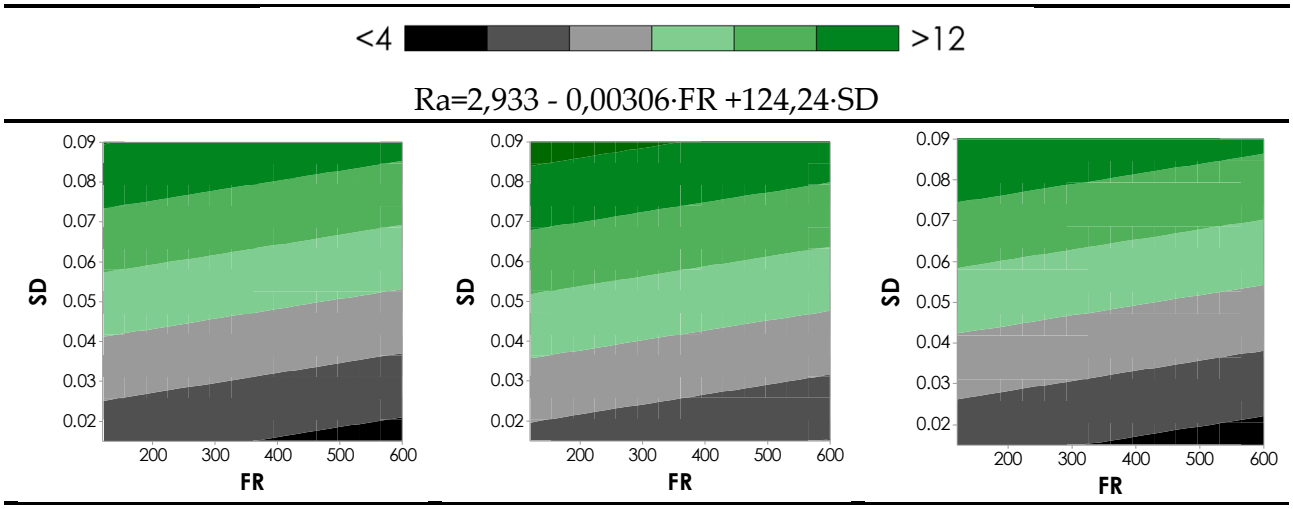

(a) (b) (c)

Figure 154 Ra contour plots according to three levels of SS: (a) 2500rpm, (b) 5000rpm and (c) 7500rpm.

The contour plots obtained are almost identical to each other; in fact, as underlined by the equation form statistical analyses in Figure 154, the Ra can be considered as a function of SD and FR.

In addition, the input parameter that most affects the Ra value is the SD: the Ra increase with SD improvement.

Therefore, the bets (minimum) value of Ra was located at the lowest value of SD.

Test number	FR, mm·min^{-1}	SS, rpm	SD, mm	Shape Accuracy
1	200	3333	0.0275	0.0298
2	200	3333	0.0775	0.0320
3	200	6667	0.0275	0.0517
4	200	6667	0.0775	0.0255
5	520	3333	0.0275	0.0240
6	520	3333	0.0775	0.0169
7	520	6667	0.0275	0.0494
8	520	6667	0.0775	0.0198
9	120	5000	0.0525	0.0458
10	600	5000	0.0525	0.0352
11	360	2500	0.0525	0.0161
12	360	7500	0.0525	0.0194
13	360	5000	0.0150	0.0513
14	360	5000	0.0900	0.0288
15	360	5000	0.0525	0.0229

Table 45 Experimental SA obtained.

Each SA value obtained from experimental tests is listed in Table 45 and ranges between 0.0169 and 0.0517. Experimental results obtained allows to determine contour plots according to the three input parameters.
Three different contour plots by varying the SS are reported in Figure 155.
Contour plots obtained at the three different values of SS show a trend that is gradually changing. In fact, although the FR effect seems secondary compared to the other two parameters, the best condition can be attributable to the middle value (360 mm·min^{-1}) of the investigated range. Starting from the lowest value (2500rpm) to the highest one (7500rpm) of SS, the optimal condition of accuracy shifts from lower-middle to highest values of SS.

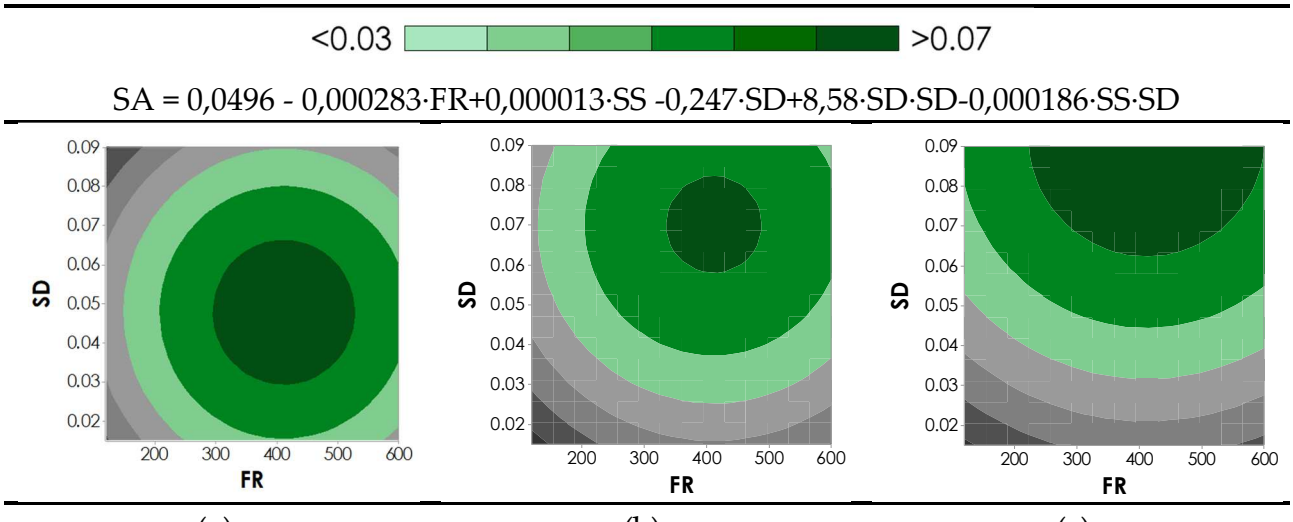

(a) (b) (c)

Figure 155 Shape Accuracy contour plots according to three levels of SS: (a) 2500rpm, (b) 5000rpm and (c) 7500rpm.

The last output variable considered was the thinning; in particular, the minimum value of thickness recorded was considered for each experimental test performed, as reported in

Table 46. Experimental thickness measures were carried out using a Mitutoyo 573-701 Absolute Digimatic Offset Calliper.

Test number	FR, mm·min^{-1}	SS, rpm	SD, mm	Min thickness
1	200	3333	0.0275	0.78
2	200	3333	0.0775	0.86
3	200	6667	0.0275	0.73
4	200	6667	0.0775	0.82
5	520	3333	0.0275	0.79
6	520	3333	0.0775	0.85
7	520	6667	0.0275	0.75
8	520	6667	0.0775	0.84
9	120	5000	0.0525	0.81
10	600	5000	0.0525	0.81
11	360	2500	0.0525	0.83
12	360	7500	0.0525	0.82
13	360	5000	0.0150	0.74
14	360	5000	0.0900	0.89
15	360	5000	0.0525	0.79

Table 46 Experimental Min thickness obtained.

Contour plots in Figure 156 summarize results obtained from regression analysis. As reported in the equation in the same figure, it is possible to observe that the Minimum value of thickness depends exclusively from SS and SD. Negligible effects can be associated to the other parameter investigated (FR); in fact, the three contour plots in Figure 156, related to three different FRs are almost the same.

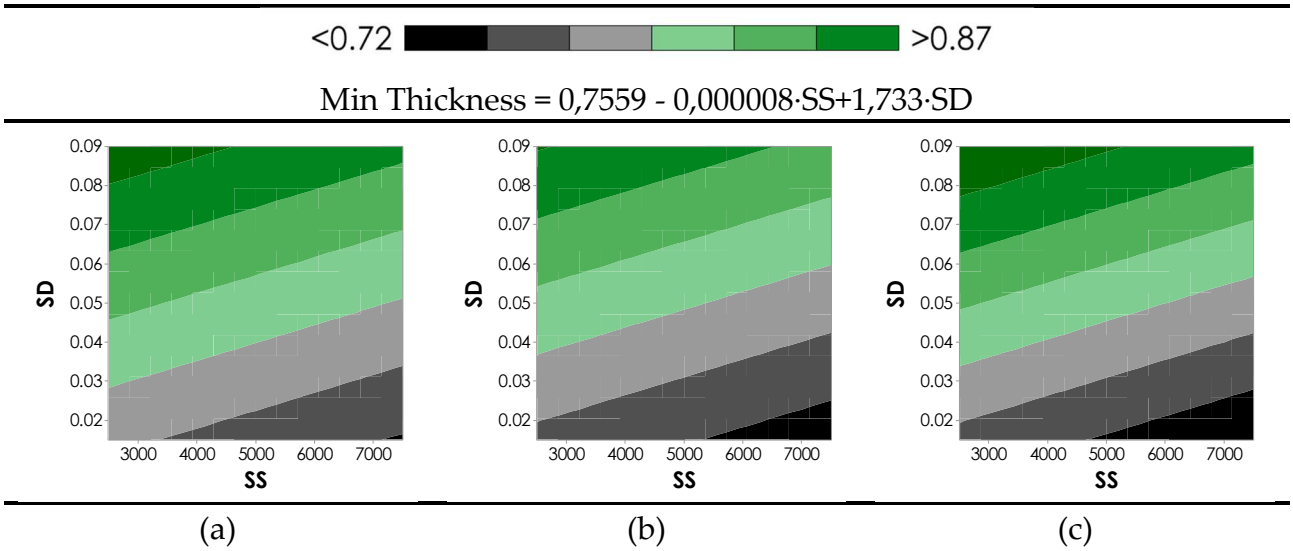

(a) (b) (c)

Figure 156 Min thickness contour plots according to three levels of FR: (a) 120 mm·min^{-1}, (b) 360 mm·min^{-1} and (c) 600 mm·min^{-1}.

Analysing all contour plots, it is possible to obtain information about the global trends of the output investigated according to the process parameter such as SD, SS and FR. Therefore, it is possible to assert that:

- The SA increases with the adoption of low value of the SD and high values of the SS. In addition, for high values of SS, the best SA happens with low values of FR. Finally, marked increase of SA can be achieved combining low FR and high SS. Therefore, high values of the SS, low value of the SD and FR seems appropriate to improve the SA response.
- Regarding Ra, results coming from contour plots reveal that the optimal conditions to increase surface roughness are the same identify for the SA. Although the SD must be clearly low to achieve good surface roughness results, FR and SD are the most significant parameters that affect Ra.
- Results in terms of thickness are in contrast with what was noted by Ra and SA; in fact, the combination low SD and FR values provide thinner parts. Since high shape accuracy leads to greater deformation, the results obtained are reasonable. However, the maximum thinning values recorded appear to be acceptable since they are equal or less than 27.4% (considering that the initial thickness of the sheet is equal to 1mm).

6.4. Comparison of the results obtained from SPF and SPIF

A global comparison between the two different methods (SPF and SPIF) are proposed below.

Considering the optimal experimental test performed for both methodologies, results in terms of Ra, SA and min thickness can be compared. Therefore, the prosthesis obtained via SPF with a strain rate of 0.0005s-1 was compared with the one deriving from SPIF with FR, SS and SD respectively equal to 360 mm·min^{-1}, 5000rpm and 0.0150mm.

Forming process	Ra, μm	Shape accuracy	Min thickness, mm
SPF	1.80	0.1101	0.74
SPIF	4.19	0.0513	0.61

Table 47 Experimental Min thickness obtained.

Results in terms of the three output analyzed are listed in Table 47. Obtained values of shape accuracy show the best capability of the SPF process to replicate the theoretical geometry; in fact, shape accuracy value for the prosthesis obtained for SPF (0.1101) is two time that obtained for SPIF (0.0513).

The thickness distribution for the prosthesis obtained by means of SPF is constantly lower than that relative to the prosthesis obtained via SPIF (Figure 157). In addition, the two profiles have trends that are not entirely comparable to each other. These considerations emphasize the difference in terms of approach attributable to each of the two technologies investigated.

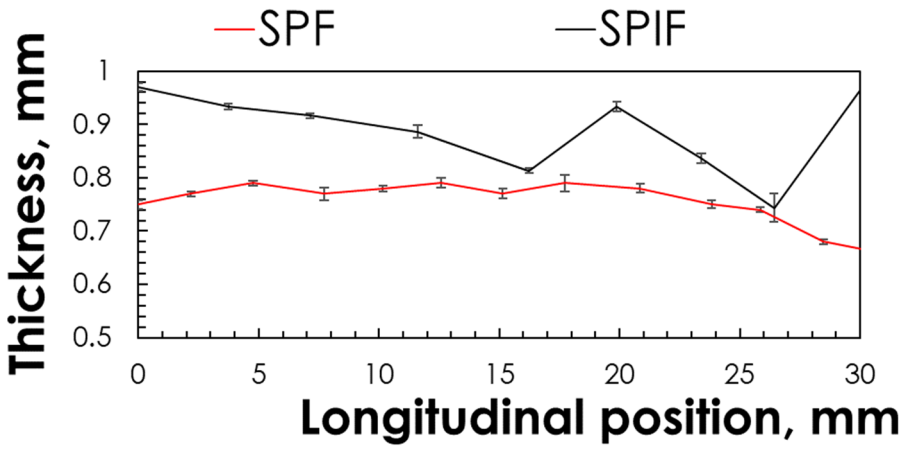

Figure 157: Comparison between thickness distribution obtained from SPF and SPIF.

Finally, comparison in terms of surface roughness suggests a greater capability of the SPF process to obtain very low Ra values, if compared with the SPIF results. In fact, the Ra value (1.800μm) coming from SPF is markedly lower than the one (4.129μm) attributable to the SPIFed prothesis.

Conclusions

Starting from the innovative Mg-based alloys manufacturing, several (thirteen) different Mg alloys were produced *ad hoc* and with the aim to obtain one (or more) able to manifest both good mechanical properties and elevated capability to be deformed. The different alloys manufactured differed from each other in terms of the type, number and quantity of the alloying elements. The manufacturing procedure and the discussion about results deriving from this experimental activity are documented respectively in Chapter 2 and Chapter 3.

The skimming phase was performed by means of hardness and tensile tests. Results coming from these tests associated to the ones deriving from metallographic analyses allowed to assert that the most performing Mg alloy produced via casting process, among all those produced, is the experimental ternary Mg-2Zn-2Ce alloy. In fact, results obtained in terms of Yield Stress, UTS and Elongation to Failure were much higher than those relating to the others Mg-based alloys manufactured. Considering the two investigated conditions of both temperature (200 and 400°C) and strain rate (0.00125 and 0.0125s^{-1}), elongation to failure (up to 55.4%) appeared to be very promising for the subsequent bulge tests. Furthermore, since UTS up to 116.4MPa was obtained, also mechanical property can be considered not negligible. In fact, the experimental Mg-2Zn-2Ce alloy, even though in as-cast condition, showed good deformation capacity during bulge tests conducted at different temperatures, failure mode being the point-like punctures rather than tearing, most probably at locations of coarse inclusions or expansion of pores created due to cracking of the second phase particles. Twinning was not observed at all while some evidence existed for contributions from non-basal slip as well as GBS.

It was shown by observations after bulge tests that the alloy had a resistance to grain coarsening. This grain size stability together with the m-values higher than 0.3 and the accompanying strain rate values varying between 4E-04 and 9E-04s^{-1} suggested a potential superplastic behavior of the alloy with industrially applicable forming times, gas pressures and temperatures. These results, compared with those relating to the AZ31B-H24 Mg alloy, demonstrate the possibility of successfully exploiting the new manufactured Mg alloy in sheet metal forming process.

In order to optimize this type of process, using an AZ31B-H24 alloy, both conventional and innovative approaches were proposed.

Numerical/experimental activities, performed by means of bulge tests and summarized in Chapter 4, were aimed at evaluating the capability of the FE model of reproducing in a reliable way the manufacturing of an AZ31 Mg alloy spherical component through gas forming at 450 °C. The experimental activity, exclusively based on gas forming tests up to a maximum value of the strain equal to 0.84, allowed to determine the constants needed for calibrating the material constitutive model suggested by Carpenter, subsequently implemented in the FE model.

This promising approach, in addition to drastically reduce the total number of tests necessary for the determination of the deformation behaviour and the microstructural evolution of the AZ31B-H24 Mg alloy, allows to calibrate the material model under typical strain-stress condition occurring during the sheet metal forming process.
Results coming from the numerical activities showed the capability of the model, based on experimentally determined constants, to predict the deformation behaviour of the AZ31B-H24 Mg alloy. This is particularly true if the thickness distributions are considered; in fact, the error between the experimental results and the numerical ones is equal or less than 6.27%.
Definitely, despite the numerical model proved to be able to correctly predict the behaviour of the manufacturing process of a spherical component applied to the AZ31B-H24 Mg alloy, it is possible to improve the performances of the same to predict the material behavior - in terms of both deformation and microstructure evolution - by implementing analytical equation which can approximate the static grain growth in a better way. In addition, an enlargement of the starting experimental database by means of extrapolation (and therefore without any further tests) could improve the fitting between numerical and experimental results.
Finally, reducing the dispersion of experimental data affecting dynamic grain growth could further improve the material behavior prediction, even when GBS creep (low pressure) is dominant respect to the DC creep mechanism (high pressures).
From a manufacturing point of view, despite the abnormal grain growth which occurred when very high values of the strain rate (pressure) were set, considering the investigated range up to 0.7 MPa it is possible to say that, by applying appropriate strain rates, sound spherical components can be obtained with a short manufacturing time. In addition, in correspondence of the same process conditions, a reduced grain growth can be obtained: this aspect is not negligible when high mechanical performances of the component are required.
Low strain rate values, on the contrary, allowed to obtain spherical components with a marked increase of the final dome height obtainable albeit with a larger area of maximum thinning.
In order to manufacture the same final component, two methodologies - in many innovative aspects - were proposed and evaluated. The first proposal was represented by a numerical/experimental approach, based on the combination of two different unconventional sheet metal forming techniques (SPIF and SPF), able to guarantee a final component with a high controlled thickness distribution. Specifically, a variable distribution, deriving from FE model optimization by implementing Enikeev and Kruglov constitutive material model, was obtained by SPIF technique; subsequently SPIFed samples were subjected to SPF process.
Performing SPF experimental test, starting from both SPIFed and undeformed (with a constant thickness) blanks, results in terms of thickness distribution showed marked differences. Considering an initial constant 1mm thick blank, the thickness obtained after forming ranges with a parabolic trend from 0.4mm (in correspondence of vessel apex) to 1mm (in the flanged zone). On the contrary, when the optimized SPIFed blank was

subjected to bulge tests, the final vessel thickness starts from 0.5mm (in correspondence of the dome apex), remains constant for a marked section (that ranges between 22.99 and 24.29mm) and then increases until it reaches the value of the undeformed condition in the flanged area.
SPIFed samples were experimentally designed and manufactured considering the so-called sine law. This law, coupled with an appropriate operating window as well as a correct discretization value (equal to 0.5mm) in the slope change, predicts very well the desired thickness distribution (with an error variable between the actual value and the theoretical one that ranges from 3.15 to 5.93%).
Starting from the promising results obtained, the proposed approach could be applied to more complicated and industrial cases study.
The other promising approach, studied in this research activity, to manufacture complex shapes was the SPF process after a localized LHT performed experimentally and numerically. Once again, numerical simulation of LHT and SPF process on LHTed samples were conducted adopting as material constitutive model those proposed respectively by Miao and Carpenter.
LHT revealed to be a valid approach to locally change the microstructure of the blank which must be deformed. In those processes in which the microstructure of the alloy strongly affects the deformation behavior (for example in the case of the superplastic forming) such a technique represents a viable solution to locally modify the material behavior (e.g. in terms of strain rate sensitivity index). However, it is possible to improve the goodness of the results obtained. Considerations regarding this aspect are directly related to what was asserted regarding the calibration procedure of the material model suggested by Carpenter.
The last part of our study involved a more complex shape such as a prosthetic cheekbone implant. The part was produced by means of SPF and SPIF processes. Optimization of the SPF were made with experimental tests supported by numerical simulations; on the contrary, SPIF process was optimized in accordance with a CCD experimental plan, based on three process parameters: Step Down, Feed rate and Spindle speed.
Experimental evidences deriving from the two techniques show a greater accuracy inherent to the SPF. Against, SPIF is less time-consuming and with accuracy - albeit lower respect to those of SPF - however acceptable.
In conclusion, the present research demonstrated that it is possible to obtain interesting results which can be decisive in the continuous design improvement of unconventional sheet metal forming processes. The integration of different processes, supported by numerical and optimization techniques, represents a skilful tool to manufacture complex components with intrinsic resistance requirements.

References

[1] S.L. Winkler, J.E. Anderson, L. Garza, W.C. Ruona, R. Vogt, T.J. Wallington, Vehicle criteria pollutant (PM, NOx, CO, HCs) emissions: how low should we go?, Npj Clim. Atmos. Sci. 1 (2018). doi:10.1038/s41612-018-0037-5.

[2] European Commission, Regulation (EU) 2019/631 - CO2 emission performance standards, (2019). https://eur-lex.europa.eu/legal-content/EN/TXT/PDF/?uri=CELEX:32019R0631&from=EN.

[3] G.S. Cole, a. M. Sherman, Light weight materials for automotive applications, Mater. Charact. 35 (1995) 3–9. doi:10.1016/1044-5803(95)00063-1.

[4] A.H. Musfirah, A.G. Jaharah, Magnesium and Aluminum Alloys in Automotive Industry, J. Appl. Sci. Res. 8 (2012) 4865–4875.

[5] E. Aghion, B. Bron, D. Eliezer, The role of the magnesium industry in protecting the environment.pdf, 117 (2001) 381–385.

[6] GADSL, Global Automotive Declarable Substance List (GADSL) - Guidance Document (2016), (2018) 1–13. https://s3.amazonaws.com/www.gadsl.org/Documents/GADSL-Guidance-Document.pdf.

[7] K. Yang, L. Tan, Control of biodegradation of magnesium (Mg) alloys for medical applications, Woodhead Publishing Limited, 2013. doi:10.1533/9780857098962.4.509.

[8] B. Luthringer, F. Feyerabend, R. Willumeit, Magnesium-Based Implants: A Mini-Review, Magnes. Res. 27 (2014) 142–154. doi:10.1684/mrh.2015.0375.

[9] J.A. Yasi, L.G. Hector, D.R. Trinkle, Prediction of thermal cross-slip stress in magnesium alloys from direct first-principles data, Acta Mater. 59 (2011) 5652–5660. doi:10.1016/j.actamat.2011.05.040.

[10] P. Guglielmi, A.A. Kaya, D. Sorgente, G. Palumbo, Deformation behaviour of a new magnesium ternary alloy, in: AIP Conf. Proc., 2018. doi:10.1063/1.5035061.

[11] E. Hsu, J.E. Carsley, R. Verma, M. Strain, M. Strain, Development of Forming Limit Diagrams of Aluminum and Magnesium Sheet Alloys at Elevated Temperatures, J. Mater. Eng. Perform. 17 (2008) 288–296. doi:10.1007/s11665-007-9196-y.

[12] F.U. Enikeev, A.A. Kruglov, An analysis of the superplastic forming of a thin circular diaphragm, Int. J. Mech. Sci. 37 (1995) 473–483. doi:10.1016/0020-7403(94)00081-T.

[13] Q. Miao, L. Hu, X. Wang, E. Wang, Grain growth kinetics of a fine-grained AZ31 magnesium alloy produced by hot rolling, J. Alloys Compd. 493 (2010) 87–90. doi:10.1016/j.jallcom.2009.12.049.

[14] A.J. Carpenter, A.R. Antoniswamy, J.T. Carter, L.G. Hector, E.M. Taleff, A mechanism-dependent material model for the effects of grain growth and anisotropy on plastic deformation of magnesium alloy AZ31 sheet at 450 C, Acta Mater. 68 (2014) 254–266. doi:10.1016/j.actamat.2014.01.043.

[15] C. Moosbrugger, Engineering Properties of Magnesium Alloys, ASM Int. (2017) 1–12.

doi:10.1002/9780470905098.ch1.
[16] C. Moosbrugger, Engineering Properties of Magnesium Alloys, ASM Int. (2017) 1–12. doi:10.1002/9780470905098.ch1.
[17] D.M. Parks, S. Ahzi, Polycrystalline plastic deformation and texture evolution for crystals lacking five independent slip systems, J. Mech. Phys. Solids. 38 (1990) 701–724. doi:10.1016/0022-5096(90)90029-4.
[18] M.R. Barnett, Twinning and the ductility of magnesium alloys. Part II. "Contraction" twins, Mater. Sci. Eng. A. 464 (2007) 8–16. doi:10.1016/j.msea.2007.02.109.
[19] A.A. Kaya, 2 - Physical metallurgy of magnesium, in: A.A.K. Mihriban O. Pekguleryuz, Karl U. Kainer (Ed.), Fundam. Magnes. Alloy Metall., Woodhead Publishing, 2013: pp. 33–84. doi:10.1533/9780857097293.
[20] R.E. Reed-Hill, Phisical Mettalurgical Principles, 1974.
[21] ASTM HANDBOOK, Vol2, ASTM publication, 2012.
[22] B.L. Mordike, T. Ebert, Magnesium Properties - applications - potential, Mater. Sci. Eng. A. 302 (2001) 37–45. doi:10.1016/S0921-5093(00)01351-4.
[23] I.J. Polmear, Magnesium alloys and applications, Mater. Sci. Technol. 10 (1994) 1–16. doi:10.1179/mst.1994.10.1.1.
[24] W.A. Monteiro, S.J. Buso, L. V Silva, New Features on Magnesium Alloys, New Featur. Magnes. Alloy. (2012) 1–14. doi:10.5772/2810.
[25] L. Ostrovsky, Y. Henn, Present state and future of magnesium application in aerospace industry, Int. Conf. "New Challenges Aeronaut. ASTEC 07. (2007) 1–5.
[26] V.S. T. Ram Prabhu, Srikanth Vedantam, Aerospace Materials and Material Technologies, Springer Singapore, 2017.
[27] M. Peron, J. Torgersen, F. Berto, Mg and its alloys for biomedical applications: Exploring corrosion and its interplay with mechanical failure, Metals (Basel). 7 (2017). doi:10.3390/met7070252.
[28] Y. Song, D. Shan, R. Chen, F. Zhang, E.H. Han, Biodegradable behaviors of AZ31 magnesium alloy in simulated body fluid, Mater. Sci. Eng. C. 29 (2009) 1039–1045. doi:10.1016/j.msec.2008.08.026.
[29] T.Hanawa, Overview of metals and applications, in: Met. Biomed. Devices, Woodhead Publishing Series in Biomaterials, 2010: pp. 3–24.
[30] A.C. Hänzi, A. Sologubenko, P. Uggowitzer, Design strategy for new biodegradable Mg-Y-Zn alloys for medical applications, Int. J. Mater. Res. (Formerly Zeitschrift Fuer Met. 100 (2009) 1127–1136. doi:10.3139/146.110157.
[31] M.P. Staiger, A.M. Pietak, J. Huadmai, G. Dias, Magnesium and its alloys as orthopedic biomaterials: A review, Biomaterials. 27 (2006) 1728–1734. doi:10.1016/j.biomaterials.2005.10.003.
[32] F. Witte, Reprint of: The history of biodegradable magnesium implants: A review, Acta Biomater. 23 (2015) S28–S40. doi:10.1016/j.actbio.2015.07.017.
[33] M. Razavi, M.H. Fathi, M. Meratian, Microstructure, mechanical properties and bio-corrosion evaluation of biodegradable AZ91-FA nanocomposites for biomedical applications, Mater. Sci. Eng. A. 527 (2010) 6938–6944. doi:10.1016/j.msea.2010.07.063.
[34] D. Persaud-Sharma, A. McGoron, Biodegradable Magnesium Alloys: A Review of

Material Development and Applications, J. Biomim. Biomater. Tissue Eng. 12 (2012) 25–39. doi:10.4028/www.scientific.net/JBBTE.12.25.
[35] I.J. Polmear, Magnesium alloys and applications, Mater. Sci. Technol. 10 (1994) 1–16. doi:10.1179/mst.1994.10.1.1.
[36] P. Sherek, A. Carpenter, Hector Louis, P. Krajewski, J. Carter, J. Lasceski, E. Taleff, The effects of strain and stress state in hot forming of mg AZ31 sheet, in: 2012: pp. 301–306. doi:10.1007/978-3-319-48203-3_55.
[37] A. Jäger, P. Lukáč, V. Gärtnerová, J. Bohlen, K.U. Kainer, Tensile properties of hot rolled AZ31 Mg alloy sheets at elevated temperatures, J. Alloys Compd. 378 (2004) 184–187. doi:10.1016/j.jallcom.2003.11.173.
[38] M. Liu, G. Yuan, Q. Wang, Y. Wei, W. Ding, Y. Zhu, Superplastic behavior and microstructural evolution in a commercial Mg-3Al-1Zn magnesium alloy, Mater. Trans. 43 (2002) 2433–2436. doi:10.2320/matertrans.43.2433.
[39] D. Sorgente, G. Palumbo, A. Piccininni, P. Guglielmi, L. Tricarico, Modelling the superplastic behaviour of the Ti6Al4V-ELI by means of a numerical/experimental approach, Int. J. Adv. Manuf. Technol. 90 (2017) 1–10. doi:10.1007/s00170-016-9235-7.
[40] D.S. Totten, G. E., Mackenzie, Handbook of aluminium, Superplastic forming, (2003) 1105–1114.
[41] A.K. Ghosh, C.H. Hamilton, Influences of material parameters and microstructure on superplastic forming, Metall. Trans. A. 13 (1982) 733–743. doi:10.1007/BF02642386.
[42] M.B. Silva, M. Skjoedr, A.G. Atkins, N. Bay, P.A.F. Martins, Single-point incremental forming and formability-failure diagrams, J. Strain Anal. Eng. Des. 43 (2008) 15–35. doi:10.1243/03093247JSA340.
[43] M. Rauch, J.Y. Hascoet, J.C. Hamann, Y. Plenel, Tool path programming optimization for incremental sheet forming applications, CAD Comput. Aided Des. 41 (2009) 877–885. doi:10.1016/j.cad.2009.06.006.
[44] J. Hamilton, K., Jeswiet, Single point incremental forming at high feed rates and rotational speeds: Surface and structural consequences, in: CIRP Ann. - Manuf. Technol., 2010: pp. 311–314.
[45] S.. Allwood, J.M., Music, O., Raithathna, A., Duncan, Closed-loop feedback control of product properties in flexible metal forming processes with mobile tools, in: CIRP Ann. – Manuf. Technol., 2009: pp. 287–290.
[46] G. Ambrogio, S. Bruschi, A. Ghiotti, L. Filice, Formability of AZ31 magnesium alloy in warm incremental forming process, Int. J. Mater. Form. 2 (2009) 5–8. doi:10.1007/s12289-009-0434-8.
[47] Q. Xie, Z. Zhu, G. Kang, Thermal activation based constitutive model for high-temperature dynamic deformation of AZ31B magnesium alloy, Mater. Sci. Eng. A. 743 (2019) 24–31. doi:10.1016/j.msea.2018.11.049.
[48] P. Changizian, A. Zarei-Hanzaki, A.A. Roostaei, The high temperature flow behavior modeling of AZ81 magnesium alloy considering strain effects, Mater. Des. 39 (2012) 384–389. doi:10.1016/j.matdes.2012.02.049.
[49] D.H. Yu, Modeling high-temperature tensile deformation behavior of AZ31B magnesium alloy considering strain effects, Mater. Des. 51 (2013) 323–330.

doi:10.1016/j.matdes.2013.04.022.
[50] Y. Dong, C. Zhang, X. Lu, C. Wang, G. Zhao, Constitutive Equations and Flow Behavior of an As-Extruded AZ31 Magnesium Alloy Under Large Strain Condition, J. Mater. Eng. Perform. 25 (2016) 2267–2281. doi:10.1007/s11665-016-2092-6.
[51] G.A. Nourollahi, M. Farahani, A. Babakhani, S.S. Mirjavadi, Compressive deformation behavior modeling of az31 magnesium alloy at elevated temperature considering the strain effect, Mater. Res. 16 (2013) 1309–1314. doi:10.1590/S1516-14392013005000149.
[52] R. Armstrong, I. Codd, R.M. Douthwaite, N.J. Petch, The plastic deformation of polycrystalline aggregates, Philos. Mag. 7 (1962) 45–58. doi:10.1080/14786436208201857.
[53] H.K. Kim, The grain size dependence of flow stress in an ECAPed AZ31 Mg alloy with a constant texture, Mater. Sci. Eng. A. 515 (2009) 66–70. doi:10.1016/j.msea.2009.02.039.
[54] A.J. Carpenter, Physics-Based Material Constitutive Models for the Simulation of High- Temperature Forming of Magnesium Alloy AZ31, (2012). http://repositories.lib.utexas.edu/handle/2152/ETD-UT-2012-08-6024.
[55] T.G. Langdon, Identifiying creep mechanisms at low stresses, Mater. Sci. Eng. A. 283 (2000) 266–273.
[56] F.U. Enikeev, A.A. Kruglov, An analysis of the superplastic forming thin circular diaphragm, Int. J. Mech. Sci. 37 (1995) 473–483.
[57] A. Science, 27 A Mechanism of Superplastic Deformation and Deformation Induced Grain Growth Based on Grain Switching Eiichi Sato*, Kazuhiko Kuribayashi* and Ryo Horiuchi*, 196 (n.d.) 27–32.
[58] Hill R., The matehematic theory of plasticity, Oxford University Press, New York, 1950.
[59] P. Guglielmi, A.A. Kaya, Y. Türe, A. Ataman, E. Arkın, D. Sorgente, G. Palumbo, Deformation Capacity of a Ternary Magnesium Alloy in a Gas-Forming Process at Elevated Temperatures, Jom. 71 (2019) 2087–2096. doi:10.1007/s11837-019-03403-0.
[60] ASTM International, Standard Test Methods for Determining Average Grain Size, Designation: E112-12, n.d.
[61] S.A. Aksenov, D. Sorgente, Investigation of stress-strain behavior of a sheet material using free bulging test, Procedia Eng. 207 (2017) 1892–1897. doi:10.1016/j.proeng.2017.10.957.
[62] D. Sorgente, G. Palumbo, A. Piccininni, P. Guglielmi, L. Tricarico, Modelling the superplastic behaviour of the Ti6Al4V-ELI by means of a numerical/experimental approach, Int. J. Adv. Manuf. Technol. 90 (2017). doi:10.1007/s00170-016-9235-7.
[63] L. Manco, L. Filice, G. Ambrogio, Analysis of the thickness distribution varying tool trajectory in single-point incremental forming, Proc. Inst. Mech. Eng. Part B J. Eng. Manuf. 225 (2011) 348–356. doi:10.1177/09544054JEM1958.
[64] J. Egger, M. Gall, A. Tax, M. Ücal, U. Zefferer, X. Li, G. Von Campe, U. Schäfer, D. Schmalstieg, X. Chen, Interactive reconstructions of cranial 3D implants under MeVisLab as an alternative to commercial planning software, PLoS One. 12 (2017). doi:10.1371/journal.pone.0172694.

[65] P. Scolozzi, Maxillofacial reconstruction using polyetheretherketone patient-specific implants by "mirroring" computational planning, Aesthetic Plast. Surg. 36 (2012) 660–665. doi:10.1007/s00266-011-9853-2.
[66] S. Tekumalla, S. Seetharaman, A. Almajid, M. Gupta, Mechanical Properties of Magnesium-Rare Earth Alloy Systems: A Review, Metals (Basel). 5 (2014) 1–39. doi:10.3390/met5010001.
[67] R.K. Mishra, A.K. Gupta, P. Rao Rama, A.K. Sachdev, A.M. Kumar, A.A. Luo, Influence of Cerium on Texture and Ductility of Magnesium Extrusions, Essent. Readings Magnes. Technol. 59 (2014) 363–368. doi:10.1002/9781118859803.ch58.
[68] J. Zhang, Y. Dou, H. Dong, Intrinsic ductility of Mg-based binary alloys: A first-principles study, Scr. Mater. 89 (2014) 13–16. doi:10.1016/j.scriptamat.2014.06.035.
[69] J. Zhang, Y. Dou, Y. Zheng, Twin-boundary segregation energies and solute-diffusion activation enthalpies in Mg-based binary systems: A first-principles study, Scr. Mater. 80 (2014) 17–20. doi:10.1016/j.scriptamat.2014.02.004.
[70] S. Tekumalla, S. Seetharaman, N. Quy Bau, W. Leong Eugene Wong, C. Sim Goh, R. Shabadi, M. Gupta, Influence of Cerium on the Deformation and Corrosion of Magnesium, J. Eng. Mater. Technol. 138 (2016) 031011. doi:10.1115/1.4033033.
[71] S. Sandlöbes, S. Zaefferer, I. Schestakow, S. Yi, R. Gonzalez-Martinez, On the role of non-basal deformation mechanisms for the ductility of Mg and Mg-Y alloys, Acta Mater. 59 (2011) 429–439. doi:10.1016/j.actamat.2010.08.031.
[72] S. Sandlöbes, M. Friák, Z. Pei, J. Neugebauer, D. Raabe, OPEN A rare-earth free magnesium alloy with improved intrinsic ductility, Sci. Rep. 7 (2017) 1–8. doi:10.1038/s41598-017-10384-0.
[73] B.L. Wu, Y.H. Zhao, X.H. Du, Y.D. Zhang, F. Wagner, C. Esling, Ductility enhancement of extruded magnesium via yttrium addition, Mater. Sci. Eng. A. 527 (2010) 4334–4340. doi:10.1016/j.msea.2010.03.054.
[74] E.A. Ball, P.B. Prangnell, Tensile-compressive yield asymmetries in high strength wrought magnesium alloys, Scr. Metall. Mater. 31 (1994) 111–116. doi:10.1016/0956-716X(94)90159-7.
[75] A. Imandoust, A review on the effect of rare-earth elements on texture evolution during processing of magnesium alloys, J. Mater. Sci. 52 (2017) 1–29. doi:10.1007/s10853-016-0371-0.
[76] C.H. Cáceres, A. Blake, The strength of concentrated Mg-Zn solid solutions, Phys. Status Solidi Appl. Res. 194 (2002) 147–158.
[77] C. Shaw, H. Jones, The contributions of different alloying additions to hardening in rapidly solidified magnesium alloys, Mater. Sci. Eng. A. 228 (1997) 856–860.
[78] Y. Guyot, I. Papantoniou, Y.C. Chai, S. Van Bael, J. Schrooten, L. Geris, A computational model for cell/ECM growth on 3D surfaces using the level set method: a bone tissue engineering case study, Biomech. Model. Mechanobiol. 13 (2014) 1361–1371. doi:10.1007/s10237-014-0577-5.
[79] C.S. Roberts, Magnesium and Its Alloys, Wiley, New York, 1960.
[80] S. Wei, T. Zhu, H. Hou, J.H. Kim, E. Kobayashi, T. Sato, M. Hodgson, W. Gao, Effects of Pb/Sn additions on the age-hardening behaviour of Mg-4Zn alloys, Mater. Sci. Eng.

A. 597 (2014) 52–61. doi:10.1016/j.msea.2013.12.048.
[81] J.H. Bae, M.S. Shim, B.C. Suh, D.W. Kim, S.H. Park, N.J. Kim, Segregation in twin-roll cast Mg alloy and its suppression through alloy design, Mater. Lett. 132 (2014) 361–364. doi:10.1016/j.matlet.2014.06.113.
[82] D. Sorgente, G. Palumbo, L. Tricarico, Material Superplastic Parameters Evaluation by a Jump Pressure Blow Forming Test, Key Eng. Mater. 344 (2007) 119–126. doi:10.4028/www.scientific.net/KEM.344.119.
[83] D. Sorgente, L.D. Scintilla, G. Palumbo, L. Tricarico, Blow forming of AZ31 magnesium alloy at elevated temperatures, Int. J. Mater. Form. 3 (2010) 13–19. doi:10.1007/s12289-009-0411-2.
[84] J. Zhang, Y. Dou, Y. Zheng, Twin-boundary segregation energies and solute-diffusion activation enthalpies in Mg-based binary systems: A first-principles study, Scr. Mater. 80 (2014) 17–20. doi:10.1016/j.scriptamat.2014.02.004.
[85] S. Sandlöbes, Z. Pei, M. Friák, L.-F. Zhu, F. Wang, S. Zaefferer, D. Raabe, J. Neugebauer, Ductility improvement of Mg alloys by solid solution: Ab initio modeling, synthesis and mechanical properties, Acta Mater. 70 (2014) 92–104. doi:10.1016/j.actamat.2014.02.011.
[86] L.W.F. Mackenzie, M.O. Pekguleryuz, The recrystallization and texture of magnesium – zinc – cerium alloys, Scr. Mater. 59 (2008) 665–668. doi:10.1016/j.scriptamat.2008.05.021.
[87] A. El-Morsy, K. Manabe, H. Nishimura, Superplastic Forming of AZ31 Magnesium Alloy Sheet into a Rectangular Pan, Mater. Trans. 43 (2002) 2443–2448.
[88] Y. Chino, M. Kado, M. Mabuchi, Compressive deformation behavior at room temperature - 773 K in Mg-0.2 mass%(0.035at.%)Ce alloy, Acta Mater. 56 (2008) 387–394. doi:10.1016/j.actamat.2007.09.036.
[89] C.H. Cáceres, A.H. Blake, Solute and temperature effects on the strain hardening behaviour of Mg-Zn solid solutions, Mater. Sci. Forum. 567–568 (2008) 45–50. doi:10.4028/www.scientific.net/MSF.567-568.45.
[90] N. Stanford, M.R. Barnett, Effect of Zn Concentration and Grain Size on Prismatic Slip in Mg-Zn Binary Alloys, in: S.N. Mathaudhu, W.H. Sillekens, N.R. Neelameggham, N. Hort (Eds.), Magnes. Technol. 2012, Springer International Publishing, Cham, 2016: pp. 207–211. doi:10.1007/978-3-319-48203-3_39.
[91] A.H. Blake, C.H. Caceres, Solid-solution hardening and softening in Mg – Zn alloys, Mater. Sci. Eng. A. 484 (2008) 161–163. doi:10.1016/j.msea.2006.10.205.
[92] J.F. Nie, Y.M. Zhu, J.Z. Liu, X.Y. Fang, Periodic Segregation of Solute Atoms in Fully Coherent Twin Boundaries, Science (80-.). 340 (2013) 957. doi:10.1126/science.1229369.
[93] S.L. Shang, W.Y. Wang, B.C. Zhou, Y. Wang, K.A. Darling, L.J. Kecskes, S.N. Mathaudhu, Z.K. Liu, ScienceDirect Generalized stacking fault energy , ideal strength and twinnability of dilute Mg-based alloys : A first-principles study of shear deformation, Acta Mater. 67 (2014) 168–180. doi:10.1016/j.actamat.2013.12.019.
[94] X.Y. Yang, Y.K. Zhu, H. Miura, T. Sakai, Static recrystallization behavior of hot-deformed magnesium alloy AZ31 during isothermal annealing, Trans. Nonferrous Met. Soc. China (English Ed. 20 (2010) 1269–1274. doi:10.1016/S1003-6326(09)60289-2.

[95] W.W.Z. Jingyi, Predicting of thickness distribution of thin components by superplastic forming, Forg. Stamp. Technol. 6 (1998) 35–39.
[96] G. Palumbo, A. Cusanno, M.L. Garcia Romeu, I. Bagudanch, N. Contessi Negrini, T. Villa, S. Farè, Single Point Incremental Forming and Electrospinning to produce biodegradable magnesium (AZ31) biomedical prostheses coated with porous PCL, Mater. Today Proc. 7 (2019) 394–401. doi:10.1016/j.matpr.2018.11.101.
[97] J. Park, J. Kim, N. Park, Y. Kim, Study of forming limit for rotational incremental sheet forming of magnesium alloy sheet, Metall. Mater. Trans. A Phys. Metall. Mater. Sci. 41 (2010) 97–105. doi:10.1007/s11661-009-0043-7.
[98] D.L. Atwell, M.R. Barnett, W.B. Hutchinson, The effect of initial grain size and temperature on the tensile properties of magnesium alloy AZ31 sheet, Mater. Sci. Eng. A. 549 (2012) 1–6. doi:10.1016/j.msea.2012.03.107.
[99] P.C. Banerjee, S. Al-Saadi, L. Choudhary, S.E. Harandi, R. Singh, Magnesium implants: Prospects and challenges, Materials (Basel). 12 (2019) 1–21. doi:10.3390/ma12010136.
[100] R. Zeng, W. Dietzel, F. Witte, N. Hort, C. Blawert, Progress and Challenge for Magnesium Alloys as Biomaterials, Adv. Eng. Mater. 10 (2008) B3–B14. doi:10.1002/adem.200800035.